Couches absorbantes pour la propagation d'ondes dans les sols non bornés à l'aide de la décomposition en sous-domaines et l'intégration temporelle hybride asynchrone

Sijia Li

▶ **To cite this version:**

Sijia Li. Couches absorbantes pour la propagation d'ondes dans les sols non bornés à l'aide de la décomposition en sous-domaines et l'intégration temporelle hybride asynchrone. Génie civil. Université de Lyon, 2019. Français. NNT : 2019LYSEI042 . tel-02900509

HAL Id: tel-02900509
https://theses.hal.science/tel-02900509v1

Submitted on 16 Jul 2020

HAL is a multi-disciplinary open access archive for the deposit and dissemination of scientific research documents, whether they are published or not. The documents may come from teaching and research institutions in France or abroad, or from public or private research centers.

L'archive ouverte pluridisciplinaire **HAL**, est destinée au dépôt et à la diffusion de documents scientifiques de niveau recherche, publiés ou non, émanant des établissements d'enseignement et de recherche français ou étrangers, des laboratoires publics ou privés.

N°d'ordre NNT : 2019LYSEI042

THESE de DOCTORAT DE L'UNIVERSITE DE LYON
opérée au sein de
Institut National des Sciences Appliquées de Lyon

Ecole Doctorale N° 162
MEGA Mécanique, Energétique, Génie Civil et Acoustique

Spécialité/discipline de doctorat :
Mécanique - Génie Mécanique - Génie Civil

Soutenue publiquement le 08/07/2019, par :

Sijia LI

Couches absorbantes pour la propagation d'ondes dans les sols non bornés à l'aide de la décomposition en sous-domaines et l'intégration temporelle hybride asynchrone

Devant le jury composé de :

CHAILLAT, Stéphanie	Chargée de recherche (HDR) ENSTA ParisTech	Rapporteur
LENTI, Luca	Chargé de recherche (HDR) IFSTTAR	Rapporteur
SHAHROUR, Isam	Professeur Université de Lille	Examinateur
KUZNETSOV, Sergey	Professeur IPM Académie des sciences de Russie	Examinateur
DJERAN-MAIGRE, Irini	Professeur INSA Lyon	Directrice de thèse
BRUN, Michaël	Maître de Conférences (HDR) INSA Lyon	Directeur de thèse

Cette thèse est accessible à l'adresse : http://theses.insa-lyon.fr/publication/2019LYSEI042/these.pdf
© [S. Li], [2019], INSA Lyon, tous droits réservés

Cette thèse est accessible à l'adresse : http://theses.insa-lyon.fr/publication/2019LYSEI042/these.pdf
© [S. Li], [2019], INSA Lyon, tous droits réservés

Département FEDORA – INSA Lyon - Ecoles Doctorales – Quinquennal 2016-2020

SIGLE	ECOLE DOCTORALE	NOM ET COORDONNEES DU RESPONSABLE
CHIMIE	**CHIMIE DE LYON** http://www.edchimie-lyon.fr Sec. : Renée EL MELHEM Bât. Blaise PASCAL, 3e étage secretariat@edchimie-lyon.fr INSA : R. GOURDON	M. Stéphane DANIELE Institut de recherches sur la catalyse et l'environnement de Lyon IRCELYON-UMR 5256 Équipe CDFA 2 Avenue Albert EINSTEIN 69 626 Villeurbanne CEDEX directeur@edchimie-lyon.fr
E.E.A.	**ÉLECTRONIQUE, ÉLECTROTECHNIQUE, AUTOMATIQUE** http://edeea.ec-lyon.fr Sec. : M.C. HAVGOUDOUKIAN ecole-doctorale.eea@ec-lyon.fr	M. Gérard SCORLETTI École Centrale de Lyon 36 Avenue Guy DE COLLONGUE 69 134 Écully Tél : 04.72.18.60.97 Fax 04.78.43.37.17 gerard.scorletti@ec-lyon.fr
E2M2	**ÉVOLUTION, ÉCOSYSTÈME, MICROBIOLOGIE, MODÉLISATION** http://e2m2.universite-lyon.fr Sec. : Sylvie ROBERJOT Bât. Atrium, UCB Lyon 1 Tél : 04.72.44.83.62 INSA : H. CHARLES secretariat.e2m2@univ-lyon1.fr	M. Philippe NORMAND UMR 5557 Lab. d'Ecologie Microbienne Université Claude Bernard Lyon 1 Bâtiment Mendel 43, boulevard du 11 Novembre 1918 69 622 Villeurbanne CEDEX philippe.normand@univ-lyon1.fr
EDISS	**INTERDISCIPLINAIRE SCIENCES-SANTÉ** http://www.ediss-lyon.fr Sec. : Sylvie ROBERJOT Bât. Atrium, UCB Lyon 1 Tél : 04.72.44.83.62 INSA : M. LAGARDE secretariat.ediss@univ-lyon1.fr	Mme Emmanuelle CANET-SOULAS INSERM U1060, CarMeN lab, Univ. Lyon 1 Bâtiment IMBL 11 Avenue Jean CAPELLE INSA de Lyon 69 621 Villeurbanne Tél : 04.72.68.49.09 Fax : 04.72.68.49.16 emmanuelle.canet@univ-lyon1.fr
INFOMATHS	**INFORMATIQUE ET MATHÉMATIQUES** http://edinfomaths.universite-lyon.fr Sec. : Renée EL MELHEM Bât. Blaise PASCAL, 3e étage Tél : 04.72.43.80.46 infomaths@univ-lyon1.fr	M. Luca ZAMBONI Bât. Braconnier 43 Boulevard du 11 novembre 1918 69 622 Villeurbanne CEDEX Tél : 04.26.23.45.52 zamboni@maths.univ-lyon1.fr
Matériaux	**MATÉRIAUX DE LYON** http://ed34.universite-lyon.fr Sec. : Stéphanie CAUVIN Tél : 04.72.43.71.70 Bât. Direction ed.materiaux@insa-lyon.fr	M. Jean-Yves BUFFIÈRE INSA de Lyon MATEIS - Bât. Saint-Exupéry 7 Avenue Jean CAPELLE 69 621 Villeurbanne CEDEX Tél : 04.72.43.71.70 Fax : 04.72.43.85.28 jean-yves.buffiere@insa-lyon.fr
MEGA	**MÉCANIQUE, ÉNERGÉTIQUE, GÉNIE CIVIL, ACOUSTIQUE** http://edmega.universite-lyon.fr Sec. : Stéphanie CAUVIN Tél : 04.72.43.71.70 Bât. Direction mega@insa-lyon.fr	M. Jocelyn BONJOUR INSA de Lyon Laboratoire CETHIL Bâtiment Sadi-Carnot 9, rue de la Physique 69 621 Villeurbanne CEDEX jocelyn.bonjour@insa-lyon.fr
ScSo	**ScSo*** http://ed483.univ-lyon2.fr Sec. : Véronique GUICHARD INSA : J.Y. TOUSSAINT Tél : 04.78.69.72.76 veronique.cervantes@univ-lyon2.fr	M. Christian MONTES Université Lyon 2 86 Rue Pasteur 69 365 Lyon CEDEX 07 christian.montes@univ-lyon2.fr

*ScSo : Histoire, Géographie, Aménagement, Urbanisme, Archéologie, Science politique, Sociologie, Anthropologie

Cette thèse est accessible à l'adresse : http://theses.insa-lyon.fr/publication/2019LYSEI042/these.pdf
© [S. Li], [2019], INSA Lyon, tous droits réservés

Cette thèse est accessible à l'adresse : http://theses.insa-lyon.fr/publication/2019LYSEI042/these.pdf
© [S. Li], [2019], INSA Lyon, tous droits réservés

Résumé

L'un des enjeux des simulations numériques de propagation d'ondes par des méthodes numériques comme celle des éléments finis, est la modélisation des milieux infinis. Le moyen le plus simple est bien-sûr de considérer un très grand maillage étendu de sorte que les ondes réfléchies aux frontières du maillage ne viennent pas perturber la solution recherchée, mais cela peut conduire à des temps de calcul rédhibitoires, en particulier lors des excitations de longue durée. Par conséquent, des conditions aux limites absorbantes et non réfléchissantes, placées aux frontières du domaine tronqué, sont requises pour modéliser les milieux infinis. Le travail de thèse a pour objet de proposer de nouvelles formulations de couches absorbantes artificielles aux frontières des maillages éléments finis pour la simulation numérique de propagation d'ondes dans des milieux infinis 2D et 3D, afin de traiter des problèmes complexes d'interaction sol-structure en dynamique transitoire.

Trois couches absorbantes sont développées : les couches absorbantes basées sur les amortissements de Rayleigh ou de Kosloff et les PML (Perfectly Matched Layers). En étudiant analytiquement la forme forte de la propagation d'ondes dans chaque milieu, il est montré que les amortissements de Kosloff et ceux provenant de la PML sont indépendants de la fréquence, ce qui n'est pas le cas de l'amortissement de Rayleigh. Les problèmes de propagation d'ondes entre un milieu élastique non dissipatif et un milieu dissipatif sont aussi étudiés en prenant en compte la forme forte des équations de propagation d'ondes à l'interface. Des conditions optimales à l'interface permettant de calibrer les caractéristiques mécaniques des couches absorbantes en sont déduites afin de réduire les ondes parasites réfléchies.

La discrétisation spatiale des couches absorbantes est conduite via la méthode aux éléments finis, tandis que la discrétisation temporelle s'appuie sur le cadre performant et flexible des méthodes dites HATI (Heterogeneous Asynchronous Time Integrator), permettant de sélectionner, selon les caractéristiques des sous-domaines du problème et les phénomènes physiques qui s'y déroulent, les schémas d'intégration temporelle et les pas de temps les mieux adaptés. Ainsi, différentes possibilités offertes par l'approche HATI sont prospectées : les parties rigides d'un problème d'interaction sol-structure, comme les barrières d'ondes, sont intégrées dans le temps avec des schémas temporels implicites, la propagation d'ondes dans les sols avec des schémas

Cette thèse est accessible à l'adresse : http://theses.insa-lyon.fr/publication/2019LYSEI042/these.pdf
© [S. Li], [2019], INSA Lyon, tous droits réservés

explicites, et enfin, les couches artificielles avec des schémas soit implicites soit explicites, en considérant des pas de temps potentiellement différents dans chaque sous-domaine.

L'efficacité des trois couches absorbantes hybrides asynchrones pour la modélisation de domaines non bornés a été illustrée dans diverses applications numériques, 2D et 3D, telles que le test de Lamb dans des milieux hétérogènes stratifiés ou des problèmes d'interaction sol-structure avec des barrières d'ondes. Les avantages et les inconvénients de chaque couche absorbante sont soigneusement analysés, de même que leur précision et leur efficacité en termes de temps de calcul. Finalement, des versions implicite ou explicite de PML asynchrone sont mises en place et testées pour des problèmes avec un nombre important de degrés de liberté. Elles s'avèrent être plus précises et performantes que les couches absorbantes basées sur des amortissements de Rayleigh et Kosloff. En particulier, la version de PML asynchrone explicite apparaît comme une excellente candidate à une implémentation future dans des codes matures de sismologie basés sur des éléments spectraux.

Ces développements ont conduit à trois publications à comité de lecture, dont deux publiées et une soumise. Une quatrième publication sera issue du dernier chapitre de cette thèse, portant sur une version explicite de PML hybride asynchrone et une application pour la simulation des effets filtrants de barrières d'ondes horizontales.

"Three-dimensional hybrid asynchronous perfectly matched layer for wave propagation in unbounded domains", S.Li, M.Brun, I.Djeran-Maigre, S.Kuznetsov, soumis à *International Journal for Numerical Methods in Engineering,* mars 2019

"Hybrid asynchronous absorbing layers based on Kosloff damping for seismic wave propagation in unbounded domains", S.Li, M.Brun, I.Djeran-Maigre, S.Kuznetsov, *Computers and Geotechnics*, (109) 2019, 69-81

"Explicit/Implicit multi-time step co-simulation in unbounded medium with Rayleigh damping and application for wave barrier", S.Li, M.Brun, I.Djeran-Maigre, S.Kuznetsov, *European Journal of Environmental and Civil Engineering*, 2018, http://dx.doi.org/10.1080/19648189.2018.1506826

Mots-clefs : Couches absorbantes de Rayleigh ; Couches absorbantes de Kosloff ; Couches parfaitement adaptées (PML) ; Propagation d'ondes ; Milieux infinis ; Couplage sous-domaines ; Intégration Temporelle Hybride Asynchrone (HATI) ; Analyse transitoire ; Barrière d'ondes

Cette thèse est accessible à l'adresse : http://theses.insa-lyon.fr/publication/2019LYSEI042/these.pdf
© [S. Li], [2019], INSA Lyon, tous droits réservés

Abstract

The purpose of this thesis is to propose novel designs and formulations of different absorbing layers at the boundaries of finite element meshes for the numerical simulation of wave propagation in unbounded 2D and 3D media, in order to deal with complex soil-structure interaction problems in transient dynamics.

Three absorbing layers are developed: Rayleigh Absorbing Layer, Kosloff Absorbing Layer and Perfectly Matched Layer (PML). By studying analytically the strong form of elastic wave propagation in each medium, the frequency-independent absorbing ability of Kosloff damping and PML is derived, whereas the attenuation due to Rayleigh damping turns out be frequency-dependent. The interface problem between a non-dissipative elastic medium and a dissipative medium has been investigated by considering the wave propagation in the continuous setting, in order to establish optimal conditions to further reduce the spurious waves reflected at the interface.

The three absorbing layers are discretized in space by the finite element method, while the time discretization is based on the powerful and flexible HATI framework (Heterogeneous Asynchronous Time Integrator), enabling adopt the most suitable time integration schemes and time steps, depending on the characteristics and physical phenomena occurring in the different subdomains.

The efficiency of three asynchronous hybrid absorbing layers for modeling unbounded domains has been illustrated in various 2D and 3D numerical applications, such as Lamb's test in stratified heterogeneous media or soil-structure interaction problems involving wave barriers. Finally, implicit and explicit versions of asynchronous PML are implemented and tested in problems with a large number of degrees of freedom. It is proved to be more accurate and efficient than the absorbing layers based on Rayleigh and Kosloff damping.

Keywords: Wave propagation, Unbounded domains, Rayleigh absorbing layers, Kosloff absorbing layers, Perfect Matched Layers (PML), Multi-subdomain coupling, Heterogeneous asynchronous time integration, Hybrid formulation, Transient analysis, Wave barrier

Cette thèse est accessible à l'adresse : http://theses.insa-lyon.fr/publication/2019LYSEI042/these.pdf
© [S. Li], [2019], INSA Lyon, tous droits réservés

Cette thèse est accessible à l'adresse : http://theses.insa-lyon.fr/publication/2019LYSEI042/these.pdf
© [S. Li], [2019], INSA Lyon, tous droits réservés

Contents

Cette thèse est accessible à l'adresse : http://theses.insa-lyon.fr/publication/2019LYSEI042/these.pdf
© [S. Li], [2019], INSA Lyon, tous droits réservés

Cette thèse est accessible à l'adresse : http://theses.insa-lyon.fr/publication/2019LYSEI042/these.pdf
© [S. Li], [2019], INSA Lyon, tous droits réservés

Cette thèse est accessible à l'adresse : http://theses.insa-lyon.fr/publication/2019LYSEI042/these.pdf
© [S. Li], [2019], INSA Lyon, tous droits réservés

Cette thèse est accessible à l'adresse : http://theses.insa-lyon.fr/publication/2019LYSEI042/these.pdf
© [S. Li], [2019], INSA Lyon, tous droits réservés

List of Figures

Cette thèse est accessible à l'adresse : http://theses.insa-lyon.fr/publication/2019LYSEI042/these.pdf
© [S. Li], [2019], INSA Lyon, tous droits réservés

Cette thèse est accessible à l'adresse : http://theses.insa-lyon.fr/publication/2019LYSEI042/these.pdf
© [S. Li], [2019], INSA Lyon, tous droits réservés

Cette thèse est accessible à l'adresse : http://theses.insa-lyon.fr/publication/2019LYSEI042/these.pdf
© [S. Li], [2019], INSA Lyon, tous droits réservés

Cette thèse est accessible à l'adresse : http://theses.insa-lyon.fr/publication/2019LYSEI042/these.pdf
© [S. Li], [2019], INSA Lyon, tous droits réservés

Cette thèse est accessible à l'adresse : http://theses.insa-lyon.fr/publication/2019LYSEI042/these.pdf
© [S. Li], [2019], INSA Lyon, tous droits réservés

Cette thèse est accessible à l'adresse : http://theses.insa-lyon.fr/publication/2019LYSEI042/these.pdf
© [S. Li], [2019], INSA Lyon, tous droits réservés

List of Tables

Cette thèse est accessible à l'adresse : http://theses.insa-lyon.fr/publication/2019LYSEI042/these.pdf
© [S. Li], [2019], INSA Lyon, tous droits réservés

Cette thèse est accessible à l'adresse : http://theses.insa-lyon.fr/publication/2019LYSEI042/these.pdf
© [S. Li], [2019], INSA Lyon, tous droits réservés

Introduction

In order to reduce the tremendous loss caused by earthquake, the prediction of wave propagation in the soil is very important for the protection of the structures. Moreover, due to the increasing intensity of machine foundations or human activities such as railway and highway traffic, it is also necessary to improve the comfort for the people who live near the vibration sources against propagating waves by exhaustive analysis of wave motion on the ground. Based on the theory of continuum mechanics, the analytical model can be established by elastodynamics governing equations for wave propagation. However, in most cases, the problem characterized by their complex geometry, boundary conditions, nonlinear material behavior laws for the soil and the structure, is too difficult to be dealt with an analytical method, requiring the use of well-established numerical methods such as the Finite Element Method (FEM), largely adopted to treat engineering problems in different fields.

Finite element method (FEM) is a widely used numerical method for solving partial differential equations corresponding to the governing equations of the physical problem. The main advantages of the FEM are its versatility and flexibility, able to deal with non-linear behavior, irregular geometry, material anisotropy and heterogeneity, in comparison to the other numerical methods. The main idea is the discretization of the physical problem into finite elements in the space dimension to obtain the approximate solutions. After the space discretization, the equation of wave propagation problem should be discretized in time for transient dynamic analysis and solved in every time step. Time integration schemes are classified as explicit time integration schemes, in which the critical time step is imposed by the Courant–Friedrichs–Lewy (CFL) condition, and unconditionally stable implicit methods. The mostly used time integration methods in commercial software such as ABAQUS, ANSYS, LS-DYNA and DIANA, are Newmark time integration schemes and Central Difference scheme.

Cette thèse est accessible à l'adresse : http://theses.insa-lyon.fr/publication/2019LYSEI042/these.pdf
© [S. Li], [2019], INSA Lyon, tous droits réservés

In the numerical simulation of wave propagation problems in unbounded domains using the finite element method, one of the critical points is how to simulate infinite media. The simplest way is to consider a very large extended numerical mesh, but it leads to important computation time, in particular when long time duration excitations are considered. Hence non-reflective boundary conditions are required for mimicking infinite or semi-infinite media in order to reduce unbounded domains to truncated domains. Several kinds of artificial boundaries in numerical methods have been studied to avoid spurious waves reflected at the boundary, such as Rayleigh absorbing layers, Kosloff absorbing boundary or Perfectly Matched Layers (PML). Because of its easy implementation and availability in many FE codes, Rayleigh absorbing layer is very convenient to apply in wave propagation simulation with the multi-layer strategy called as Absorbing Layers using Increasing Damping (ALID). However, the attenuation ability of Rayleigh damping depends on the frequency and the introduction of Rayleigh matrix will decrease the value of the critical time step in explicit time integration scheme. In Kosloff medium, the wave travels without changing shape and the wave amplitude decreases with distance at a frequency independent rate. Even though it is rarely studied, some similarities between Kosloff absorbing boundary and the PML have been proved have been proved in the literature and is thoroughly studied in this thesis. PML (Perfect Matched Layers) is very popular for modelling infinite media, because of its independency on frequency and non-reflecting feature at the interface. The only drawback is that PML is difficult to implement in FE codes. In most formulations, the complex-coordinate-stretched equations used to introduce the PML, also serve to describe the interior domain, resulting in increasing computational cost.

Generally, the numerical model of wave propagation problem includes different physical domains. For example, in the numerical simulation of wave propagation in soil–structure interaction (SSI), the numerical model is composed of at least four parts: the vibration source, the bounded soil, the structure and the absorbing layer. Taking into account the different characteristics of each part, hybrid time integration schemes, asynchronous time steps and non-matching meshes are desired to satisfy the requirement of each part and reach the best computation efficiency. As a result, the standard homogeneous synchronous time integration approach using the same time integration scheme and the same time step is far from being optimal. Heterogeneous (different time integration schemes) asynchronous (different time steps depending on subdomains) time integration (HATI), based on the dual approach and proposed by Combescure and Gravouil in 2001

Cette thèse est accessible à l'adresse : http://theses.insa-lyon.fr/publication/2019LYSEI042/these.pdf
© [S. Li], [2019], INSA Lyon, tous droits réservés

(GC method) and extended later by Brun *et al.* in 2015 (BGC-macro and BGC-micro method) has been successfully carried out in various applications by coupling different subdomains independently, such as structure-structure interaction, soil-structure interaction and fluid-structure interaction. The BGC-micro method is an extended version of the GC method, enabling to use more modern time integrators than the ones from the Newmark family, endowed with high frequency filtering capabilities such as the α – Generalized time integration schemes.

The thesis aims to propose novel designs and formulations of different methods for modeling 2D and 3D infinite media in wave propagation simulation. Three absorbing layers (Rayleigh Absorbing Layer, Kosloff Absorbing Layer, and Perfect Matched Layer) are developed and implemented by the finite element method. Taking into account the different characteristics of each subdomain in the numerical model of wave propagation problem, the hybrid asynchronous formulations using the dual Schur approach, are implemented to enable the appropriate time integration scheme and independent time step in each subdomain, in the framework of Heterogeneous (different time integration schemes) Asynchronous (different time steps depending on subdomains) Time Integration (HATI).

The dissertation is organized in five chapters as follows:

Chapter 1 summarizes different aspects concerning the numerical simulation of wave propagation in unbounded domains. The principles of Finite Element method including the space discretization and time discretization are summarized. In the following, the previous researches for modelling unbounded domain relevant to Rayleigh absorbing layer, Kosloff absorbing boundary and Perfectly Matched Layers (PML) are presented, as well as a brief literature review on the development of heterogeneous (different time integration schemes) asynchronous (different time steps depending on subdomains) time integration (HATI).

Chapter 2 presents a simple and accurate method for modeling two-dimensional and three-dimensional unbounded domains based on Rayleigh damping. Subdomain decomposition strategy is applied in order to couple physical medium with Rayleigh absorbing layers, based on the GC method, in the framework of HATI. The proposed absorbing region is called Hybrid (different time integrators) Asynchronous (different time steps) Absorbing Layers using Increasing Damping (HA-ALID Rayleigh), enabling to integrate the Rayleigh absorbing layer using independent time integrators and time steps, without affecting the critical time step in the domain of interest handled

Cette thèse est accessible à l'adresse : http://theses.insa-lyon.fr/publication/2019LYSEI042/these.pdf
© [S. Li], [2019], INSA Lyon, tous droits réservés

with an explicit time integration. In order to highlight the accuracy of the method, numerical applications including Lamb's test and a wave barrier problem are considered to assess the HA-ALID Rayleigh efficiency using multi-time step Abaqus Explicit/Implicit co-simulation and self-developed FEM codes.

Chapter 3 investigates the capabilities of the Kosloff formulation to set up efficient HA-Kosloff ALID for modelling two-dimensional and three-dimensional unbounded domains, in comparison to Rayleigh formulation. Firstly, the design of Kosloff absorbing layer is proposed by using the strong form of elastic wave propagation in Kosloff medium. The absorbing ability, which is independent of frequency, is derived in the form of a logarithmic decrement, as well as optimal conditions to reduce the spurious waves reflected at the interface between physical domain and Kosloff absorbing layer domain. The weak formulation of the coupled problem, involving the interior domain and Kosloff absorbing layer, is given according to a dual coupling approach with the introduction of Lagrange multipliers, which enables integrate different subdomains in time with different time integrators associated with their own time step, according to HATI methods. Finally, numerical tests are carried out to illustrate the efficiency of HA-Kosloff ALID in terms of accuracy and CPU time, in comparison to HA-Rayleigh ALID and HA-PML.

Chapter 4 focuses on the development of one hybrid (different time integrators) asynchronous (different time steps) three-dimensional unsplit−field displacement-based PML formulation for three-dimensional problems in heterogeneous elastic infinite media. The frequency-independent absorbing ability and reflectionless feature at the interface between the non-dissipative interior domain and the PML are proved, on the basis of the strong form of wave propagation in PML media. The weak formulation leading to a novel efficient method for calculating the internal force in PML domain has been coupled with interior domain using the dual Schur approach, enabling unconditionally stable implicit time integration scheme in the PML with its own time step, whereas the interior domain is handled by the classical finite element formulation without complex-valued stretched coordinates, and explicit second-order accurate time integrator with a time step satisfying the CFL condition. Examples of three-dimensional semi-infinite bar, Lamb's test, and one classical soil–structure interaction problem with PML-truncated semi-infinite heterogeneous media are investigated to illustrate the efficiency of the hybrid asynchronous formulation in terms of accuracy and CPU time.

Cette thèse est accessible à l'adresse : http://theses.insa-lyon.fr/publication/2019LYSEI042/these.pdf
© [S. Li], [2019], INSA Lyon, tous droits réservés

Chapter 5 deals with a more complex 3D SSI situation, such as the mitigation of ground surface vibration through Horizontal Wave Barrier (HWB), set up close to an excited plate, representing, for instance, the slab track excited by the tramway wheels. Contrarily to the previous chapters, an explicit version of PML is developed in order to reduce the computation time for large simulations and compared to HA-Rayleigh ALID and HA-Kosloff ALID for modelling three-dimensional unbounded domains. Moreover, it is shown that better accuracy can be achieved when considering fine time steps in the HA-PML and HA-Kosloff ALID. Finally, it is shown that explicit HA-PML is the most efficient option for three-dimensional absorbing layers. A 3D numerical study of the Horizontal Wave Barrier (HWB) is then carried out, in the context of vibration isolation against the ground surface wave propagation produced by trains and tramways.

Chapter 6 presents the overall conclusions for the development in the thesis, as well as the perspectives for further studies.

Cette thèse est accessible à l'adresse : http://theses.insa-lyon.fr/publication/2019LYSEI042/these.pdf
© [S. Li], [2019], INSA Lyon, tous droits réservés

Cette thèse est accessible à l'adresse : http://theses.insa-lyon.fr/publication/2019LYSEI042/these.pdf
© [S. Li], [2019], INSA Lyon, tous droits réservés

Chapter 1

State of the Art

In this first chapter, the strong form of the wave propagation in elastic media is given with a view to introducing space and time discretization for the numerical simulation. First, strong forms for different damping formulations are reminded, including Rayleigh damping, Kosloff damping and Perfectly Matched Layers (PML). Second, we focus on finite element method for the space discretization, whereas the time integration uses the flexible and powerful framework of Heterogeneous (different time integration schemes) Asynchronous (different time steps) Time Integrator. Newmark time integration schemes are employed in this thesis, including the unconditionally stable implicit Newmark scheme, called also Constant Average Acceleration scheme in the literature, as well as the conditionally stable explicit Newmark scheme. The methods and damping formulations briefly presented in this chapter will be employed to set up Heterogeneous Asynchronous Rayleigh and Kosloff absorbing layers as well as Heterogeneous Asynchronous PML, in 2D and 3D finite element transient dynamic analyses, thoroughly detailed in the next chapters.

Cette thèse est accessible à l'adresse : http://theses.insa-lyon.fr/publication/2019LYSEI042/these.pdf
© [S. Li], [2019], INSA Lyon, tous droits réservés

1.1 Wave propagation in elastic media

Wave propagation is a physical phenomenon which describes the evolution and progression of propagating waves in elastic media. Based on the theory of continuum mechanics, the linear elastodynamics governing equations for wave propagation in an homogeneous and isotropic medium Ω are shown below:

$$\rho \partial_t^2 \underline{u} = div\left(\underline{\underline{\sigma}}(\underline{u})\right) \tag{1.1}$$

$$\underline{\underline{\sigma}} = \lambda \mathrm{tr}\left(\underline{\underline{\varepsilon}}(\underline{u})\right) + 2\mu \underline{\underline{\varepsilon}}(\underline{u}) \tag{1.2}$$

$$\underline{\underline{\varepsilon}} = \frac{1}{2}\left[grad(\underline{u}) + grad(\underline{u})^T\right] \tag{1.3}$$

where $\underline{u}$ is the displacement vector field governed by before-mentioned equations, $\underline{\underline{\sigma}}$ is the stress tensor, $\underline{\underline{\varepsilon}}$ is strain tensor, λ and μ are Lamé's coefficients, ρ is the density, respectively. The first equation is the equation of motion, the second equation represents Hooke's law and the last equation is the deformation equation. Eqs. (1.1) to (1.3) constitute the strong form of wave propagation in an elastic medium. The Neumann conditions and Dirichlet conditions are given on the boundary Γ:

$$\begin{cases} \underline{\underline{\sigma}} \cdot n = \underline{g}^N & \text{on } \Gamma_N \\ \underline{u} = \underline{u}^D & \text{on } \Gamma_D \end{cases} \tag{1.4}$$

Here, in the context of civil engineering problems, the wave propagation is produced by the ground vibration, including earthquake and human activities, such as railway and highway traffic (Semblat and Pecker, 2009). There are four types of waves propagating in the soil at the same time, involving P-wave, S-wave, Rayleigh wave and Love wave, as shown in Fig.1-1(Heirbrant, 2006). P-wave and S-wave are elastic body waves, which travel into the body of the soil. P-wave is the fastest wave and also called longitudinal wave or pressure wave, because the propagation direction is the same as the motion direction of particles in the medium. Similarly, S-wave is also called transverse wave or shear wave and the propagation direction is perpendicular to the motion direction of particles.

Cette thèse est accessible à l'adresse : http://theses.insa-lyon.fr/publication/2019LYSEI042/these.pdf
© [S. Li], [2019], INSA Lyon, tous droits réservés

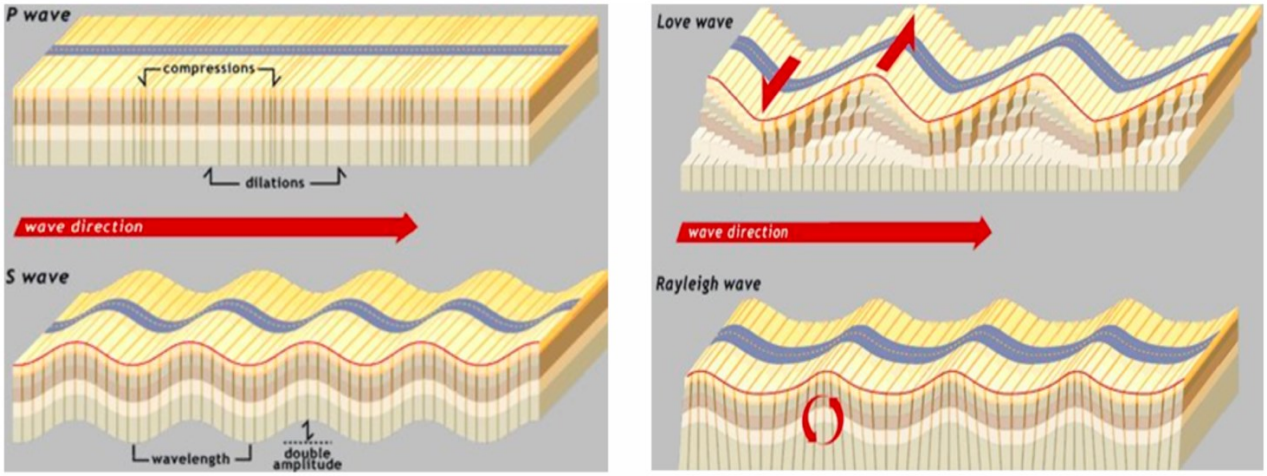

Figure 1-1 Waves propagating in the soil

Different from P-wave and S-wave, Love wave and Rayleigh wave are surface waves. Love wave is horizontally polarized and the result of the S-wave interference, which can be observed in case of a low-velocity layer overlying a high-velocity layer. The velocity of Love wave is smaller than P-wave and S-wave, but faster than Rayleigh wave. Rayleigh waves are surface waves propagating along the surface and include both longitudinal and transverse motions. With the increasing distance from the surface, the amplitude of Rayleigh waves decreases exponentially.

Based on the elastic wave theory, the P-wave and S-wave velocities are expressed as:

$$v_p = \sqrt{\frac{E(1-\nu)}{\rho(1+\nu)(1-2\nu)}} \tag{1.5}$$

$$v_S = \sqrt{\frac{E}{2\rho(1+\nu)}} \tag{1.6}$$

where E is Young's modulus and ν the Poisson coefficient. A good approximation of the Rayleigh-wave velocity is given by:

$$v_R = \frac{0.87 + 1.12\nu}{1+\nu} v_S \tag{1.7}$$

Cette thèse est accessible à l'adresse : http://theses.insa-lyon.fr/publication/2019LYSEI042/these.pdf
© [S. Li], [2019], INSA Lyon, tous droits réservés

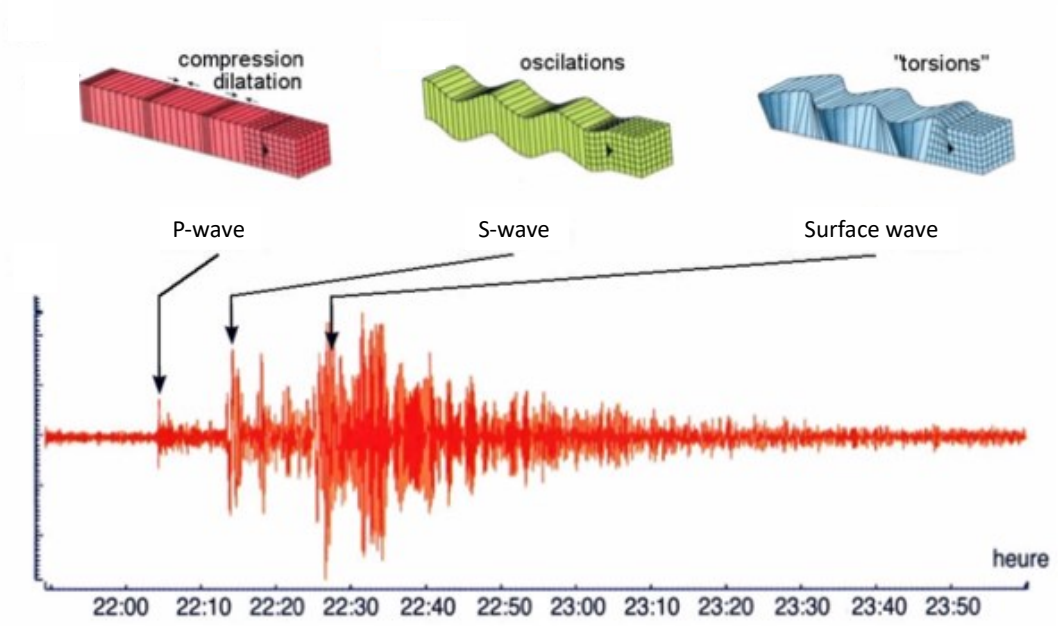

Figure 1-2 The time history of seismic waves recorded at an observation point

Due to the higher speeds, the P and S waves generated by an earthquake arrive before the surface waves, as shown in Fig.1-2 (Viora, 2017). However, the particle motion of surface waves is larger than that of body waves, the surface waves carry most of the energy and tend to cause more damage (Milsom, 2003).

In the case of one-dimension, the velocity v of P-waves is equal to $\sqrt{\frac{E}{\rho}}$ and $\sqrt{\frac{\mu}{\rho}}$ for S-wave. The harmonic wave propagating in one-dimension elastic medium can be expressed in complex form which can greatly facilitate the calculation, as below:

$$u(x,t) = u_0\, exp(\, i(\omega_0 t - k_0 x)) \tag{1.8}$$

The prediction of wave propagation in the soil is very important for the protection of the buildings against propagating waves, in order to reduce the tremendous loss caused by earthquake and improve the comfort for the people who live near the vibration sources. However, in most cases, the problem characterized by their complex geometry, boundary conditions, nonlinear material behavior laws for the soil, is too difficult to be dealt with an analytical method, requiring

Cette thèse est accessible à l'adresse : http://theses.insa-lyon.fr/publication/2019LYSEI042/these.pdf
© [S. Li], [2019], INSA Lyon, tous droits réservés

the use of well-established numerical methods such as the Finite Element Method (Hughes, 1987; Belytschko *et al*., 2000; Zienkiewicz, 2005; Smith *et al*., 2014).

1.2 Finite element method

Finite element method (FEM) is a numerical method for solving partial differential equations which are the governing equations of the physical problem. The main idea is the discretization of the physical problem into small finite elements in the space dimension to obtain the approximate solutions. Firstly, the strong form (differential equation) should be transformed to the weak form (integral equation) by introducing test functions, according to the virtual power principle. Then, the continuum domain will be discretized into finite elements and appropriate shape functions depending on the element type are applied to discretize continuous quantities to discrete nodal quantities, leading to the global matrix equation, which can be assembled from the element-wise matrices. Finally, after taking into account the boundary conditions, the nodal solutions can be obtained. Today, FEM is widely used to treat engineering problems in different fields, including structural analysis, transient analysis, and fluid flow. Some commercial software for numerical simulation based on FEM are available, such as ABAQUS, ANSYS, LS-DYNA and Diana. The main advantages of the finite element method in comparison to the other numerical methods, are its versatility and flexibility, able to deals with non-linear behaviors, irregular geometry, material anisotropy and heterogeneity.

1.2.1 Spatial discretization by finite element method

Here, we concentrate on the discretization of wave propagation in elastic media in space. Let Ω be a bounded domain with a regular boundary Γ. The domain Ω is characterized by its density ρ, Young's modulus E, Poisson's coefficient ν, $\underline{u}^D$ the Dirichlet prescribed displacement on Γ_D and $\underline{g}^N$ the traction force at the Neumann condition on Γ_N. By introducing the test function $\underline{v}$ belonging to the appropriate space $\underline{v} \in W^* = \left\{\underline{v} \in \left(H(\Omega)\right)^d and\ \underline{v} = 0\ on\ \Gamma_D\right\}$, where d is the space

Cette thèse est accessible à l'adresse : http://theses.insa-lyon.fr/publication/2019LYSEI042/these.pdf
© [S. Li], [2019], INSA Lyon, tous droits réservés

dimension, we seek the solution belonging to the space $W = \left\{\underline{u} \in \left(H(\Omega)\right)^d and\ \underline{u} = \underline{u}^D on\ \Gamma_D\right\}$, satisfying the following weak form:

$$\int_\Omega \rho \underline{v} \cdot \underline{\ddot{u}} d\Omega + \int_\Omega \underline{\underline{\varepsilon}}(\underline{v}) : \underline{\underline{\sigma}} d\Omega = \int_\Gamma \underline{v} \cdot \underline{g}^N d\Gamma \tag{1.9}$$

The weak form is also called the principle of virtual power, where the stress tensor $\underline{\underline{\sigma}}$ satisfies the behavior law given in Eq. (1.2). Then, we follow the classical lines of the finite element discretization with shape functions, the semi-discrete equation in space can be derived:

$$\mathbf{M\ddot{U} + KU = F^{ext}} \tag{1.10}$$

The global mass matrix **M** and the global stiffness matrix **K** are assembled from their respective element-level matrices:

$$\mathbf{M^e} = \int_{\Omega^e} \rho \mathbf{N^T N}\, \mathrm{d}\Omega \tag{1.11}$$

$$\mathbf{K^e} = \int_{\Omega^e} \mathbf{B^T D B}\, \mathrm{d}\Omega \tag{1.12}$$

In the following, the two-dimensional case is detailed under the plane-strain assumption. The material constitutive matrix is expressed as:

$$\mathbf{D} = \frac{E(1-\nu)}{(1+\nu)(1-2\nu)} \begin{bmatrix} 1 & \frac{\nu}{1-\nu} & 0 \\ \frac{\nu}{1-\nu} & 1 & 0 \\ 0 & 0 & \frac{1-2\nu}{2(1-\nu)} \end{bmatrix} \tag{1.13}$$

The element-level matrices can be obtained in every 4-nodes rectangular element by using the following linear shape functions:

$$\begin{cases} N_1 = (1-\xi)(1-\eta)/4 \\ N_2 = (1+\xi)(1-\eta)/4 \\ N_3 = (1+\xi)(1+\eta)/4 \\ N_4 = (1-\xi)(1+\eta)/4 \end{cases} \tag{1.14}$$

Cette thèse est accessible à l'adresse : http://theses.insa-lyon.fr/publication/2019LYSEI042/these.pdf
© [S. Li], [2019], INSA Lyon, tous droits réservés

The approximation of the displacement is given by: $u_e(x,y) = \mathbf{N}(x,y)\mathbf{U_e}$, where $\mathbf{U_e}$ gathers the nodal displacements of the 4 nodes, of size 8×1; the matrix $\mathbf{N}(x,y,z)$, of size 2×8, contains the nodal shape functions: $\mathbf{N}(x,y,z) = [N_1\mathbf{I} \quad N_2\mathbf{I} \quad N_3\mathbf{I} \quad N_4\mathbf{I}]$, with $\mathbf{I}$ the 2×2 identity matrix. The matrix **B** will be expressed as below,

$$\mathbf{B} = [\mathbf{B_1}\ \mathbf{B_2}\ \mathbf{B_3}\ \mathbf{B_4}], \quad \boldsymbol{B_i} = \begin{bmatrix} \frac{\partial N_i}{\partial x} & 0 \\ 0 & \frac{\partial N_i}{\partial y} \\ \frac{\partial N_i}{\partial y} & \frac{\partial N_i}{\partial x} \end{bmatrix} \tag{1.15}$$

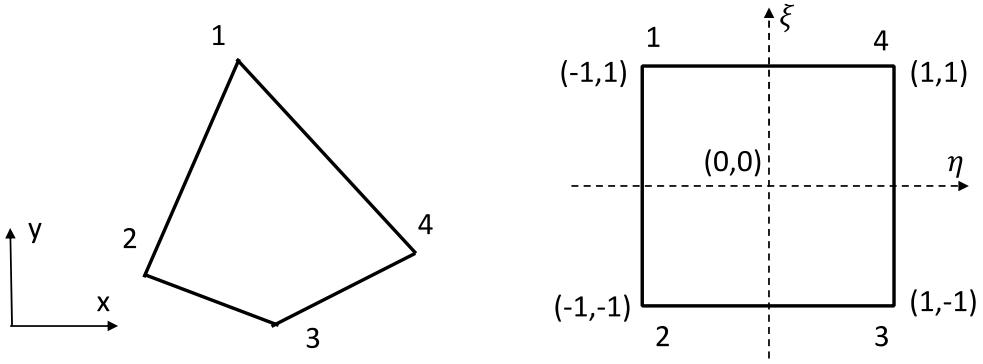

Figure 1-3 4-nodes rectangular finite element

Next, the matrices defined in the global coordinates (x,y) should be expressed in local (ξ,η) coordinate systems to facilitate the calculation of the integrals. If coordinate relation functions are the same as shape functions, the elements are called isoparametric elements. The relationship for coordinate transformation is shown in the following:

$$x = \sum_{i=1}^{4} N_i(\xi,\eta)x_i \tag{1.16}$$

$$y = \sum_{i=1}^{4} N_i(\xi,\eta)y_i \tag{1.17}$$

By using the above relationship, the matrices in the global coordinates are computed in local (ξ,η) coordinate systems:

Cette thèse est accessible à l'adresse : http://theses.insa-lyon.fr/publication/2019LYSEI042/these.pdf
© [S. Li], [2019], INSA Lyon, tous droits réservés

$$\mathbf{M^e} = \int_{\Omega^e} \rho N(x,y)^T N(x,y) dx\, dy = \int_{-1}^{1}\int_{-1}^{1} \rho N(\xi,\eta)^T N(\xi,\eta) \det|\mathbf{J}(\xi,\eta)|\, d\xi\, d\eta \quad (1.18)$$

$$\mathbf{K^e} = \int_{\Omega^e} B(x,y)^T D B(x,y) dx\, dy = \int_{-1}^{1}\int_{-1}^{1} B(\xi,\eta)^T D B(\xi,\eta) \det|\mathbf{J}(\xi,\eta)|\, d\xi\, d\eta \quad (1.19)$$

with **J** the Jacobian matrix:

$$\mathbf{J}(\xi,\eta) = \begin{bmatrix} \frac{\partial N_1}{\partial \xi} & \frac{\partial N_2}{\partial \xi} & \frac{\partial N_3}{\partial \xi} & \frac{\partial N_4}{\partial \xi} \\ \frac{\partial N_1}{\partial \eta} & \frac{\partial N_2}{\partial \eta} & \frac{\partial N_3}{\partial \eta} & \frac{\partial N_4}{\partial \eta} \end{bmatrix} \begin{bmatrix} x_1 & y_1 \\ x_2 & y_2 \\ x_3 & y_3 \\ x_4 & y_4 \end{bmatrix} \quad (1.20)$$

In most of the cases, the integrals in above matrices are difficult to calculate by analytical method. Therefore, in finite element implementation, they are usually evaluated by using Gauss–Legendre quadrature (Irons, 1966). In two-dimensional full integration with linear shape functions, four Gauss points $\left(\pm\sqrt{1/3}, \pm\sqrt{1/3}\right)$ with the same weighting coefficients equal to 1 are required, giving the following elementary mass and stiffness matrices:

$$\mathbf{M^e} = \int_{-1}^{1}\int_{-1}^{1} \rho \mathbf{N}(\xi,\eta)^T \mathbf{N}(\xi,\eta) \det|\mathbf{J}|\, d\xi\, d\eta = \sum_{i=1}^{2}\sum_{j=1}^{2} w_i w_j \rho \mathbf{N}(\xi,\eta)^T \mathbf{N}(\xi,\eta) \det|\mathbf{J}| \quad (1.21)$$

$$\mathbf{K^e} = \int_{-1}^{1}\int_{-1}^{1} \mathbf{B}(\xi,\eta)^T \mathbf{D}\mathbf{B}(\xi,\eta) \det|\mathbf{J}|\, d\xi\, d\eta = \sum_{i=1}^{2}\sum_{j=1}^{2} w_i w_j \mathbf{B}(\xi,\eta)^T \mathbf{D}\mathbf{B}(\xi,\eta) \det|\mathbf{J}| \quad (1.22)$$

1.2.2 Time discretization in transient dynamics

After the space discretization by finite element method, the matrix equation of wave propagation problem should be discretized in time for transient dynamics analysis and solved in every time step. Time integration schemes classified as explicit and implicit methods for transient dynamics are widely studied. Some famous time integration methods, such as Newmark scheme (Newmark, 1959), Runge–Kutta scheme (Demailly, 2006), and Hilber–Hughes–Taylor (Hilber *et al*., 1977) scheme have been developed and applied successfully in numerical simulations of

Cette thèse est accessible à l'adresse : http://theses.insa-lyon.fr/publication/2019LYSEI042/these.pdf
© [S. Li], [2019], INSA Lyon, tous droits réservés

different fields by finite element method. Nowadays, the mostly used time integration methods in commercial software for numerical simulation based on FEM are Newmark schemes.

The classical approximate Newmark formulas in terms of the displacements and velocities at the end of this time step (a time step Δt is defined by the beginning time t_n and the end time t_{n+1}) are expressed in acceleration format as below:

$$\mathbf{U^{n+1}} = \mathbf{U^{n,p}} + \beta \Delta t^2 \ddot{\mathbf{U}}^{\mathbf{n+1}} \tag{1.23}$$

$$\dot{\mathbf{U}}^{\mathbf{n+1}} = \dot{\mathbf{U}}^{\mathbf{n,p}} + \gamma \Delta t \ddot{\mathbf{U}}^{\mathbf{n+1}} \tag{1.24}$$

β and γ are the classical parameters of the Newmark scheme. The predictor quantities are defined as:

$$\mathbf{U^{n,p}} = \mathbf{U^n} + \Delta t \dot{\mathbf{U}}^{\mathbf{n}} + \Delta t^2 \left(\frac{1}{2} - \beta\right) \ddot{\mathbf{U}}^n \tag{1.25}$$

$$\dot{\mathbf{U}}^{\mathbf{n,p}} = \dot{\mathbf{U}}^{\mathbf{n}} + \Delta t(1-\gamma) \ddot{\mathbf{U}}^{\mathbf{n}} \tag{1.26}$$

By introducing the expressions of the kinematic quantities into Eq. (1.10), it leads to the equation of motion written in the form below:

$$\widetilde{\mathbf{M}} \ddot{\mathbf{U}}^{\mathbf{n+1}} = \mathbf{F^{ext}} - \mathbf{K U^{n,p}} \tag{1.27}$$

with the effective stiffness matrix defined by:

$$\widetilde{\mathbf{M}} = \mathbf{M} + \beta \Delta t^2 \mathbf{K} \tag{1.28}$$

When γ=0.5 and β=0.25, it is an implicit time integration scheme unconditionally stable. With γ=0.5 and β=0, it is an explicit time integration scheme, called Newmark explicit scheme where the mass matrix **M** is lumped in order to avoid system solving in Eq. (1.28). In terms of stability, the critical time step in explicit scheme is imposed by the Courant–Friedrichs–Lewy condition (Courant *et al*., 1928). To ensure the stability the time step in explicit scheme must be smaller than the critical time step imposed by the CFL condition. An approximation of the CFL condition is written as the smallest transient time of a P wave across the smallest elements in the mesh:

$$\Delta t \leq \frac{L_{\min}}{v_p} \tag{1.29}$$

Cette thèse est accessible à l'adresse : http://theses.insa-lyon.fr/publication/2019LYSEI042/these.pdf
© [S. Li], [2019], INSA Lyon, tous droits réservés

For 4-nodes rectangular element with dimension L_1 and L_2, Flanagan and Belytschko (1981) have shown that, the critical time step is:

$$\Delta t \leq \frac{1}{v_p \sqrt{(\frac{1}{L_1})^2 + (\frac{1}{L_2})^2}} \tag{1.30}$$

In Abaqus/Explicit, the stable time increment chosen will be less than this estimate by a factor between $1/\sqrt{2}$ and 1 in a two-dimensional model and between $1/\sqrt{3}$ and 1 in a three-dimensional model. It is important to note that stability of the explicit Newmark scheme with viscous terms in equation of motion can be affected in comparison to the case without damping. Indeed, when a velocity-dependent term is taken into account in the semi-discrete equation of motion, it is useful to write this term with a time lag in order to make the resolution completely explicit. As underlined by Belytschko *et al*. (2000), the introduced time lag for the velocity-dependent term decreases the stable time step. In the following, we will employ two slightly different versions of the explicit schemes: for a non-dissipative medium, the explicit Newmark scheme is employed, without the need to write the velocity at the mid-step, whereas, when damping is introduced into the equation of motion, Central Difference scheme is adopted with the time lag for the velocity-dependent term.

1.3 Multi-time step subdomain coupling method

As shown in the Fig.1-4, let Ω be a bounded domain belonging to $\mathbb{R}^2$ with a regular boundary, which is composed of two subdomains Ω_1 and Ω_2, $\Omega_1 \cap \Omega_2 = \varnothing$ and $\partial\Omega_1 \cap \partial\Omega_2 = \Gamma_I$, Γ_I is the interface between the two subdomains. Based on the physical phenomena and computational considerations, the subdomain Ω_1 needs to be integrated by explicit scheme in time, while the subdomain Ω_2 requires the implicit time integration scheme. For example, in the numerical simulation of wave propagation in soil–structure interaction (SSI), the classical time discretization for wave propagation in soil is an explicit scheme for predicting in an accurate and efficient way the high-frequency propagating waves, while it uses an implicit scheme for the stiffer structure with non-linear mechanical behavior. In terms of time-stepping, the time step in subdomain Ω_1 should be enough small on the basis of the CFL condition, taking into account the material characteristics and the mesh. On the contrary, the implicit time integration scheme in subdomain

Cette thèse est accessible à l'adresse : http://theses.insa-lyon.fr/publication/2019LYSEI042/these.pdf
© [S. Li], [2019], INSA Lyon, tous droits réservés

Ω_2 is unconditionally stable. Thus, it advocates for an asynchronous time integration which is beneficial to optimize the computation time, with a fine time step in subdomain Ω_1 and an independent large time step in subdomain Ω_2. In this case, the standard homogeneous synchronous time integration approach using the same time integration scheme and the same time step is no longer relevant. Therefore, many studies were carried out in the last years on developing subdomain approach in order to set up numerical methods for coupling different subdomains at the interface more independently.

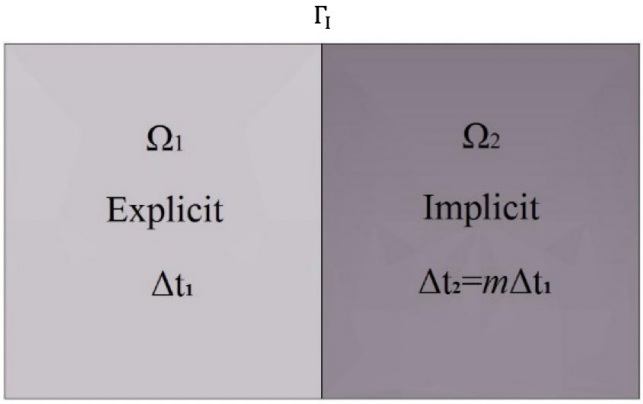

Figure 1-4 Subdomain Ω_1 integrated by an explicit scheme with fine time step and subdomain Ω_2 integrated by an implicit scheme with large time step

Generally, the HATI in finite element calculations can be classified in two types. The first is based on the primal approach, by imposing directly the continuity of subdomain kinematic quantities on nodes at the interface in a strong way. Hughes and Liu (1978) proposed one Explicit/Implicit mixed method, using the same time step in all the subdomains. Belytshko *et al.* (1979) developed one multi-time step algorithm for homogeneous time integration. However, by adopting asynchronous time step in subdomains, the main difficulty of the primal approach resides in the stability problem, produced by the interpolation of nodal values in the subdomain with large time step, in order to obtain the displacements, velocities or accelerations relative to the subdomain with fine time step (Belytshko and Lu, 1992; Klisinski and Mostrom, 1998; Daniel, 1998). The second type of coupling approach is the dual approach. Instead of imposing directly the continuity of subdomain kinematic quantities on nodes, the kinematic continuity at the interface between two non-overlapping subdomains is ensured in a weak way by means of Lagrange multipliers, which enable to couple different subdomains more independently. Based on the dual approach, Farhat

Cette thèse est accessible à l'adresse : http://theses.insa-lyon.fr/publication/2019LYSEI042/these.pdf
© [S. Li], [2019], INSA Lyon, tous droits réservés

and Roux (1991), Farhat *et al.* (1994) proposed Finite Element Tearing and Interconnecting Method (FETI). Later, in the framework of the FETI method, Combescure and Gravouil (2001, 2002) developed an extension of the method allowing different schemes and different time steps in each subdomain, called the GC coupling method. Using the continuity of velocities imposed at the interface, it was demonstrated that the coupling GC method is stable for any Newmark integrators (implicit and explicit) with their own time step depending on subdomains, according to the energy method (Hughes, 1987). When adopting the same time step, second order of accuracy is achieved. It leads to the first order of accuracy when different time steps are adopted due to a slight spurious dissipation at the interface. Recently, the GC method has been extended to couple other time integration schemes (Gravouil *et al.*, 2015; Brun *et al.*, 2015), leading to the proposition of a general framework, called Heterogeneous (different time integration schemes) Asynchronous (different time steps depending on subdomains) Time Integration (HATI). Co-simulations based on the GC coupling method have been successfully carried out in various applications by differently integrating in time partitions of a complex problem: structure-structure interaction problem in structural dynamics (Brun *et al.*, 2012; 2014), soil-structure interaction (Brun *et al.*, 2015), non-smooth dynamics with impacts and contacts (Fekak *et al*. 2017), and fluid-structure interaction (Nunez-Ramirez *et al.*, 2017).

Here, one example of Explicit/Implicit co-simulation in accordance with Fig.1-4, is given to illustrate the GC coupling algorithm. An independent explicit integrator with the fine time step Δt_1 will be adopted for the elastic subdomain Ω_1 and a different implicit integrator with the large time step Δt_2 will be used for elastic subdomain Ω_2 based on the subdomain strategy proposed by Gravouil and Combescure, $\Delta t_2 = m\Delta t_1$, m is the time step ratio between two subdomains. The velocity continuity condition is imposed at the fine time-scale, associated with the explicit time integration, whereas the implicit partition is integrated with the large time scale. In other words, the equilibrium of subdomain 2 is prescribed at time $t_m = \Delta t_2$, while the equilibrium of subdomain 1 is prescribed at time $t_j = j\Delta t_1$ $(j = 1, 2 \ldots m)$. The problem of subdomain Ω_1 and subdomain Ω_2 can be written by the finite element method as below,

Subdomain Ω_1 at the fine time step:

$$\mathbf{M_1}\ddot{\mathbf{U}}_\mathbf{1}^\mathbf{j} + \mathbf{K_1}\mathbf{U}_\mathbf{1}^\mathbf{j} = \mathbf{F}_\mathbf{1}^{\mathbf{ext,j}} - \mathbf{L}_\mathbf{1}^\mathbf{T}\boldsymbol{\lambda}^\mathbf{j} \tag{1.31}$$

Cette thèse est accessible à l'adresse : http://theses.insa-lyon.fr/publication/2019LYSEI042/these.pdf
© [S. Li], [2019], INSA Lyon, tous droits réservés

Subdomain Ω_2 at the large time step:

$$\mathbf{M_2}\ddot{\mathbf{U}}_2^{\mathbf{m}} + \mathbf{K_2}\mathbf{U}_2^{\mathbf{m}} = \mathbf{F}_2^{\mathbf{ext,m}} - \mathbf{L}_2^{\mathbf{T}}\boldsymbol{\lambda}^{\mathbf{m}} \tag{1.32}$$

At the interface, the continuity of velocities is imposed at time t_j as:

$$\mathbf{L_1}\dot{\mathbf{U}}_1^{\mathbf{j}} + \mathbf{L_2}\dot{\mathbf{U}}_2^{\mathbf{j}} = 0 \tag{1.33}$$

where $\boldsymbol{\lambda}$ is the Lagrange multiplier vector corresponding to the nodal forces at the interface, $\mathbf{L_1}$ and $\mathbf{L_2}$ are the boolean matrices, operating on nodal vectors associated with the two subdomains $\Omega_1$and Ω_2. In the case of non-matching meshes, mortar approach has to be applied, leading to non-boolean constraint matrices $\mathbf{L_1}$ and $\mathbf{L_2}$ (Zuchowski *et al.*, 2018). $\mathbf{M_i}$ and $\mathbf{K_i}$ are the mass and the stiffness matrices of subdomains $\Omega_1$and Ω_2 respectively,

$$\widetilde{\mathbf{M}}_1\ddot{\mathbf{U}}_1^{\mathbf{j}} = \mathbf{F}_1^{\mathbf{ext,j}} - \mathbf{K_1}\mathbf{U}_1^{\mathbf{j-1,p}} - \mathbf{L}_1^{\mathbf{T}}\boldsymbol{\lambda}^{\mathbf{j}} \tag{1.34}$$

$$\widetilde{\mathbf{M}}_2\ddot{\mathbf{U}}_2^{\mathbf{m}} = \mathbf{F}_2^{\mathbf{ext,m}} - \mathbf{K_2}\mathbf{U}_2^{\mathbf{0,p}} - \mathbf{L}_2^{\mathbf{T}}\boldsymbol{\lambda}^{\mathbf{m}} \tag{1.35}$$

with the effective stiffness matrices defined for the two subdomains by:

$$\widetilde{\mathbf{M}}_1 = \mathbf{M_1} \tag{1.36}$$

$$\widetilde{\mathbf{M}}_2 = \mathbf{M_2} + \beta_2\Delta t_2^2\mathbf{K_2} \tag{1.37}$$

The kinematic quantities are divided into two parts: the free and the linked quantities. The free quantities are calculated by taking into account the internal and external forces, whereas the linked quantities are obtained from the interface loads given by the Lagrange multiplier vector $\boldsymbol{\lambda}$. It was demonstrated (Combescure and Gravouil, 2001; 2002) that the kinematic continuity condition can be expressed as a reduced-size interface problem as follows:

$$\mathbf{H}\boldsymbol{\lambda}^{\mathbf{j}} = \boldsymbol{b}^{\boldsymbol{j}} \tag{1.38}$$

with the interface operator and the right-hand side member vector defined by:

$$\begin{cases} \mathbf{H} = \gamma_1\Delta t_1\mathbf{L_1}\widetilde{\mathbf{M}}_1^{-1}\mathbf{L}_1^{\mathbf{T}} + \gamma_2\Delta t_2\mathbf{L_2}\widetilde{\mathbf{M}}_2^{-1}\mathbf{L}_2^{\mathbf{T}} \\ \boldsymbol{b}^{\boldsymbol{j}} = \mathbf{L_1}\dot{\mathbf{U}}_1^{\mathbf{free,j}} + \mathbf{L_2}\dot{\mathbf{U}}_2^{\mathbf{free,j}} \end{cases} \tag{1.39}$$

The interface operator $\mathbf{H}$ is called the Steklov-Poincaré operator which can be viewed as the condensed effective stiffness matrix on the degrees of freedom belonging to the interface between

Cette thèse est accessible à l'adresse : http://theses.insa-lyon.fr/publication/2019LYSEI042/these.pdf
© [S. Li], [2019], INSA Lyon, tous droits réservés

the two subdomains. The right hand-side vector $\boldsymbol{b}^j$ only depends on the free velocities computed in both subdomains without considering the interface forces; it can be seen as a predictor value projected to the degrees of freedom belonging to the interface.

Finally, once derived the Lagrange multiplier vector, the quantities related to the interface forces can be computed and the time step is completed by summing these linked quantities to the free quantities previously obtained.

1.4 Absorbing layers for modeling unbounded domains

For the numerical simulation of wave propagation problems in unbounded domains using the finite element method, one of the critical points is infinite media modelling. The simplest way is to consider a very large extended numerical mesh, but it leads to important computation times, in particular when long time duration excitations are considered. Hence, non-reflective boundary conditions are required at the boundary of the truncated domain for mimicking infinite or semi-infinite media, as shown in Fig.1-5. In the thesis, we focus on three artificial boundaries in numerical methods for modeling unbounded domains: Rayleigh absorbing layers, Kosloff absorbing boundary, and PML (Perfectly Matched Layers).

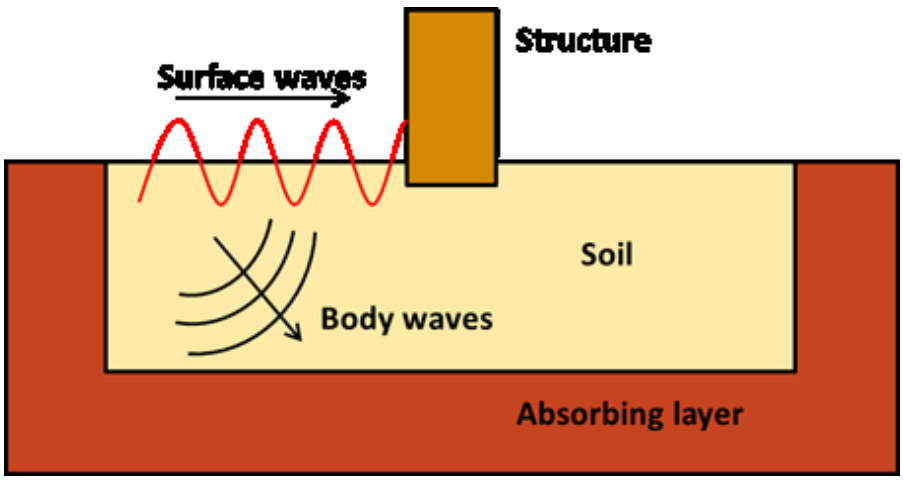

Figure 1-5 The truncated domain in soil–structure interaction problem

Cette thèse est accessible à l'adresse : http://theses.insa-lyon.fr/publication/2019LYSEI042/these.pdf
© [S. Li], [2019], INSA Lyon, tous droits réservés

1.4.1 Rayleigh damping

The Rayleigh matrix is one classical method for modelling damping in dynamic transient analysis by Finite Element method. The expression of the classical viscous Rayleigh damping matrix is denoted by:

$$\mathbf{C} = \alpha_M \mathbf{M} + \alpha_K \mathbf{K} \tag{1.40}$$

where $\mathbf{M}$ and $\mathbf{K}$ are the mass matrix and stiffness matrix, respectively. α_M is the Rayleigh coefficient proportional to the mass matrix, and α_K is the Rayleigh coefficient proportional to the stiffness matrix. Thus, $\mathbf{C}$ is the sum of two terms: one is proportional to the mass matrix, the other to the stiffness matrix. The relationship between the damping ratio ξ as a function of the angular frequency ω and the two coefficients of the Rayleigh absorbing layer is given below:

$$\xi = \frac{\alpha_M}{2\omega} + \frac{\alpha_K \omega}{2} \tag{1.41}$$

Because the Rayleigh damping has been integrated in many commercial FE software, it is very convenient to set absorbing layers by the Rayleigh matrix. Rayleigh absorbing layer was introduced first by Israeli and Orszag (1977). Then Semblat *et al.* (2011) and Rajagopal *et al.* (2012) introduced more convenient techniques for implementing efficient absorbing conditions into commercial finite element codes, called Absorbing Layers using Increasing Damping (ALID), based on Rayleigh viscous damping matrix associated with an increasing damping ratio in the thickness of the absorbing region. Analytical models enabling to select the ALID parameters are developed by the authors to provide quick and valuable results, satisfying a desired accuracy. It was also noted that the introduction of the Rayleigh matrix decreases the value of the critical time step when using explicit scheme. A strong form for the wave propagation in the continuous dissipative medium, corresponding to the introduction of the classical viscous Rayleigh damping matrix into the classical semi-discrete equation of motion, has been given by Zafati *et al.* (2014, 2015). A clear relationship between the parameters of the absorbing layer and its target efficiency in terms of attenuation was obtained. Next, the strong form of the wave propagation in Rayleigh medium is employed to obtain optimal conditions at the interface so as to minimize the spurious wave reflections. The displacement vector field $\underline{u}$ in the Rayleigh domain was given by the following equations:

Cette thèse est accessible à l'adresse : http://theses.insa-lyon.fr/publication/2019LYSEI042/these.pdf
© [S. Li], [2019], INSA Lyon, tous droits réservés

$$\rho\partial_t^2\underline{u} + \alpha_M\rho\partial_t\underline{u} = \mathrm{div}\left(\underline{\underline{\sigma}}(\underline{u})\right) \tag{1.42}$$

$$\underline{\underline{\sigma}} = \lambda\mathrm{tr}\left(\underline{\underline{\varepsilon}}(\underline{u})\right) + 2\mu\underline{\underline{\varepsilon}}(\underline{u}) + \alpha_K\left(\lambda\mathrm{tr}\left(\underline{\underline{\varepsilon}}(\partial_t\underline{u})\right) + 2\mu\underline{\underline{\varepsilon}}(\partial_t\underline{u})\right) \tag{1.43}$$

$$\underline{\underline{\varepsilon}} = \frac{1}{2}\left[grad(\underline{u}) + grad(\underline{u})^T\right] \tag{1.44}$$

Eqs. (1.42) to (1.44) constitute the strong form of the wave propagation into a Rayleigh medium, σ , ε, λ, μ, ρ being the stress matrix, strain matrix, Lamé coefficients and the density related to the Rayleigh domain, respectively. It was shown that the parameters α_M and α_K introduced in Eqs (1.42) and (1.43) correspond to the two classical parameters of the viscous Rayleigh damping matrix (Belytschko *et al*., 2000; Zafati *et al.*, 2015).

1.4.2 Kosloff absorbing boundary

Absorbing boundary based on a simple modification in the wave propagating equation, was proposed by Kosloff and Kosloff (1986). The governing equations in elastodynamics are modified in order to introduce a specific damping, called in the following Kosloff damping. The displacement vector field $\underline{u}$ in the Kosloff medium is governed by the modified equations:

$$\rho\partial_t^2\underline{u} = \mathrm{div}\left(\underline{\underline{\sigma}}(\underline{u})\right) - 2\rho\gamma\partial_t\underline{u} - \rho\gamma^2\underline{u} \tag{1.45}$$

$$\underline{\underline{\sigma}} = \lambda\mathrm{tr}\left(\varepsilon(\underline{u})\right) + 2\mu\varepsilon(\underline{u}) \tag{1.46}$$

$$\underline{\underline{\varepsilon}} = \frac{1}{2}\left[grad(\underline{u}) + grad(\underline{u})^T\right] \tag{1.47}$$

Eqs. (1.45) to (1.47) constitute the strong form of the wave propagation in a Kosloff medium, σ, ε, λ, μ, ρ, γ being the stress matrix, strain matrix, Lamé's coefficients, the density and damping ratio, respectively. It can be seen that the strong form of the equation of motion, in Eq. (1.45), has been changed with two additional damping terms related to displacements and velocities. The other two equations correspond to the elastic constitutive relationship and the definition of the infinitesimal strain. In Kosloff medium, the wave travels without changing shape and the wave

Cette thèse est accessible à l'adresse : http://theses.insa-lyon.fr/publication/2019LYSEI042/these.pdf
© [S. Li], [2019], INSA Lyon, tous droits réservés

amplitude decreases with distance at a frequency independent rate. On the contrary, one of the drawbacks of the viscous Rayleigh damping in FE software is its dependence with respect to frequencies in the problem. Some similarities between PML and Kosloff absorbing boundary have been discussed by Carcione and Kosloff (2013). It was shown that in the case of SH waves, a modified Kosloff formulation matches the split formulation of the PML, before the spatial and time discretization, highlighting the relation between the two approaches. Consequently, it is interesting to explore the capabilities of setting up efficient and convenient absorbing layers based on Kosloff damping for modelling infinite media, which could be independent of frequency and easy to be implemented with a convenient finite element expression.

1.4.3 PML (Perfectly Matched Layers)

PML (Perfectly Matched Layers) proposed by Bérenger (1994) and reinterpreted by Chew and Weedon (1994) is becoming increasingly used for dealing with infinite media in the context of finite difference, finite element and spectral element methods. The PML medium is built by applying a complex-valued coordinate stretching to the elastic wave equation, providing the same attenuation for all frequencies and non-reflecting feature in continuous setting for all angles of incidence at the interface, and these properties make it more efficient than the other absorbing layers. The PML was originally developed for the electromagnetic waves by Bérenger (1994). The technique was then adapted to the elastodynamic equations. The first implementations of PML were carried out according to a velocity-stress format, using mainly the finite difference method and a split procedure for the components of velocities with respect to the interface (Chew and Liu, 1996; Collino and Tsoga, 2001). Then, the unsplit-formulation was developed by Wang *et al.* (2003), called C−PML, requiring the computation of convolution integrals. Next, Matzen (2011) extended the C-PML approach to the finite element method. Basu and Chopra (2003, 2004) proposed an unsplit straightforward displacement-based formulation without the need of convolution integrals calculation for time-domain elastodynamics by finite element method. Then, this work was extended to three-dimension and successfully implemented in the Finite Element software LS-DYNA and DIANA (Basu, 2009). In most formulations, the complex-coordinate-stretched equations used to introduce the PML, also serve to describe the interior domain (reduced

Cette thèse est accessible à l'adresse : http://theses.insa-lyon.fr/publication/2019LYSEI042/these.pdf
© [S. Li], [2019], INSA Lyon, tous droits réservés

to the original unstretched system), resulting in an unuseful complexity and additional computational cost. Kucukcoban and Kallivokas (2011,2013) derived a hybrid formulation coupling an unsplit mixed form PML with a standard displacement-only form in the interior domain, which has been extended to three-dimension by Fathi *et al.* (2015). The derived PML turns out to be very efficient, but the mixed formulation is more difficult to be implemented in FE context than a classical displacement-based approach.

The PML model is formulated by introducing the complex-valued stretching functions into the classical elastodynamic equations in the frequency domain. The main idea is to replace the real coordinates x_i which denotes the x, y and z coordinates for the index equal to 1, 2 and 3, by the complex ones $\tilde{x}_i : \mathbb{R} \to \mathbb{C}$. The complex coordinates are defined by:

$$\frac{\partial \tilde{x}_i}{\partial x_i} = \lambda_i(x_i) = 1 + f_i^e(x_i) + \frac{f_i^p(x_i)}{i\omega} \tag{1.48}$$

In the above, ω denotes angular frequency, the damping function f_i^p which is positive real-valued as a function of x_i, serves to attenuate the propagating waves in the x_i direction, and the damping function f_i^e attenuates the evanescent waves. Here, we concentrate on the propagating waves, so the damping function f_i^p will be used to control the attenuation intensity. The PML formulation is obtained by modifying the governing equations defined in the frequency domain. The classical three-dimensional strong form in elastic medium has been changed as below:

$$\sum\nolimits_j \frac{1}{\lambda_j(x_j)} \frac{\partial \sigma_{ij}}{\partial x_j} = -\omega^2 \rho u_i \tag{1.49}$$

$$\sigma_{ij} = \sum\nolimits_{k,l} C_{ijkl} \varepsilon_{kl} \tag{1.50}$$

$$\varepsilon_{ij} = \frac{1}{2}\left[\frac{1}{\lambda_j(x_j)} \frac{\partial u_i}{\partial x_j} + \frac{1}{\lambda_i(x_i)} \frac{\partial u_j}{\partial x_i}\right] \tag{1.51}$$

where C_{ijkl} are the components of the elastic constitutive tensor.

Cette thèse est accessible à l'adresse : http://theses.insa-lyon.fr/publication/2019LYSEI042/these.pdf
© [S. Li], [2019], INSA Lyon, tous droits réservés

1.5 Conclusion

This chapter has summarized different aspects concerning the numerical simulation of wave propagation in unbounded domains. At the beginning, the basic knowledge of the wave propagation in elastic medium is presented. The prediction of wave propagation in the soil is very important for the protection of the people and the buildings against propagating waves produced by dynamic sources. However, it turns out to be difficult to solve the problem by analytical methods, due to the complexity of the model in engineering cases. For this reason, the principle of Finite Element method has been introduced. The space and time discretization of wave propagation problem in two-dimensional elastic media has been given, as an example, by using 4-node isoparametric rectangular elements and Newmark integration schemes for linear transient.

Generally, the numerical model of wave propagation problem includes different physical domains. Taking into account the different characteristics of each part, heterogeneous time integration schemes, based on domain decomposition method, are suitable to satisfy the requirement of each part and reach the best computational efficiency. Consequently, the framework of HATI (Heterogeneous Asynchronous Time Integrator) is briefly presented, based on the dual approach.

One of the critical points of wave propagation simulation in unbounded domains using the finite element method is how to simulate infinite media. Non-reflective boundary conditions are required at the boundary of the truncated domain for mimicking infinite or semi-infinite media. The previous research works on absorbing layers for modelling unbounded domain are briefly presented. In the following, novel designs and hybrid formulations of three absorbing layers, Rayleigh absorbing layers, Kosloff absorbing layers and PML (Perfect Matched Layers), will be developed and implemented by the finite element method for modelling two-dimensional and three-dimensional infinite media. Numerous numerical applications will be carried out to illustrate the efficiency of the hybrid approach for modeling unbounded domains.

Cette thèse est accessible à l'adresse : http://theses.insa-lyon.fr/publication/2019LYSEI042/these.pdf
© [S. Li], [2019], INSA Lyon, tous droits réservés

Cette thèse est accessible à l'adresse : http://theses.insa-lyon.fr/publication/2019LYSEI042/these.pdf
© [S. Li], [2019], INSA Lyon, tous droits réservés

Chapter 2

Hybrid asynchronous Rayleigh absorbing layer

Absorbing Layers using Increasing Damping (ALID), based on Rayleigh viscous damping, are considered for modeling 2D and 3D infinite medium. The strong form of wave propagation in a Rayleigh medium is first briefly presented, enabling us to derive improved relationships for mechanical parameters of the absorbing layers in order to minimize the wave reflection at the interface between the elastic medium and the Rayleigh medium. An efficient ALID can be set up, whose design depends on the desired target absorbing accuracy. Secondly, the weak formulation of the decomposed problem based on the coupling GC method is obtained in order to derive the discretization in space and time algorithm able to couple Abaqus/Explicit with Abaqus/Implicit with their independent time steps. The proposed absorbing region is called Hybrid (different time integrators) Asynchronous (different time steps) Absorbing Layers using Increasing Damping (HA-ALID). In numerical applications, Lamb's test is considered to assess the HA-ALID efficiency using Abaqus co-simulation: several profiles (linear, quadratic, square-root) of the damping ratio in the thickness of the HA-ALID are investigated so as to optimize the absorbing effect into the HA-ALID while minimizing the spurious wave reflection at the interface with the elastic domain. The efficiency of the proposed method is compared with non-reflective conditions available in Abaqus/Explicit, highlighting the very good behavior of the co-simulation strategy. In addition, a simulation of a wave barrier problem is carried out using the co-simulation and compared to an Abaqus/Explicit simulation with infinite elements with the same mesh for the domain of interest. Finally, hybrid asynchronous Rayleigh absorbing layers is extended for

Cette thèse est accessible à l'adresse : http://theses.insa-lyon.fr/publication/2019LYSEI042/these.pdf
© [S. Li], [2019], INSA Lyon, tous droits réservés

modelling three-dimensional unbounded domains using explicit/implicit and explicit/explicit co-simulations. The difference of two co-simulation strategies will be compared in terms of accuracy and computation time. The straightforward 3D extension of HA-Rayleigh ALID highlights the convenience of the Rayleigh damping layers for setting up absorbing layers.

The part of this work devoted to transient 2D analyses has been published in European Journal of Environmental and Civil Engineering:

Li S, Brun M, Djeran-Maigre I, and Kuznetsov S (2018). Explicit/implicit multi-time step co-simulation in unbounded medium with Rayleigh damping and application for wave barrier. European Journal of Environmental and Civil Engineering.

Cette thèse est accessible à l'adresse : http://theses.insa-lyon.fr/publication/2019LYSEI042/these.pdf
© [S. Li], [2019], INSA Lyon, tous droits réservés

2.1 The design of ALID (Absorbing Layers using Increasing Damping)

Rayleigh absorbing layer aims at damping out all the incident waves from the domain of interest while minimizing the spurious waves reflected at the boundary of the truncated domain. For this purpose, the optimal conditions at the interface between a non-dissipative elastic medium Ω_1 and a dissipative Rayleigh medium Ω_2 can be established by considering the continuous problem of wave propagation. A strong form for the wave propagation in the continuous dissipative medium Ω_2, corresponding to the introduction of the classical viscous Rayleigh damping matrix into the classical semi-discretized of the equation of motion in 3D medium, has been obtained by Zafati *et al.* (2014,2015). Indeed, the classical expression of the Rayleigh matrix can be derived from the weak form of the previous equations as it will be shown in section 2.2. The displacement vector field $\underline{u}$ in the Rayleigh domain was given by the following equations:

$$\rho_2 \partial_t^2 \underline{u_2} + \alpha_M \rho_2 \partial_t \underline{u_2} = \mathrm{div}\left(\underline{\underline{\sigma_2}}\left(\underline{u_2}\right)\right) \tag{2.1}$$

$$\underline{\underline{\sigma_2}} = \lambda_2 \mathrm{tr}\left(\underline{\underline{\varepsilon_2}}\left(\underline{u_2}\right)\right) + 2\mu_2 \underline{\underline{\varepsilon_2}}\left(\underline{u_2}\right) + \alpha_K \left(\lambda_2 \mathrm{tr}\left(\underline{\underline{\varepsilon_2}}\left(\partial_t \underline{u_2}\right)\right) + 2\mu_2 \underline{\underline{\varepsilon_2}}\left(\partial_t \underline{u_2}\right)\right) \tag{2.2}$$

$$\underline{\underline{\varepsilon_2}} = \frac{1}{2}\left[grad\left(\underline{u_2}\right) + grad\left(\underline{u_2}\right)^T\right] \tag{2.3}$$

Eqs. (2.1) to (2.3) constitute the strong form of the wave propagation into a Rayleigh medium, σ_2 , ε_2, λ_2, μ_2, ρ_2 being the stress matrix, strain matrix, Lamé coefficients, the density, Young's modulus and Poisson's ratio related to the Rayleigh domain Ω_2, respectively.

The strong form of the wave propagation in Rayleigh medium is employed to obtain optimal conditions at the interface between an elastic domain Ω_1 and a dissipative Rayleigh medium Ω_2 so as to minimize the spurious wave reflections. The argument is developed for 1D wave propagation problem by distinguishing the P-waves and the S-waves in their strong form, written as:

$$\rho_2 \partial_t^2 u_2 + \alpha_M \rho_2 \partial_t u_2 = (\lambda_2 + 2\mu_2)\partial_x^2 u_2 + \alpha_K (\lambda_2 + 2\mu_2)\partial_x^2 \partial_t u_2 \quad P-wave \tag{2.4}$$

$$\rho_2 \partial_t^2 u_2 + \alpha_M \rho_2 \partial_t u_2 = \mu_2 \partial_x^2 u_2 + \alpha_K \mu_2 \partial_x^2 \partial_t u_2 \qquad S-wave \tag{2.5}$$

Cette thèse est accessible à l'adresse : http://theses.insa-lyon.fr/publication/2019LYSEI042/these.pdf
© [S. Li], [2019], INSA Lyon, tous droits réservés

By introducing the harmonic solution $u(x,t) = u_0 \exp(i(\omega_0 t - kx))$, the expression of the propagating wave in the 1D Rayleigh medium can be obtained, with the assumption between damping ratio ξ and the dominant angular frequency ω_0 as: $\frac{\alpha_M}{\omega_0} = \alpha_K \omega_0 = \xi$ (Zafati *et al.,* 2015):

$$u_2(x,t) = u_0 \exp\left(\frac{-\omega_0 \xi x}{V_2\sqrt{1+\xi^2}}\right) \exp\left(i\left(\omega_0 t - \frac{\omega_0 x}{V_2\sqrt{1+\xi^2}}\right)\right) \tag{2.6}$$

After analytically solving the interface problem using the previous strong form, the relationship for minimizing the spurious reflections at the interface was obtained (Zafati *et al.,* 2015):

$$\begin{cases} E_2 = \dfrac{E_1}{1+\xi^2} \\ \nu_2 = \nu_1 \\ \rho_2 = \rho_1 \end{cases} \tag{2.7}$$

where E_1 and E_2 are Young's moduli, ν_1 and ν_2 are Poisson's ratios, ρ_1 and ρ_2 are the densities of subdomains Ω_1 and Ω_2, respectively. The decay of the amplitude δ is expressed in a logarithmic form with respect to the thickness of the Rayleigh absorbing layer Δx as follows:

$$\delta = \ln\left(\frac{|u_2(x)|}{|u_2(x+\Delta x)|}\right) = \frac{\omega_0 \xi \Delta x}{v_\rho} \tag{2.8}$$

where Δx denotes the thickness of the Rayleigh medium, ξ the damping ratio of the Rayleigh absorbing layer and v_ρ represents the velocity of P wave in the domain of interest. For achieving a target value of the logarithmic decrement, we can use the relationship in Eq. (2.8) to design the Rayleigh medium by choosing its damping ratio and thickness. The velocity of P waves is higher than the velocity of S waves in the same medium. In other words, based on the above relationships, in order to reach the same logarithmic decrement, the necessary layer thickness for damping out S waves is smaller than the one related to P waves. For the design of absorbing layer, the velocity of P waves will be chosen to make sure that all the waves can be attenuated according to the target decrement.

Cette thèse est accessible à l'adresse : http://theses.insa-lyon.fr/publication/2019LYSEI042/these.pdf
© [S. Li], [2019], INSA Lyon, tous droits réservés

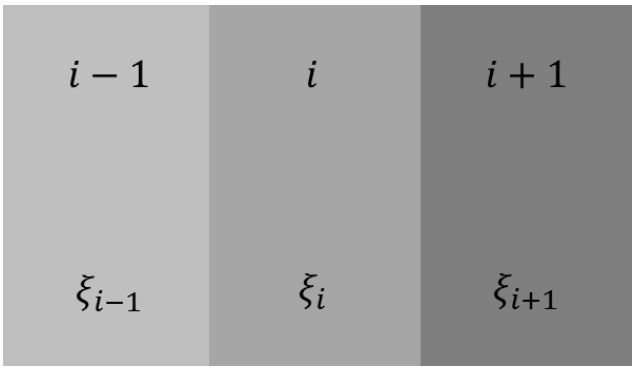

Figure 2-1 Absorbing Layers using Increasing Damping

The Absorbing Layers using Increasing Damping, called ALID, proposed by Semblat *et al.* (2011) and Rajagopal *et al.* (2012), are considered by tuning the elastic parameters of each layer depending on the selected damping ratio as given by the optimal conditions in Eq. (2.7). The main idea is to divide the Rayleigh absorbing medium into several uniform layers as shown in Fig.2-1, so that the decrements produced by each layer can be multiplied. Because of the logarithmic form of decrement, the total logarithmic decrement can be easily obtained. Due to the difference of damping ratio between subdomains Ω_1 and Ω_2, spurious waves will be produced, though optimal conditions given by Eq. (2.7) are applied. Indeed, it is important to note that non-reflective conditions between an elastic and a Rayleigh medium were obtained under the following assumptions: 1D wave propagation (normal incidence), continuous setting in space and in time, harmonic waves. Thus, in a more general problem with non-harmonic waves, after spatial and time discretization, Eq. (2.7) provides only approximate conditions used for the ALID design.

It is crucial to control the difference of damping ratios between subdomains. Indeed, the evolution of damping ratio in layers has an important influence on the efficiency of the ALID. Here, a nonlinear increase of damping ratio is adopted to achieve a better accuracy than a simple linear increase. The parameters of each layer satisfying the optimal conditions at each interface are given by:

Cette thèse est accessible à l'adresse : http://theses.insa-lyon.fr/publication/2019LYSEI042/these.pdf
© [S. Li], [2019], INSA Lyon, tous droits réservés

$$\begin{cases} E_2^{(i+1)} = \dfrac{1+\xi_i^2}{1+\xi_{i+1}^2} E_2^{(i)} \\ E_2^{(1)} = \dfrac{1}{1+\xi_1^2} E_1 \\ \nu_2^{(i)} = \nu_1 \\ \rho_2^{(i)} = \rho_1 \\ \xi_i = \xi_0 \left(\dfrac{x}{L}\right)^n \end{cases} \tag{2.9}$$

where $E_2^{(i)}$ denotes Young's modulus, ξ_i the damping ratio, $\nu_2^{(i)}$ Poisson's ratio, $\rho_2^{(i)}$ the density of each layer i in the subdomain Ω_2, n the power of the damping function, x the distance in the thickness of the ALID, L the thickness of the ALID including all sublayers (i). The total logarithmic decrement δ is written as:

$$\begin{cases} \delta_i = \dfrac{\xi_0 \omega_0}{v_\rho} \left(\dfrac{x}{L}\right)^n \Delta x \\ \delta = \sum_{i=1}^{N_e} \delta_i = \int_0^L \dfrac{\xi_0 \omega_0}{v_\rho} \left(\dfrac{x}{L}\right)^n dx = \dfrac{\xi_0 \omega_0 L}{(n+1) v_\rho} \end{cases} \tag{2.10}$$

where δ_i represents the logarithmic decrement of each sublayer i, N_e is the number of layers, Δx represents the thickness of each layer which is assumed to be constant. The reflection coefficient R is given by:

$$R = e^{-2\delta} \tag{2.11}$$

For example, if the goal is to reach a target logarithmic decrement δ=ln (10), this means that 90% of the amplitude of the incident will be absorbed from the interface to the end of the damping layers. Next, the attenuation also occurs for the reflection process from the end of the damping layer towards the interface. Thus, the incident wave is attenuated by 99% in the ALID and the reflection coefficient R is theoretically equal to 1%, under the 1D harmonic wave propagation assumption and before the discretization in time and in space. By calculating Eq. (2.10) in the integral form, a new general design formula for the system of Rayleigh absorbing layers with reflection coefficient R is derived:

$$\xi_0 = \frac{(n+1)}{2L\omega_0} \times v_\rho \times \ln\left(\frac{1}{R}\right) \tag{2.12}$$

Cette thèse est accessible à l'adresse : http://theses.insa-lyon.fr/publication/2019LYSEI042/these.pdf
© [S. Li], [2019], INSA Lyon, tous droits réservés

2.2 Weak form and space discretization for HA-ALID

The elastic wave propagation from an elastic non-dissipative medium to a Rayleigh medium should be discretized in space and in time. Let Ω be a bounded domain belonging to $\mathbb{R}^2$ with a regular boundary. J= [0, T] is the time interval of interest. The domain Ω is divided into two partitions Ω_1 and Ω_2, as shown in Fig.1-4, such as: $\Omega_1 \cap \Omega_2 = \emptyset$ and $\partial\Omega_1 \cap \partial\Omega_2 = \Gamma_I$. Γ_I denotes the interface between the two subdomains, subdomain Ω_1 representing the non-dissipative medium (the domain of interest) and subdomain Ω_2 the Rayleigh medium.

The subdomain Ω_1 is characterized by its density ρ_1, Young's modulus E_1, Poisson coefficient ν_1, $\underline{b}_1$ the body force, $\underline{u}_1^D$ the Dirichlet prescribed displacement on Γ_1^D and $\underline{g}_1^N$ the traction force at the Neumann condition on Γ_1^N. The subdomain Ω_2 is characterized by its density ρ_2, Young's modulus E_2, Poisson coefficient ν_2, $\underline{b}_2$ the body force , $\underline{u}_2^D$ the Dirichlet prescribed displacement on Γ_2^D, $\underline{g}_2^N$ the traction force at the Neumann condition on Γ_2^N and the parameters α_M and α_K introduced in the strong form of the wave equation in Eqs (2.1) and (2.2).

In order to write the weak form of the coupled problem in Ω divided into two partitions Ω_1 and Ω_2, test functions $\underline{v}_1$ and $\underline{v}_2$ belonging to the appropriate spaces W_1^* and W_2^* must be introduced:

$$\begin{cases} \underline{v}_1 \in W_1^*, W_1^* = \left\{ \underline{v}_1 \in \left(H^1(\Omega_1)\right)^d \text{and } \underline{v}_1 = 0 \text{ on } \Gamma_1^D \right\} \\ \underline{v}_2 \in W_2^*, W_2^* = \left\{ \underline{v}_2 \in \left(H^1(\Omega_2)\right)^d \text{and } \underline{v}_2 = 0 \text{ on } \Gamma_2^D \right\} \end{cases} \tag{2.13}$$

The solutions $\underline{u}_1$ and $\underline{u}_2$ belong to the appropriate spaces W_1 and W_2:

$$\begin{cases} \underline{u}_1(t) \in W_1, W_1 = \left\{ \underline{u}_1 \in \left(H^1(\Omega_1)\right)^d \text{and } \underline{u}_1 = u_1^D \text{ on } \Gamma_1^D \right\} \\ \underline{u}_2(t) \in W_2, W_2 = \left\{ \underline{u}_2 \in \left(H^1(\Omega_2)\right)^d \text{and } \underline{u}_2 = u_2^D \text{ on } \Gamma_2^D \right\} \end{cases} \tag{2.14}$$

where d is the space dimension (equal to 1, 2 or 3). The introduction of the Lagrange multiplier field allows us to glue the velocities of the two subdomains at the interface Γ_I. They belong to the adapted dual trace space Q, defined at the interface.

Cette thèse est accessible à l'adresse : http://theses.insa-lyon.fr/publication/2019LYSEI042/these.pdf
© [S. Li], [2019], INSA Lyon, tous droits réservés

All the above considered space variables are assumed to be sufficiently smooth and regular. Using a dual Schur formulation, the principle of virtual power for transient dynamics can be written. Find the solution $\underline{u}_1(t) \in W_1$, $\underline{u}_2(t) \in W_2$ and $\underline{\lambda}(t) \in Q$, for which the following weak form is satisfied $\forall \underline{v}_1 \in W_1^*$, $\forall \underline{v}_2 \in W_2^*$ and $\forall \underline{\mu} \in Q^*$:

$$\int_{\Omega_1} \rho_1 \underline{v}_1 \cdot \ddot{\underline{u}}_1 d\Omega + \int_{\Omega_1} \underline{\underline{\varepsilon}}(\underline{v}_1) : \underline{\underline{\sigma}}_1 d\Omega + \int_{\Omega_2} \rho_2 \underline{v}_2 \cdot \ddot{\underline{u}}_2 d\Omega + \int_{\Omega_2} \underline{\underline{\varepsilon}}(\underline{v}_2) : \underline{\underline{\sigma}}_2 d\Omega + \alpha_M \int_{\Omega_2} \rho_2 \underline{v}_2 \cdot \dot{\underline{u}}_2 d\Omega + \int_{\Gamma_I} \underline{v}_1 \cdot \underline{\lambda} d\Gamma + \int_{\Gamma_I} \underline{v}_2 \cdot \underline{\lambda} d\Gamma + \int_{\Gamma_I} \underline{\mu} \cdot (\dot{\underline{u}}_1 - \dot{\underline{u}}_2) d\Gamma = \int_{\Omega_1} \underline{v}_1 \cdot \underline{b}_1 d\Omega + \int_{\Gamma_1^N} \underline{v}_1 \cdot \underline{g}_1^N d\Gamma + \int_{\Omega_2} \underline{v}_2 \cdot \underline{b}_2 d\Omega + \int_{\Gamma_2^N} \underline{v}_2 \cdot \underline{g}_2^N d\Gamma \quad (2.15)$$

where the stress tensor $\underline{\underline{\varepsilon}}_2$ satisfies the behavior law given in Eq. (2.2). Then, we follow the classical lines of the finite element discretization. At the interface between the subdomains, the continuity of velocities is imposed by the following condition:

$$\mathbf{L_1}\dot{\mathbf{U}}_\mathbf{1} + \mathbf{L_2}\dot{\mathbf{U}}_\mathbf{2} = \mathbf{0} \quad (2.16)$$

where $\mathbf{L_1}$ and $\mathbf{L_2}$ are the Boolean matrices in the case of matching meshes at the interface. They operate on nodal vectors associated with the two subdomains Ω_1 and Ω_2 and pick out the degrees of freedom belonging to the interface Γ_I in order to ensure the kinematic continuity at the interface.

Thus, the restricted velocities at the interface can be obtained from the global nodal velocity vectors $\dot{\mathbf{U}}_\mathbf{1}$ and $\dot{\mathbf{U}}_\mathbf{2}$ by the relationships:

$$\begin{cases} \dot{\mathbf{U}}_\mathbf{1}^\Gamma = \mathbf{L_1}\dot{\mathbf{U}}_\mathbf{1} \\ \dot{\mathbf{U}}_\mathbf{2}^\Gamma = \mathbf{L_2}\dot{\mathbf{U}}_\mathbf{2} \end{cases} \quad (2.17)$$

Same relationships hold for the global virtual nodal velocities $\mathbf{V_1}$ and $\mathbf{V_2}$. Thus, interface terms involving the Lagrange multiplier field in Eq. (2.16) can be expressed as:

$$\begin{cases} \int_{\Gamma_I} \underline{v}_1 \cdot \underline{\lambda} d\Gamma = \mathbf{V}_\mathbf{1}^\mathbf{T} \mathbf{L}_\mathbf{1}^\mathbf{T} \boldsymbol{\lambda} \\ \int_{\Gamma_I} \underline{v}_2 \cdot \underline{\lambda} d\Gamma = \mathbf{V}_\mathbf{2}^\mathbf{T} \mathbf{L}_\mathbf{2}^\mathbf{T} \boldsymbol{\lambda} \end{cases} \quad (2.18)$$

Cette thèse est accessible à l'adresse : http://theses.insa-lyon.fr/publication/2019LYSEI042/these.pdf
© [S. Li], [2019], INSA Lyon, tous droits réservés

2.3 Time discretization of HA-ALID

For the time discretization, the GC method proposed by Gravouil and Combescure (2001, 2002) is employed. Adopting the continuity of velocities at the interface, it was demonstrated that the coupling GC method is stable for any Newmark integrators (implicit and explicit) with their own time step depending on subdomains. When adopting the same time step, second order of accuracy is achieved. It leads to the first order of accuracy when different time steps are adopted due to a slight spurious dissipation at the interface. As illustrated in Fig. 1-4, an explicit time integrator with a fine time step Δt_1 is adopted for the subdomain Ω_1 and an implicit time integrator with a large time step Δt_2 is used for subdomain Ω_2, with $\Delta t_2 = m\Delta t_1$, m being the time step ratio between two subdomains. In this way, hybrid (different schemes associated) asynchronous (different time steps depending on subdomains) ALID can be obtained, called HA-ALID. The equilibrium of subdomain 2 is prescribed at time t_m at the end of the large time Δt_2, while the equilibrium of subdomain 1 is prescribed at every time $t_j = j\Delta t_1$ (j =1, 2...m) at the fine time scale. The gluing of the velocity at the interface is written at the fine time scale.

Using the GC method, the wave propagation can be simulated using a time step satisfying the CFL condition, without being affected by the specific formulation adopted for the absorbing region at the boundary of the truncated mesh. Moreover, the multi-time step capabilities enable us to use a large time step in subdomain Ω_2. Finally, the weak form given in Eq. (2.15) with the velocity continuity equation in Eq. (2.16), can be expressed in the following discrete form in space and time:

$$\mathbf{M_1}\ddot{\mathbf{U}}_\mathbf{1}^\mathbf{j} + \mathbf{K_1}\mathbf{U}_\mathbf{1}^\mathbf{j} = \mathbf{F}_\mathbf{1}^{\mathbf{ext,j}} - \mathbf{L}_\mathbf{1}^\mathbf{T}\boldsymbol{\lambda}^j \qquad \text{at time } t = t_j \qquad (2.19)$$

$$\mathbf{M_2}\ddot{\mathbf{U}}_\mathbf{2}^\mathbf{m} + (\alpha_M\mathbf{M_2} + \alpha_K\mathbf{K_2})\dot{\mathbf{U}}_\mathbf{2}^\mathbf{m} + \mathbf{K_2}\mathbf{U}_\mathbf{2}^\mathbf{m} = \mathbf{F}_\mathbf{2}^{\mathbf{ext,m}} - \mathbf{L}_\mathbf{2}^\mathbf{T}\boldsymbol{\lambda}^\mathbf{m} \qquad \text{at time } t = t_m \qquad (2.20)$$

$$\mathbf{L_1}\dot{\mathbf{U}}_\mathbf{1}^\mathbf{j} + \mathbf{L_2}\dot{\mathbf{U}}_\mathbf{2}^\mathbf{j} = 0 \qquad \text{at time } t = t_j \qquad (2.21)$$

where $\mathbf{M_i}$ and $\mathbf{K_i}$ are the mass and the stiffness matrices of subdomains Ω_1 and Ω_2 (i=1, 2). The first equation is the discrete equation of motion of subdomains Ω_1 written at time t_j (fine time scale), whereas the second equation is the discrete equations of motion of subdomains Ω_2 written at time t_m (large time scale). On right hand side of the above equations, the interface forces enable the subdomains to be glued at their interface Γ_I. The last equation is the velocity continuity.

Cette thèse est accessible à l'adresse : http://theses.insa-lyon.fr/publication/2019LYSEI042/these.pdf
© [S. Li], [2019], INSA Lyon, tous droits réservés

It is important to note that the expression of the classical viscous Rayleigh damping matrix, denoted by $\mathbf{C}_2=\alpha_M\mathbf{M}_2+\alpha_K\mathbf{K}_2$, is retrieved in the discrete equation of motion of subdomain Ω_2. As a result, the α_M and α_K parameters introduced in the strong form of the wave equation given in Eqs. (2.1) and (2.2) represent the classical constant parameters of the viscous Rayleigh damping matrix. In structural dynamics, this matrix is classically introduced in the discrete equation of motion, with parameters chosen so as to match two damping ratio values at two different frequencies.

Newmark time integration schemes (Newmark, 1959) can be adopted for the time discretization, for example, characterized by the parameters γ_2=0.5 and β_2=0.25 for the implicit time integration and the parameters γ_1=0.5 and β_1=0 for the explicit time integration scheme. By introducing the approximate Newmark formulas, it leads to the equations of motion written as:

$$\widetilde{\mathbf{M}}_1\ddot{\mathbf{U}}_1^{\mathbf{j}} = \mathbf{F}_1^{\mathbf{ext,j}} - \mathbf{K}_1\mathbf{U}_1^{\mathbf{j-1,p}} - \mathbf{L}_1^{\mathbf{T}}\boldsymbol{\lambda}^{\mathbf{j}} \tag{2.22}$$

$$\widetilde{\mathbf{M}}_2\ddot{\mathbf{U}}_2^{\mathbf{m}} = \mathbf{F}_2^{\mathbf{ext,m}} - \mathbf{C}_2\dot{\mathbf{U}}_2^{\mathbf{0,p}} - \mathbf{K}_2\mathbf{U}_2^{\mathbf{0,p}} - \mathbf{L}_2^{\mathbf{T}}\boldsymbol{\lambda}^{\mathbf{m}} \tag{2.23}$$

where $\mathbf{U}_1^{\mathbf{j-1,p}}$ and $\dot{\mathbf{U}}_2^{\mathbf{0,p}}$ denote the predictor values in terms of displacement and velocity, classically introduced through the approximate Newmark formulae; they correspond to quantities known at the beginning of the fine step and of the large time step, respectively.

The effective stiffness matrices $\widetilde{\boldsymbol{M}}_1$ and $\widetilde{\boldsymbol{M}}_2$ related to the two subdomains are defined by:

$$\widetilde{\boldsymbol{M}}_1 = \boldsymbol{M}_1 + \beta_1\Delta t_1^2\boldsymbol{K}_1 \tag{2.24}$$

$$\widetilde{\mathbf{M}}_2 = \mathbf{M}_2 + \beta_2\Delta t_2^2\mathbf{K}_2 + \gamma_2\Delta t_2\mathbf{C}_2 \tag{2.25}$$

The kinematic quantities are divided into two parts: the free and the linked quantities in the coupling GC method. The free quantities are calculated by taking into account the internal and external forces, without considering the interface forces, whereas the linked quantities are obtained from the interface loads given by the Lagrange multiplier vector $\boldsymbol{\lambda}$.

It was demonstrated that the kinematic continuity condition can be expressed as a reduced-size interface problem as follows:

$$\mathbf{H}\boldsymbol{\lambda}^{\mathbf{j}} = \mathbf{b}^{\mathbf{j}} \tag{2.26}$$

with the interface operator and the right-hand side member vector defined by:

Cette thèse est accessible à l'adresse : http://theses.insa-lyon.fr/publication/2019LYSEI042/these.pdf
© [S. Li], [2019], INSA Lyon, tous droits réservés

$$\begin{cases} \mathbf{H} = \gamma_1 \Delta t_1 \mathbf{L_1} \widetilde{\mathbf{M}}_\mathbf{1}^{-\mathbf{1}} \mathbf{L_1^T} + \gamma_2 \Delta t_2 \mathbf{L_2} \widetilde{\mathbf{M}}_\mathbf{2}^{-\mathbf{1}} \mathbf{L_2^T} \\ \mathbf{b^j} = \mathbf{L_1} \dot{\mathbf{U}}_\mathbf{1}^{\mathbf{free,j}} + \mathbf{L_2} \dot{\mathbf{U}}_\mathbf{2}^{\mathbf{free,j}} \end{cases} \tag{2.27}$$

2.4 Effectiveness of Hybrid Asynchronous Absorbing Layers using Increasing Damping (HA-ALID)

In order to evaluate the effectiveness of HA-ALID, 2D Lamb's test has been simulated using Abaqus Explicit/Implicit co-simulation. In Lamb's test, the concentrated load applied to the surface of an infinite half space medium generates three types of waves propagating through the soil, involving P, S waves and Rayleigh waves (Lamb, 1903). So 2D Lamb's test can be considered as a good test for assessing the performance of the HA-ALID using Abaqus co-simulation. Non-harmonic waves are investigated by considering a Ricker incident waves defined by:

$$Ric(t, t_p, t_s) = A\left(2\pi^2 \frac{(t-t_s)^2}{t_p^2} - 1\right) \exp\left(-\pi^2 \frac{(t-t_s)^2}{t_p^2}\right) \tag{2.28}$$

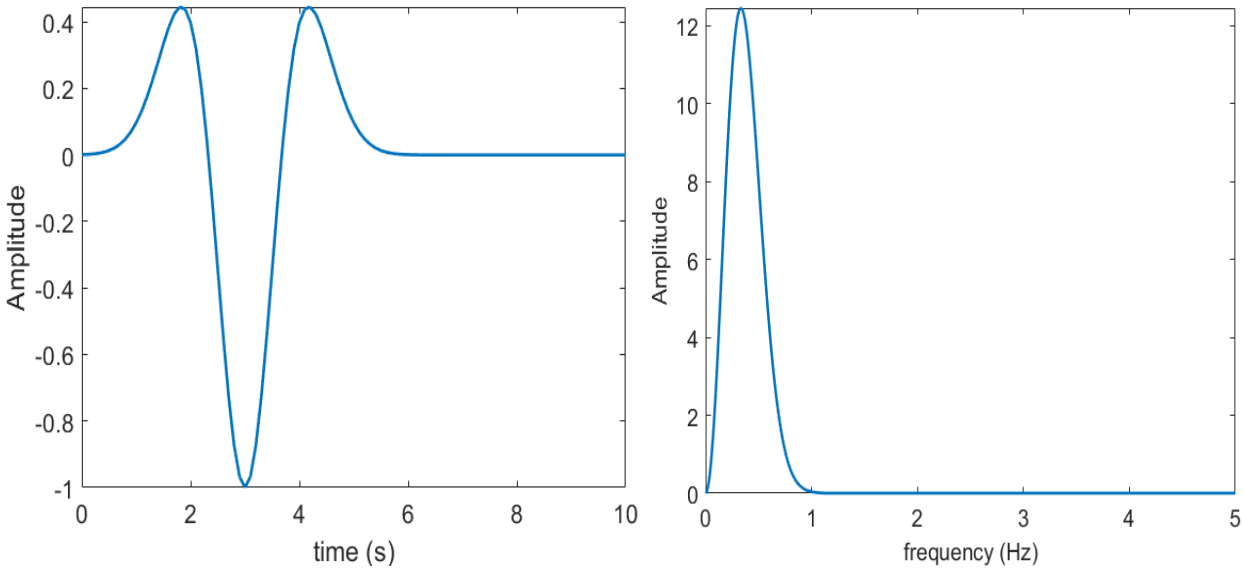

Figure 2-2 Waveform and Fourier transform of the Ricker wavelet

Cette thèse est accessible à l'adresse : http://theses.insa-lyon.fr/publication/2019LYSEI042/these.pdf
© [S. Li], [2019], INSA Lyon, tous droits réservés

The Ricker wave, plotted in time domain and in frequency domain in Fig.2-2, has three parameters: the fundamental period t_p, the time shift t_s and the amplitude A. The chosen values are: t_p=3s, t_s=3s and A =1MN. In this section, the first example of 2D Lamb's test is simulated with a single Rayleigh absorbing layer by using a homogeneous time step in both subdomains. Secondly, HA-ALID are tested so as to significantly reduce the scale of the absorbing medium at the boundary of the truncated mesh in comparison to the single-layer case. The effect of nonlinear increase of damping ratio and heterogeneous time steps on the accuracy will be investigated. Finally, a comparison will be carried out between results obtained by HA-ALID using Abaqus Explicit/Implicit co-simulation, infinite element using Abaqus Explicit, and reference results provided by an extended mesh using Abaqus Explicit.

2.4.1 Single absorbing layer

Lamb's test is set up considering a single absorbing layer as illustrated in Fig.2-3, composed of a bounded soil (subdomain 1) with a size of λ (wavelength of P-waves) and a single absorbing layer (subdomain 2) with the thickness of 3.6λ, designed to achieve a target logarithmic decrement $\delta = \ln(10)$.

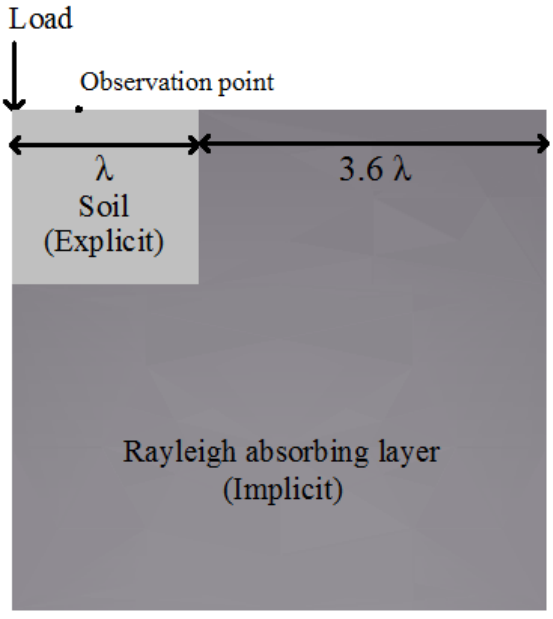

Figure 2-3 2D Lamb's test with a single absorbing layer using explicit/implicit co-simulation

Cette thèse est accessible à l'adresse : http://theses.insa-lyon.fr/publication/2019LYSEI042/these.pdf
© [S. Li], [2019], INSA Lyon, tous droits réservés

The soil is assumed to be linear elastic with the following material characteristics: ρ_1=1700kg/m^3, E_1=10MPa and ν_1= 0.24 for the density, Young's modulus and Poisson's ratio, respectively. The material characteristics of the Rayleigh absorbing layer are computed from the optimal conditions given in Eqs (2.7), by adopting a damping ratio ξ=0.1 and taking into account a dominant angular frequency corresponding to the fundamental period t_p of the Ricker wave. It gives: ρ_2=1700kg/m^3, E_2=9.9MPa, ν_2= 0.24 for the density, Young's modulus and Poisson's ratio, respectively. An homogeneous time step satisfying the CFL condition is taken in both subdomains. The subdomain soil is integrated in time with an explicit scheme, whereas the Rayleigh absorbing layer is integrated with an implicit scheme. An observation point is located at a distance equal to 20m from the load point. The model is spatially discretized using 4-node bilinear plane strain quadrilateral elements with the size of λ/50 for both subdomains, guaranteeing a good quality of the numerical prediction for the wave propagation problem. The P-wave, S-wave and Rayleigh wave velocities are: V_P =83.27m/s, V_S=48.7m/s, V_R=44.73m/s.

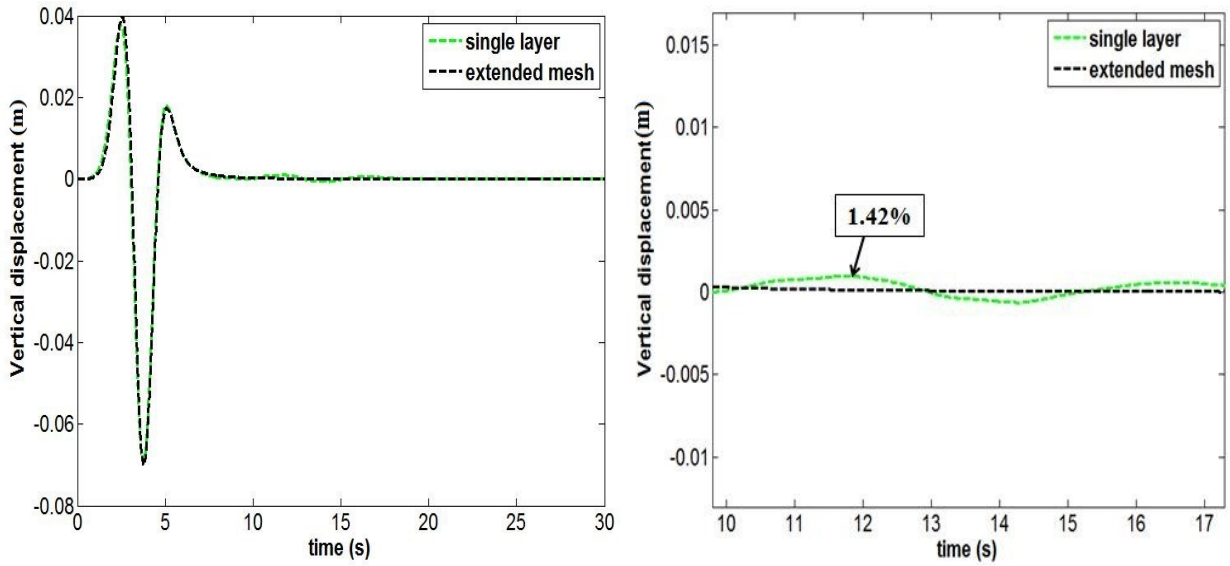

Figure 2-4 Vertical displacements at observation point using a single layer

Cette thèse est accessible à l'adresse : http://theses.insa-lyon.fr/publication/2019LYSEI042/these.pdf
© [S. Li], [2019], INSA Lyon, tous droits réservés

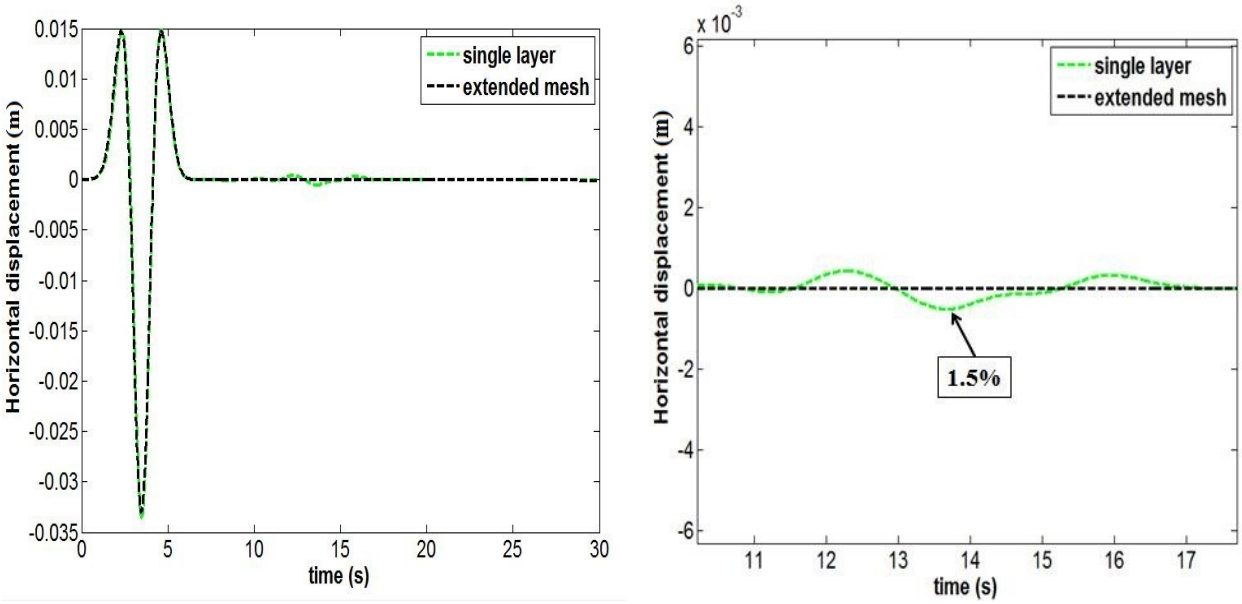

Figure 2-5 Horizontal displacements at observation point using a single layer

Figure 2-4 and 2-5 show the horizontal and vertical displacements in Lamb's test with a single absorbing layer in comparison to the reference results obtained from an extended mesh, free of spurious reflected waves in the observation period. The horizontal and vertical displacements of the reflected spurious wave are less than 1.5% with respect to the horizontal and vertical amplitudes of the incident wave. By comparing these results to our target equal to 1% for the reflection coefficient R, small discrepancies are observed, due to the non-normal incidence of waves, non-harmonic nature of the Ricker wavelet, and the space-time discretization of the problem. Results obtained by Abaqus Explicit/Implicit co-simulation with a single layer and an homogeneous time step in two subdomains are in good agreement with the reference results, highlighting the excellent behavior of the Rayleigh absorbing layer. Next, a multi-layer strategy (HA-ALID) will be used to reduce the scale of the absorbing region.

2.4.2 HA-ALID in Lamb's test

The HA-ALID for the Lamb's test is depicted in Figure 2-6. The size and material parameters of the soil domain are the same as in the previous example. We consider 10 sublayers in the absorbing region and a size of $\lambda/10$ for each sublayer; ξ_0 in Eqs (2.9) is chosen equal to 1. Thanks

Cette thèse est accessible à l'adresse : http://theses.insa-lyon.fr/publication/2019LYSEI042/these.pdf
© [S. Li], [2019], INSA Lyon, tous droits réservés

to the multi-layer strategy, the thickness L of the absorbing region can be reduced from 3.6λ for the previous one layer case to λ. The damping ratio of each layer depends on the selected profile of the damping ratio evolution in the thickness of the HA-ALID and three types of profile are investigated: linear, quadratic and square root. The other material parameters of layers can be calculated on the basis of the optimal conditions at the interface given in Eqs (2.9).

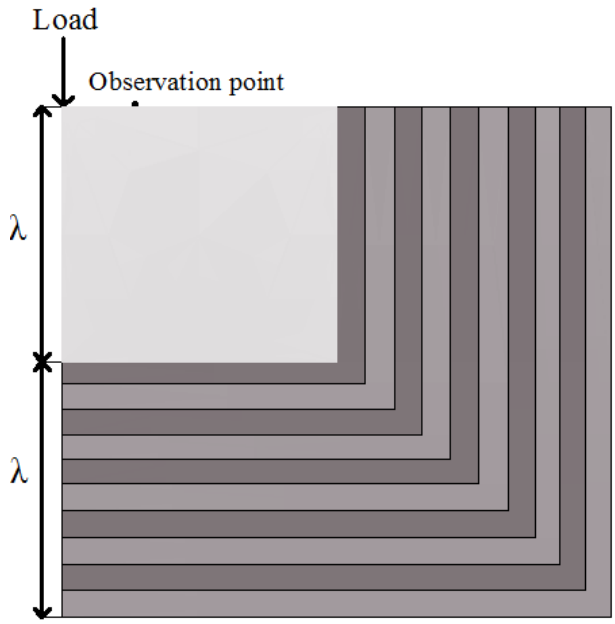

Figure 2-6 2D Lamb's test with the multi-layer strategy using explicit/implicit co-simulation

2.4.2.1 Influence of the evolution of the damping ratio in the HA-ALID

Due to the difference of damping ratio, spurious waves are produced at the interface between subdomain Ω_1 and Ω_2, corresponding to the HA-ALID. In the same way, spurious waves are produced between different layers of the HA-ALID. Therefore, it is crucial to control the evolution of damping ratio in layers. Three kinds of evolution functions are tested to find out which kind has the best performance: $\xi_i = \xi_0 \frac{i}{N_e}$, $\xi_i = \xi_0 \left(\frac{i}{N_e}\right)^2$, $\xi_i = \xi_0 \sqrt{\frac{i}{N_e}}$. The values of damping ratio and the derived reflection coefficient corresponding to the ALID are given in Table 2-1. It can be noted that reflection coefficients are less than 1% for the three damping ratio profiles.

Cette thèse est accessible à l'adresse : http://theses.insa-lyon.fr/publication/2019LYSEI042/these.pdf
© [S. Li], [2019], INSA Lyon, tous droits réservés

Table 2-1 Evolution of the damping ratio for different profiles (linear, quadratic, square-root)

Functions / i	$\xi_0 \frac{i}{N_e}$	$\xi_0 \left(\frac{i}{N_e}\right)^2$	$\xi_0 \sqrt{\frac{i}{N_e}}$
1	0.1	0.01	0.316
2	0.2	0.04	0.447
3	0.3	0.09	0.548
4	0.4	0.16	0.632
5	0.5	0.25	0.707
6	0.6	0.36	0.775
7	0.7	0.49	0.837
8	0.8	0.64	0.894
9	0.9	0.81	0.949
10	1.0	1.0	1.0
Reflection coefficient	0. 1%	0.8%	0.01%

Figures 2-7 and 2-8 compare the results obtained at the observation point using different damping profiles and an homogeneous time step in comparison to the reference results obtained from the extended mesh. The horizontal and vertical displacements of the reflected spurious wave by using the quadratic function performs best: 0.3% with respect to the horizontal amplitude of the incident wave and 1% with respect to the vertical amplitude of the incident wave, even though its reflection coefficient based on Eq. (2.10) is the biggest as seen in Table.2-1 (0.8% in comparison to 0.1% and 0.01% for the two others).

The results obtained with the linear function are better than that of the square root function. It highlights that the evolution of damping ratio in layers has an important influence on the performance of HA-ALID. The difference of damping ratios between subdomain Ω_1 and the first layers of the HA-ALID Ω_2 is the smallest by using the quadratic function: this is certainly why the

Cette thèse est accessible à l'adresse : http://theses.insa-lyon.fr/publication/2019LYSEI042/these.pdf
© [S. Li], [2019], INSA Lyon, tous droits réservés

best results are obtained by the quadratic function. The bigger the difference of damping ratios between subdomain Ω_1 and Ω_2 is, the bigger spurious waves are produced, even though Young's modulus is modified so as to satisfy the optimal conditions in Eqs. (2.9) for harmonic waves with normal incidence. It can also be remarked that the difference of damping ratio for the last sublayers provided by the quadratic function grows bigger than that of linear function or square root function. However, the generated spurious waves from the last layers have little impact on the global results, because the spurious waves caused by these last layers are strongly attenuated by the others layers before coming back into the domain of interest.

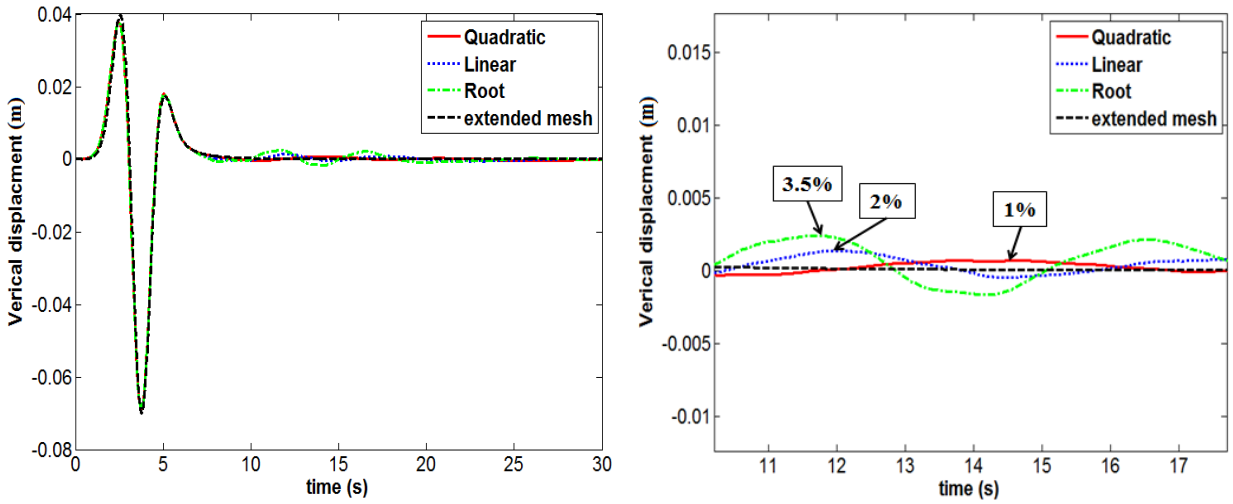

Figure 2-7 Vertical displacements at observation point using different damping ratio profiles

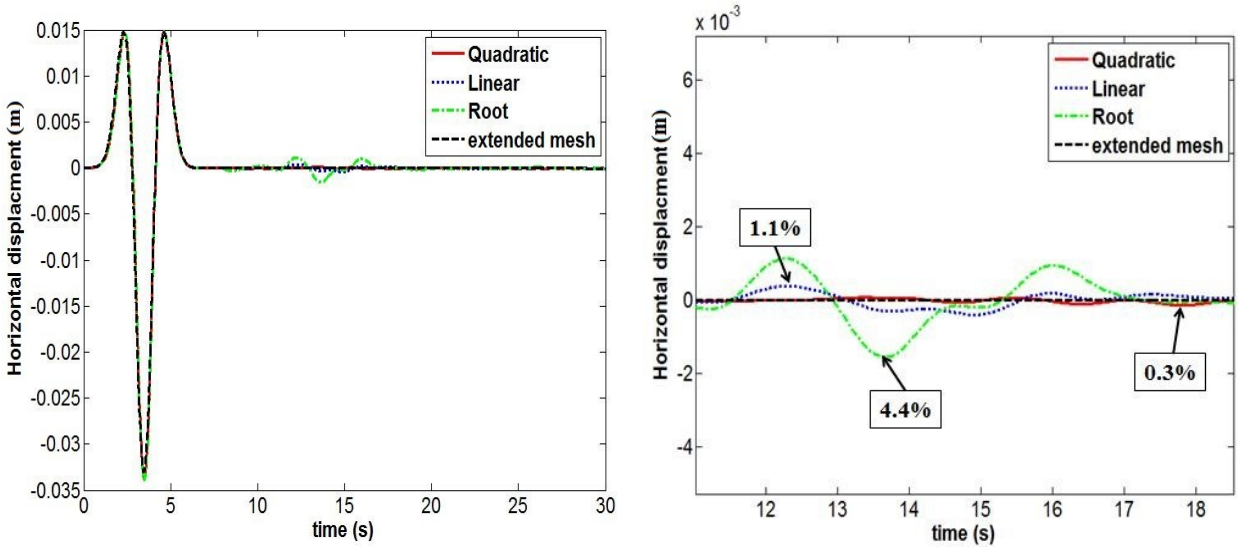

Figure 2-8 Horizontal displacements at the observation point using different damping ratio profiles

Cette thèse est accessible à l'adresse : http://theses.insa-lyon.fr/publication/2019LYSEI042/these.pdf
© [S. Li], [2019], INSA Lyon, tous droits réservés

2.4.2.2 Effect of the time step ratio on the accuracy of the HA-ALID

The subdomain soil and HA-ALID are integrated with an explicit scheme and an implicit scheme, respectively. An homogeneous time step can be adopted, which satisfies the CFL condition without damping. Indeed, using the implicit time integration for the HA-ALID, we avoid the decrease of the critical time step in the explicit framework due to the introduction of the Rayleigh damping into the discrete equation of motion, as it is noted in Abaqus/Explicit documentation (ABAQUS, 2013). Moreover, as explained in section 2.3, it is possible to use a larger time step in HA-ALID, because we use an unconditionally stable implicit scheme. In this part, the subdomain soil is integrated with Abaqus/Explicit with a fine time step, whereas the HA-ALID are dealt with Abaqus/Implicit associated with a large time step in order to reduce the computation time.

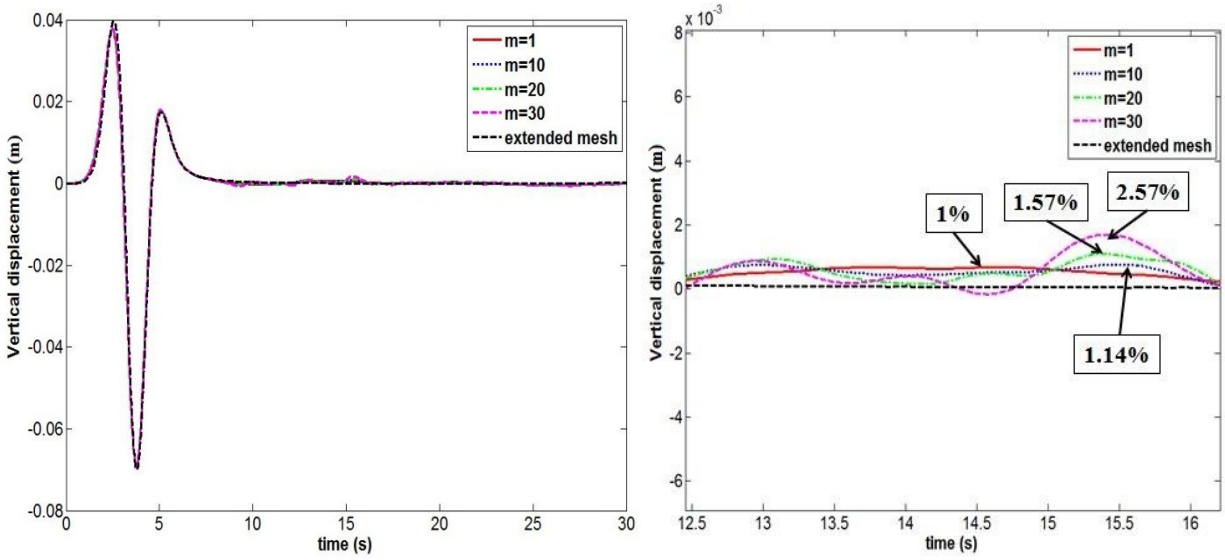

Figure 2-9 Vertical displacements at the observation point using different time step ratios

Cette thèse est accessible à l'adresse : http://theses.insa-lyon.fr/publication/2019LYSEI042/these.pdf
© [S. Li], [2019], INSA Lyon, tous droits réservés

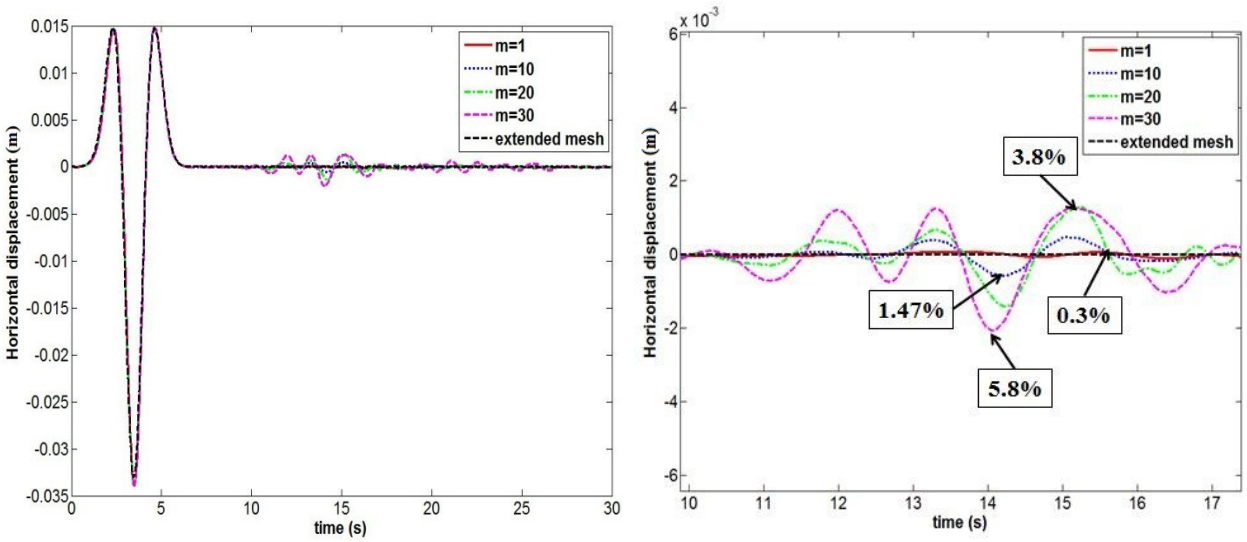

Figure 2-10 Horizontal displacements at the observation point using different time step ratios

The horizontal and vertical displacements of the observation point with different time step ratios m ($\Delta t_2 = m\Delta t_1$) equal to 10, 20, and 30, are shown in Figures 2-9 and 2-10. The kinetic and internal energies are computed for different time step ratios as shown in Figure 2-11. In order to distinguish the difference between them, the L^2 norm error in time is computed between energies of HA-ALID and those of extended mesh (reference results). Considering a quantity E over the time interval [0, T], the L^2 norm is defined by:

$$err = \frac{\left\| E^{(m)} - E_{\text{ref}} \right\|_{L^2([0,T])}}{\left\| E_{\text{ref}} \right\|_{L^2([0,T])}} \tag{2.29}$$

$E^{(m)}$ is the kinetic or internal energy obtained by Abaqus Explicit/Implicit co-simulation with the time step ratio m and E_{ref} is the reference energy obtained from the extended mesh.

The reflected spurious waves recorded at the observation point grow bigger with the increase of the time step ratio m. It can be observed that in comparison to the displacements given by reference results, the vertical amplitude of the spurious wave varies from 1% to 2.57% with respect to the vertical amplitude of the incident wave, while the horizontal amplitude of the spurious wave varies from 0.3% to 5.8% with respect to that of the incident wave. From Table.2-2, it can be noted that the error in kinetic energy increases from 0.48% to 1.12% when the time step ratio increasing from 1 to 30, whereas the error in internal energy increases from 0.43% to 0.95%. It can be observed that the errors remain small and stable in terms of energy.

Cette thèse est accessible à l'adresse : http://theses.insa-lyon.fr/publication/2019LYSEI042/these.pdf
© [S. Li], [2019], INSA Lyon, tous droits réservés

Based on these results, the time step ratio m has to be chosen under 10 without significant influence on the accuracy of HA-ALID. The observed decrease of accuracy as the time step ratio increases can be explained by the following points. First, due to the increase of the time step in the implicit scheme, the numerical errors grow. Second, the GC coupling algorithm is known to be dissipative as soon as heterogeneous time steps are used between the subdomains, generating spurious waves at the interface.

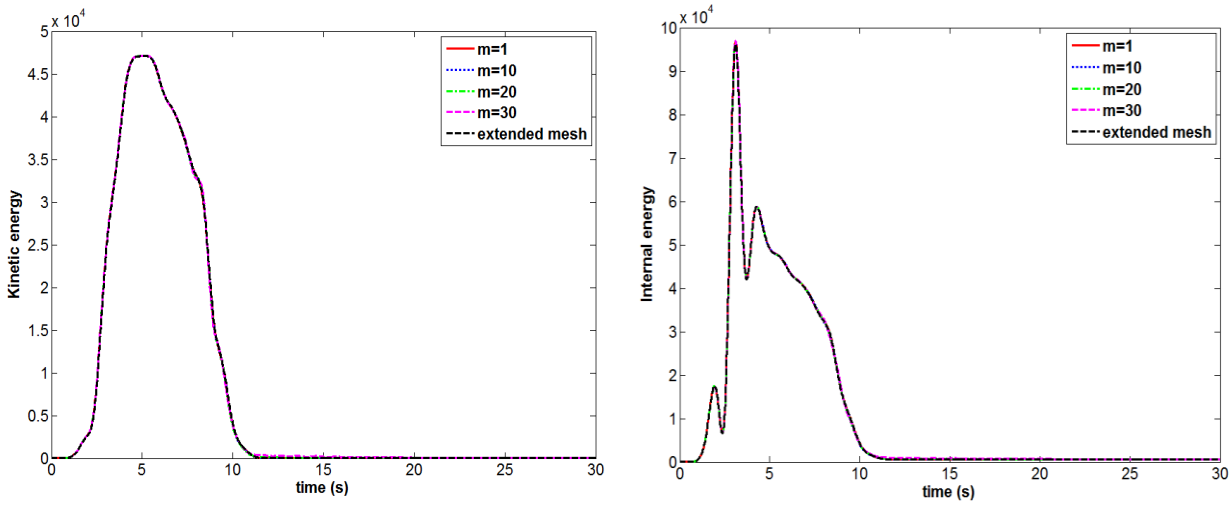

Figure 2-11 Kinetic and internal energies computed using different time step ratios

Table 2-2 Relative energy errors of different time step ratio

	Kinetic energy	Internal energy
m=1	0. 48%	0.43%
m=10	0.67%	0.45%
m=20	0.77%	0.63%
m=30	1.12%	0.95%

Cette thèse est accessible à l'adresse : http://theses.insa-lyon.fr/publication/2019LYSEI042/these.pdf
© [S. Li], [2019], INSA Lyon, tous droits réservés

2.5 Comparison between infinite elements and Rayleigh absorbing layers in Abaqus

Infinite elements available in Abaqus/Explicit allow to deal with unbounded media. To further validate the accuracy of the HA-ALID using Abaqus Explicit/Implicit multi-time step co-simulation, we compare their performance with infinite elements available in Abaqus/Explicit. Thus, a numerical model is established using Abaqus/Explicit with the same mesh and materials as our previous explicit/implicit simulations: HA-ALID are just replaced with Abaqus infinite elements.

The horizontal and vertical displacements of three numerical models at the observation point are shown in Figures 2-12 and 2-13. We can observe that the results obtained by Abaqus Explicit/Implicit co-simulation and reference results are in a good agreement: the reflected spurious wave is 1.47 % in terms of the horizontal displacement, 1.14 % in terms of the vertical displacement when the time step ratio m is equal to 10. In comparison, the reflected spurious wave produced by infinite element is equal to 10.4 % with respect of the vertical amplitude of the incident wave and 17.6% with respect of the horizontal amplitude of the incident wave. In conclusion, HA-ALID has a much better accuracy than Abaqus infinite elements. In the following section, the relevance of the proposed HA-ALID will be assessed in the case of a wave barrier problem.

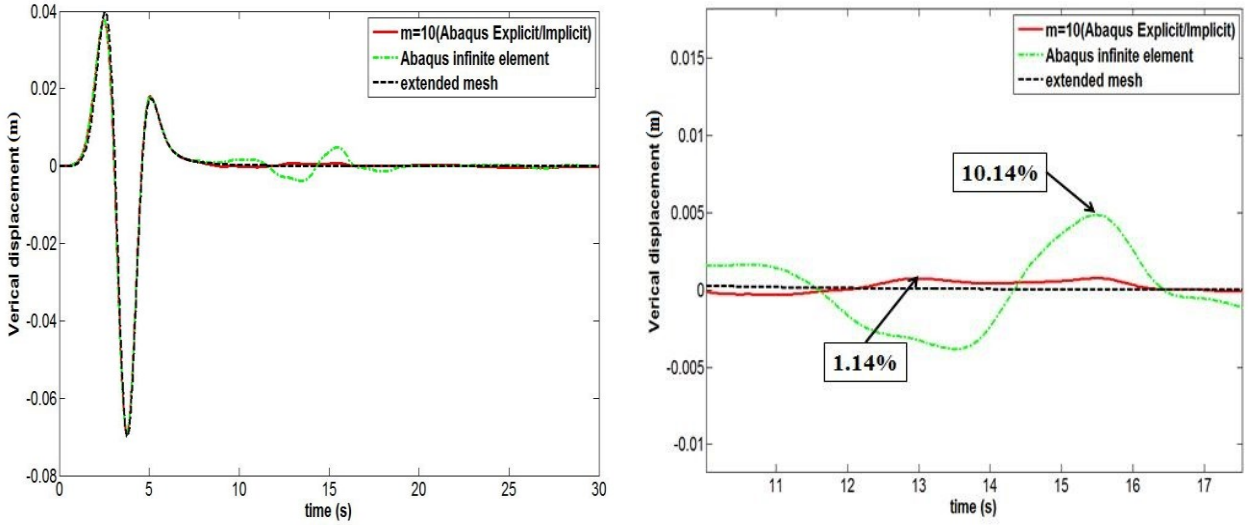

Figure 2-12 Vertical displacements at the observation point using different methods

Cette thèse est accessible à l'adresse : http://theses.insa-lyon.fr/publication/2019LYSEI042/these.pdf
© [S. Li], [2019], INSA Lyon, tous droits réservés

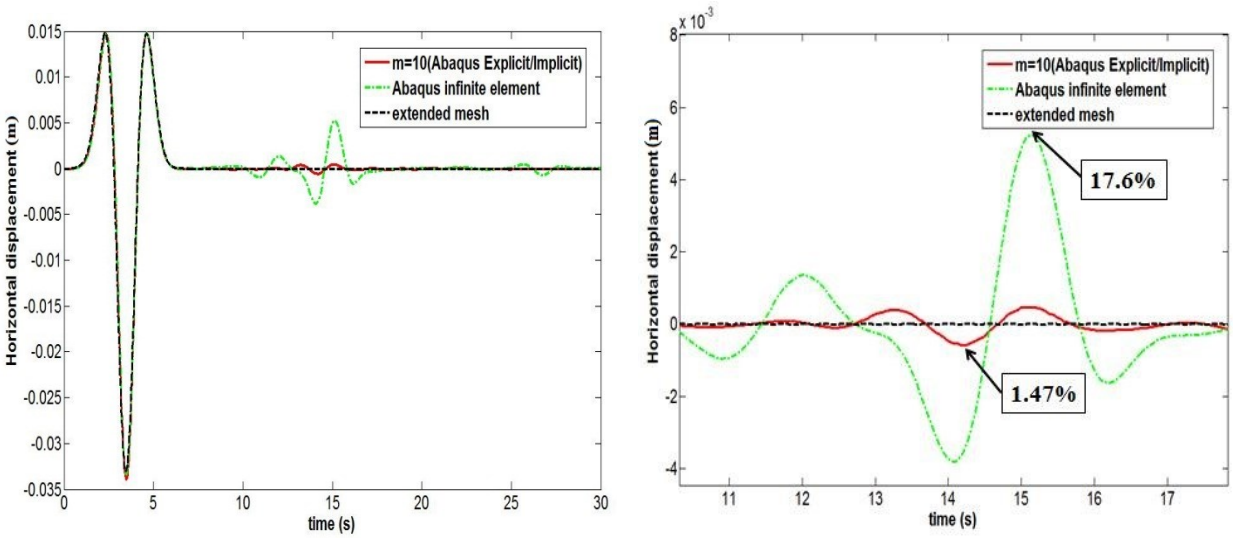

Figure 2-13 Horizontal displacements at the observation point using different methods

2.6 An application in wave barrier numerical simulation

Due to the increasing vibrations caused by human activities, the performance of wave barriers for reducing the distress to adjacent structures and annoyance to people, have been studied for more than 30 years. As illustrated in Figure 2-14, the wave barrier configuration studied by Beskos *et al.* (1991) and Al-Hussaini *et al.* (1986), is investigated. In this case, it was shown that the major part of the vibration energy is transferred by Rayleigh waves which may cause strong ground motions on nearby structures. An application of HA-ALID is carried out for this case of wave barrier.

In this soil-barrier configuration, D is the depth of the barrier, equal to 5 m, W is the width of the barrier, equal to 0.5m, L_1 is the distance from the dynamic load to the barrier equal to 25m and L_2 is the distance from the barrier to the point of interest equal to 25m. The total length of the model is 120m and the depth is 25m. The inclination angle U of the barrier is given as 90°. A dynamic load P with a width of r equal to 1.25 m is applied to the left top surface of the soil, producing a Rayleigh wave to simulate dynamic events such as the compaction, blasting and seismic waves. The dynamic periodic load in the numerical model is $P = P_0\cos(\omega_0 t)$, ω_0=100π, P=1000N, the material properties of soil and barrier are shown below. In the soil, the P-wave, S-wave and Rayleigh-wave velocities are: V_P =475.7m/s, V_S=274.64m/s, V_R=252.62m/s. In order to achieve a

Cette thèse est accessible à l'adresse : http://theses.insa-lyon.fr/publication/2019LYSEI042/these.pdf
© [S. Li], [2019], INSA Lyon, tous droits réservés

good accuracy in predicting the propagating waves into the soil, the finite element size is kept as $\lambda_P/50$ for both subdomains.

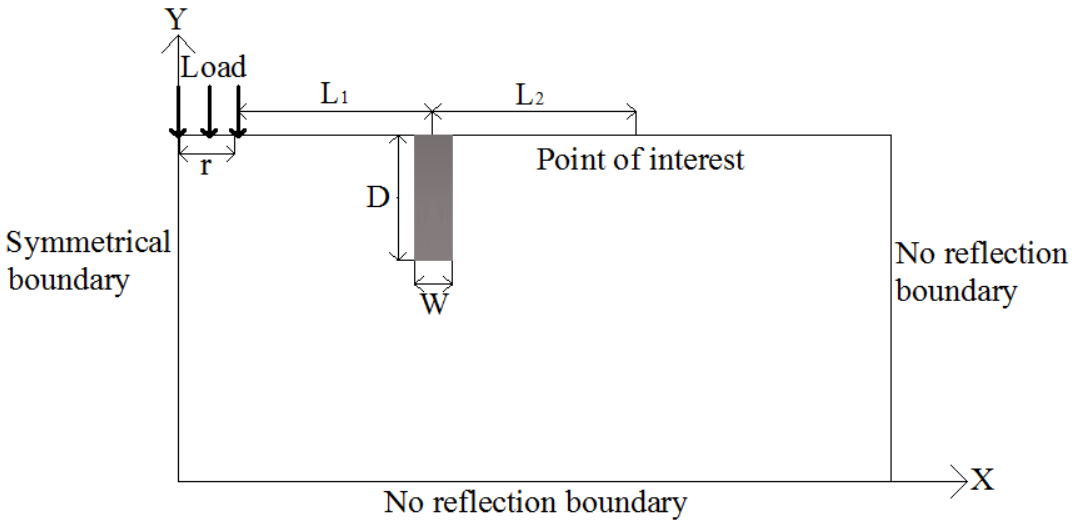

Figure 2-14 Investigated configuration of a 2D soil-barrier system

Table 2-3 Material properties of soil and barrier

Material	Density ρ(kg/m3)	Poisson's ratio v	Young's modulus E(GPa)
Soil	1750	0.25	0.33
Barrier	2397.5	0.25	11.30

HA-ALID adopts a quadratic evolution of damping ratio. Taking advantage of the partition strategy through Abaqus Explicit/Implicit co-simulation, the 2D soil-barrier system is divided into three partitions integrated in time with their own time integrator and time step: soil subdomain (explicit scheme), barrier subdomain (implicit scheme, with a large time step ratio m equal to 10), Rayleigh absorbing layers subdomain (implicit scheme, with a large time step ratio m equal to 10), as shown in Figure 2-15.

Cette thèse est accessible à l'adresse : http://theses.insa-lyon.fr/publication/2019LYSEI042/these.pdf
© [S. Li], [2019], INSA Lyon, tous droits réservés

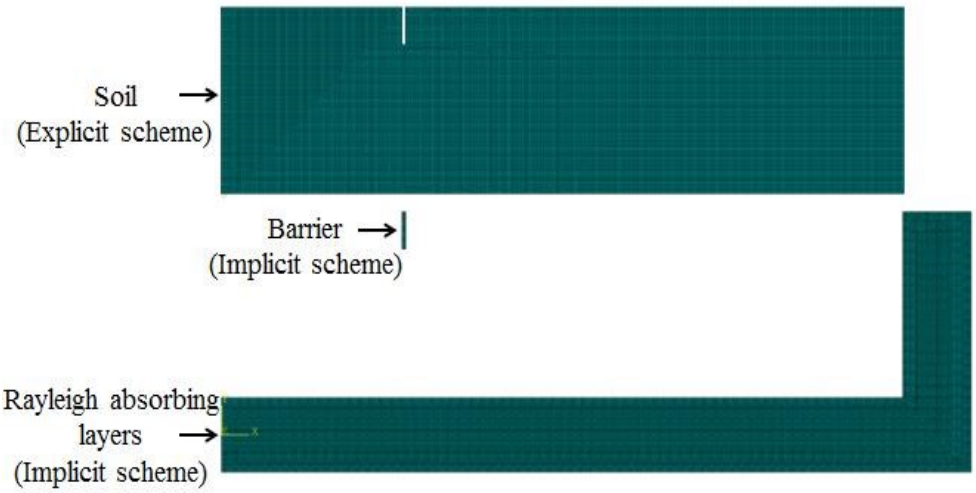

Figure 2-15 Wave-barrier model split in three partitions: soil, solid barrier, ALID.

In the solid barrier, the P-wave velocity is equal to 2378.21m/s. In a full explicit computation using Abaqus/Explicit, the time step must satisfy the smallest time step depending on finite element sizes and material characteristics. HA-ALID involve large values of damping ratios for absorbing the incident waves. In Abaqus/Explicit documentation, recommended values are provided so as to guarantee the stability of the explicit time integration scheme:

$$\Delta t \leq \frac{2}{w_{\max}}\left(\sqrt{1+\xi_{\max}^2}-\xi_{\max}\right) \tag{2.30}$$

$$\xi_{\max} = \frac{\alpha_M}{2\omega_{\max}} + \frac{\alpha_K \omega_{\max}}{2} \tag{2.31}$$

Applying the above formulae to the layers composing the ALID leads to a strong decrease of the critical time step in a full explicit computation. Table 2-4 resumes the critical time steps depending on the partition under consideration (soil, barrier, ALID). It can be noted that ALID have a large impact on the time step size.

Table 2-4 Critical time steps for each partition in full explicit computations

Soil	Barrier	Rayleigh layers	Time step adopted
$269\text{x}10^{-6}$	$53.8\text{x}10^{-6}$	$27.5\text{x}10^{-6}$	$27.5\text{x}10^{-6}$

Cette thèse est accessible à l'adresse : http://theses.insa-lyon.fr/publication/2019LYSEI042/these.pdf
© [S. Li], [2019], INSA Lyon, tous droits réservés

When adopting HA-ALID using Abaqus Explicit/Implicit multi time step co-simulation, the critical time step in the soil is unaffected by the models of the solid barrier and the HA-ALID. Time step sizes for the different partitions are given in Table 2-5, highlighting the interest of the co-simulation. Using HA-ALID, a time step equal to $250x10^{-6}$s can be used in the soil, whereas a full explicit computation requires a value of $27.5x10^{-6}$s related to the absorbing layers.

Table 2-5 Critical time steps for each partition in explicit/implicit multi time step co-simulations

Soil	Barrier	Rayleigh layers
$250x10^{-6}$	$2500x10^{-6}$	$2500x10^{-6}$

Figures 2-16 shows the vertical displacements of the observation point with HA-ALID, compared to the results obtained using infinite elements with the same configuration and the reference results obtained from an extended mesh free of spurious reflected waves from the boundary during the observation period. It turns out that the results of HA-ALID agree well with the reference results, contrary to the full explicit computation with infinite elements: the errors in terms of vertical displacements obtained using infinite elements can be greater than 10%, whereas the biggest error with HA-ALID is equal to 2.7% with respect to the amplitude of reference results.

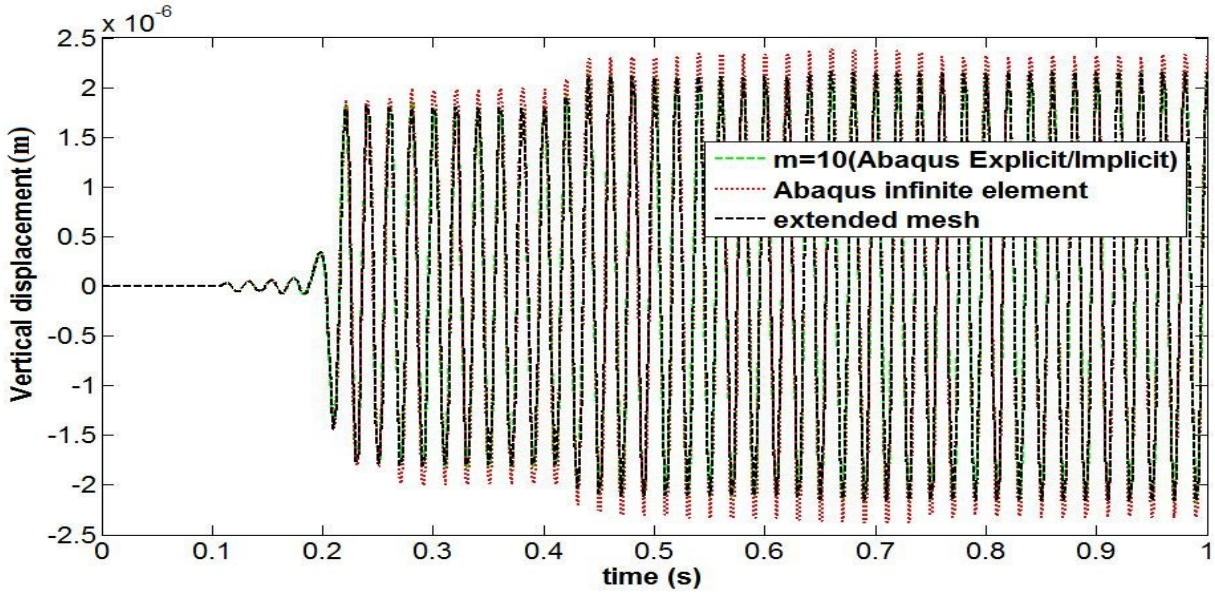

Cette thèse est accessible à l'adresse : http://theses.insa-lyon.fr/publication/2019LYSEI042/these.pdf
© [S. Li], [2019], INSA Lyon, tous droits réservés

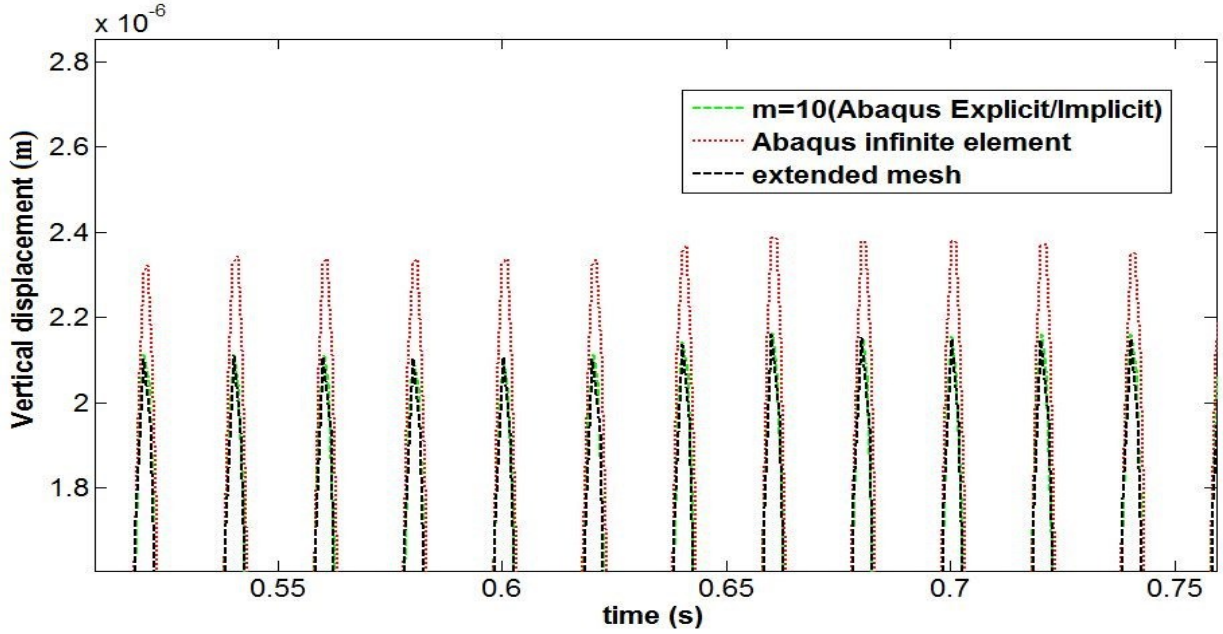

Figure 2-16 Vertical displacements and local zoom at the observation point using HA-ALID with *m*=10 and infinite elements in a full explicit computation

The isolation effect of the installation of the barrier can be assessed by the parameter A_r (amplitude reduction ratio), which provides a quantitative evaluation of the screening effect of the barrier. Its expression is given by: $A_r = A_b/A_s$, where A_b is the displacement amplitude with the barrier and A_s the displacement amplitude without the barrier. For example, A_r = 0.8 means that 20% reduction of the vibration has been reached due to the installation of the barrier. The reduction ratio of vertical displacement on the surface beyond the barrier can be plotted in Figure 2-17, for the three computations. From this figure, it can be concluded that the reduction ratios obtained by HA-ALID have a better agreement with the reference results than those obtained by infinite elements.

Cette thèse est accessible à l'adresse : http://theses.insa-lyon.fr/publication/2019LYSEI042/these.pdf
© [S. Li], [2019], INSA Lyon, tous droits réservés

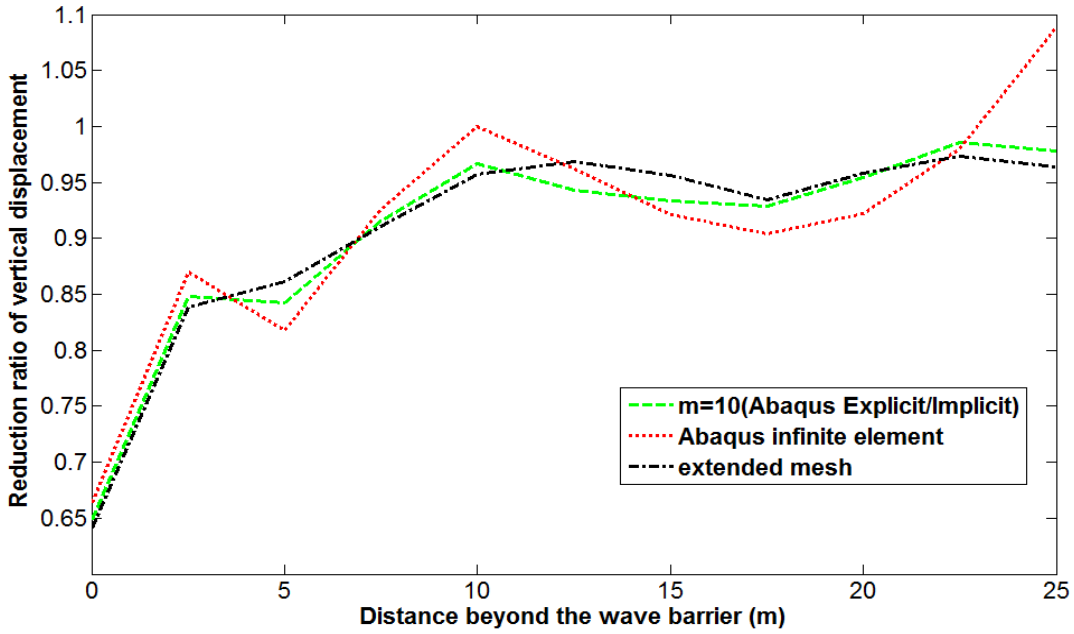

Figure 2-17 Reduction ratio of vertical displacements using HA-ALID with m=10 and infinite elements in a full explicit computation

2.7 Extension to three-dimensional unbounded domains modelling

In comparison with two-dimensional numerical simulation, three-dimensional numerical simulation can describe more details of the physical phenomena under certain circumstances and bring up more precise results. For instance, in the study of wave barrier shown in section 2.6, the depth and the width of the barrier are defined, without taking in account the length of the barrier in the third direction, due to the restrictions of two-dimensional simulation. Hence, in order to better simulate the wave propagation, it is necessary to extend our hybrid asynchronous Rayleigh absorbing layers for modelling three-dimensional unbounded domain, which is very straightforward due to the convenience of the Rayleigh damping in the FE context. On the other hand, three-dimensional models are always more complex, because more elements and degrees of freedom are needed to describe the physical problem. In previous 2D explicit/implicit co-simulations, the subdomain Ω_1 soil was integrated by explicit scheme and the critical time step was not affected by the introduction of Rayleigh matrix in the subdomain Ω_2. For Rayleigh absorbing layers, because of the unconditionally stable implicit scheme, it was possible to use a larger time

Cette thèse est accessible à l'adresse : http://theses.insa-lyon.fr/publication/2019LYSEI042/these.pdf
© [S. Li], [2019], INSA Lyon, tous droits réservés

step. However, when adopting Newmark implicit scheme, system solving with the effective stiffness matrix in subdomain Ω_2 is required, contrarily to the explicit case. This can be very costly in the three-dimensional case. As a consequence, besides the classical Newmark implicit scheme, the Central Difference scheme is also applied in subdomain Ω_2, leading to explicit/explicit multi-time step co-simulation. Multi-time step capabilities are needed because of the reduction of the critical time step by the introduction of Rayleigh damping (Belytschko *et al*., 2000). The difference between the two co-simulation strategies is analyzed in terms of accuracy and computation time.

2.7.1 Space discretization in three-dimension

The space discretization for Rayleigh absorbing layers in two- dimension has been described in section 2.2 and 2.3. In three-dimension space, the modification is only the 8-nodes cube element in place of the 4-nodes rectangular elements, as shown in Fig.2-18.

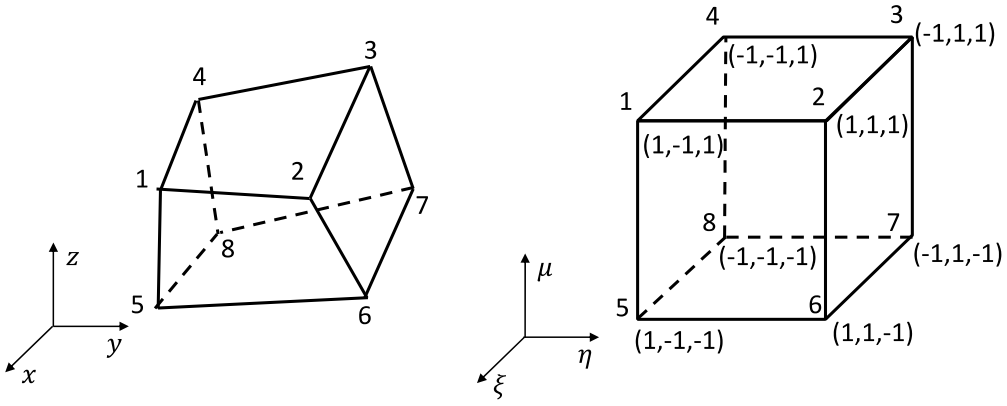

Figure 2-18 8-nodes hexahedral element

We consider in the following the space discretization for a classical 8-nodes hexahedral element with linear shape functions. The approximation of the displacement is given by: $u_e(x,y,z) = \mathbf{N}(x,y,z)\mathbf{U_e}$, where $\mathbf{U_e}$ gathers the nodal displacements of the 8 nodes, of size 24×1; the matrix $\mathbf{N}(x,y,z)$, of size 3×24, contains the nodal shape functions: $\mathbf{N}(x,y,z) = [N_1\mathbf{I} \quad N_2\mathbf{I} \quad \cdots \quad N_8\mathbf{I}]$, with $\mathbf{I}$ the 3×3 identity matrix. The linear shape functions are expressed as:

Cette thèse est accessible à l'adresse : http://theses.insa-lyon.fr/publication/2019LYSEI042/these.pdf
© [S. Li], [2019], INSA Lyon, tous droits réservés

$$\begin{cases} N_1 = (1-\xi)(1-\eta)(1-\mu)/8 \\ N_2 = (1+\xi)(1-\eta)(1-\mu)/8 \\ N_3 = (1+\xi)(1+\eta)(1-\mu)/8 \\ N_4 = (1-\xi)(1+\eta)(1-\mu)/8 \\ N_5 = (1-\xi)(1-\eta)(1+\mu)/8 \\ N_6 = (1+\xi)(1-\eta)(1+\mu)/8 \\ N_7 = (1+\xi)(1+\eta)(1+\mu)/8 \\ N_8 = (1-\xi)(1+\eta)(1+\mu)/8 \end{cases} \tag{2.32}$$

The element-level matrices can be obtained by adopting a quadrature formula in every hexahedral element. The matrix **B** will be expressed as below:

$$\mathbf{B} = [\mathbf{B_1}\ \mathbf{B_2}\ \mathbf{B_3}\ \mathbf{B_4}\ \mathbf{B_5}\ \mathbf{B_6}\ \mathbf{B_7}\ \mathbf{B_8}]$$

$$\boldsymbol{B_i} = \begin{bmatrix} \frac{\partial N_i}{\partial x} & 0 & 0 \\ 0 & \frac{\partial N_i}{\partial y} & 0 \\ 0 & 0 & \frac{\partial N_i}{\partial z} \\ 0 & \frac{\partial N_i}{\partial z} & \frac{\partial N_i}{\partial y} \\ \frac{\partial N_i}{\partial z} & 0 & \frac{\partial N_i}{\partial x} \\ \frac{\partial N_i}{\partial y} & \frac{\partial N_i}{\partial x} & 0 \end{bmatrix} \tag{2.33}$$

The material constitutive matrix **D** is expressed as:

$$\mathbf{D} = \begin{bmatrix} k+4\mu/3 & k-2\mu/3 & k-2\mu/3 \\ k-2\mu/3 & k+4\mu/3 & k-2\mu/3 \\ k-2\mu/3 & k-2\mu/3 & k+4\mu/3 \\ \mu & 0 & 0 \\ 0 & \mu & 0 \\ 0 & 0 & \mu \end{bmatrix} \tag{2.34}$$

where μ is shear modulus, k is bulk modulus. Next, the matrices defined in the global coordinates (x, y, z) should be transformed in local (ξ, η, μ) coordinate systems, as demonstrated in Fig 2-18. The relationship for three-dimensional coordinate transformation in isoparametric elements is shown in the following:

Cette thèse est accessible à l'adresse : http://theses.insa-lyon.fr/publication/2019LYSEI042/these.pdf
© [S. Li], [2019], INSA Lyon, tous droits réservés

$$x = \sum_{i=1}^{8} N_i(\xi, \eta, \mu) x_i \tag{2.35}$$

$$y = \sum_{i=1}^{8} N_i(\xi, \eta, \mu) y_i \tag{2.36}$$

$$z = \sum_{i=1}^{8} N_i(\xi, \eta, \mu) z_i \tag{2.37}$$

By using the above relationship, the matrices in the global coordinates will be transformed in local (ξ, η, μ) coordinate system with **J** the Jacobian matrix:

$$\mathbf{J} = \begin{bmatrix} \partial x/\partial \xi & \partial y/\partial \xi & \partial z/\partial \xi \\ \partial x/\partial \eta & \partial y/\partial \eta & \partial z/\partial \eta \\ \partial x/\partial \mu & \partial y/\partial \mu & \partial z/\partial \mu \end{bmatrix} \tag{2.38}$$

2.7.2 Time discretization of explicit/explicit co-simulation

The time discretization for hybrid asynchronous Rayleigh absorbing layers using co-simulation explicit/implicit in two- dimension has been described in section 2.3. Here, we focus on the time discretization for explicit/ explicit co-simulation. As illustrated in Fig. 2-19, the subdomain Ω_1 soil is integrated by Newmark explicit scheme and the critical time step is not affected by the subdomain Ω_2. The subdomain Ω_2 Rayleigh absorbing layer is integrated by the Central Difference explicit scheme with a smaller time step Δt_2 reduced by the introduction of Rayleigh matrix. With respect to explicit/implicit co-simulation, the advantage of the proposed explicit/explicit co-simulation is to be able to avoid system solving thanks to the diagonalized form of the lumped mass matrix, while the disadvantage is that the time step in subdomain Ω_2 is reduced by Rayleigh damping.

Cette thèse est accessible à l'adresse : http://theses.insa-lyon.fr/publication/2019LYSEI042/these.pdf
© [S. Li], [2019], INSA Lyon, tous droits réservés

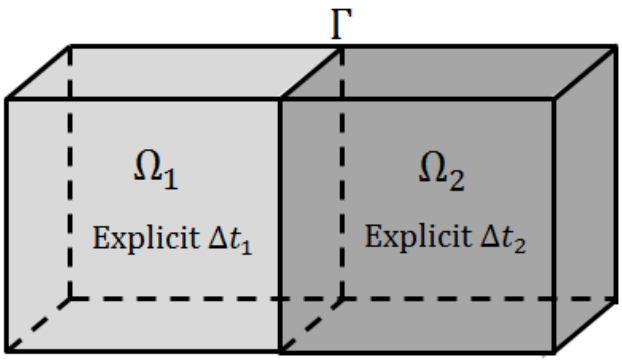

Figure 2-19 Three-dimensional explicit/ explicit co-simulation

The approximate update formulas of the Central Difference explicit scheme in terms of the displacements and velocities at the end of the time step (a time step Δt is defined by the beginning time t_n and the end time t_{n+1}) are expressed using known values of velocities $\dot{\mathbf{U}}^{\mathbf{n-1/2}}$, which is the mid step velocity related to the previous time step, and of displacements $\mathbf{U}^{\mathbf{n}}$:

$$\dot{\mathbf{U}}^{\mathbf{n+1/2}} = \dot{\mathbf{U}}^{\mathbf{n-1/2}} + \Delta t \ddot{\mathbf{U}}^{\mathbf{n}} \tag{2.39}$$

$$\mathbf{U}^{\mathbf{n+1}} = \mathbf{U}^{\mathbf{n}} + \Delta t \dot{\mathbf{U}}^{\mathbf{n+1/2}} \tag{2.40}$$

Contrarily to the previously presented explicit/implicit co-simulations, in the explicit/explicit co-simulation, the equilibrium of subdomain 1 is prescribed at time t_m at the end of the large time Δt_2, while the equilibrium of subdomain 2 is prescribed at every time $t_j = j\Delta t_1$ (j =1, 2...m) at the fine time scale, because of the reduction of the critical time step by the introduction of Rayleigh damping. Finally, the weak form given in Eq. (2.15) with the velocity continuity equation in Eq. (2.16), can be expressed in the following discrete form in space and time:

$$\mathbf{M_1}\ddot{\mathbf{U}}_\mathbf{1}^\mathbf{m} + \mathbf{K_1}\mathbf{U}_\mathbf{1}^\mathbf{m} = \mathbf{F}_\mathbf{1}^{\mathbf{ext,m}} - \mathbf{L}_\mathbf{1}^\mathbf{T}\boldsymbol{\lambda}^\mathbf{m} \quad \text{at time } t = t_j \tag{2.41}$$

$$\mathbf{M_2}\ddot{\mathbf{U}}_\mathbf{2}^\mathbf{j} + (\alpha_M\mathbf{M_2} + \alpha_K\mathbf{K_2})\dot{\mathbf{U}}_\mathbf{2}^{\mathbf{j-1/2}} + \mathbf{K_2}\mathbf{U}_\mathbf{2}^\mathbf{j} = \mathbf{F}_\mathbf{2}^{\mathbf{ext,j}} - \mathbf{L}_\mathbf{2}^\mathbf{T}\boldsymbol{\lambda}^\mathbf{j} \quad \text{at time } t = t_m \tag{2.42}$$

$$\mathbf{L_1}\dot{\mathbf{U}}_\mathbf{1}^\mathbf{j} + \mathbf{L_2}\dot{\mathbf{U}}_\mathbf{2}^\mathbf{j} = 0 \quad \text{at time } t = t_j \tag{2.43}$$

where $\mathbf{M_i}$ and $\mathbf{K_i}$ are the mass and the stiffness matrices of subdomains Ω_1 and Ω_2 (i=1, 2). The first equation is the discrete equation of motion of subdomain Ω_1 written at time t_m (large time

Cette thèse est accessible à l'adresse : http://theses.insa-lyon.fr/publication/2019LYSEI042/these.pdf
© [S. Li], [2019], INSA Lyon, tous droits réservés

scale), whereas the second equation is the discrete equations of motion of subdomains Ω_2 written at time t_j (fine time scale). On the right-hand side of the above equations, the interface forces enable the subdomains to be glued at their interface Γ_I. The gluing of the velocity at the interface is written at the fine time scale.

By introducing the approximate time integration schemes, it leads to the equations of motion written as:

$$\mathbf{M_1}\ddot{\mathbf{U}}_\mathbf{1}^\mathbf{m} = \mathbf{F}_\mathbf{1}^{\mathbf{ext,m}} - \mathbf{K_1}\mathbf{U}_\mathbf{1}^{\mathbf{0,p}} - \mathbf{L}_\mathbf{1}^\mathbf{T}\boldsymbol{\lambda}^\mathbf{m} \tag{2.44}$$

$$\mathbf{M_2}\ddot{\mathbf{U}}_\mathbf{2}^\mathbf{j} = \mathbf{F}_\mathbf{2}^{\mathbf{ext,j}} - \mathbf{C_2}\dot{\mathbf{U}}_\mathbf{2}^{\mathbf{j}-\frac{\mathbf{1}}{\mathbf{2}}} - \mathbf{K_2}\mathbf{U}_\mathbf{2}^\mathbf{j} - \mathbf{L}_\mathbf{2}^\mathbf{T}\boldsymbol{\lambda}^\mathbf{j} \tag{2.45}$$

We can see that the effective stiffness matrices are now replaced with lumped mass matrices. With the use of diagonal ("lumped") mass matrix, the computational efficiency in terms of inverse calculation will be optimized. The kinematic quantities are divided into two parts: the free and the linked quantities in the coupling GC method. The free quantities are calculated by taking into account the internal and external forces, without considering the interface forces, whereas the linked quantities are obtained from the interface loads given by the Lagrange multiplier vector $\boldsymbol{\lambda}$. It is demonstrated that the kinematic continuity condition can be expressed as a reduced-size interface problem as follows:

$$\mathbf{H}\boldsymbol{\lambda}^\mathbf{j} = \mathbf{b}^\mathbf{j} \tag{2.46}$$

with the interface operator and the right-hand side member vector defined by:

$$\begin{cases} \mathbf{H} = \frac{1}{2}\Delta t_1 \mathbf{L_1}{\mathbf{M_1}}^{-\mathbf{1}}\mathbf{L}_\mathbf{1}^\mathbf{T} + \frac{1}{2}\Delta t_2 \mathbf{L_2}{\mathbf{M_2}}^{-\mathbf{1}}\mathbf{L}_\mathbf{2}^\mathbf{T} \\ \mathbf{b}^\mathbf{j} = \mathbf{L_1}\dot{\mathbf{U}}_\mathbf{1}^{\mathbf{free,j}} + \mathbf{L_2}\dot{\mathbf{U}}_\mathbf{2}^{\mathbf{free,j}} \end{cases} \tag{2.47}$$

2.7.3 Numerical examples

In order to evaluate the effectiveness of three-dimensional HA-ALID, simple 3D Lamb's test will be carried out using different co-simulation strategies. Non-harmonic waves are investigated by considering a Ricker incident wave. The Ricker wave, plotted in time domain and in frequency

Cette thèse est accessible à l'adresse : http://theses.insa-lyon.fr/publication/2019LYSEI042/these.pdf
© [S. Li], [2019], INSA Lyon, tous droits réservés

domain in Figure 2-2, has three parameters: the fundamental period t_p, the time shift t_s and the amplitude$A$. The chosen values are: t_p=3s, t_s=3s and A =1MN.

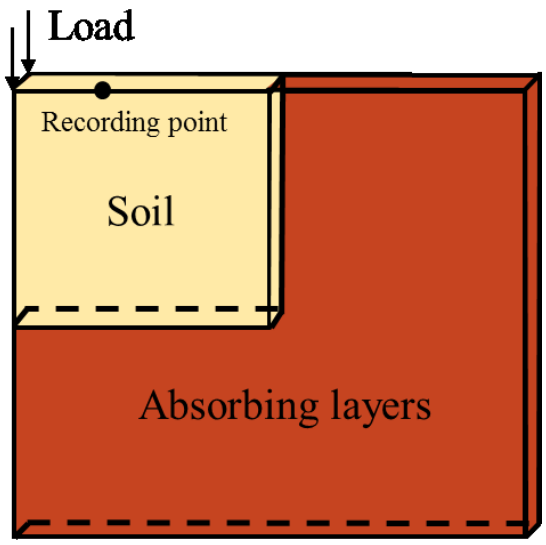

Figure 2-20 3D Lamb's test using explicit/implicit and explicit/explicit co-simulation

The example of 3D Lamb's test is simulated with one 3D element in the thickness direction as shown in Fig.2-20, so as to reduce the computation time in the case of implicit Rayleigh absorbing layers. The soil is assumed to be linear elastic with the dimension 250m x 250m x 5m (element size 5m x 5m x 5m) and the following material characteristics: ρ_1=1700kg/m^3, E_1=10MPa and ν_1= 0.24 for the density, Young's modulus and Poisson's ratio, respectively. The P-wave, S-wave and Rayleigh wave velocities are: V_P =83.27m/s, V_S=48.7m/s, V_R=44.73m/s. The thickness of absorbing layers is 250m. A recording point is located at 20m from the loading point on the surface. The ALID design employed the following parameters based on Eq. (2.12): $R_{attenution}$ equal to 0.01, n equal to 2 and a design frequency f_0 equal to 0.33 Hz. The other material parameters of layers can be calculated on the basis of the optimal conditions at the interface given in Eq. (2.9).

In case of explicit/implicit co-simulation, the subdomain soil is integrated in time by an explicit scheme with a fine time step (Δt_1=0.025s) imposed by the CFL condition, whereas the Rayleigh absorbing layer is integrated by an implicit scheme with larger time step Δt_1=m Δt_2, m= 1, 10, 20, 30. In case of explicit/explicit co-simulation, the subdomain soil is also integrated in time by Newmark explicit scheme with the time step (Δt_1=0.025s) imposed by the CFL condition, but the

Cette thèse est accessible à l'adresse : http://theses.insa-lyon.fr/publication/2019LYSEI042/these.pdf
© [S. Li], [2019], INSA Lyon, tous droits réservés

Rayleigh absorbing layer is integrated by Central Difference scheme with a smaller time step $\Delta t_2 = 1/10 \Delta t_1$, reduced due to the introduction of Rayleigh damping in the elastic media.

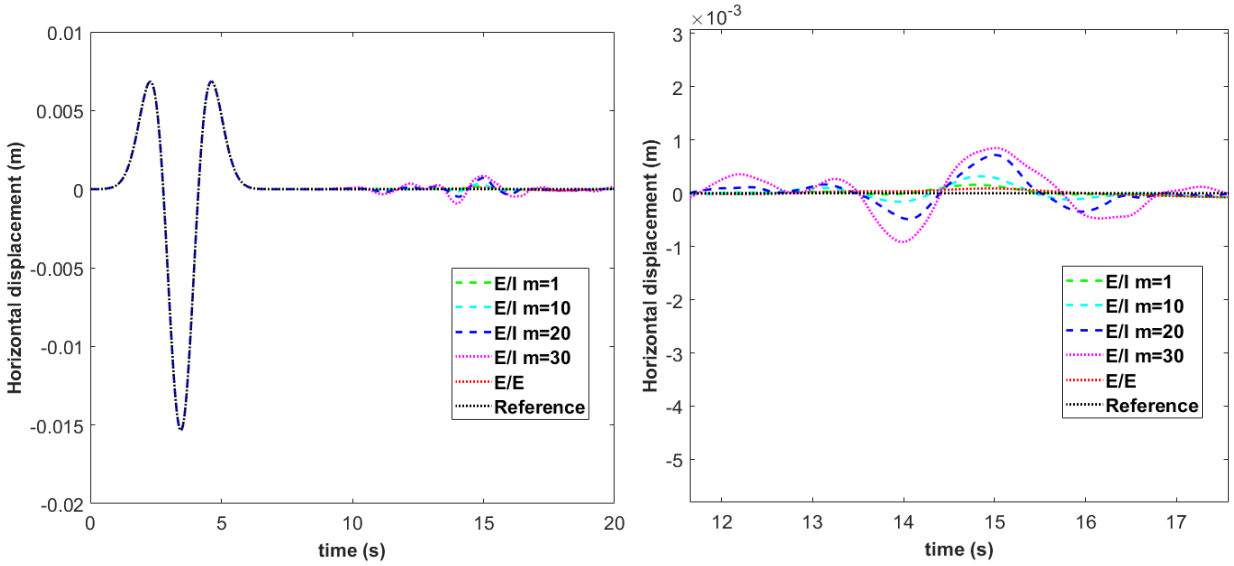

Figure 2-21 Horizontal displacements at observation point using different co-simulation strategies

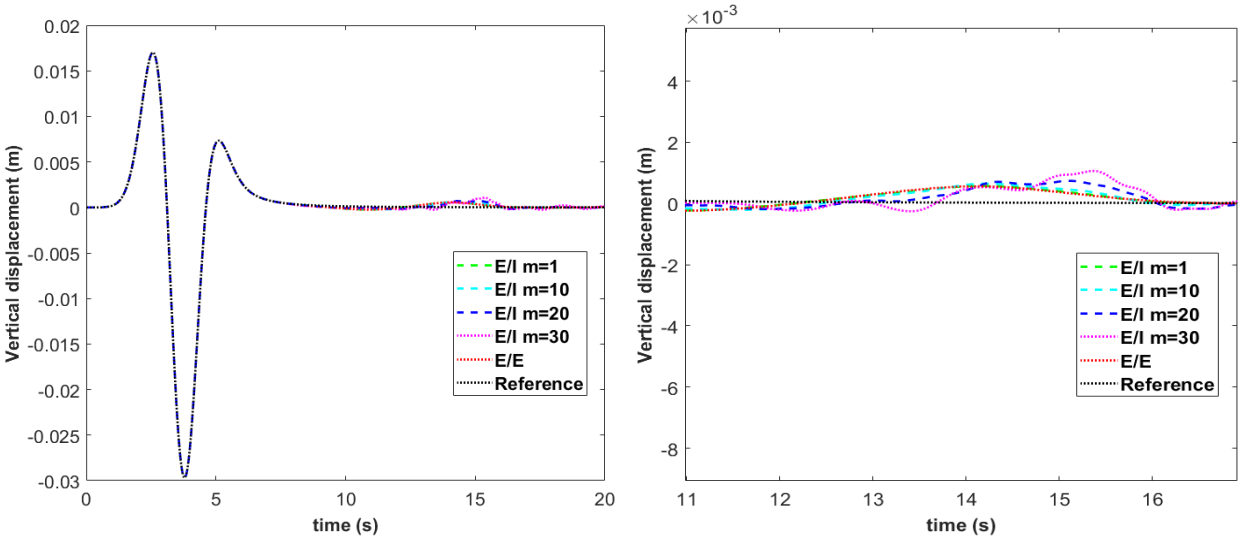

Figure 2-22 Vertical displacements at observation point using different co-simulation strategies

Figures 2-21 and 2-22 show the horizontal and vertical displacements in Lamb's test for different co-simulations in comparison to the reference results obtained from an extended mesh, free of spurious reflected waves in the observation period. In the case of explicit/implicit co-simulation, with respect to the amplitude of the incident wave, the horizontal reflected spurious

Cette thèse est accessible à l'adresse : http://theses.insa-lyon.fr/publication/2019LYSEI042/these.pdf
© [S. Li], [2019], INSA Lyon, tous droits réservés

waves are 1.02%, 2.07%, 4.68%, 5.97% for m= 1, 10, 20, 30, respectively; the vertical reflected spurious waves are 1.84%, 2.09%, 2.43%, 3.52% for m= 1, 10, 20, 30, respectively. Similar to the 2D Lamb's test, the reflected spurious waves recorded at the observation point augment with the increasing time step ratio m, because the GC coupling algorithm is known to be dissipative as soon as heterogeneous time steps are used between the subdomains, generating spurious waves at the interface. The snapshots of displacement magnitude at different times for time ratio m= 1 are displayed in Figure 2-23. No obvious reflections can be observed at the interface or from the boundaries, indicating very satisfactory performance of three-dimensional HA-ALID.

Table 2-6 Reflections using different co-simulation strategies (Rayleigh)

	Vertical displacement	Horizontal displacement
E/I m=1	1.84%	1.02%
E/I m=10	2.09%	2.07%
E/I m=20	2.43%	4.68%
E/I m=30	3.52%	5.97%
E/E	1.80%	0.58%

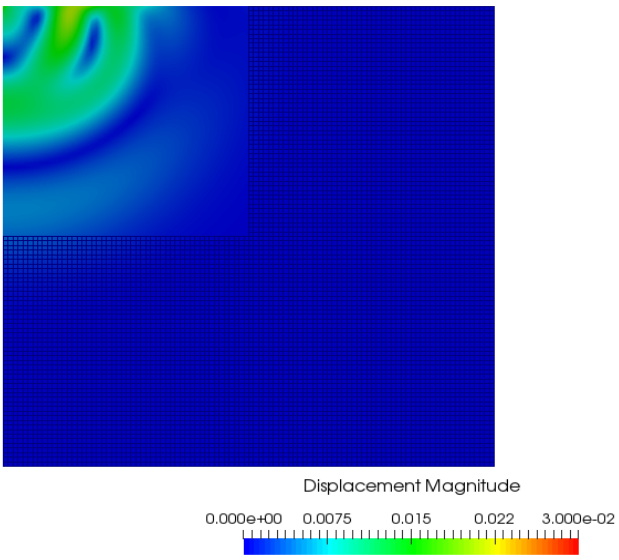

(a) t = 5s

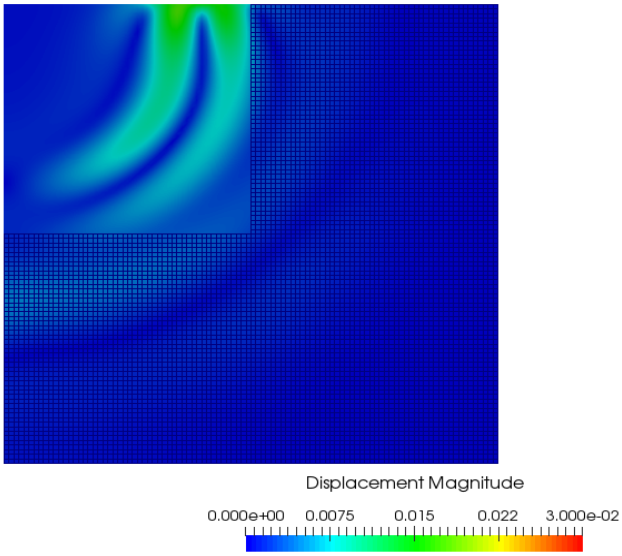

(b) t = 7.5s

Cette thèse est accessible à l'adresse : http://theses.insa-lyon.fr/publication/2019LYSEI042/these.pdf
© [S. Li], [2019], INSA Lyon, tous droits réservés

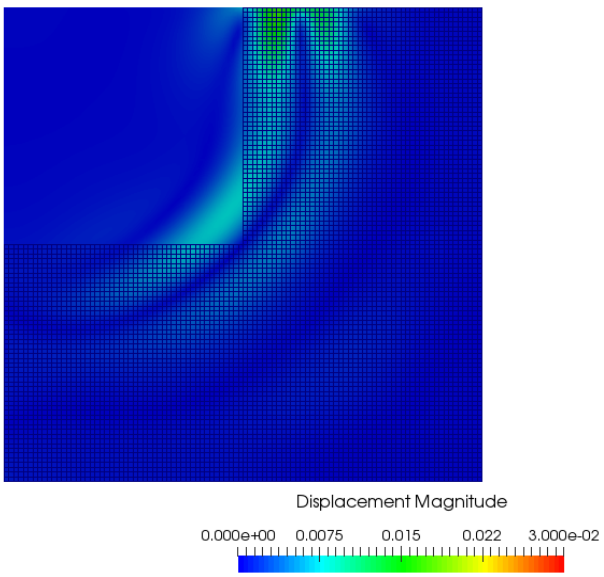

(c) t = 10s

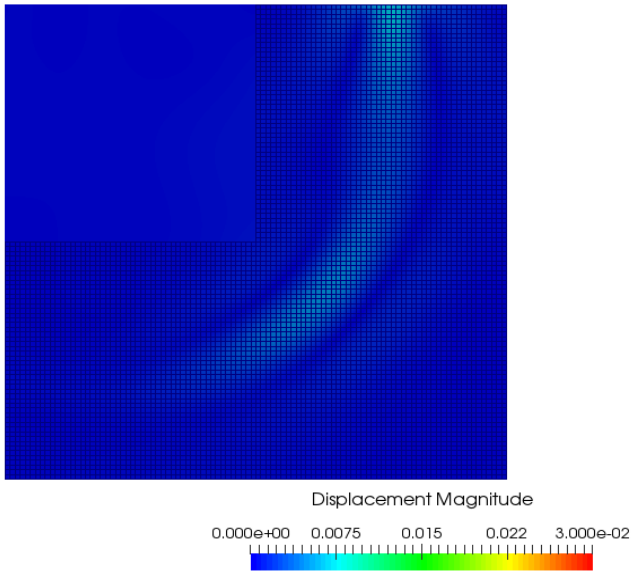

(d) t = 12.5s

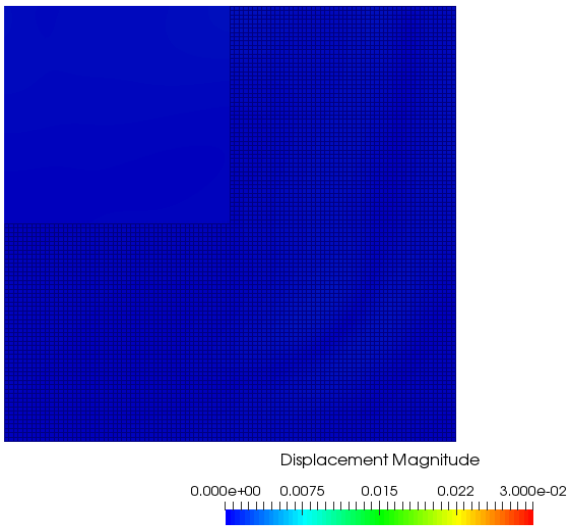

(e) t = 15s

Figure 2-23 Snapshots of displacement magnitude at different times for E/I (m=1)

In case of explicit/explicit co-simulation (Δt_2=1/10Δt_2), the horizontal reflected spurious wave is 0.58% and the vertical reflected spurious wave is 1.80%, with respect to the amplitude of the incident wave. The L^2 norm error in time is computed between energies of HA-ALID and those of extended mesh (reference results). For explicit/implicit co-simulation, the error in kinetic energy increases from 0.06% to 0.32% when the time step ratio increasing from 1 to 30, whereas the error

Cette thèse est accessible à l'adresse : http://theses.insa-lyon.fr/publication/2019LYSEI042/these.pdf
© [S. Li], [2019], INSA Lyon, tous droits réservés

in internal energy increases from 0.09% to 0.84%. For explicit/explicit co-simulation, the error in kinetic energy is 0.05%, and the error in internal energy increases from 0.08%. It can be observed that the accuracy in explicit/explicit co-simulation (Δt_2=1/10Δt_1) is at the same level of explicit/implicit co-simulation (m=1).

In terms of the computation time, the CPU times are resumed in Table.2-8 in a normalized form divided by CPU time of the co-simulation explicit/implicit (m=1). We see that, with the increase of the time step ratio, the CPU time's decrease. It implies that using explicit/implicit co-computation, not only the critical time step in the soil partition is not affected by the introduction of damping layer, but also large time steps can be adopted in absorbing layer domain to reduce the computation time. When the time ratio is bigger than 20, the reduction for the computation time is not significant, this is because, in this case, the time stepping become one small part of the CPU time, most of the computation time is dedicated to the other procedure in finite element method, such as matrix assemblage. It can also be observed that in comparison with explicit/implicit co-simulation, the computation time for co-simulation explicit/explicit is the least, thanks to the diagonalization of the effective stiffness matrix of absorbing layer subdomain, even though the time step in the absorbing layer is 10 times smaller than the time step in the subdomain soil. As a conclusion, in 3D Lamb's test, HA-ALID using co-simulation explicit/explicit has the same precision level as co-simulation explicit/implicit (m=1), but less computation time than co-simulation explicit/implicit (m=30), as shown in Table 2-8.

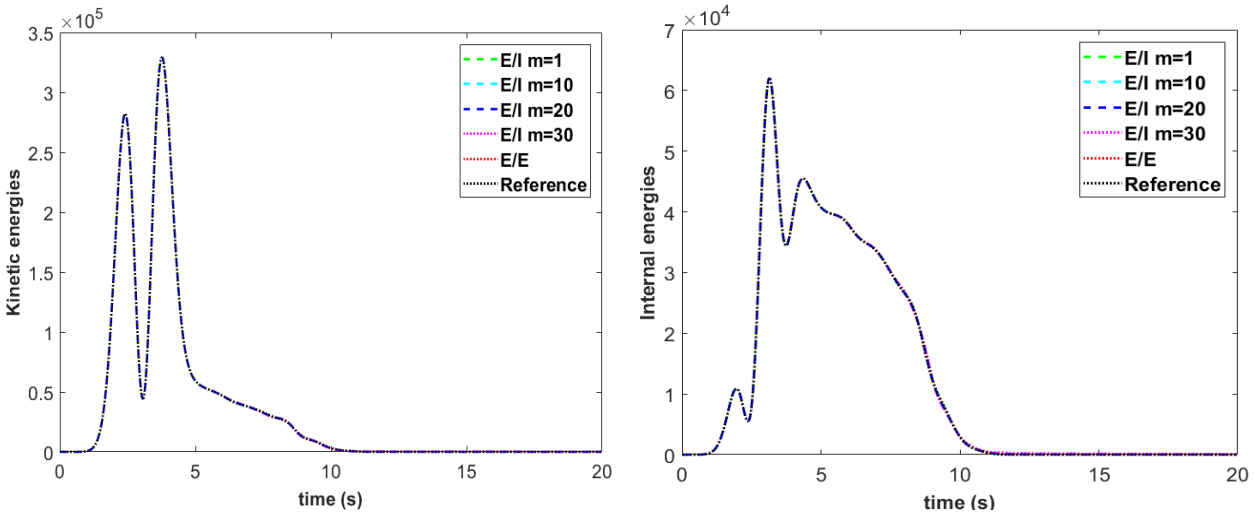

Figure 2-24 Kinetic and internal energies computed using different co-simulation strategies

Cette thèse est accessible à l'adresse : http://theses.insa-lyon.fr/publication/2019LYSEI042/these.pdf
© [S. Li], [2019], INSA Lyon, tous droits réservés

Table 2-7 Relative energy errors of different co-simulations (Rayleigh)

	Kinetic energy	Internal energy
E/I m=1	0. 06%	0.09%
E/I m=10	0.12%	0.18%
E/I m=20	0.21%	0.40%
E/I m=30	0.32%	0.84%
E/E	0.05%	0.08%

Table 2-8 Normalized CPU time of different co-simulations (Rayleigh)

	m=1	m=10	m=20	m=30	E/E
Normalized CPU time	1	0.26	0.20	0.19	0.18

2.8 Conclusion

Absorbing Layers with Increasing Damping (ALID) can be easily set up for damping out the incident waves at the boundary of a Finite Element mesh thanks to the availability of the viscous Rayleigh damping matrix in commercial FE codes. In this chapter, a simple and accurate method for modeling unbounded domains is proposed using co-simulation. Subdomain decomposition strategy is applied for problems coupling physical medium with Rayleigh absorbing layers, based on HATI method.

In order to highlight the accuracy of the method, 2D Lamb's test and a wave barrier problem have been studied using HA-Rayleigh ALID with a quadratic profile of damping ratio in the thickness direction of the HA-Rayleigh ALID. Very satisfactory results have been achieved in terms of kinematic quantities and energies. The obtained results showed that spurious waves reflected at the boundary of the truncated mesh are much lower than the ones generated by non-reflective conditions available in Abaqus/Explicit for modeling infinite medium (infinite elements). On the other hand, some interesting benefits of the HA-Rayleigh ALID can be underlined in

Cette thèse est accessible à l'adresse : http://theses.insa-lyon.fr/publication/2019LYSEI042/these.pdf
© [S. Li], [2019], INSA Lyon, tous droits réservés

comparison to the classical ALID. First, large time steps can be adopted in the solid barrier and in the HA-Rayleigh ALID in comparison to the fine time step in the soil medium corresponding to the CFL condition. Second, the critical time step in the soil partition is unaffected by the choice of damping matrix in the layers of the HA-Rayleigh ALID, related to the stiffness or mass matrices, contrary to the case of a full explicit computation for which the critical time step can be significantly reduced.

Finally, hybrid asynchronous Rayleigh absorbing layers is extended for modelling three-dimensional unbounded domains using explicit/implicit and explicit/explicit co-simulations. The difference between the two co-simulation strategies is compared in terms of accuracy and computation time by 3D Lamb's test. Taking into account its advantages in accuracy and CPU time, HA-Rayleigh ALID using co-simulation explicit/explicit turns out to be more suitable for three-dimensional wave propagation simulation.

Cette thèse est accessible à l'adresse : http://theses.insa-lyon.fr/publication/2019LYSEI042/these.pdf
© [S. Li], [2019], INSA Lyon, tous droits réservés

Cette thèse est accessible à l'adresse : http://theses.insa-lyon.fr/publication/2019LYSEI042/these.pdf
© [S. Li], [2019], INSA Lyon, tous droits réservés

Chapter 3

Hybrid asynchronous Kosloff absorbing layer

One of the drawbacks of the viscous Rayleigh damping in FE software is its dependence with respect to frequencies in the problem. As a result, it is interesting to explore the capabilities of other damping formulations than Rayleigh damping, while remaining very simple to be easily set up in a general FE software. In this chapter, the capabilities of the Kosloff damping are investigated to set up efficient HA-Kosloff ALID and compared with Rayleigh formulation. First, the design of Kosloff absorbing layer is proposed by using the strong form of elastic wave propagation in Kosloff medium. The absorbing ability of Kosloff absorbing layer associated with a performance criterion is derived in the form of a logarithmic decrement and proved to be independent of frequency. A general formula for designing Kosloff absorbing layers using a multi-layer strategy is derived. In addition, optimal conditions are obtained to avoid the spurious waves reflected at the interface between physical domain and Kosloff absorbing layer domain. In the case of non-harmonic waves, Kosloff absorbing layer is found to be less sensitive to the design parameters in comparison to Rayleigh absorbing layer. Secondly, the weak formulation of the decomposed problem is given in order to derive the space discretization. Kosloff formulation turns out to have a very simple finite element expression which corresponds to two new matrices, similar to the mass matrix, operating on velocities and displacements in semi-discrete equation of motion. For the time discretization, the GC method proposed by Gravouil and Combescure, belonging to more general HATI methods, is employed in order to integrate, in a decoupled manner, the domain of interest and the absorbing layer. Then, Lamb's test illustrates the efficiency of HA-Kosloff ALID in terms of accuracy and

Cette thèse est accessible à l'adresse : http://theses.insa-lyon.fr/publication/2019LYSEI042/these.pdf
© [S. Li], [2019], INSA Lyon, tous droits réservés

CPU time, in comparison to HA-Rayleigh ALID in Chapter 2 and the HA-PML (Brun *et al.*, 2016). The differences among the approaches are analyzed to demonstrate the advantages and disadvantages of each approach. Finally, HA-Kosloff ALID is extended for modelling three-dimensional unbounded domains using explicit/implicit and explicit/explicit co-simulations. The two co-simulation strategies are compared in terms of accuracy and computation time.

The main part of this chapter, devoted to 2D transient analysis, has been published recently in Computers and Geotechnics:

Li S, Brun M, Zafati E, Djeran-Maigre I and Kuznetsov S (2019). Hybrid asynchronous absorbing layers based on Kosloff damping for seismic wave propagation in unbounded domains. Computers and Geotechnics, 109, 69-81.

Cette thèse est accessible à l'adresse : http://theses.insa-lyon.fr/publication/2019LYSEI042/these.pdf
© [S. Li], [2019], INSA Lyon, tous droits réservés

3.1 Introduction

PML proposed by Bérenger (1994) is becoming increasingly used for dealing with infinite media in the context of finite difference method, as well as in the finite and spectral element methods. Although PML tends to be now considered as the most effective way to model infinite media, the PML implementation is not straightforward in a general purpose finite element software. Thus, more convenient techniques were recently developed in the finite element context, based on simple damping formulations such as the viscous damping Rayleigh matrix in Chapter 2. However, one of the drawbacks of the viscous Rayleigh damping in FE software is its dependence with respect to frequencies in the problem. Consequently, it is interesting to explore the capabilities of other damping formulations than Rayleigh damping, while remaining very simple to be easily set up in a general FE software. Absorbing boundary based on a simple modification in the wave propagating equation, was proposed by Kosloff and Kosloff (1986): in Kosloff medium, the wave travels without changing shape and the wave amplitude decreases with distance at a frequency independent rate. Some similarities between PML and Kosloff absorbing boundary have been discussed by Carcione and Kosloff (2013). It was shown that in the case of SH waves, a modified Kosloff formulation matches the split formulation of the PML, before the spatial and time discretization, highlighting the relation between the two approaches. Here, the Kosloff damping formulation is explored with a view to setting up efficient and convenient absorbing layers for modelling infinite media. The hybrid time integration capabilities are useful to integrate, in a decoupled manner, the domain of interest and the absorbing layer. The resulting absorbing layer will be called Hybrid Asynchronous-Kosloff Absorbing Layers using Increasing Damping (HA-Kosloff ALID), making use of Heterogeneous (different time integrators, that is hybrid integration) Asynchronous (different time steps) Time Integrator developed by Combescure and Gravouil (2001, 2002).

3.2 Strong form of the wave propagation in a Kosloff medium

The design of Kosloff absorbing layer aims at damping out all the incident waves from the domain of interest while minimizing the spurious waves reflected at the boundary of the truncated

Cette thèse est accessible à l'adresse : http://theses.insa-lyon.fr/publication/2019LYSEI042/these.pdf
© [S. Li], [2019], INSA Lyon, tous droits réservés

domain. For this purpose, using the strong form for the wave propagation in the Kosloff medium, the absorbing ability of Kosloff absorbing layer related to a target performance criterion will be quantified in the form of logarithmic decrement. The optimal conditions at the interface between a non-dissipative elastic medium Ω_1 and a dissipative Kosloff medium Ω_2 will be analytically established by considering the continuous problem of wave propagation.

3.2.1 Governing equations of a Kosloff medium

The governing equations in elastodynamics are modified by Kosloff and Kosloff (Kosloff & Kosloff, 1986) in order to introduce a specific damping, called in the following Kosloff damping. The displacement vector field $\underline{u_2}$ in the Kosloff medium Ω_2 is governed by the modified equations:

$$\rho_2 \partial_t^2 \underline{u_2} = \mathrm{div}\left(\underline{\underline{\sigma_2}}\left(\underline{u_2}\right)\right) - 2\rho_2\gamma\partial_t\underline{u_2} - \rho_2\gamma^2\underline{u_2} \tag{3.1}$$

$$\underline{\underline{\sigma_2}} = \lambda_2 \mathrm{tr}\left(\underline{\underline{\varepsilon_2}}\left(\underline{u_2}\right)\right) + 2\mu_2\underline{\underline{\varepsilon_2}}\left(\underline{u_2}\right) \tag{3.2}$$

$$\underline{\underline{\varepsilon_2}} = \frac{1}{2}\left[grad\left(\underline{u_2}\right) + grad\left(\underline{u_2}\right)^T\right] \tag{3.3}$$

Eqs. (3.1) to (3.3) constitute the strong form of the propagation in a Kosloff medium, σ_2 , ε_2, λ_2, μ_2, ρ_2, γ being the stress matrix, strain matrix, Lamé's coefficients, the density and damping ratio, respectively. It can be seen that the strong form of the equation of motion, in Eq. (1), has been changed with two additional damping terms related to displacements and velocities. The other two equations correspond to the elastic constitutive relationship and the definition of the infinitesimal strain. It will be shown in the following that the induced damping enables us to damp out the amplitude of a propagating wave in a Kosloff medium, irrespective of its frequency.

Cette thèse est accessible à l'adresse : http://theses.insa-lyon.fr/publication/2019LYSEI042/these.pdf
© [S. Li], [2019], INSA Lyon, tous droits réservés

3.2.2 1D wave propagation in a Kosloff medium

The argument is developed for 1D wave propagation problem by distinguishing the P-waves and the S-waves in their strong form, written as:

$$\rho\partial_t^2\underline{u} = (\lambda + 2\mu)\partial_x^2\underline{u} - 2\rho\gamma\partial_t\underline{u} - \rho\gamma^2\underline{u} \qquad \mathrm{P} - waves \tag{3.4}$$

$$\rho\partial_t^2\underline{u} = \mu\partial_x^2\underline{u} - 2\rho\gamma\partial_t\underline{u} - \rho\gamma^2\underline{u} \qquad \mathrm{S} - waves \tag{3.5}$$

By introducing harmonic solutions in its complex form $u(x,t) = u_0\exp(i(\omega_0 t - kx))$ into the above wave propagation equations, the expression of the wave number k can be obtained:

$$k = \frac{\omega_0}{v}\left(1 - i\frac{\gamma}{\omega_0}\right) \tag{3.6}$$

with the velocity v equal to $\sqrt{\frac{\lambda+2\mu}{\rho}}$ for P-wave and $\sqrt{\frac{\mu}{\rho}}$ for S-wave. The expression of the propagating wave in the 1D Kosloff medium is shown below,

$$u(x,t) = u_0\, exp(\, i(\omega_0 t - k_0 x))\, exp\left(-\frac{\gamma x}{v}\right) \tag{3.7}$$

The above expression confirms the fact that all the frequency components are equally attenuated due to the decay factor γ/v which is frequency independent as underlined by Carcione and Kosloff (2013).

In order to design efficient absorbing layers based on the Kosloff damping, we assess the logarithmic decrement of the propagating wave. Using the previous expression in Eq. (3.7), the relationship between the logarithmic decrement is expressed as a function of the thickness Δx and the damping ratio γ of the Kosloff absorbing layer:

$$\delta = \ln\left(\frac{|u(x)|}{|u(x+\Delta x)|}\right) = \frac{\gamma\Delta x}{v_p} \tag{3.8}$$

It can be seen that the frequency wave ω_0 has no influence on the absorbing ability of Kosloff absorbing layer with regard to the logarithmic decrement, which means that all waves with all frequencies can be attenuated in the same way. In other words, Kosloff damping turns out to be independent of frequency. The velocity of P waves is higher than the velocity of S waves in the

Cette thèse est accessible à l'adresse : http://theses.insa-lyon.fr/publication/2019LYSEI042/these.pdf
© [S. Li], [2019], INSA Lyon, tous droits réservés

same medium. As a result, based on the above relationships, in order to reach the same logarithmic decrement, the necessary layer thickness for damping out S waves is smaller than the one related to P waves. In the following, the velocity of P waves v_p will be adopted for the design of absorbing layer so as to ensure that all the waves are attenuated according to the target decrement.

3.2.3 Optimal conditions at the interface between an elastic medium and a Kosloff medium

The wave propagation problem from an elastic medium to a Kosloff medium is considered below in the case of the 1D harmonic wave. Three components have to be taken into account: the incident wave u_1, the transmitted wave u_2, and the reflected wave u_R, as shown in Fig.3-1.

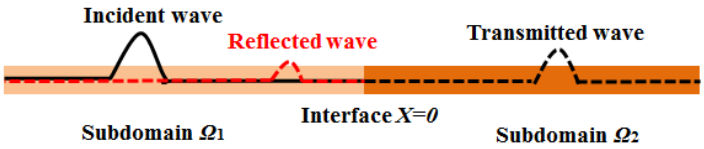

Figure 3-1 Wave propagation from elastic medium to Kosloff medium.

$$u_1(x,t) = A\,\exp[i\omega_0(t-\frac{x}{v_1})] \tag{3.9}$$

$$u_2(x,t) = T\,\exp[i\omega_0(t-\frac{x}{v_2})]\exp[-\frac{\gamma x}{v_2}] \tag{3.10}$$

$$u_R(x,t) = R\,exp[i\omega_0(t+\frac{x}{v_1})] \tag{3.11}$$

Based on the continuity of displacements and equilibrium of stresses at the interface, we can write:

$$u_2(x=0,t) = u_1 + u_R\ (x=0,t) \tag{3.12}$$

$$k_2\partial_x u_2(x=0,t) = k_1(\partial_x u_1 + \partial_x u_R)(x=0,t) \tag{3.13}$$

with k_1 equal to $\lambda_1 + 2\mu_1$ for P-waves or $2\mu_1$ for S-waves while k_2 equal to $(\lambda_2 + 2\mu_2)$ for P-waves or $2\mu_2$ for S-waves, where E_1 and E_2 are Young's moduli, ρ_1 and ρ_2 are the densities of

Cette thèse est accessible à l'adresse : http://theses.insa-lyon.fr/publication/2019LYSEI042/these.pdf
© [S. Li], [2019], INSA Lyon, tous droits réservés

subdomains Ω_1 and Ω_2, where $\lambda_1, \mu_1, \lambda_2, \mu_2$ are Lamé's coefficients in subdomain Ω_1 and Ω_2, respectively. The reflection coefficient $R_{interface}$ at the interface can be obtained as:

$$\frac{R}{A} = \frac{-\rho_2 v_2 \left(1 - i\frac{\gamma}{\omega_0}\right) + \rho_1 v_1}{\rho_2 v_2 \left(1 - i\frac{\gamma}{\omega_0}\right) + \rho_1 v_1} \tag{3.14}$$

By setting the ratio $\alpha = \frac{\rho_2 v_2}{\rho_1 v_1}$, the interface refection coefficient can be written:

$$\frac{R}{A} = \frac{1 - \alpha\left(1 - i\frac{\gamma}{\omega_0}\right)}{1 + \alpha\left(1 - i\frac{\gamma}{\omega_0}\right)} \tag{3.15}$$

If we want to reduce reflection at the interface, the modulus of the above complex valued reflection coefficient should be minimized. It leads to the following relationship:

$$\alpha = \frac{1}{\sqrt{1 + (\frac{\gamma}{\omega_0})^2}} \tag{3.16}$$

Now, we can give a simple condition on material properties of the Kosloff medium so as to reduce the reflected waves in the case of harmonic waves for P-waves and S-waves in 1D medium:

$$\begin{cases} E_2 = \dfrac{E_1}{1 + (\frac{\gamma}{\omega_0})^2} \\ \rho_2 = \rho_1 \\ \nu_2 = \nu_1 \end{cases} \tag{3.17}$$

where E_1 and E_2 are Young's moduli, ρ_1 and ρ_2 are the densities of subdomains Ω_1 and Ω_2, respectively. The above relationships show that, though the Kosloff medium is independent of frequency in terms of decrement, the optimal conditions at the interface depend on the frequency. Therefore, in the case of non-harmonic waves, there will be still some reflections at the interface. This is why we thoroughly evaluate in the following the effect of the chosen f_0 in terms of spurious reflections generated at the interface.

Cette thèse est accessible à l'adresse : http://theses.insa-lyon.fr/publication/2019LYSEI042/these.pdf
© [S. Li], [2019], INSA Lyon, tous droits réservés

3.2.4 Design of Kosloff absorbing layer using a multi-layer strategy

The Absorbing Layers using Increasing Damping (ALID), proposed by Semblat *et al.* (2011), Rajagopal *et al.* (2012) and improved by Zafati *et al.* (2014), as shown in Fig.3-2, is considered by tuning the elastic parameters of each layer depending on the selected absorbing parameters as given by the optimal conditions in Eqs. (3.17). The main idea is to divide the Kosloff absorbing medium into several uniform layers, so that the decrements produced by each layer can be multiplied. Because of the logarithmic form of decrement, the total logarithmic decrement can be easily obtained. The evolution of damping ratio in layers has an important influence on the efficiency of the ALID. Here, a nonlinear increase of damping ratio is adopted to achieve a better accuracy.

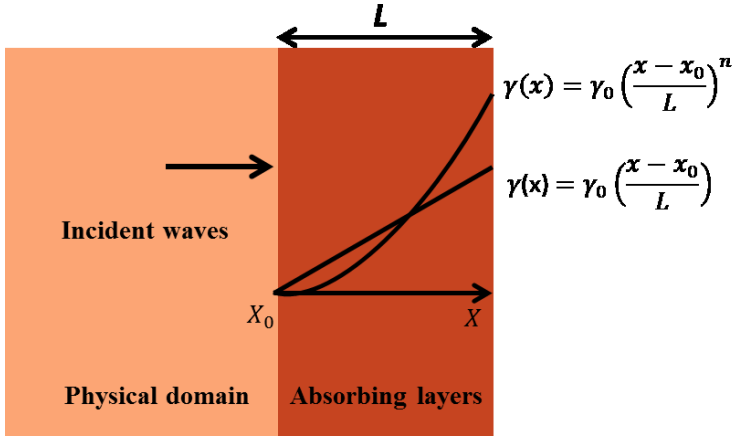

Figure 3-2 Evolution of the damping ratios in multi-layer absorbing subdomain

The parameters of each layer, indexed by (i) varying from 1 to N, which satisfies the optimal conditions at each interface, are given by:

Cette thèse est accessible à l'adresse : http://theses.insa-lyon.fr/publication/2019LYSEI042/these.pdf
© [S. Li], [2019], INSA Lyon, tous droits réservés

$$\begin{cases} E_2^{(i+1)} = \dfrac{1+(\frac{\gamma_i}{\omega_0})^2}{1+(\frac{\gamma_{i+1}}{\omega_0})^2} E_2^{(i)} \\ E_2^{(1)} = \dfrac{1}{1+(\frac{\gamma_1}{\omega_0})^2} E_1 \\ \nu_2^{(i)} = \nu_1 \\ \rho_2^{(i)} = \rho_1 \\ \gamma_i = \gamma_0 \left(\dfrac{x_i}{L}\right)^n \end{cases} \tag{3.18}$$

where $E_2^{(i)}$ the Young's modulus, γ_i the damping ratio, $\nu_2^{(i)}$ Poisson's ratio, $\rho_2^{(i)}$ the density of each layer i in the subdomain Ω_2, ω_0 the chosen frequency to design absorbing layers, γ_0 the damping ratio in the last layer, n the power of the damping function, x_i the distance of each sublayer (i) from the interface of the ALID, varying according L the thickness of the ALID including all sublayers (i). By integrating the logarithmic decrement in Eq. (3.8) along the thickness of the ALID, and using the polynomial form of the damping parameter γ_i in Eq. (3.18), the total logarithmic decrement δ can be assessed as:

$$\begin{cases} \delta_i = \gamma_0 \left(\dfrac{x}{L}\right)^n \dfrac{\Delta x}{v_\rho} \sqrt{1+(\frac{\gamma_1}{\omega_0})^2} \geq \gamma_0 \left(\dfrac{x}{L}\right)^n \dfrac{\Delta x}{v_\rho} \\ \delta = \sum_{i=1}^{N} \delta_i = \int_0^L \dfrac{\gamma_0}{v_\rho} \left(\dfrac{x}{L}\right)^n dx = \dfrac{\gamma_0 L}{(n+1)v_\rho} \end{cases} \tag{3.19}$$

Here, we can see that the simple modification on material properties of the Kosloff medium for reducing the reflection at the interface also increases the absorbing ability of the Kosloff medium. In order to facilitate the integration, the absorbing ability obtained by the right side of the inequation is conservative. The attenuation coefficient $R_{attenution}$ for the system of absorbing layers is defined by:

$$R_{attenution} = \left(\frac{|u(x+L)|}{|u(x)|}\right)^2 = e^{-2\delta} \tag{3.20}$$

If the goal is to reach a target logarithmic decrement δ = ln (10), it means that 90% of the amplitude of the incident wave will be absorbed from the interface to the end of the ALID. Next, the attenuation also occurs for the reflection process from the end of the ALID towards the interface.

Cette thèse est accessible à l'adresse : http://theses.insa-lyon.fr/publication/2019LYSEI042/these.pdf
© [S. Li], [2019], INSA Lyon, tous droits réservés

Hence, the incident wave is attenuated by 99% and the attenuation coefficient $R_{attenution}$ is theoretically equal to 1% before the space and time discretization.

Finally, we can propose the general formula to design Kosloff absorbing layers based on the 1D harmonic wave problem in a Kosloff medium. After choosing the $R_{attenution}$, the total thickness L and the power m of the damping function, γ_0 can be obtained:

$$\gamma_0 = \frac{(n+1)}{2L} \times v_\rho \times \ln(\frac{1}{R_{attenution}}) \tag{3.21}$$

It is important to remark that the general formula to design Kosloff absorbing layers is similar to that of PML proposed by Collino and Tsogka (2001), based on one-dimensional wave propagation ideas, β_0 being the damping parameter in the last PML layer:

$$\beta_0 = \frac{(n+1)}{2L} \times v_\rho \times \ln(\frac{1}{R_{attenution}}) \tag{3.22}$$

Indeed, the capabilities of the PML to damp out incident wave is very similar to the Kosloff damping but the behavior at the interface is different in the two cases, because it is well known the no reflection occurs at a PML interface for all the frequencies. This is not the case for Kosloff and Rayleigh damping as discussed in the next section.

3.2.5 1D non-harmonic wave propagation at the interface between an elastic medium and ALID: comparison between Rayleigh and Kosloff damping

In order to establish optimal condition at the interface, harmonic waves have been previously considered. The relationship shows that, though the Kosloff medium is independent of frequency in terms of decrement, the optimal conditions at the interface depend on the frequency. Therefore, in the case of non-harmonic waves, different reflections will occur at the interface, quantified by the interface reflection coefficient $R_{interface}$. We investigate the influence of the chosen frequency f_0 on the interface reflection coefficient $R_{interface}$ in the case of Kosloff damping. $R_{interface}$ related to Kosloff layer for another frequency f, which is different from f_0, has been derived from Eq. (3.15) as shown below:

Cette thèse est accessible à l'adresse : http://theses.insa-lyon.fr/publication/2019LYSEI042/these.pdf
© [S. Li], [2019], INSA Lyon, tous droits réservés

$$R_{interface} = \frac{1 - \alpha\left(1 - i\frac{\gamma}{\omega_0}\frac{\omega_0}{\omega}\right)}{1 + \alpha\left(1 - i\frac{\gamma}{\omega_0}\frac{\omega_0}{\omega}\right)} \tag{3.23}$$

$$\alpha = \frac{1}{\sqrt{1 + (\frac{\gamma}{\omega_0})^2}} \tag{3.24}$$

For comparison purpose, the case of the Rayleigh damping is reminded and new insights will be provided for a relevant choice of the design frequency f_0. The design of Rayleigh ALID is written as:

$$\xi_0 = \frac{(n+1)}{2L\omega_0} \times v_\rho \times \ln(\frac{1}{R_{attenution}}) \tag{3.25}$$

which is only valid for harmonic waves due to the dependence of the Rayleigh damping on frequency. As a result, the attenuation coefficient $R_{attenution}$ has also to be assessed in the case of non-harmonic waves as a function of the chosen design frequency f_0. Here, it should be remarked that it is not the case of the Kosloff damping as shown by the previous design relation given in Eq. (3.21).

From the assumption adopted in Rayleigh damping ($\frac{\alpha_M}{\omega_0} = \alpha_K\omega_0 = \xi$), the form of the complex wave number is given by:

$$k_p(\omega) = \frac{\omega}{V_p}\sqrt{\frac{1 - \xi^2 - i\xi\left(\frac{\omega_0}{\omega} + \frac{\omega}{\omega_0}\right)}{1 + \xi^2\frac{\omega^2}{{\omega_0}^2}}} \tag{3.26}$$

The dimensionless imaginary part of $k_p(\omega)$ was proved to increase with increasing $\frac{\omega}{\omega_0}$, corresponding to the increase of the amplitude of the reflected wave (Zafati *et al.*, 2015). It means that the high frequencies decay more quickly than the low frequencies. In other words, the relatively small f_0 can make more frequencies be attenuated over the $R_{attenution}$ defined by f_0 .Thus, it is beneficial to consider a relatively small f_0, in terms of absorbing ability for non- harmonic waves in Rayleigh absorbing layer.

Cette thèse est accessible à l'adresse : http://theses.insa-lyon.fr/publication/2019LYSEI042/these.pdf
© [S. Li], [2019], INSA Lyon, tous droits réservés

For a given frequency f, the interface reflection coefficient $R_{interface}$ between an elastic medium and a Rayleigh medium designed at f_0 frequency is expressed as (Zafati *et al.*, 2015):

$$R_{interface} = \frac{1 - \alpha\sqrt{1 + \xi^2 - i\xi\left(\frac{\omega_0}{\omega} - \frac{\omega}{\omega_0}\right)}}{1 + \alpha\sqrt{1 + \xi^2 - i\xi\left(\frac{\omega_0}{\omega} - \frac{\omega}{\omega_0}\right)}} \tag{3.27}$$

$$\alpha = \frac{1}{\sqrt{1 + \xi^2}} \tag{3.28}$$

The interface reflection coefficients $R_{interface}$ for Kosloff and Rayleigh cases are plotted in Figures 3-3 and 3-4 for a frequency ratio f/f_0. It can be remarked that, for the Kosloff damping, the interface reflection coefficient decreases when the frequency ratio increases. Thus, it advocates the choice of a design frequency f_0 less than the dominant frequency present in the investigated problem so as the frequency ratio increases, leading to a very low reflection coefficient. In the case of Rayleigh damping, same analysis can be conducted because small frequency ratio leads to much higher interface reflection coefficient than high frequency ratio. Consequently, taking into account the benefits of the relatively small frequency f_0 in terms of decrement for Rayleigh layer and in terms of interface reflection for both Kosloff and Rayleigh layers, one method to reduce the reflection for the case of non-harmonic waves is to define the f_0 relatively small.

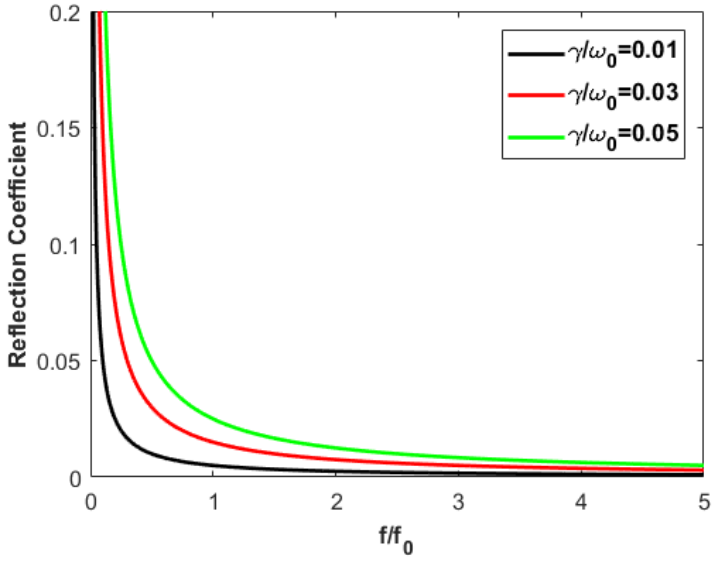

Figure 3-3 Kosloff $R_{\text{interface}}$ using different f/f_0 and γ/ω_0

Cette thèse est accessible à l'adresse : http://theses.insa-lyon.fr/publication/2019LYSEI042/these.pdf
© [S. Li], [2019], INSA Lyon, tous droits réservés

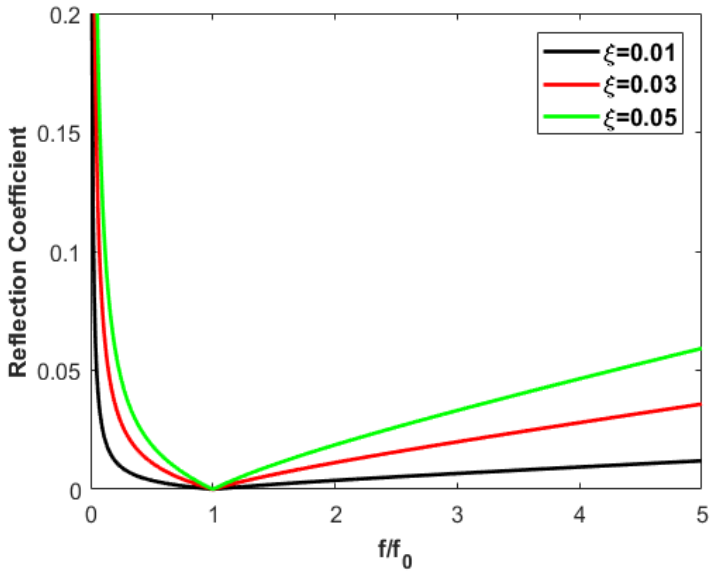

Figure 3-4 Rayleigh $R_{\text{interface}}$ using different f/f_0 and ξ

Secondly, the figures also show that, with ξ and γ/ω_0 increasing, the interface reflection coefficient $R_{interface}$ increases in both figures. Due to the dependence of the absorbing ability on frequency in the case of Rayleigh damping, with a smaller chosen frequency f_0, the damping ratio ξ of Rayleigh layer based on the general design formula Eq. (3.25) will be bigger, so it leads to the increase of reflection for all the frequencies. Regarding Kosloff layer, a decreased design frequency f_0 gives a higher frequency-dependent damping parameter γ/ω_0. It implies that the chosen frequency should not be defined too small. As a result, a compromise has to be found to select a design frequency f_0 sufficiently small in comparison to the dominant frequency, without affecting to much the reflection coefficient. This will be verified in the following numerical investigations.

Finally, from the comparison between Figures 3-3 and 4-4, in the high frequency range, it can be highlighted that $R_{interface}$ related to the Kosloff damping is much less affected by the increase of the frequency-dependent damping parameter γ/ω_0 than the one related to the Rayleigh damping with increasing damping ratio ξ. The interface reflection coefficient tends to very low values for Kosloff damping when frequency ratio increases, contrarily to Rayleigh damping. It is important because it means a better interface behavior of the Kosloff ALID than the Rayleigh ALID.

Cette thèse est accessible à l'adresse : http://theses.insa-lyon.fr/publication/2019LYSEI042/these.pdf
© [S. Li], [2019], INSA Lyon, tous droits réservés

3.3 The space and time discretization for HA-Kosloff ALID

The elastic wave propagation from an elastic non-dissipative medium to a dissipative medium should be discretized in space and time. In this section, the hybrid time integration of the ALID based on Kosloff damping is presented.

Let Ω be a bounded domain belonging to $\mathbb{R}^2$ with a regular boundary. $J = [0, T]$ is the time interval of interest. The domain Ω is divided into two partitions Ω_1 and Ω_2, as shown in Fig.1-4, such as: $\Omega_1 \bigcap \Omega_2 = \emptyset$ and $\partial\Omega_1 \bigcap \partial\Omega_2 = \Gamma$. Γ denotes the interface between the two subdomains, subdomain Ω_1 representing the non-dissipative medium (the domain of interest) and subdomain Ω_2 the Kosloff medium. The goal is to integrate the domain of interest Ω_1 using a conditionally stable explicit time integration scheme suitable for modeling the wave propagation, while integrating the Kosloff ALID with an unconditionally stable implicit time integration scheme in order to not decrease the size of the critical time step in Ω_1.

3.3.1 Weak form and space discretization

The subdomain Ω_1 is characterized by its density ρ_1, Young's modulus E_1, Poisson's coefficient ν_1, $\underline{b_1}$ the body force, $\underline{u_1^D}$ the Dirichlet prescribed displacement on Γ_1^D and $\underline{g_1^N}$ the traction force at the Neumann condition on Γ_1^N. The subdomain Ω_2 is characterized by its density ρ_2, Young's modulus E_2, Poisson's coefficient ν_2, $\underline{b_2}$ the body force, $\underline{u_2^D}$ the Dirichlet prescribed displacement on Γ_2^D, $\underline{g_2^N}$ the traction force at the Neumann condition on Γ_2^N and the Kosloff damping parameter γ introduced in the strong form of the wave equation in Eq. (3.1) .

In order to write the weak form of the coupled problem in Ω divided into two partitions Ω_1 and Ω_2, test functions $\underline{v_1}$ and $\underline{v_2}$ belonging to the appropriate spaces W_1^* and W_2^* must be introduced:

$$\begin{cases} \underline{v_1} \in W_1^*, W_1^* = \left\{ \underline{v_1} \in \left(H^1(\Omega_1)\right)^d \text{ and } \underline{v_1} = 0 \text{ on } \Gamma_1^D \right\} \\ \underline{v_2} \in W_2^*, W_2^* = \left\{ \underline{v_2} \in \left(H^1(\Omega_2)\right)^d \text{ and } \underline{v_2} = 0 \text{ on } \Gamma_2^D \right\} \end{cases} \tag{3.29}$$

The solutions $\underline{u_1}$ and $\underline{u_2}$ belong to the appropriate spaces W_1 and W_2:

Cette thèse est accessible à l'adresse : http://theses.insa-lyon.fr/publication/2019LYSEI042/these.pdf
© [S. Li], [2019], INSA Lyon, tous droits réservés

$$\begin{cases} \underline{u}_1(t) \in W_1, W_1 = \left\{ \underline{u}_1 \in \left(H^1(\Omega_1)\right)^d and\ \underline{u}_1 = u_1^D\ on\ \Gamma_1^D \right\} \\ \underline{u}_2(t) \in W_2, W_2 = \left\{ \underline{u}_2 \in \left(H^1(\Omega_2)\right)^d and\ \underline{u}_2 = u_2^D\ on\ \Gamma_2^D \right\} \end{cases} \tag{3.30}$$

where d is the space dimension (equal to 1, 2 or 3). According to a dual Schur approach, the introduction of the Lagrange multipliers allows us to glue the velocities of the two subdomains at the interface Γ (Gravouil and Combescure, 2001; 2002). The Lagrange multipliers belong to the adapted dual trace space related to the interface between the two subdomains, denoted by Q. All the considered space variables are assumed to be sufficiently smooth and regular.

Next, using a dual Schur formulation, the principle of virtual power for transient dynamics can be written. Find the solution $\underline{u}_1(t) \in W_1$, $\underline{u}_2(t) \in W_2$ and $\underline{\lambda}(t) \in Q$, for which the following weak form is satisfied $\forall \underline{v}_1 \in W_1$, $\forall \underline{v}_2 \in W_2$ and $\forall \underline{\mu} \in Q$:

$$\begin{aligned} &\int_{\Omega_1} \rho_1 \underline{v}_1 \cdot \ddot{\underline{u}}_1 d\Omega + \int_{\Omega_1} \underline{\underline{\varepsilon}}(\underline{v}_1) : \underline{\underline{\sigma}}_1 d\Omega + \int_{\Omega_2} \rho_2 \underline{v}_2 \cdot \ddot{\underline{u}}_2 d\Omega + \int_{\Omega_2} \underline{\underline{\varepsilon}}(\underline{v}_2) : \underline{\underline{\sigma}}_2 d\Omega + \int_{\Omega_2} 2\rho_2 \gamma \underline{v}_2 \cdot \dot{\underline{u}}_2 d\Omega \\ &+ \int_{\Omega_2} \rho_2 \gamma^2 \underline{v}_2 \cdot \underline{u}_2 d\Omega + \int_{\Gamma_I} \underline{v}_1 \cdot \underline{\lambda} d\Gamma + \int_{\Gamma_I} \underline{v}_2 \cdot \underline{\lambda} d\Gamma + \int_{\Gamma_I} \underline{\mu} \cdot \left(\dot{\underline{u}}_1 - \dot{\underline{u}}_2\right) d\Gamma \\ &= \int_{\Omega_1} \underline{v}_1 \cdot \underline{b}_1 d\Omega + \int_{\Gamma_1^N} \underline{v}_1 \cdot \underline{g}_1^N d\Gamma + \int_{\Omega_2} \underline{v}_2 \cdot \underline{b}_2 d\Omega + \int_{\Gamma_2^N} \underline{v}_2 \cdot \underline{g}_2^N d\Gamma \end{aligned} \tag{3.31}$$

where the stress tensor $\underline{\underline{\varepsilon}}_2$ satisfies the behavior law given in Eq. (3.2). Then, we follow the classical lines of the finite element discretization. At the interface between the subdomains, the continuity of velocities is imposed by the following condition:

$$\mathbf{L_1}\dot{\mathbf{U}}_\mathbf{1} + \mathbf{L_2}\dot{\mathbf{U}}_\mathbf{2} = \mathbf{0} \tag{3.32}$$

where $\mathbf{L_1}$ and $\mathbf{L_2}$ are the Boolean matrices in the case of matching meshes at the interface; they operate on nodal vectors associated with the two subdomains Ω_1 and Ω_2; they pick out the degrees of freedom belonging to the interface Γ in order to ensure the kinematic continuity at the interface.

Thus, the restricted velocities at the interface can be obtained from the global nodal velocity vectors $\dot{\mathbf{U}}_\mathbf{1}$and $\dot{\mathbf{U}}_\mathbf{2}$ by the relationships:

$$\begin{cases} \dot{\mathbf{U}}_\mathbf{1}^\mathbf{\Gamma} = \mathbf{L_1}\dot{\mathbf{U}}_\mathbf{1} \\ \dot{\mathbf{U}}_\mathbf{2}^\mathbf{\Gamma} = \mathbf{L_2}\dot{\mathbf{U}}_\mathbf{2} \end{cases} \tag{3.33}$$

Cette thèse est accessible à l'adresse : http://theses.insa-lyon.fr/publication/2019LYSEI042/these.pdf
© [S. Li], [2019], INSA Lyon, tous droits réservés

Same relationships hold for the global virtual nodal velocities $\mathbf{V_1}$ and $\mathbf{V_2}$. Finally, interface terms involving the Lagrange multiplier field can be expressed as:

$$\begin{cases} \int_{\Gamma_I} \underline{v}_1 \cdot \underline{\lambda} d\Gamma = \mathbf{V_1^T L_1^T \lambda} \\ \int_{\Gamma_I} \underline{v}_2 \cdot \underline{\lambda} d\Gamma = \mathbf{V_2^T L_2^T \lambda} \end{cases} \tag{3.34}$$

From the weak form of the global problem in Eq. (3.31), the semi-discrete equations in space can be derived, corresponding to the two equations of motion related to the two subdomains, completed with a kinematic condition. In the following, the hybrid integration of this set of equations will be carried out in order to propose a hybrid asynchronous Kosloff ALID.

3.3.2 Time discretization of the Hybrid Asynchronous absorbing layers

As illustrated in Fig.1-4, an explicit time integrator with a fine time step Δt_1 is adopted for the subdomain Ω_1 and an implicit time integrator with a large time step Δt_2 is used for subdomain Ω_2, with $\Delta t_2 = m\Delta t_1$, m being the time step ratio between two subdomains. In this way, hybrid (different schemes associated) asynchronous (different time steps depending on subdomains) absorbing layers can be obtained. The equilibrium of subdomain 2 is prescribed at time t_m at the end of the large time Δt_2, while the equilibrium of subdomain 1 is prescribed at every time $t_j = j\Delta t_1$ (j =1, 2...m) at the fine time scale. The gluing of the velocity at the interface is written at the fine time scale.

Finally, the weak form given in Eq. (3.31) with the velocity continuity equation in Eq. (3.32) and the expression of the interface terms as a function of the Lagrange multipliers in Eq. (3.34), can be expressed in the following discrete form in space and time:

$$\mathbf{M_1 \ddot{U}_1^j + K_1 U_1^j = F_1^{ext,j} - L_1^T \lambda^j} \qquad \text{at time } t = t_j \tag{3.35}$$

$$\mathbf{M_2 \ddot{U}_2^m + C_1 \dot{U}_2^m + C_2 U_2^m + K_2 U_2^m = F_2^{ext,m} - L_2^T \lambda^m} \quad \text{at time } t = t_m \tag{3.36}$$

$$\mathbf{L_1 \dot{U}_1^j + L_2 \dot{U}_2^j = 0} \qquad \text{at time } t = t_j \tag{3.37}$$

Cette thèse est accessible à l'adresse : http://theses.insa-lyon.fr/publication/2019LYSEI042/these.pdf
© [S. Li], [2019], INSA Lyon, tous droits réservés

$$\mathbf{C_1} = \sum 2 \int_{\Omega} \rho\gamma \quad [\mathbf{N^e}]^{\mathbf{T}}[\mathbf{N^e}] d\Omega \tag{3.38}$$

$$\mathbf{C_2} = \sum \int_{\Omega} \rho\gamma^2 [\mathbf{N^e}]^{\mathbf{T}}[\mathbf{N^e}] d\Omega \tag{3.39}$$

where $\mathbf{N^e}$ is the shape function matrix associated with the element indexed by *e*, belonging to the subdomain Ω_2. Here, we can see that Kosloff formulation turns out to have a very simple finite element expression which corresponds to two new matrices, similar to the mass matrix, operating on velocities and displacements in semi-discrete equation of motion. The first equation is the discrete equation of motion of subdomains Ω_1 written at time t_j (fine time scale), whereas the second equation is the discrete equations of motion of subdomains Ω_2 written at time t_m (large time scale). On right hand side of the above equations, the interface forces enable the subdomains to be glued at their interface Γ. The third equation is the velocity continuity.

Newmark time integration schemes (Newmark, 1959) are adopted for the time discretization, characterized by the parameters γ_2=0.5 and β_2=0.25 for the implicit time integration and the parameters γ_1=0.5 and β_1=0 for the explicit time integration scheme. By introducing the approximate Newmark scheme, it leads to the equations of motion written as:

$$\widetilde{\mathbf{M}}_1 \ddot{\mathbf{U}}_1^{\mathbf{j}} = \mathbf{F}_1^{\mathbf{ext,j}} - \mathbf{K}_1 \mathbf{U}_1^{\mathbf{j-1,p}} - \mathbf{L}_1^{\mathbf{T}} \boldsymbol{\lambda}^{\mathbf{j}} \tag{3.40}$$

$$\widetilde{\mathbf{M}}_2 \ddot{\mathbf{U}}_2^{\mathbf{m}} = \mathbf{F}_2^{\mathbf{ext,m}} - \mathbf{C}_1 \dot{\mathbf{U}}_2^{\mathbf{0,p}} - \mathbf{C}_2 \mathbf{U}_2^{\mathbf{0,p}} - \mathbf{K}_2 \mathbf{U}_2^{\mathbf{0,p}} - \mathbf{L}_2^{\mathbf{T}} \boldsymbol{\lambda}^{\mathbf{m}} \tag{3.41}$$

where $\mathbf{U}_1^{\mathbf{j-1,p}}$ and $\dot{\mathbf{U}}_2^{\mathbf{0,p}}$ denote the predictor values in terms of displacement and velocity, classically introduced in approximate Newmark formula; they correspond to quantities known at the beginning of the fine step and of the large time step, respectively.

The effective stiffness matrices $\widetilde{\mathbf{M}}_1$ and $\widetilde{\mathbf{M}}_2$ related to the two subdomains are defined by:

$$\widetilde{\mathbf{M}}_1 = \mathbf{M}_1 + \beta_1 \Delta t_1^2 \mathbf{K}_1 \tag{3.42}$$

$$\widetilde{\mathbf{M}}_2 = \mathbf{M}_2 + \beta_2 \Delta t_2^2 (\mathbf{K}_2 + \mathbf{C}_2) + \gamma_2 \Delta t_2 \mathbf{C}_1 \tag{3.43}$$

The kinematic quantities are divided into two parts: the free and the linked quantities in the coupling GC method. The free quantities are calculated by taking into account the internal and

Cette thèse est accessible à l'adresse : http://theses.insa-lyon.fr/publication/2019LYSEI042/these.pdf
© [S. Li], [2019], INSA Lyon, tous droits réservés

external forces, without considering the interface forces, whereas the linked quantities are obtained from the interface loads given by the Lagrange multiplier vector $\boldsymbol{\lambda}$.

It was demonstrated that the kinematic continuity condition can be expressed as a reduced-size interface problem as follows:

$$\mathbf{H}\boldsymbol{\lambda}^{\mathbf{j}} = \mathbf{b}^{\mathbf{j}} \tag{3.44}$$

with the interface operator and the right-hand side member vector defined by:

$$\begin{cases} \mathbf{H} = \gamma_1 \Delta t_1 \mathbf{L_1} \widetilde{\mathbf{M}}_\mathbf{1}^{-\mathbf{1}} \mathbf{L}_\mathbf{1}^{\mathbf{T}} + \gamma_2 \Delta t_2 \mathbf{L_2} \widetilde{\mathbf{M}}_\mathbf{2}^{-\mathbf{1}} \mathbf{L}_\mathbf{2}^{\mathbf{T}} \\ \mathbf{b}^{\mathbf{j}} = \mathbf{L_1} \dot{\mathbf{U}}_\mathbf{1}^{\mathbf{free,j}} + \mathbf{L_2} \dot{\mathbf{U}}_\mathbf{2}^{\mathbf{free,j}} \end{cases} \tag{3.45}$$

3.4 Numerical applications

3.4.1 Numerical models with different chosen f_0

In order to explore the influence of the chosen frequency f_0 on the effectiveness of absorbing layers based on Kosloff and Rayleigh damping, numerical models of a semi-infinite elastic bar subjected to horizontal displacement at the free end, are established as shown in Figure 3-5.

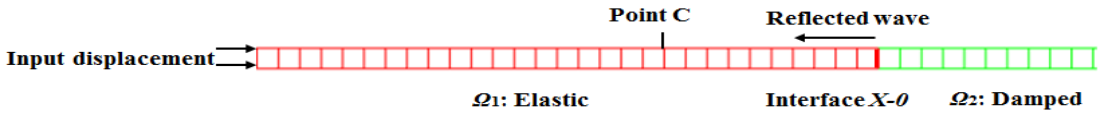

Figure 3-5 Numerical model of a semi-infinite elastic bar subjected to horizontal displacement

It simulates the propagation of *P* waves from a non-dissipative elastic medium to a dissipative medium. The simulation is conducted by using a homogeneous time step in both subdomains, the elastic subdomain is integrated in time with an explicit scheme and the subdomain related to the absorbing layer with an implicit scheme. On the basis of the general design formulas given in Eqs. (3.21, 3.25), we set the following parameters: $R_{attenution}$ equal to 0.01 (1% of reflection coming from the end of the absorbing layer), n equal to 2, and the size of the absorbing layer is kept as a

Cette thèse est accessible à l'adresse : http://theses.insa-lyon.fr/publication/2019LYSEI042/these.pdf
© [S. Li], [2019], INSA Lyon, tous droits réservés

constant, equal to 500m. As previously discussed in section 3.2.5, we will study the propagating P-wave for different chosen design frequencies f_0, or equivalently, for design periods T_0=1/f_0. The soil is assumed to be linear elastic with the following material characteristics: ρ_1=1700kg/m^3, E_1=10MPa and ν_1= 0.24. The velocity of P-waves C_p is 83m/s. The model is composed of a soil subdomain with a size of 2000m. The recording point is located at 1750m from the left end of the model in order to facilitate the distinction between the wave reflection at the interface and the wave reflection coming from the end of the absorbing layer. Non-harmonic waves are investigated by considering a Ricker incident wave. The Ricker wave has three parameters: the fundamental period t_p, the time shift t_s and the amplitude A. The chosen values are: t_p=3s, t_s=3s and A =1. The fundamental period giving the dominant period of the present waves in the problem, the design period T_0 should be chosen higher than the dominant period so as to improve the behavior of the absorbing layer in terms of wave reflections as discussed previously. It is equivalent to choose the design frequency f_0 less than the dominant Ricker frequency 1/ t_p equal to 0.33 Hz.

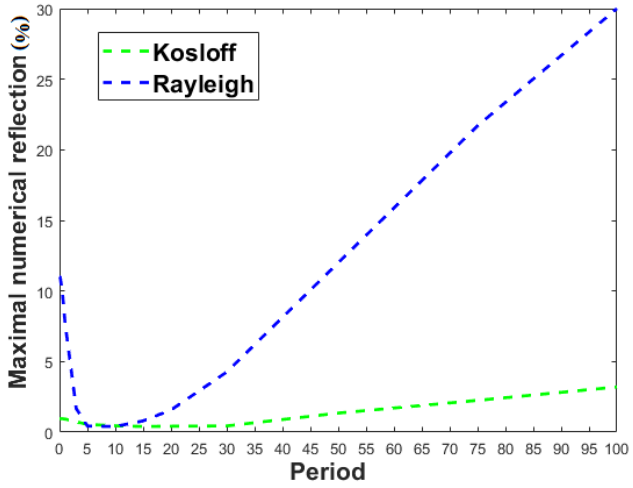

Figure 3-6 Maximal numerical reflection with different chosen periods T_0 (s)

The maximal numerical reflection coefficients for different design period T_0 are compared in Figure 3-6 for Kosloff and Rayleigh layers. It is clearly highlighted that the numerical reflection of Kosloff absorbing layer is always acceptable with different period changing from 0.01s to 100 s. On the contrary, the choice of the design period in the case of Rayleigh damping is much more sensitive than the one in the case of Kosloff damping. For Kosloff damping, the best result corresponding to 0.4% of reflection is obtained for a design period of 15 s, which is much larger

Cette thèse est accessible à l'adresse : http://theses.insa-lyon.fr/publication/2019LYSEI042/these.pdf
© [S. Li], [2019], INSA Lyon, tous droits réservés

than the Ricker dominant period equal to 3 s. For Rayleigh damping, the lowest value of the reflection coefficient equal to 0.4% is obtained at the design period T_0 of 10s. Here, it has been confirmed that the relatively smaller value f_0 leads to better results.

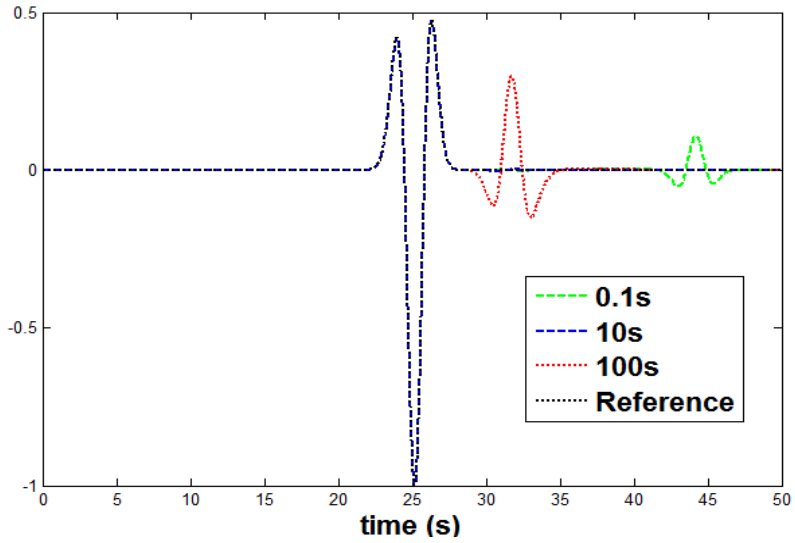

Figure 3-7 Horizontal displacement at point C for Rayleigh with different chosen periods

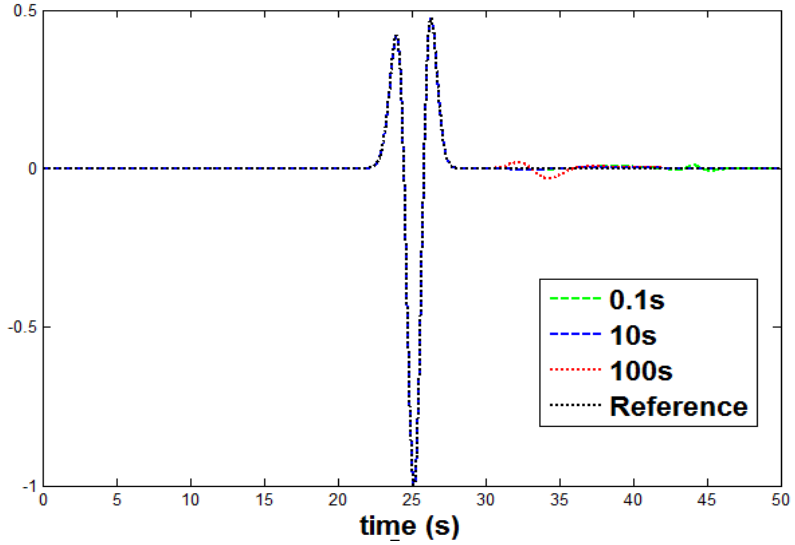

Figure 3-8 Horizontal displacement at point C for Kosloff with different chosen periods

Next, we will investigate where the maximal reflection comes from. The complete time history of the wave propagation at the point of observation for the design periods T_0 equal to 0.1s, 10s, 100s is shown in Figure 3-7 for Rayleigh absorbing layer and Figure 3-8 for Kosloff absorbing layer. The observed wave reflection includes both the reflected waves coming from the interface,

Cette thèse est accessible à l'adresse : http://theses.insa-lyon.fr/publication/2019LYSEI042/these.pdf
© [S. Li], [2019], INSA Lyon, tous droits réservés

characterized by the previously discussed ratio $R_{interface}$, and from the end of the absorbing layer, characterized by the ratio $R_{attenuation}$ used for the design of the absorbing layers.

As shown in Figures 3-7 and 3-8, for a design period equal to 10s which is higher than the dominant period of the problem (t_p equal to 3s), or equivalently, for a design frequency f_0 smaller than the the dominant frequency of the problem, both layers provide good results as expected. Next, we discuss the extreme cases: a very low value of the design period and a very high value of the design period.

For design period equal to 0.1s, corresponding to a frequency equal to 10 Hz which is much higher than the dominant frequency of the investigated problem (0.33 Hz), there will be more frequencies which will decay less than the $R_{attenution}$ defined by f_0. It leads to the increase of reflection from the end of absorbing layer. With the velocity of P-waves C_p equal to 83 m/s in this model, the reflection coming from the end of the ALID, arrives at the point of observation at 39 s, as observed in Fig. 3-7 for Rayleigh layer. With regard to Kosloff, the design frequency has no influence on the attenuation coefficient because of the independence of Kosloff in terms of decrement, with a high frequency, Kosloff layer still can obtain a good accuracy less than 1%, as shown in Figure 3-8.

For design period equal to 100 s, corresponding to a frequency equal to 0.01 Hz which is much lower than the dominant frequency of the problem, it leads to the increase of reflection at the interface $R_{interface}$for all the frequencies. Taken into account the P-wave velocity of 83m/s in this model, the reflection coming from the interface arrives at the point of observation at 27 s, for both Kosloff and Rayleigh layers in Figures 3-7 and 3-8. However, it can be noted that the influence of chosen design frequency on the reflection at the interface for Kosloff is much less than for Rayleigh, as previously shown in section 3.2.5 by the $R_{interface}$. As a conclusion, the interface behavior can be clearly improved by the introduction of the Kosloff damping in comparison to the Rayleigh damping when low design frequency is selected.

In brief, in the case of Rayleigh layer, if the spectrum range of the incident wave is close to the dominant frequency, with an appropriate design chosen frequency, the waves will penetrate the Rayleigh medium with small reflections from the interface and from the end. However, for the waves which have a broad frequency range, it is more difficult to choose an appropriate design

Cette thèse est accessible à l'adresse : http://theses.insa-lyon.fr/publication/2019LYSEI042/these.pdf
© [S. Li], [2019], INSA Lyon, tous droits réservés

frequency f_0. It is explained first, by the fact that the absorbing ability of Rayleigh medium, characterized by $R_{attenution}$, depends on frequency, and second, by the sensitivity of the amount of spurious reflections at the interface, characterized by $R_{interface}$, to the design frequency f_0. On the contrary, the absorbing ability of the Kosloff damping is independent of frequency ($R_{attenution}$), and concerning the interface reflection ($R_{interface}$), Kosloff damping is less sensitive than Rayleigh damping. Hence, Kosloff layer better deals with broad frequency range waves in comparison to Rayleigh layer.

3.4.2 Lamb's test

In order to evaluate the effectiveness of hybrid asynchronous Kosloff absorbing layers, Lamb's test has been simulated. In Lamb's test, the concentrated load applied to the surface of an infinite half space medium generates three types of waves propagating through the soil, involving P, S waves and Rayleigh waves (Lamb, 1903). Consequently, Lamb's test can be considered as a good test for assessing the performance of absorbing layer. Non-harmonic waves are investigated by considering a Ricker incident waves as used in section 3.4.1 with the chosen values t_p=3s, t_s=3s and A =1MN.

In this section, Lamb's test is conducted by setting up HA- Kosloff ALID. Results obtained from HA- Rayleigh ALID and HA-PML based on the PML formulation proposed by Basu and Chopra (Basu & Chopra, 2003; Basu & Chopra, 2004) are also calculated for comparison purpose. The soil subdomain is integrated in time with an explicit scheme and the subdomain related to the absorbing layer with an implicit scheme. As illustrated in Fig.2-6, the numerical model for three different absorbing layers is the same, composed of a bounded soil (subdomain 1) with a size of 250m and absorbing layers (subdomain 2) with the thickness of 250m. The ALID design, given in Eq. (3.21), employed the following parameters: $R_{attenution}$ equal to 0.01, n equal to 2 and a design frequency f_0 equal to 0.1 Hz, chosen less than the Ricker dominant frequency equal to $1/t_p$=0.33 Hz. A recording point is located at 20m from the loading point on the surface.

In the case that an homogeneous time step satisfying the CFL condition applied in both subdomains, the vertical and horizontal displacements of three numerical models at the observation

Cette thèse est accessible à l'adresse : http://theses.insa-lyon.fr/publication/2019LYSEI042/these.pdf
© [S. Li], [2019], INSA Lyon, tous droits réservés

point are shown in Figures 3-9 and 3-10. We can observe that PML is the most precise, the reflected spurious wave being 0.27%, in terms of the vertical displacement, and 0.81% in terms of the horizontal displacement. In comparison, the reflected spurious waves of Kosloff and Rayleigh are in the same level with the chosen frequency f_0 equal to 0.1Hz. With respect to the vertical displacement, the reflected spurious wave is 1.38% for Kosloff and 1.51% for Rayleigh. With respect to the horizontal displacement, the reflected spurious wave is 0.94% for Kosloff and 1.15% for Rayleigh. Thus, it has shown that behavior of the Kosloff absorbing layer is very satisfactory for 2D non-harmonic waves composed of body and surface waves.

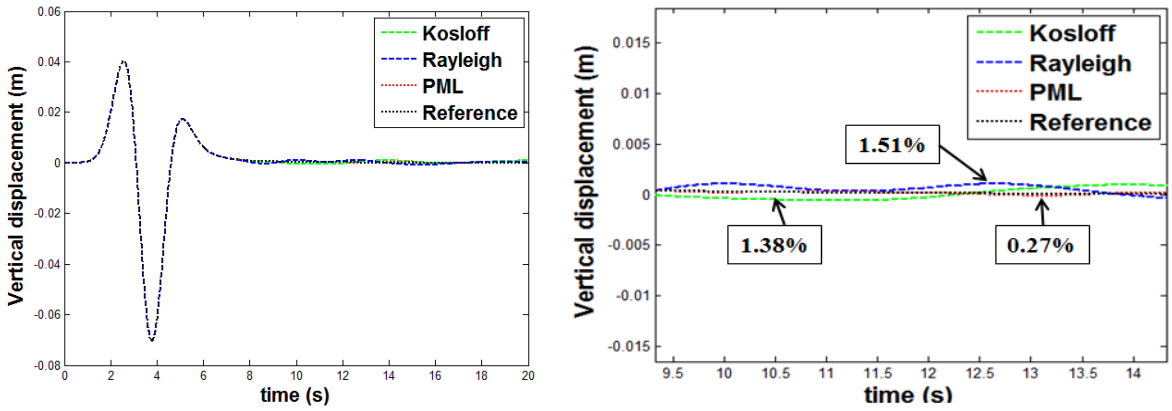

Figure 3-9 Vertical displacements at the observation point using different absorbing layers

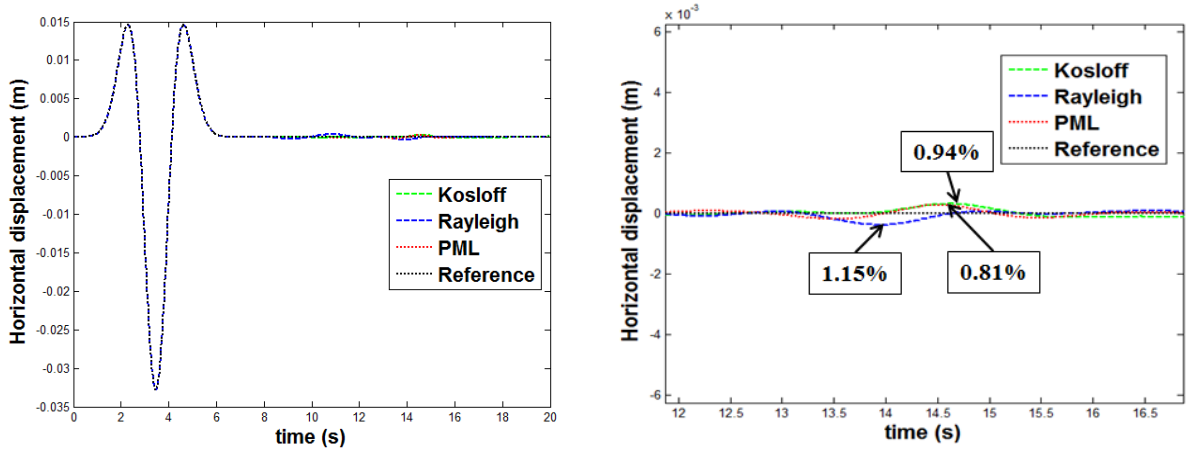

Figure 3-10 Horizontal displacements at the observation point using different absorbing layers

The kinetic and internal energies of the soil domain are computed for different absorbing layers as shown in Fig.3-11. The reference results are computed from an extended mesh by keeping the same characteristics of the previous models (finite element size, material and loading

Cette thèse est accessible à l'adresse : http://theses.insa-lyon.fr/publication/2019LYSEI042/these.pdf
© [S. Li], [2019], INSA Lyon, tous droits réservés

characteristics). All results are very close between each other. Then, in order to distinguish the difference between the different results, the L_2 norm error in time is computed between energies for different absorbing layers, as shown in Eq. (2.29). From Table.3-1, it can be observed that the errors are small for three types of absorbing layers. The errors of Kosloff and PML are clearly smaller than the errors of Rayleigh, because their absorbing capabilities are independent of frequency and better behavior at the interface.

Table 3-1 Relative energy errors of different absorbing layers

	Kinetic energy	Internal energy
Kosloff	0. 12%	0.08%
Rayleigh	0.58%	0.25%
PML	0.15%	0.10%

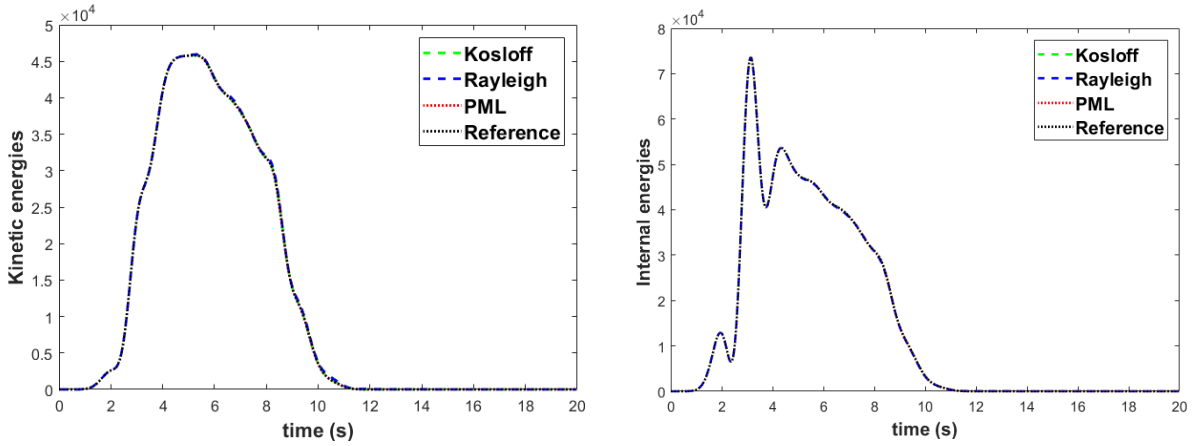

Figure 3-11 Kinetic and internal energies computed using different absorbing layers

Table 3-2 Normalized CPU Time for different absorbing layers

	CPU time
Kosloff	1.00
Rayleigh	1.02
PML	1.39

The CPU times are given in Table.3-2 in a normalized form divided by CPU time of Kosloff layers. It can be concluded that, for the same numerical model, Kosloff layers and Rayleigh layers require almost the same CPU time. PML is more complex, so it takes more CPU time.

Cette thèse est accessible à l'adresse : http://theses.insa-lyon.fr/publication/2019LYSEI042/these.pdf
© [S. Li], [2019], INSA Lyon, tous droits réservés

3.4.3 Effect of the time step ratio

Using the implicit time integration for the absorbing subdomain, we avoid the decrease of the critical time step in the explicit framework due to the introduction of damping into the discrete equation of motion. Moreover, as explained in section 3.3, it is possible to use a larger time step in the absorbing subdomain, because we use an unconditionally stable implicit scheme. The influence of heterogeneous time steps on the accuracy is investigated. The subdomain soil is integrated with Newmark explicit scheme with a fine time step, whereas absorbing layers are dealt with Newmark implicit scheme associated with a large time step in order to reduce the computation time in the absorbing layers. The horizontal and vertical displacements of the observation point for different absorbing layers with different time step ratios m ($\Delta t_2 = m\ \Delta t_1$) equal to 1, 5 and 10, are shown from Fig.3-12 to Fig.3-17. In terms of vertical displacements, the reflections of Kosloff and Rayleigh remain low with an increasing time step ratio m. It is not the case for PML, for which we observe increasing spurious reflections with the increase of the time step ratio m, with, for example, the amplitude of the reflected wave varying from 0.27% to 2.5% with respect to the vertical amplitude of the incident wave.

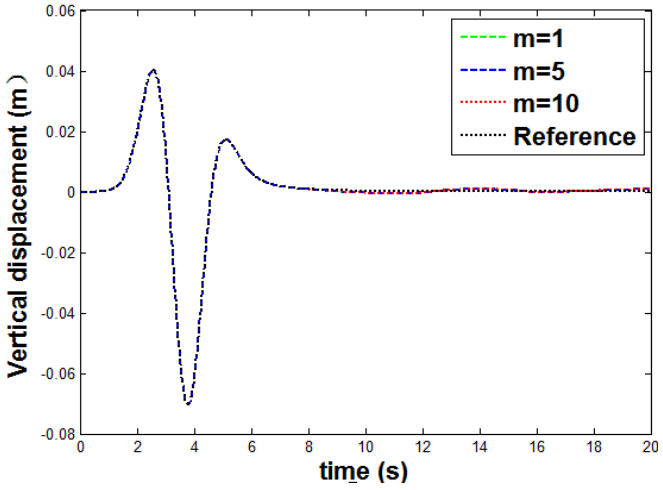

Figure 3-12 Vertical displacements for Kosloff using different time step ratios

Cette thèse est accessible à l'adresse : http://theses.insa-lyon.fr/publication/2019LYSEI042/these.pdf
© [S. Li], [2019], INSA Lyon, tous droits réservés

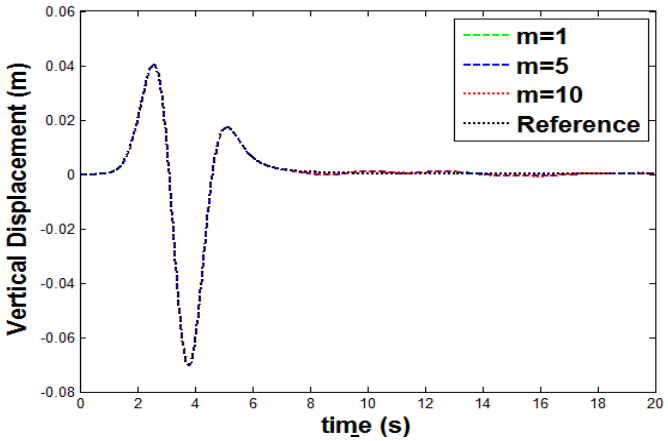

Figure 3-13 Vertical displacements for Rayleigh using different time step ratios

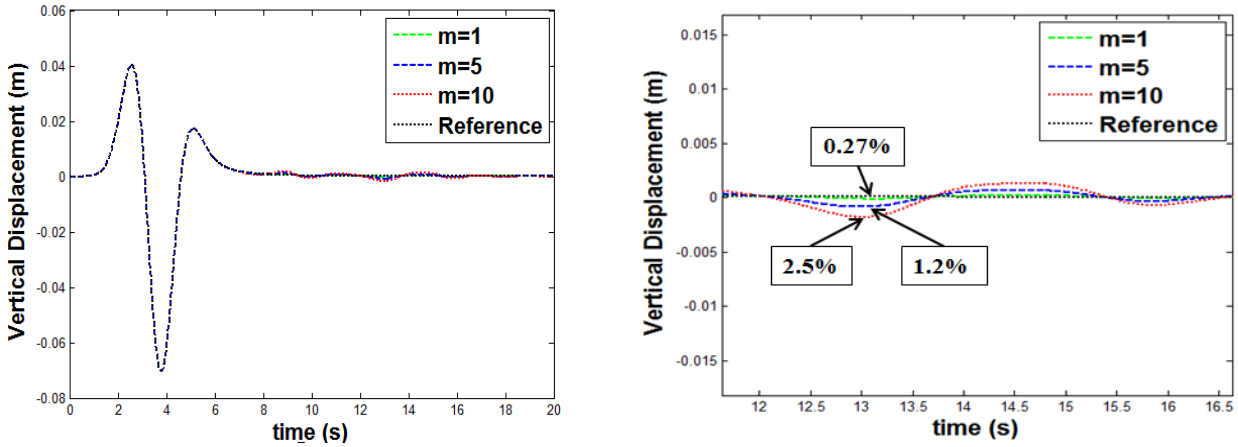

Figure 3-14 Vertical displacements for PML at the observation point using different time step ratios

For horizontal displacements, it can be observed that, in comparison to the displacements given by reference results, the vertical amplitude of the spurious wave for Kosloff varies from 0.94% to 1.92% with respect to the horizontal amplitude of the incident wave. It can be seen that the HA-Kosloff ALID performs slightly better than HA-Rayleigh ALID, with spurious wave amplitude varying from 1.15% to 2.06%. For PML, the reflections increase from 0.81% to 6.06%, confirming the sensitivity of the HA-PML with the time step ratio in comparison to the HA-Kosloff ALID and HA-Rayleigh ALID.

Cette thèse est accessible à l'adresse : http://theses.insa-lyon.fr/publication/2019LYSEI042/these.pdf
© [S. Li], [2019], INSA Lyon, tous droits réservés

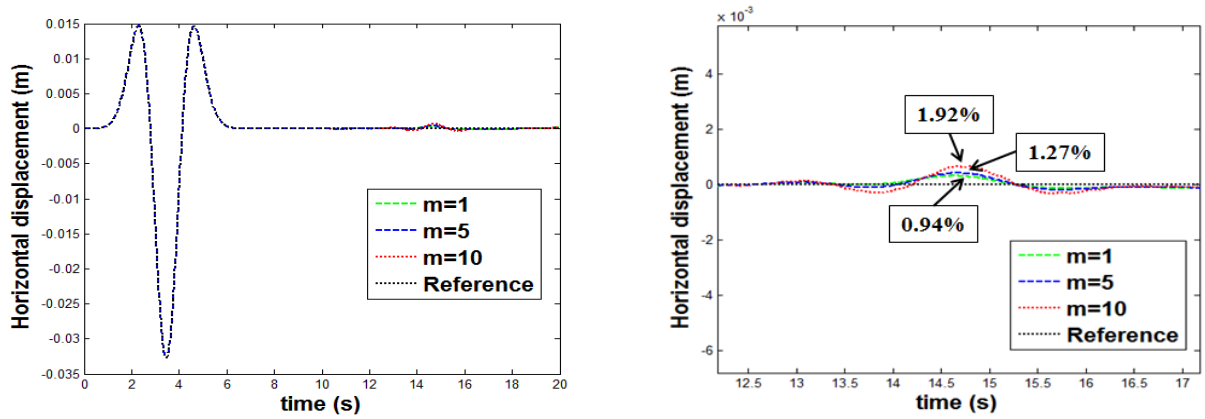

Figure 3-15 Horizontal displacements for Kosloff at the observation point using different time step ratios

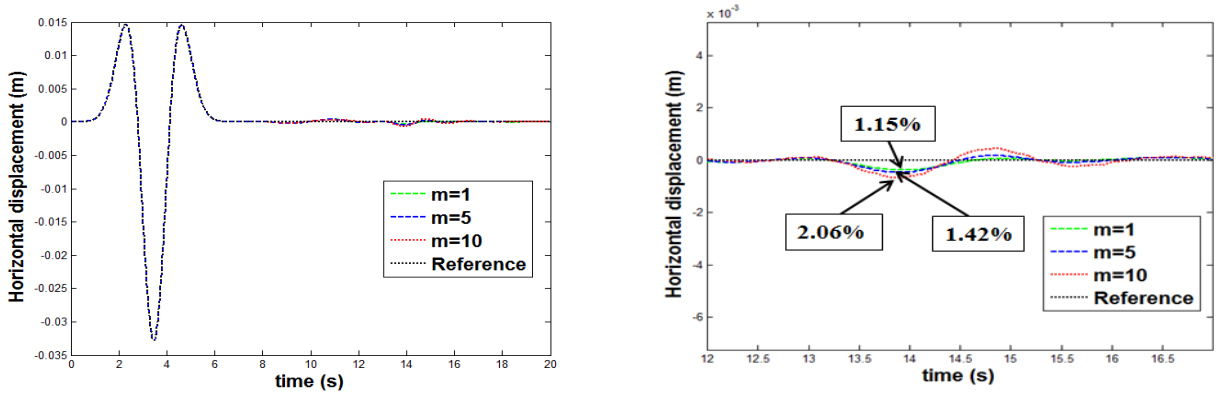

Figure 3-16 Horizontal displacements for Rayleigh at the observation point using different time step ratios

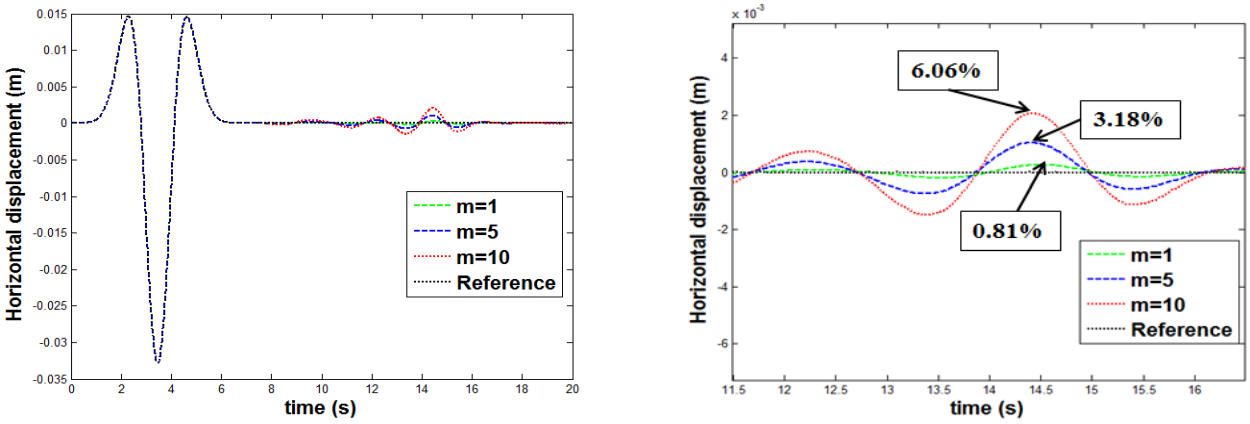

Figure 3-17 Horizontal displacements for PML at the observation point using different time step ratios

Cette thèse est accessible à l'adresse : http://theses.insa-lyon.fr/publication/2019LYSEI042/these.pdf
© [S. Li], [2019], INSA Lyon, tous droits réservés

The CPU times are resumed in Table.3-3 in a normalized form, that is divided by CPU time of the HA- Kosloff ALID for different time step ratios m. It shows that, with increasing different time step ratio, the CPU times related to the different absorbing layers decrease significantly, highlighting the strong interest of the hybrid asynchronous time integration. It implies that using explicit/implicit co-computation, not only the critical time step in the soil partition is not affected by the introduction of damping layer, but also large time steps can be adopted in absorbing layer domain to reduce the computation time.

Table 3-3 Normalized CPU Time for different methods using different time step ratios m

	Kosloff	Rayleigh	PML
m=1	1.00	1.02	1.39
m=5	0.44	0.46	0.70
m=10	0.36	0.40	0.58

The observed decrease of accuracy as the time step ratio increases, for all the previously investigated absorbing layers, can be explained by the following points. Firstly, the GC coupling algorithm is known to be dissipative as soon as heterogeneous time steps are used between the subdomains, generating spurious waves at the interface. It has been demonstrated that for GC method, when adopting the same time step, second order of accuracy is achieved and it leads to the first order of accuracy when adopting different time steps due to a slight spurious dissipation at the interface (Gravouil and Combescure, 2001; Brun *et al.*, 2015). Secondly, the reason why the accuracy of PML decreases more strongly than in the cases of Rayleigh and Kosloff damping can be found in Basu and Chopra's formulation (Basu and Chopra, 2003; Basu and Chopra, 2004; Basu, 2009), also adopted by commercial finite element codes LS-DYNA and Diana: one additional relationship was required to calculate the strain rate, $\dot{\varepsilon}(t_n) \approx (\varepsilon_n - \varepsilon_{n-1})/\Delta t_2$, Δt_2 being the time step in PML subdomain. As the time step increases, the error produced by this assumption may increase.

In order to confirm this last point, additional implicit–implicit co-simulations with homogeneous time steps (same time step in both subdomains), have been carried out. In such a way, the influence of heterogeneous time steps in the results is avoided and the time step can be increased while maintaining the stability of the co-simulation, because of the unconditional

Cette thèse est accessible à l'adresse : http://theses.insa-lyon.fr/publication/2019LYSEI042/these.pdf
© [S. Li], [2019], INSA Lyon, tous droits réservés

stability of the implicit time integration scheme. Both subdomains (soil and absorbing layers) are integrated with a constant average acceleration scheme (CAA) associated with the same time step, increasing from 0.025s to 0.25s depending on co-simulations, that is from a value corresponding to the CFL condition to a value ten times bigger. Maximal horizontal and vertical reflections for different absorbing layers are plotted in Fig.3-18. It can be seen that the reflections of Kosloff and Rayleigh hardly grow, with an increasing homogeneous time step in both subdomains. On the contrary, the horizontal and vertical reflections of PML quickly grow and become bigger than the reflections of Kosloff and Rayleigh cases. It can be concluded that, when the time step increases, the PML based on Basu and Chopra's formulation turns out to be less precise.

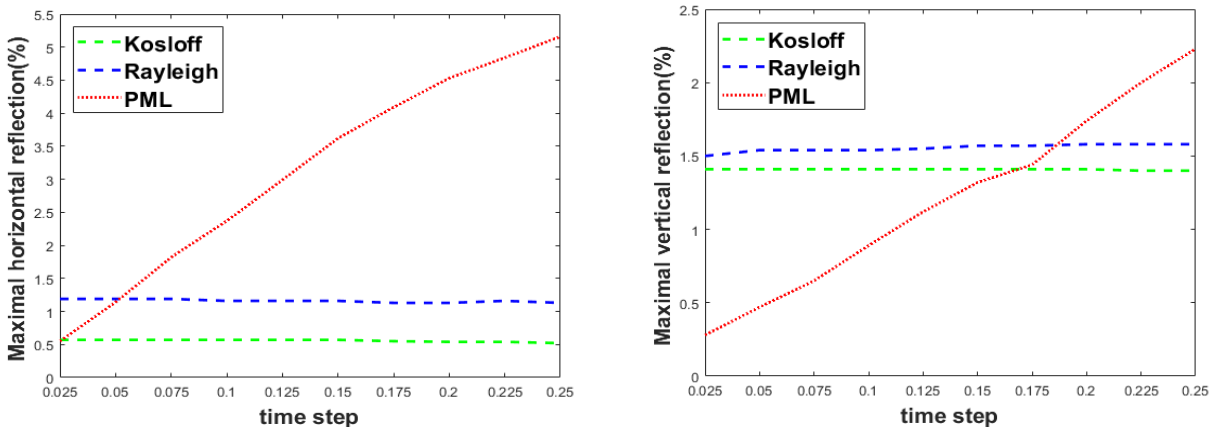

Figure 3-18 Maximal horizontal and vertical reflections for PML at the observation point for different homogeneous time steps using implicit-implicit co-simulations

Overall, PML is the most accurate absorbing layer for a time step size close to the CFL condition and has the strong advantage to not require a design frequency as done in Kosloff and Rayleigh absorbing layers. However, it is more complex to be implemented in finite element software and it is observed that HA-PML produces more reflection with the increase of the time step ratio m. Kosloff absorbing layer is independent of frequency in terms of decrement and less sensitive to the influence of the chosen frequency f_0 at the interface in comparison to Rayleigh absorbing layer. In addition, the implementation of Kosloff damping in a finite element code is straightforward and the computation is quicker in comparison to the PML. Moreover, HA-Kosloff ALID is more accurate than HA-PML as the time step ratio increases. Therefore, Kosloff can be an alternative of PML to treat wave propagation problems.

Cette thèse est accessible à l'adresse : http://theses.insa-lyon.fr/publication/2019LYSEI042/these.pdf
© [S. Li], [2019], INSA Lyon, tous droits réservés

3.5 Three-dimensional hybrid asynchronous Kosloff absorbing layer

3.5.1 Space and time discretization in three-dimension

As done in Chapter 2 for HA-Rayleigh ALID, it is very straightforward to extend the 2D hybrid asynchronous Kosloff absorbing layers to the 3D case. The space discretization for Kosloff absorbing layers in two- dimension and the time discretization for hybrid asynchronous Kosloff absorbing layers using explicit/implicit co-simulation in two- dimension have been described in section 3.3. In three-dimension space, the modification in three-dimension is only the 8-nodes cube element in place of the 4-nodes rectangular elements. Here, we focus on the time discretization for explicit/ explicit co-simulation by using the GC coupling method (Combescure and Gravouil, 2001; 2002). The subdomain Ω_1 soil is integrated by Newmark explicit scheme with time step Δt_1, and the Kosloff absorbing layers are integrated by Central Difference scheme with time step Δt_2. Contrarily to Rayleigh absorbing layers, the introduction of Kosloff damping will not affect the time step in subdomain Ω_2, as shown in the following. Therefore, in the context of matching meshes, the same time step imposed by the CFL condition can be applied in both subdomains. In the case of non-matching meshes, different time steps imposed by the CFL condition can be also defined in each subdomain independently.

Using the GC method, the wave propagation in the subdomain soil can be simulated, independently of the specific formulation adopted for the absorbing region at the boundary of the truncated mesh. Here, the same time step imposed by the CFL condition is applied in both subdomains for explicit/explicit co-simulation, the equilibrium of subdomain 1 and subdomain 2 is prescribed at every time $t_j = j\Delta t_1 = j\Delta t_2$. Finally, the weak form given in Eq. (3.31) with the velocity continuity equation in Eq. (3.32), can be expressed in the following discrete form in space and time:

$$\mathbf{M_1}\ddot{\mathbf{U}}_1^{\mathbf{j}} + \mathbf{K_1}\mathbf{U}_1^{\mathbf{j}} = \mathbf{F}_1^{\mathbf{ext,j}} - \mathbf{L}_1^{\mathbf{T}}\boldsymbol{\lambda}^{\mathbf{j}} \tag{3.46}$$

$$\mathbf{M_2}\ddot{\mathbf{U}}_2^{\mathbf{j}} + \mathbf{C_1}\dot{\mathbf{U}}_2^{\mathbf{j-1/2}} + \mathbf{C_2}\mathbf{U}_2^{\mathbf{j}} + \mathbf{K_2}\mathbf{U}_2^{\mathbf{j}} = \mathbf{F}_2^{\mathbf{ext,j}} - \mathbf{L}_2^{\mathbf{T}}\boldsymbol{\lambda}^{\mathbf{j}} \tag{3.47}$$

$$\mathbf{L_1}\dot{\mathbf{U}}_1^{\mathbf{j}} + \mathbf{L_2}\dot{\mathbf{U}}_2^{\mathbf{j}} = \mathbf{0} \tag{3.48}$$

Cette thèse est accessible à l'adresse : http://theses.insa-lyon.fr/publication/2019LYSEI042/these.pdf
© [S. Li], [2019], INSA Lyon, tous droits réservés

By introducing the approximate time integration schemes, it leads to the equations of motion written as:

$$\mathbf{M_1}\ddot{\mathbf{U}}_\mathbf{1}^\mathbf{j} = \mathbf{F}_\mathbf{1}^{\mathbf{ext,j}} - \mathbf{K_1}\mathbf{U}_\mathbf{1}^{\mathbf{j-1,p}} - \mathbf{L}_\mathbf{1}^\mathbf{T}\boldsymbol{\lambda}^\mathbf{j} \tag{3.49}$$

$$\mathbf{M_2}\ddot{\mathbf{U}}_\mathbf{2}^\mathbf{j} = \mathbf{F}_\mathbf{2}^{\mathbf{ext,j}} - \mathbf{C_1}\dot{\mathbf{U}}_\mathbf{2}^{\mathbf{j-1/2}} - \mathbf{C_2}\mathbf{U}_\mathbf{2}^\mathbf{j} - \mathbf{K_2}\mathbf{U}_\mathbf{2}^\mathbf{j} - \mathbf{L}_\mathbf{2}^\mathbf{T}\boldsymbol{\lambda}^\mathbf{j} \tag{3.50}$$

We can see that the effective stiffness matrix related to the absorbing layer in explicit/implicit co-simulation, is now replaced with diagonal lumped matrices, avoiding costly system solving. The kinematic continuity condition can be expressed as a reduced-size interface problem as follows:

$$\mathbf{H}\boldsymbol{\lambda}^\mathbf{j} = \mathbf{b}^\mathbf{j} \tag{3.51}$$

with the interface operator and the right-hand side member vector defined by:

$$\begin{cases} \mathbf{H} = \frac{1}{2}\Delta t_1 \mathbf{L_1}\mathbf{M_1}^{-\mathbf{1}}\mathbf{L}_\mathbf{1}^\mathbf{T} + \frac{1}{2}\Delta t_2 \mathbf{L_2}\mathbf{M_2}^{-\mathbf{1}}\mathbf{L}_\mathbf{2}^\mathbf{T} \\ \mathbf{b}^\mathbf{j} = L_1 \dot{U}_1^{\mathrm{free},j} + L_2 \dot{U}_2^{\mathrm{free},j} \end{cases} \tag{3.52}$$

3.5.2 Numerical examples

In order to evaluate the effectiveness of three-dimensional Kosloff absorbing layers, simple 3D Lamb's tests are carried out using different co-simulation strategies. Non-harmonic waves are investigated by considering a Ricker incident wave. The three parameters of Ricker wave are the fundamental period t_p, the time shift t_s and the amplitude$A$. The chosen values are: t_p=3s, t_s=3s and A =1MN. The example of 3D Lamb's test is simulated with one 3D element in the thickness direction as shown in Fig.2-20. The soil is assumed to be linear elastic with the dimension 250m x 250m x 5m (element size 5m x 5m x 5m) and the following material characteristics: ρ_1=1700kg/m3, E_1=10MPa and ν_1= 0.24 for the density, Young's modulus and Poisson's ratio, respectively. The P-wave, S-wave and Rayleigh wave velocities are: V_P =83.27m/s, V_S=48.7m/s, V_R=44.73m/s. The thickness of absorbing layers is 250m. The ALID design employed the following parameters based on Eq. (3.20): $R_{attenution}$ equal to 0.01, n equal to 2 and a design frequency f_0 equal to 0.1 Hz, chosen less than the Ricker dominant frequency equal to $1/t_p$=0.33 Hz. A recording point is located at 20m from the loading point on the surface.

Cette thèse est accessible à l'adresse : http://theses.insa-lyon.fr/publication/2019LYSEI042/these.pdf
© [S. Li], [2019], INSA Lyon, tous droits réservés

In case of explicit/implicit co-simulation, the subdomain soil is integrated in time by an explicit scheme with a fine time step (Δt_1=0.025s) imposed by the CFL condition, whereas the Kosloff absorbing layer is integrated by an implicit scheme with lager time step Δt_1=m Δt_2, m= 1,10,20,30. In case of explicit/explicit co-simulation, the subdomain soil is integrated in time by Newmark explicit scheme with the time step (Δt_1=0.025s), and the Kosloff absorbing layer is integrated by Central Difference scheme with the same time step Δt_2=Δt_1, imposed by the CFL condition.

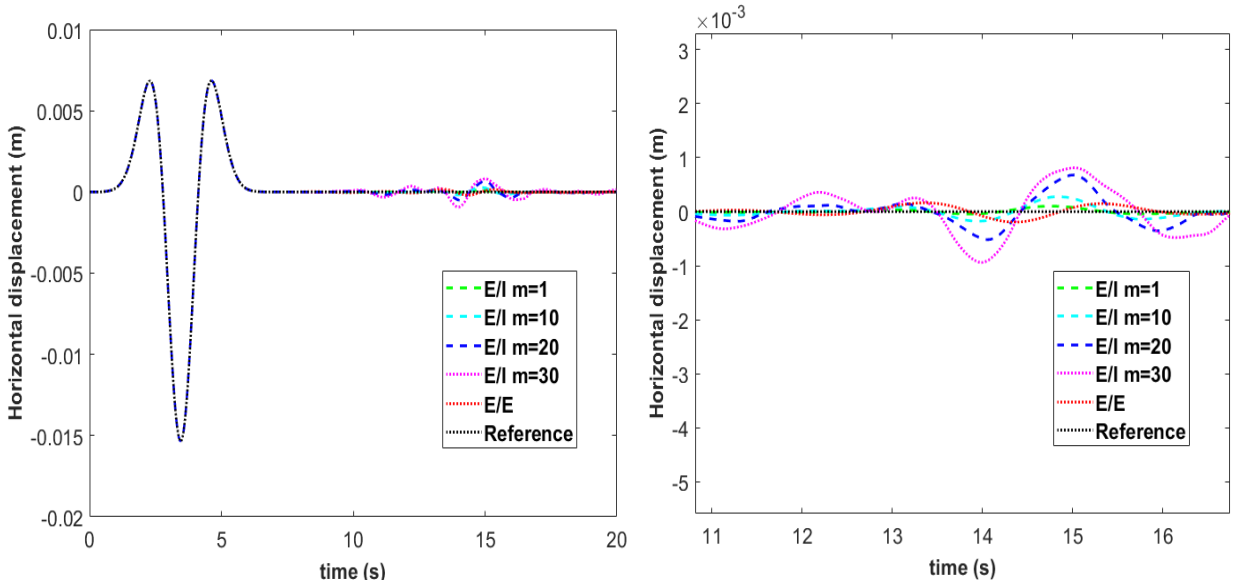

Figure 3-19 Horizontal displacements at the observation point using different co-simulation strategies

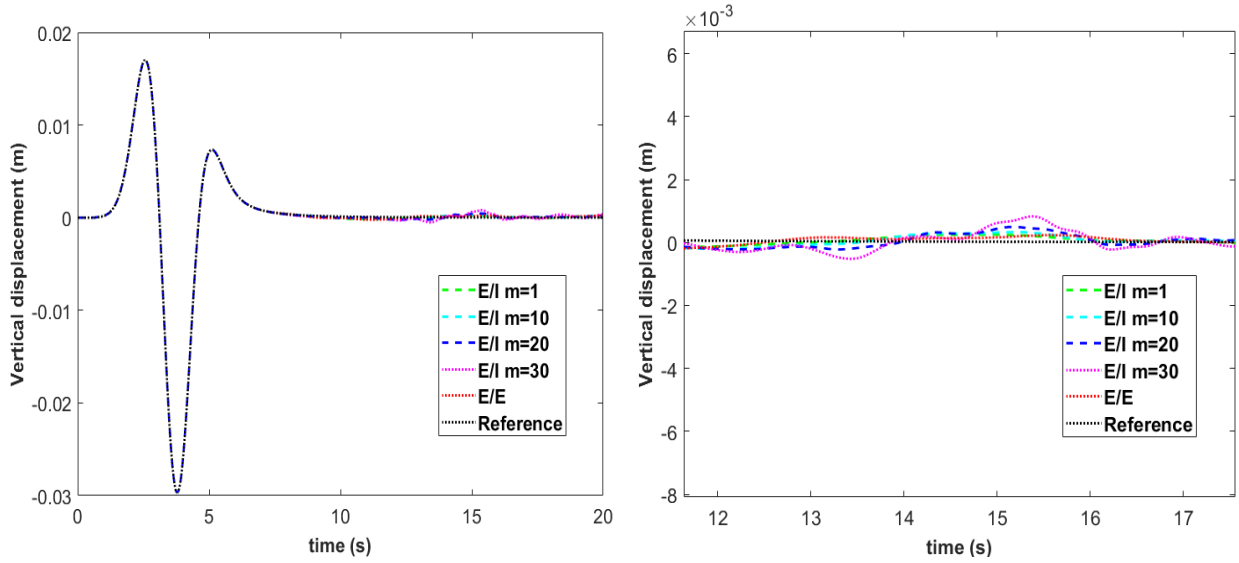

Figure 3-20 Horizontal displacements at the observation point using different co-simulation strategies

Cette thèse est accessible à l'adresse : http://theses.insa-lyon.fr/publication/2019LYSEI042/these.pdf
© [S. Li], [2019], INSA Lyon, tous droits réservés

Figures 3-19 and 3-20 show the horizontal and vertical displacements in Lamb's test with different co-simulations in comparison to the reference results obtained from an extended mesh, free of spurious reflected waves in the observation period. In the case of explicit/implicit co-simulation, the reflected spurious waves, recorded at the observation point, grow with the increase of the time step ratio m, as explained in 2D.

Table 3-4 Reflections using different co-simulation strategies (Kosloff)

	Vertical displacement	Horizontal displacement
E/I m=1	0.82%	0.66%
E/I m=10	1.05%	1.80%
E/I m=20	1.60%	4.41%
E/I m=30	2.73%	6.13%
E/E	1.26%	0.98%

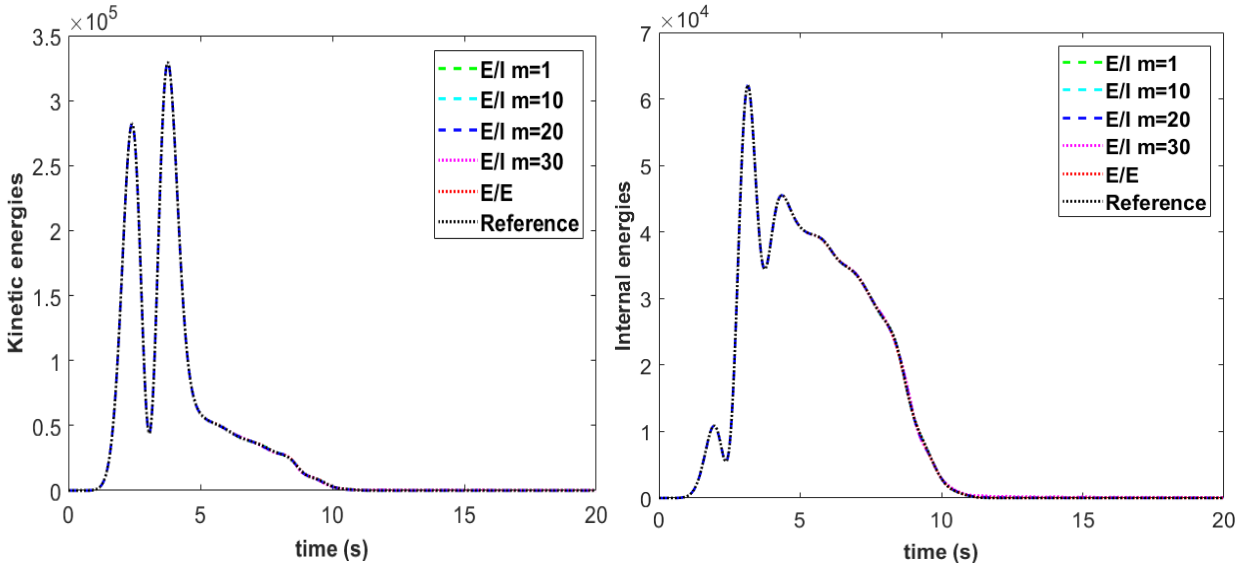

Figure 3-21 Kinetic and internal energies computed using different co-simulation strategies

With respect to the amplitude of the incident wave, the horizontal reflected spurious waves are 0.66%, 1.80%, 4.41%, 6.13% for m= 1, 10, 20, 30, respectively; the vertical reflected spurious waves are 0.82%, 1.05%, 1.6 %, 2.73% for m= 1,10,20,30, respectively. In case of explicit/explicit co-simulation (Δt_1=Δt_2), the horizontal reflected spurious wave is 1.26% and the vertical reflected

Cette thèse est accessible à l'adresse : http://theses.insa-lyon.fr/publication/2019LYSEI042/these.pdf
© [S. Li], [2019], INSA Lyon, tous droits réservés

spurious wave is 0.98%, with respect to the amplitude of the incident wave. It can be noted that the accuracy in explicit/explicit co-simulation ($\Delta t_1 = \Delta t_2$) is at the same level of explicit/implicit co-simulation (m=1). From Table.3-5, it can be observed that the errors remain small and stable in terms of energy.

Table 3-5 Relative energy errors of different co-simulations (Kosloff)

	Kinetic energy	Internal energy
E/I m=1	0. 03%	0.07%
E/I m=10	0.12%	0.17%
E/I m=20	0.20%	0.39%
E/I m=30	0.31%	0.83%
E/E	0.08%	0.21%

Table 3-6 Normalized CPU Time of different co-simulations (Kosloff)

	m=1	m=10	m=20	m=30	E/E
Normalized CPU time	1	0.24	0.20	0.19	0.15

In terms of the computation time, the CPU times are resumed in Table.3-6 in a normalized form divided by CPU time of the co-simulation explicit/implicit (m=1). As in Chapter 2, we see that, with the increase time step ratio, the CPU time decreases, using explicit/implicit co-computation. It is observed that in comparison with explicit/implicit co-simulation, the computation time for co-simulation explicit/explicit is the least.

The snapshots of displacement magnitude at different times for co-simulation explicit/explicit ($\Delta t_1 = \Delta t_2$) are displayed in Figure 3-22. No obvious reflections can be observed at the interface or from the boundaries, indicating very satisfactory performance of three-dimensional Kosloff absorbing layers using explicit/explicit co-simulation.

Cette thèse est accessible à l'adresse : http://theses.insa-lyon.fr/publication/2019LYSEI042/these.pdf
© [S. Li], [2019], INSA Lyon, tous droits réservés

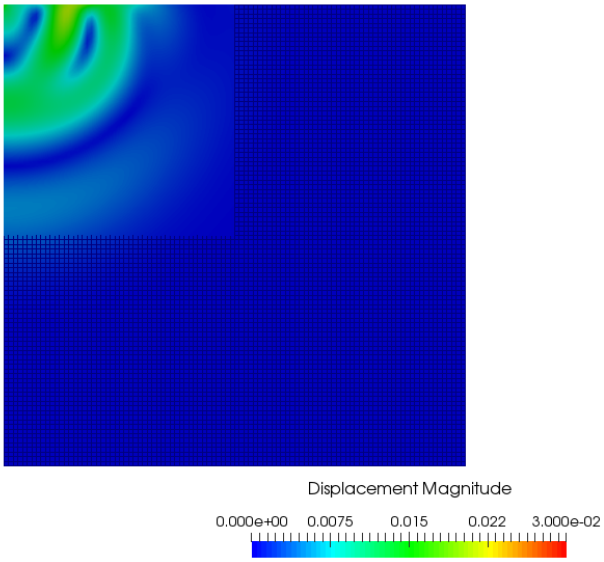

(a) t = 5s

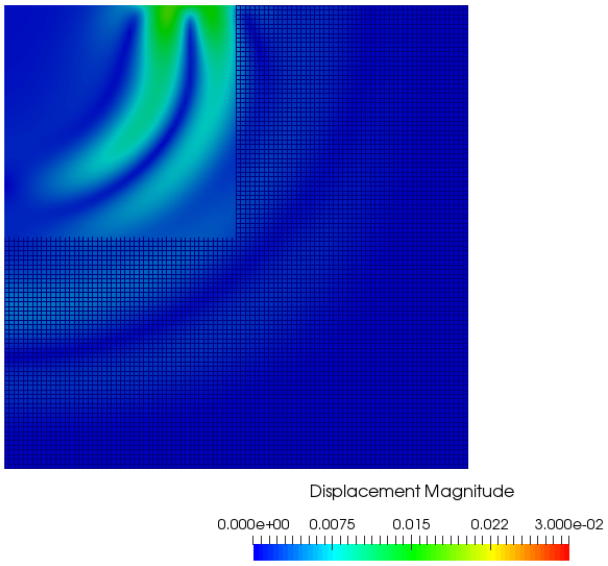

(b) t = 7.5s

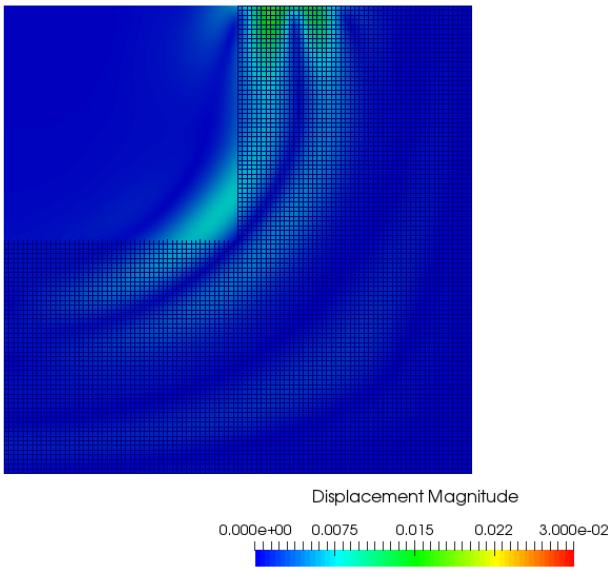

(c) t = 10s

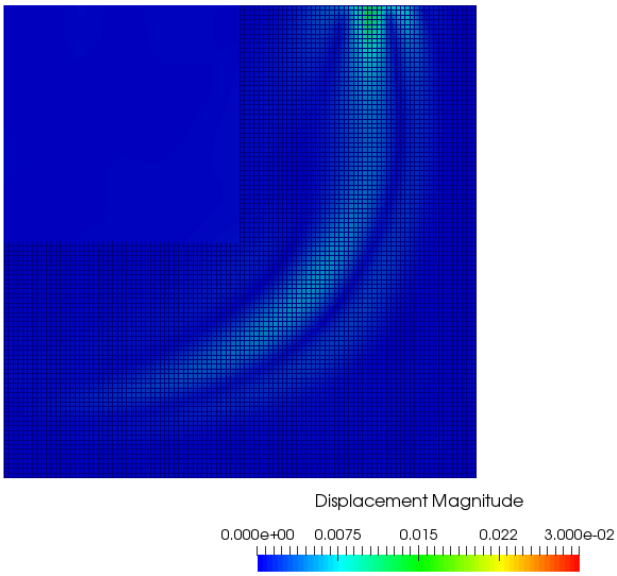

(d) t = 12.5s

Cette thèse est accessible à l'adresse : http://theses.insa-lyon.fr/publication/2019LYSEI042/these.pdf
© [S. Li], [2019], INSA Lyon, tous droits réservés

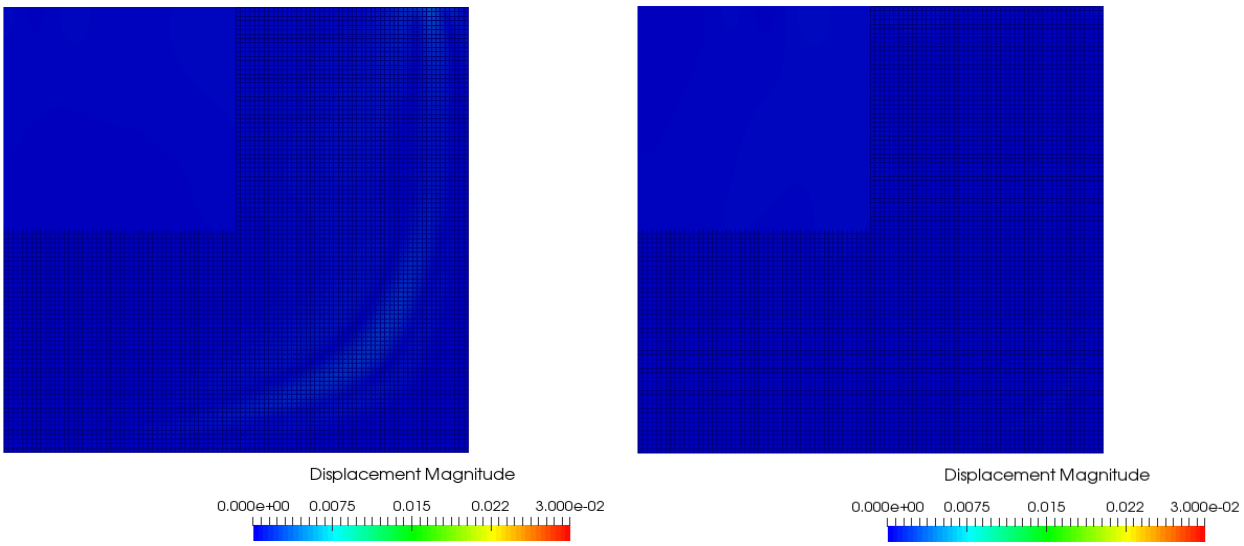

(e) t = 15s (f) t = 17.5s

Figure 3-22 Snapshots of displacement magnitude at different times for E/E

3.6 Conclusion

In this chapter, a new version of absorbing layer for modeling unbounded domain using finite element approach has been proposed on the basis of a specific damping formulation proposed by D. Kosloff and R. Kosloff (1986). Indeed, an interesting feature of the Kosloff damping for setting up efficient absorbing layers lies in its frequency independence. From the strong form of the wave propagation problem, optimal conditions at the interface between two media (elastic and Kosloff media) have been given as well as design equations for setting up the Kosloff absorbing layers. The advantages of the Kosloff damping have been highlighted in comparison to the classical Rayleigh damping, commonly available in general purpose finite element codes. Then the absorbing region has been integrated independently of the domain of interest in time. It leads to the proposition of a new version of absorbing layers, called Hybrid Asynchronous – Kosloff Absorbing Layers with Increasing Damping (HA-Kosloff ALID), and that is much more convenient to implement in a finite element code than PML techniques. Moreover, HA-Kosloff ALID turns out to be more precise than HA-PML when the time step size increases in the absorbing layers.

Cette thèse est accessible à l'adresse : http://theses.insa-lyon.fr/publication/2019LYSEI042/these.pdf
© [S. Li], [2019], INSA Lyon, tous droits réservés

Results of 2D elastodynamics problems obtained from HA-Kosloff ALID have been compared with HA-Rayleigh ALID and HA-PML. HA-Kosloff ALID turns out to be a relevant tool for easily modelling the wave propagation in an unbounded domain. Its implementation in the finite element context is very easy, it behaves better than the HA-Rayleigh ALID and it requires less CPU time than a PML formulation in the same numerical model. Another advantage of the HA-Kosloff ALID with respect to the HA-PML is its straightforward extension to three-dimensional elastodynamics problems. Thus, 3D hybrid asynchronous Kosloff absorbing layers has been easily extended to the 3D case using explicit/implicit and explicit/explicit co-simulation. The difference between the two strategies co-simulation is compared in terms of accuracy and computation time.

Cette thèse est accessible à l'adresse : http://theses.insa-lyon.fr/publication/2019LYSEI042/these.pdf
© [S. Li], [2019], INSA Lyon, tous droits réservés

Cette thèse est accessible à l'adresse : http://theses.insa-lyon.fr/publication/2019LYSEI042/these.pdf
© [S. Li], [2019], INSA Lyon, tous droits réservés

Chapter 4

Three-dimensional hybrid asynchronous PML

In this chapter, we focus on the development of one hybrid (different time integrators) asynchronous (different time steps) three-dimensional unsplit−field displacement-based PML formulation for modelling heterogeneous elastic infinite media, extending previous works done in two dimension (Brun *et al.,* 2016). The proposed unsplit 3D PML formulation is implemented in the framework of Hybrid Asynchronous Time Integrator (HATI), using a novel efficient method for calculating the internal force. Contrarily to Rayleigh and Kosloff absorbing layers, the extension of PML to three-dimensional elastodynamics problems is not straightforward, due to different formulations and additional unknowns introduced when the 3D PML is expressed in the time domain.

By studying the strong form of wave propagation in PML media, the classical design equation of the PML is derived, enabling us to choose appropriate parameters for the PML. The frequency-independent absorbing capabilities of the PML turns out to be very similar to the case of absorbing layers with Kosloff damping (1986), but with the advantage of being reflectionless at the interface between the non-dissipative interior domain and the PML. The weak formulation leading to a novel efficient method for calculating the internal force in three-dimensional PML domain has been coupled with the interior domain using the dual Schur approach. It allows to avoid the introduction of complex-coordinate-stretched equations in the interior domain and enables the appropriate time integration scheme in the PML with its own time step to be chosen, independently of the choice of

Cette thèse est accessible à l'adresse : http://theses.insa-lyon.fr/publication/2019LYSEI042/these.pdf
© [S. Li], [2019], INSA Lyon, tous droits réservés

the time scheme in the domain of interest. Examples of three-dimensional semi-infinite bar, Lamb's test, and one classical soil–structure interaction problem with PML-truncated semi-infinite heterogeneous media are implemented to illustrate the efficiency of the hybrid asynchronous formulation in terms of accuracy and CPU time.

This chapter is a modified version of the article submitted to International Journal for Numerical Methods in Engineering:

Li S, Brun M, Zafati E, Djeran-Maigre I and Kuznetsov S (2019). Three-dimensional hybrid asynchronous perfectly matched layer for wave propagation in unbounded domains. International Journal for Numerical Methods in Engineering.

Cette thèse est accessible à l'adresse : http://theses.insa-lyon.fr/publication/2019LYSEI042/these.pdf
© [S. Li], [2019], INSA Lyon, tous droits réservés

4.1 Design of Perfectly Matched Layer

The PML model is formulated by introducing the complex-valued stretching functions into the classical elastodynamic equations in the frequency domain. The main idea is to replace the real coordinates x_i, which denotes the x, y and z coordinates for the index equal to 1, 2 and 3, by the complex ones $\tilde{x}_i : \mathbb{R} \rightarrow \mathbb{C}$. The complex coordinates are defined by:

$$\frac{\partial \tilde{x}_i}{\partial x_i} = \lambda_i(x_i) = 1 + f_i^e(x_i) + \frac{f_i^p(x_i)}{i\omega} \tag{4.1}$$

In the above equation, ω denotes the circular frequency, the attenuation function f_i^p which is positive real-valued as a function of x_i, serves to attenuate the propagating waves in the x_i direction, whereas the scaling function f_i^e attenuates the evanescent waves by stretching the coordinate variable x_i. It has to be noted that this expression is the same as the ones chosen by Kucukcoban and Kallivokas (2013) and Fathi *et al.* (2015). It is slightly different from the one adopted by Basu and Chopra (2003, 2004) and Basu (2009) in order to avoid introducing a characteristic length of the problem under consideration.

In the following, we focus on the propagating waves in the 1D case, in order to design the PML attenuation performance by studying the effect of the damping function f_i^p on the attenuation in the PML as well as on the wave reflection at the interface between a non-dissipative elastic medium and the dissipative PML. Indeed, the design of PML aims at damping out all the incident waves from the domain of interest while minimizing the spurious waves reflected at the boundary of the truncated domain. For this purpose, the strong form of wave propagation in 1D PML media is investigated in order to obtain the absorbing capabilities of PML. It will be shown that attenuation formulation proposed by Kosloff and Kosloff (1986), shares the same absorbing and frequency-independent capabilities of the PML, as underlined by Carcione and Kosloff (2013). In addition, the non-reflecting characteristic at the interface between a non-dissipative elastic medium and PML medium will be analytically demonstrated by considering the continuous problem of wave propagation, contrarily to the Kosloff medium which is not reflectionless in theory at the interface.

Cette thèse est accessible à l'adresse : http://theses.insa-lyon.fr/publication/2019LYSEI042/these.pdf
© [S. Li], [2019], INSA Lyon, tous droits réservés

4.1.1 1D Wave propagation in PML medium

The governing equations in elastodynamics are modified by the complex-coordinate-stretching. The displacement in one–dimensional PML medium is governed by the modified equations:

$$\frac{1}{\lambda(x)}\frac{\partial \sigma}{\partial x} = -\rho\omega^2 u \tag{4.2}$$

$$\varepsilon = \frac{1}{\lambda(x)}\frac{\partial u}{\partial x} \tag{4.3}$$

$$\sigma = E\varepsilon \tag{4.4}$$

Eqs. (4.2) to (4.4) constitute the strong form in frequency domain of one–dimensional PML medium, σ, ε, ρ, being the scalar values, denoting the stress, the strain and the density, respectively. E is Young's modulus for P waves. For S waves, same equations hold by replacing Young's modulus E by shear modulus G. It can be seen that the equation of motion and deformation equation have been modified with the introduction of complex-valued stretching function $\lambda(x)$, the elastic constitutive relationship remains intact.

The deformation equation and the elastic constitutive relationship are used to replace the stress term in the equation of wave propagation as:

$$E\frac{1}{\lambda(x)^2}\frac{\partial^2 u}{\partial x^2} = -\rho\omega^2 u \tag{4.5}$$

We adopt the following scaling and attenuation functions $f^e = 0$, $f^p = \beta$, β being a constant positive real value. It gives the expression of the complex-valued stretching function:

$$\lambda(x) = 1 - \frac{i\beta}{\omega} \tag{4.6}$$

Introduce $\lambda(x)$ in the equation of motion:

$$E\frac{\partial^2 u}{\partial x^2} = \rho(\omega i)^2 u + 2\rho(\omega i)u\beta + \rho u\beta^2 \tag{4.7}$$

The dependence of the complex coordinates on the factor $i\omega$ allows for an easy application of the inverse Fourier transform when expressing the PML in the time domain. So, we apply the

Cette thèse est accessible à l'adresse : http://theses.insa-lyon.fr/publication/2019LYSEI042/these.pdf
© [S. Li], [2019], INSA Lyon, tous droits réservés

inverse Fourier transform to obtain the wave propagation in the time domain of PML medium as follows:

$$E\frac{\partial^2 u}{\partial x^2} = \rho\ddot{u} + 2\rho\dot{u}\beta + \rho u\beta^2 \tag{4.8}$$

Here, it can be remarked that the above equation of motion is the same as the Kosloff damping formulation originally proposed by Kosloff and Kosloff (1986) before the seminal paper of Bérenger (1994) on PML for electromagnetic waves. As a result, it will be shown in the following that same attenuation capabilities will be derived for Kosloff medium as the ones related to PML medium.

By introducing the harmonic solution $u(x,t) = u_0\exp(i(\omega_0 t - kx))$, the expression of the wave number k can be obtained:

$$k = \frac{\omega_0}{v}\left(1 - i\frac{\beta}{\omega_0}\right) \tag{4.9}$$

where v denotes the velocity of P waves or S waves. The expression of the propagating wave in the 1D PML medium is shown below:

$$u(x,t) = u_0\, exp(\, i(\omega_0 t - k_0 x))\, exp\left(-\frac{\beta x}{v}\right) \tag{4.10}$$

Using the previous expression in Eq. (4.10), the absorbing capability of PML is given in form of logarithmic decrement as a function of the thickness and the constant attenuation scalar of the PML:

$$\delta = \ln\left(\frac{|u(x)|}{|u(x+\Delta x)|}\right) = \frac{\beta\Delta x}{v} \tag{4.11}$$

It can be seen that the wave frequency ω_0 has no influence on the absorbing ability of PML with regard to the logarithmic decrement, which means that all waves with all frequencies can be attenuated in the same way. Thus, PML turns out to be independent of frequency. The velocity of P waves is higher than the velocity of S waves for the same medium. In other words, based on the above relationships, in order to reach the same logarithmic decrement, the layer thickness for damping out S waves is smaller than the one related to P waves. As a result, the velocity of P waves v_p will be adopted for the design of absorbing layer. Again, it should be remarked that PML

Cette thèse est accessible à l'adresse : http://theses.insa-lyon.fr/publication/2019LYSEI042/these.pdf
© [S. Li], [2019], INSA Lyon, tous droits réservés

medium has the same wave propagation form in the time domain as in Kosloff medium because both media have the same equation of motion as given in Eq. (4.8). However, the behavior of the PML medium at the interface with the non-dissipative medium turns out to be better than the Kosloff medium. In comparison with Kosloff medium, the change in the deformation equation will lead PML to achieve a non-reflecting characteristic at the interface between elastic media and PML medium, as demonstrated in the following.

4.1.2 Wave propagation from elastic media into PML medium

The wave propagation problem from an elastic medium to a PML medium is considered below in the case of the 1D harmonic waves. Three components have to be taken into account: the incident wave u_1, the transmitted wave u_2, and the reflected wave u_R, as shown in Fig.4-1.

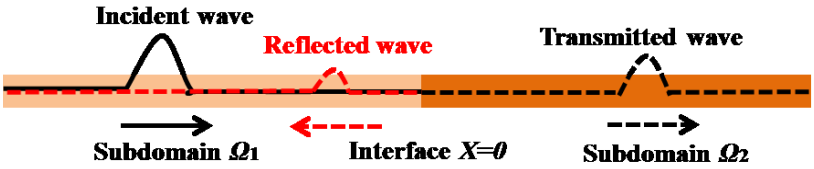

Figure 4-1 Wave propagation from elastic medium to PML medium

$$u_1(x,t) = A\exp[i\omega_0(t - \frac{x}{v_1})] \tag{4.12}$$

$$u_2(x,t) = T\exp[i\omega_0(t - \frac{x}{v_2})]\exp[-\frac{\beta x}{v_2}] \tag{4.13}$$

$$u_R(x,t) = R\exp[i\omega_0(t + \frac{x}{v_1})] \tag{4.14}$$

Based on the continuity of displacements and equilibrium of stresses at the interface, we can write:

$$u_2(x=0,t) = u_1 + u_R(x=0,t) \tag{4.15}$$

Cette thèse est accessible à l'adresse : http://theses.insa-lyon.fr/publication/2019LYSEI042/these.pdf
© [S. Li], [2019], INSA Lyon, tous droits réservés

$$\frac{E_2}{\lambda(x)}\partial_x u_2(x=0,t) = E_1(\partial_x u_1 + \partial_x u_R)(x=0,t) \tag{4.16}$$

From the continuity of displacements at the interface Eq. (4.15), we have

$$T = A + R \tag{4.17}$$

By substituting Eqs. (4.12-4.14) in Eq. (16) and using the definition of the complex stretching function given in Eq. (4.6), the continuity of stresses can be expressed as:

$$\frac{E_2}{1+\frac{\beta}{i\omega_0}}\left[\left(-\frac{i\omega_0}{v_2}\right)T + \left(-\frac{\beta}{v_2}\right)T\right] = E_1\left(\frac{i\omega_0}{v_1}R - \frac{i\omega_0}{v_1}A\right) \tag{4.18}$$

Assuming the same Young modulus and wave velocities in both media, and using the definition of the complex stretching function given in Eq. (4.6), the continuity of stresses at the interface can be simplified as:

$$T = A - R \tag{4.19}$$

Finally, taken into account the Eq. (4.17), we derive the remarkable property of the PML:

$$T = A, R = 0 \tag{4.20}$$

This means that the incident wave is equal to the transmitted wave; no reflected wave will be produced at the interface. In other words, the PML is completely reflectionless in theory and this is true for all constant attenuation parameters γ. As underlined before, the difference between the two formulations lies in the interface behavior, which is reflectionless in the case of the PML in contrast to the Kosloff medium. The introduction of the complex-valued stretching function in the deformation equation leads PML to achieve a non-reflecting characteristic at the interface. Nonetheless, this property is only valid in the absence of discretization. We note that, although there is no reflection at the interface analytically, the spatial discretization will introduce spurious reflections at the interface, so optimal PML's parameters need to be applied in order to minimize these numerical reflections. The real-valued positive functions should be monotonically increasing and vanish at the interface so that the contrast is minimized, in the discrete setting, between the physical domain and the unphysical PML. Classically, the damping function f^p is written as a polynomial of degree n as shown below:

Cette thèse est accessible à l'adresse : http://theses.insa-lyon.fr/publication/2019LYSEI042/these.pdf
© [S. Li], [2019], INSA Lyon, tous droits réservés

$$\beta(x) = \beta_0 \left(\frac{x - x_0}{L}\right)^n \tag{4.21}$$

where β_0 is user-tunable scalar parameters. In fact, the larger β_0 is, the larger the discretization errors become. In other words, more spurious reflected waves will be produced at the interface with larger β_0, as it will be shown in the following numerical investigations.

The logarithmic decrement of PML domain δ is obtained by integrating Eq. (4.11) in the thickness of the PML:

$$\delta = \int_{x_0}^{L} \frac{\beta_0}{v_\rho} \left(\frac{x - x_0}{L}\right)^n dx = \frac{\beta_0 L}{(\mathrm{n}+1) v_\rho} \tag{4.22}$$

We define the attenuation coefficient $R_{attenution}$ from the logarithmic decrement:

$$R_{attenuation} = \left(\frac{|u(x+L)|}{|u(x)|}\right)^2 = e^{-2\delta} \tag{4.23}$$

For instance, if the goal is to reach a target logarithmic decrement δ=ln (10), it means that 90% of the amplitude of the incident wave will be absorbed from the interface to the end of PML. Next, the attenuation also occurs for the reflection process from the end of the PML towards the interface. Hence, the incident wave is attenuated by 99% and the attenuation coefficient $R_{attenution}$ is theoretically equal to 1% before the space and time discretization.

Finally, we can propose the general formula to design PML based on the presented 1D harmonic wave problem in PML medium. After choosing the $R_{attenuation}$, the total thickness L and the power n of the damping function, β_0 can be obtained:

$$\beta_0 = \frac{(n+1)}{2L} \times v_\rho \times \ln\left(\frac{1}{R_{attenuation}}\right) \tag{4.24}$$

4.2 Three-dimensional PML

In this section, the discrete formulation of the PML for three-dimensional elastodynamics will be presented, leading to the novel efficient method for calculating the internal force in PML domain.

Cette thèse est accessible à l'adresse : http://theses.insa-lyon.fr/publication/2019LYSEI042/these.pdf
© [S. Li], [2019], INSA Lyon, tous droits réservés

The main steps of the PML development will be resumed and the details about matrices related to the derivatives of the shape functions of the hexahedral element, combined with attenuation and scaling functions of the PML, can be found in Appendix A.

4.2.1 Strong form of the three-dimensional PML

As shown in section 4.1, the PML formulation is obtained by modifying the governing equations defined in frequency domain. The frequency-domain equations for PML is obtained by applying the complex-valued stretching functions related to the three directions:

$$\sum_j \frac{1}{\lambda_j(x_j)} \frac{\partial \sigma_{ij}}{\partial x_j} = -\omega^2 \rho u_j \tag{4.25}$$

$$\sigma_{ij} = \sum\nolimits_{k,l} C_{ijkl} \varepsilon_{ij} \tag{4.26}$$

$$\varepsilon_{ij} = \frac{1}{2}\left[\frac{1}{\lambda_j(x_j)} \frac{\partial u_i}{\partial x_j} + \frac{1}{\lambda_i(x_i)} \frac{\partial u_j}{\partial x_i}\right] \tag{4.27}$$

where C_{ijkl} are the components of the elastic constitutive tensor.

Then, we introduce the following notations for the PML region: Ω_{PML} is the region of the PML, bounded by the $\Gamma_{PML} = \Gamma_{PML}^D + \Gamma_{PML}^N$, where $\Gamma_{PML}^D \cap \Gamma_{PML}^N = \emptyset$, defining the decomposition of the boundary conditions into Dirichlet and Neumann conditions. In addition, $\underline{g_N}$ denotes the prescribed tractions on Γ_{PML}^N and $J = [0, T]$ is the time interval of interest.

Thanks to the introduction of the stretching functions expressed in Eq. (4.1), the inverse Fourier transform can be easily applied to the previous frequency-domain equations, leading to the following equations in time domain:

$$div\left(\underline{\underline{\sigma}}\ \underline{\underline{\tilde{F}}}^{ee} + \underline{\underline{\Sigma}}\ \underline{\underline{\tilde{F}}}^{ep} + \underline{\underline{\tilde{\Sigma}}}\ \underline{\underline{\tilde{F}}}^{pp}\right) = \rho f_M \underline{\ddot{u}} + \rho f_C \underline{\dot{u}} + \rho f_K \underline{u} + \rho f_H \underline{U} \tag{4.28}$$

$$\underline{\underline{\sigma}} = \underline{\underline{C}} : \underline{\underline{\varepsilon}} \tag{4.29}$$

Cette thèse est accessible à l'adresse : http://theses.insa-lyon.fr/publication/2019LYSEI042/these.pdf
© [S. Li], [2019], INSA Lyon, tous droits réservés

$$\underline{\underline{F}}^{eT}\,\underline{\underline{\dot{\varepsilon}}}\,\underline{\underline{F}}^{e}+\left(\underline{\underline{F}}^{pT}\,\underline{\underline{\varepsilon}}\,\underline{\underline{F}}^{e}+\underline{\underline{F}}^{eT}\,\underline{\underline{\varepsilon}}\,\underline{\underline{F}}^{p}\right)+\underline{\underline{F}}^{pT}\,\underline{\underline{E}}\,\underline{\underline{F}}^{p}$$
$$=\frac{1}{2}\left[\underline{\underline{F}}^{eT}\left(\nabla\,\underline{\dot{u}}\right)+\left(\nabla\,\underline{\dot{u}}\right)^{T}\underline{\underline{F}}^{e}\right]+\frac{1}{2}\left[\underline{\underline{F}}^{pT}\left(\nabla\,\underline{u}\right)+\left(\nabla\,\underline{u}\right)^{T}\underline{\underline{F}}^{p}\right] \tag{4.30}$$

The first equation of the above system is the equation of motion in the PML, complemented with clamped Dirichlet conditions and zero traction forces at the Neumann conditions:

$$\begin{cases}\underline{u}=0 & on\ \ \Gamma_{PML}^{D}\\ \left(\underline{\underline{\sigma}}\,\underline{\underline{\tilde{F}}}^{ee}+\underline{\underline{\Sigma}}\,\underline{\underline{\tilde{F}}}^{ep}+\underline{\underline{\tilde{\Sigma}}}\,\underline{\underline{\tilde{F}}}^{pp}\right)\underline{n}=0 & on\ \ \Gamma_{PML}^{N}\end{cases} \tag{4.31}$$

In addition to the stress tensor, the time-domain PML involves the time-integral of the stress tensor and the time-integral of the time-integral stress tensor, defined by:

$$\underline{\underline{\Sigma}}=\int_0^t\underline{\underline{\sigma}}\,\mathrm{d}t,\ \ \underline{\underline{\tilde{\Sigma}}}=\int_0^t\underline{\underline{\Sigma}}\mathrm{d}t \tag{4.32}$$

It is also noted that the equation of motion is now a third-order differential equation, with four fields: the classical displacement, velocity and acceleration fields, complemented with the time integral of the displacement expressed as: $\underline{U}=\int_0^t\underline{u}\,\mathrm{d}\tau$. Same equation of motion has been obtained by Basu (2009) with one multiplicative factor coming from a slightly different choice of the stretching function as previously discussed. The second equation represents the classical constitutive relationship for an elastic medium. The third equation is the PML strain-deformation relationship, identical to Basu's formulation, which involves the time-integral of the displacement and the time integral of the strain tensor given by:

$$\underline{U}=\int_0^t\underline{u}\,\mathrm{d}t,\ \ \underline{\underline{E}}=\int_0^t\underline{\underline{\varepsilon}}\,\mathrm{d}t \tag{4.33}$$

All the matrices involved in Eqs (4.28) and (4.30) depend on scaling functions $f_i^e(x_i)$ and attenuation functions $f_i^p(x_i)$. Their expressions are given in Appendix A.

Cette thèse est accessible à l'adresse : http://theses.insa-lyon.fr/publication/2019LYSEI042/these.pdf
© [S. Li], [2019], INSA Lyon, tous droits réservés

4.2.2 Weak form of the three-dimensional PML

The space discretization is displacement-based, following a standard finite element formulation as proposed by Basu (2009). The space and time discretization is summarized in the following, before presenting the time coupling of hybrid multi-time step PML with the physical domain. Let $\underline{v}$ be the test function belonging to an appropriate space, the weak formulation is obtained by integrating over the computational domain:

$$\int_\Omega \rho f_M \underline{v} \cdot \underline{\ddot{u}} \mathrm{d}\Omega + \int_\Omega \rho f_C \underline{v} \cdot \underline{\dot{u}} \mathrm{d}\Omega + \int_\Omega \rho f_K \underline{v} \cdot \underline{u} \mathrm{d}\Omega + \int_\Omega \rho f_H \underline{v} \cdot \underline{U} \mathrm{d}\Omega + \int_\Omega \underline{\underline{\tilde{\varepsilon}}}^{ee} : \underline{\underline{\sigma}} \mathrm{d}\Omega + \int_\Omega \underline{\underline{\tilde{\varepsilon}}}^{ep} : \underline{\underline{\Sigma}} \mathrm{d}\Omega + \int_\Omega \underline{\underline{\tilde{\varepsilon}}}^{pp} : \underline{\underline{\tilde{\Sigma}}} \mathrm{d}\Omega = \int_{\Gamma_N} \underline{v} \cdot \left(\underline{\underline{\sigma}} \, \underline{\underline{\tilde{F}}}^{ee} + \underline{\underline{\Sigma}} \, \underline{\underline{\tilde{F}}}^{ep} + \underline{\underline{\tilde{\Sigma}}} \, \underline{\underline{\tilde{F}}}^{pp} \right) \cdot \underline{n} \mathrm{d}\Gamma \quad (4.34)$$

with the expression of the modified strain tensors, taking into account the scaling and damping functions:

$$\begin{cases} \underline{\underline{\tilde{\varepsilon}}}^{ee} = \frac{1}{2}\left[(\nabla \underline{v}) \, \underline{\underline{\tilde{F}}}^{ee} + \underline{\underline{\tilde{F}}}^{eeT} (\nabla \underline{v})^T \right] \\ \underline{\underline{\tilde{\varepsilon}}}^{ep} = \frac{1}{2}\left[(\nabla \underline{v}) \, \underline{\underline{\tilde{F}}}^{ep} + \underline{\underline{\tilde{F}}}^{epT} (\nabla \underline{v})^T \right] \\ \underline{\underline{\tilde{\varepsilon}}}^{pp} = \frac{1}{2}\left[(\nabla \underline{v}) \, \underline{\underline{\tilde{F}}}^{pp} + \underline{\underline{\tilde{F}}}^{ppT} (\nabla \underline{v})^T \right] \end{cases} \quad (4.35)$$

The internal force is expressed as:

$$p_{int}^e = \int_\Omega \underline{\underline{\tilde{\varepsilon}}}^{ee} : \underline{\underline{\sigma}} d\Omega + \int_\Omega \underline{\underline{\tilde{\varepsilon}}}^{ep} : \underline{\underline{\Sigma}} d\Omega + \int_\Omega \underline{\underline{\tilde{\varepsilon}}}^{pp} : \underline{\underline{\tilde{\Sigma}}} d\Omega \quad (4.36)$$

4.2.3 Finite element discretization

We consider in the following the space discretization for a classical 8-node hexahedral element with linear shape functions. The approximation of the displacement is given by: $u_e(x, y, z) = \mathbf{N}(x, y, z)\mathbf{U_e}$, where $\mathbf{U_e}$ gathers the nodal displacements of the 8 nodes, of size 24×1; the matrix $\mathbf{N}(x, y, z)$, of size 3×24, contains the nodal shape functions: $\mathbf{N}(x, y, z) = [N_1\mathbf{I} \quad N_2\mathbf{I} \quad \cdots \quad N_8\mathbf{I}]$, with $\mathbf{I}$ the 3×3 identity matrix.

Cette thèse est accessible à l'adresse : http://theses.insa-lyon.fr/publication/2019LYSEI042/these.pdf
© [S. Li], [2019], INSA Lyon, tous droits réservés

Introducing the finite element discretization into the weak form of the equation of motion in Eq. (34), the semi-discrete equation of motion can be derived:

$$\mathbf{M\ddot{U}} + \mathbf{C\dot{U}} + \mathbf{KU} + \overline{\mathbf{K}}\overline{\mathbf{U}} + \mathbf{P_{int}} = \mathbf{P_{ext}} \tag{4.37}$$

The inertial system matrices **M**, **C**, **K** and $\overline{\mathbf{K}}$ are assembled from their respective element-level matrices. The element-level matrices are obtained by adopting a quadrature formula in every hexahedral element:

$$\boldsymbol{M}^{\mathbf{e}} = \int_{\Omega^{\mathrm{e}}} \rho f_M \mathbf{N}^{\mathbf{T}}\mathbf{N}\,\mathrm{d}\Omega \tag{4.38}$$

$$\mathbf{C}^{\mathbf{e}} = \int_{\Omega^{e}} \rho f_C \mathbf{N}^{\mathbf{T}}\mathbf{N}\,\mathrm{d}\Omega \tag{4.39}$$

$$\mathbf{K}^{\mathbf{e}} = \int_{\Omega^{e}} \rho f_K \mathbf{N}^{\mathbf{T}}\mathbf{N}\,\mathrm{d}\Omega \tag{4.40}$$

$$\overline{\mathbf{K}}^{\mathbf{e}} = \int_{\Omega^{e}} \rho f_H \mathbf{N}^{\mathbf{T}}\mathbf{N}\,\mathrm{d}\Omega \tag{4.41}$$

Taking into account Eq. (4.35), the internal force term $\mathbf{P}_{\mathbf{int}}^{\mathbf{e}}$ can be written as:

$$\mathbf{P}_{\mathbf{int}}^{\mathbf{e}} = \int_{\Omega^{e}} \widetilde{\mathbf{B}}^{\mathbf{eeT}}\widehat{\boldsymbol{\sigma}}\mathrm{d}\Omega + \int_{\Omega^{e}} \widetilde{\mathbf{B}}^{\mathbf{epT}}\widehat{\boldsymbol{\Sigma}}\mathrm{d}\Omega + \int_{\Omega^{e}} \widetilde{\mathbf{B}}^{\mathbf{ppT}}\widehat{\widehat{\boldsymbol{\Sigma}}}\mathrm{d}\Omega \tag{4.42}$$

where the matrices $\widetilde{\mathbf{B}}^{\mathbf{ee}}$, $\widetilde{\mathbf{B}}^{\mathbf{ep}}$ and $\widetilde{\mathbf{B}}^{\mathbf{pp}}$ depend on the derivatives of the shape functions and the scaling and attenuation functions of the PML. Their expressions are placed in Appendix A. In Eq. (4.42), we use the Voigt notation, with $\widehat{\boldsymbol{\sigma}}$ representing the 6-component vector of stresses and $\widehat{\boldsymbol{\Sigma}}$, $\widehat{\widehat{\boldsymbol{\Sigma}}}$ the successive time integrals of stresses.

For the time stepping procedure over the time step $[t_n; t_{n+1}]$, additional relationships are assumed:

$$\widehat{\mathbf{E}}_{\mathbf{n+1}} = \widehat{\mathbf{E}}_{\mathbf{n}} + \widehat{\boldsymbol{\varepsilon}}_{\mathbf{n}}\Delta t, \quad \widehat{\boldsymbol{\Sigma}}_{\boldsymbol{n+1}} = \widehat{\boldsymbol{\Sigma}}_{\boldsymbol{n}} + \widehat{\boldsymbol{\sigma}}_{\mathbf{n}}\Delta t, \qquad \widehat{\widehat{\boldsymbol{\Sigma}}}_{\mathbf{n+1}} = \widehat{\widehat{\boldsymbol{\Sigma}}}_{\boldsymbol{n}} + \widehat{\widehat{\boldsymbol{\Sigma}}}\Delta t \tag{4.43}$$

$$\hat{\dot{\boldsymbol{\varepsilon}}}_{\mathbf{n+1}} = \frac{\widehat{\boldsymbol{\varepsilon}}_{\mathbf{n+1}} - \widehat{\boldsymbol{\varepsilon}}_{\mathbf{n}}}{\Delta t} \tag{4.44}$$

Cette thèse est accessible à l'adresse : http://theses.insa-lyon.fr/publication/2019LYSEI042/these.pdf
© [S. Li], [2019], INSA Lyon, tous droits réservés

Using the assumptions given in Eq. (4.44), the third equation of the system in Eq. (4.30) leads to the expression of the strain $\hat{\boldsymbol{\varepsilon}}_{\mathbf{n+1}}$ at the end of the time step:

$$\hat{\boldsymbol{\varepsilon}}_{\mathbf{n+1}} = \frac{1}{\Delta t}\left[\frac{1}{\Delta t}\hat{\mathbf{F}}^{\boldsymbol{\varepsilon}}\hat{\boldsymbol{\varepsilon}}_{\mathbf{n}} - \hat{\mathbf{F}}^{\mathbf{Q}}\hat{\mathbf{E}}_{\mathbf{n}} + \mathbf{B}^{\boldsymbol{\varepsilon}}\dot{\mathbf{U}}_{\mathbf{n+1}} + \mathbf{B}^{\mathbf{Q}}\mathbf{U}_{\mathbf{n+1}}\right] \tag{4.45}$$

The matrices $\hat{\mathbf{F}}^{\boldsymbol{\varepsilon}}$ and $\hat{\mathbf{F}}^{\mathbf{Q}}$, $\mathbf{B}^{\boldsymbol{\varepsilon}}$, $\mathbf{B}^{\mathbf{Q}}$ depending on derivatives of shape functions as well as scaling and attenuation functions are defined in Appendix A. It has to be noted that the above strain-deformation relationship in the three-dimensional case is the same as in the two-dimensional case (Brun *et al.,* 2016).

Here, the internal force is decomposed into two parts. A first part of the internal force will contain only known quantities at the time t_n, whereas the remaining part will contain the unknown quantities at the time t_{n+1}. Thus, the element-wise internal force vector $\mathbf{P}^{\mathbf{e}}_{\mathbf{n+1}}$ can be written in terms of the element velocity and displacement vectors ($\dot{\mathbf{U}}^{\mathbf{e}}_{\mathbf{n+1}}$ and $\mathbf{U}^{\mathbf{e}}_{\mathbf{n+1}}$) as well as a term, denoted $\mathbf{P}(\boldsymbol{\varepsilon}^{\mathbf{e}}_{\mathbf{n}},\ \mathbf{E}^{\mathbf{e}}_{\mathbf{n}},\ \boldsymbol{\Sigma}^{\mathbf{e}}_{\mathbf{n}},\ \widetilde{\boldsymbol{\Sigma}}^{\mathbf{e}}_{\mathbf{n}})$, depending only on known quantities at the beginning of the time step. The element-wise internal force $\mathbf{P}^{\mathbf{e}}_{\mathbf{n+1}}$ is written as:

$$\mathbf{P}^{\mathbf{e}}_{\mathbf{n+1}} = \left(\int_{\Omega_e} \widetilde{\mathbf{B}}^{\mathbf{T}}\frac{1}{\Delta t}\mathbf{D}\mathbf{B}^{\boldsymbol{\varepsilon}}d\Omega\right)\dot{\mathbf{U}}_{\mathbf{n+1}} + \left(\int_{\Omega_e} \widetilde{\mathbf{B}}^{\mathbf{T}}\frac{1}{\Delta t}\mathbf{D}\mathbf{B}^{\mathbf{Q}}d\Omega\right)\mathbf{U}_{\mathbf{n+1}} + \mathbf{P}\left(\boldsymbol{\varepsilon}^{\mathbf{e}}_{\mathbf{n}}, \mathbf{E}^{\mathbf{e}}_{\mathbf{n}},\ \boldsymbol{\Sigma}^{\mathbf{e}}_{\mathbf{n}},\ \widetilde{\boldsymbol{\Sigma}}^{\mathbf{e}}_{\mathbf{n}}\right) \tag{4.46}$$

with the matrix $\widetilde{\mathbf{B}}$ defined as a function of the previous matrices $\widetilde{\mathbf{B}}^{\mathbf{ee}}$, $\widetilde{\mathbf{B}}^{\mathbf{ep}}$ and $\widetilde{\mathbf{B}}^{\mathbf{pp}}$ and the time step as follows:

$$\widetilde{\mathbf{B}} = \widetilde{\mathbf{B}}^{\mathbf{ee}} + \Delta t\widetilde{\mathbf{B}}^{\mathbf{ep}} + \Delta t^2\ \widetilde{\mathbf{B}}^{\mathbf{pp}} \tag{4.47}$$

The known part of the internal force at the beginning of the time step is given by:

$$\mathbf{P}\left(\boldsymbol{\varepsilon}^{\mathbf{e}}_{\mathbf{n}}, \mathbf{E}^{\mathbf{e}}_{\mathbf{n}},\ \boldsymbol{\Sigma}^{\mathbf{e}}_{\mathbf{n}},\ \widetilde{\boldsymbol{\Sigma}}^{\mathbf{e}}_{\mathbf{n}}\right) = \left(\int_{\Omega_e} \widetilde{\mathbf{B}}^{\mathbf{T}}\frac{1}{\Delta t^2}\mathbf{D}\mathbf{F}^{\boldsymbol{\varepsilon}}\boldsymbol{\varepsilon}_{\mathbf{n}}d\Omega\right) - \left(\int_{\Omega_e} \widetilde{\mathbf{B}}^{\mathbf{T}}\frac{1}{\Delta t}\mathbf{D}\mathbf{F}^{\mathbf{Q}}\mathbf{E}_{\mathbf{n}}d\Omega\right)$$

$$+\left(\int_{\Omega_e} \widetilde{\mathbf{B}}^{\mathbf{ep}^{\mathbf{T}}}\boldsymbol{\Sigma}_{\mathbf{n}}\,d\Omega\right) + \left(\int_{\Omega_e} \widetilde{\mathbf{B}}^{\mathbf{pp}^{\mathrm{T}}}\widetilde{\boldsymbol{\Sigma}}_{\mathbf{n}}d\Omega\right) + \left(\int_{\Omega_e} \widetilde{\mathbf{B}}^{\mathbf{pp}^{\mathbf{T}}}\Delta t\,\boldsymbol{\Sigma}_{\boldsymbol{n}}d\Omega\right) \tag{4.48}$$

In order to express the part of the internal force which has to be computed at the end of the time step given by the two first terms in Eq. (4.46), the element-level matrices are defined by:

Cette thèse est accessible à l'adresse : http://theses.insa-lyon.fr/publication/2019LYSEI042/these.pdf
© [S. Li], [2019], INSA Lyon, tous droits réservés

$$\tilde{\mathbf{C}}^{\mathbf{e}} = \int_{\Omega_e} \widetilde{\mathbf{B}}^{\mathbf{T}} \frac{1}{\Delta t} \mathbf{D} \mathbf{B}^{\boldsymbol{\varepsilon}} d\Omega \tag{4.49}$$

$$\tilde{\mathbf{K}}^{\mathbf{e}} = \int_{\Omega_e} \widetilde{\mathbf{B}}^{\mathbf{T}} \frac{1}{\Delta t} \mathbf{D} \mathbf{B}^{\mathbf{Q}} d\Omega \tag{4.50}$$

These two matrices can be viewed as one viscous matrix operating on velocities and one additional stiffness matrix operating on displacements. Finally, after assembling the element matrices given in Eqs. (4.38-4.41) and Eqs. (4.49-4.50), the space and time discrete equation of motion is obtained at the end time t_{n+1}:

$$\mathbf{M}\ddot{\mathbf{U}}_{\mathbf{n+1}} + \left(\mathbf{C} + \tilde{\mathbf{C}}\right)\dot{\mathbf{U}}_{\mathbf{n+1}} + \left(\mathbf{K} + \tilde{\mathbf{K}}\right)\mathbf{U}_{\mathbf{n+1}} + \bar{\mathbf{K}}\bar{\mathbf{U}}_{\mathbf{n+1}} + \mathbf{P}\left(\boldsymbol{\varepsilon}_{\mathbf{n}}, \mathbf{E}_{\mathbf{n}}, \boldsymbol{\Sigma}_{\mathbf{n}}, \tilde{\boldsymbol{\Sigma}}_{\mathbf{n}}\right) = \mathbf{F}_{\mathbf{ext}} \tag{4.51}$$

The above equation is third-order in time, requiring specific time integration procedure. Analogous third-order discrete form in time has been derived by Fathi *et al.* (2015) by following a mixed approach in the PML, with unknown kinematic quantities at the time t_{n+1} as above, completed with unknown stress quantities. Then, the authors opted for a hybrid treatment, initially developed by Kucukcoban *et al.* (2013) in 2D problems, where the domain of interest is classically dealt with a displacement-only formulation, coupled with the mixed displacement-stress formulation in the PML region. The coupling between the partitions belongs to primal coupling technique, with some degrees of freedom shared by the two partitions.

Here, a dual approach is preferred for coupling the elastic domain and the PML. Indeed, the elastic domain and the PML will be integrated in time, using the powerful and flexible framework of Hybrid Asynchronous Time Integrator (HATI), in order to be able to choose in each partition the appropriate time integrator with its own time step, while conserving classical finite element formulation in other subdomains.

Cette thèse est accessible à l'adresse : http://theses.insa-lyon.fr/publication/2019LYSEI042/these.pdf
© [S. Li], [2019], INSA Lyon, tous droits réservés

4.3 Hybrid multi-time step coupling between the physical domain and PML

Let Ω be a bounded domain belonging to $\mathbb{R}^3$ with a regular boundary. J= [0, T] is the time interval of interest. The domain Ω is divided into two partitions Ω_1 and Ω_2, as shown in Fig.1-4, such as: $\Omega_1 \bigcap \Omega_2 = \emptyset$ and $\partial\Omega_1 \bigcap \partial\Omega_2 = \Gamma_I$. Γ_I denotes the interface between the two subdomains, subdomain Ω_1 representing the non-dissipative medium (the domain of interest) and subdomain Ω_2 the PML medium. The subdomain 1 is related to a linear elastic behavior and the subdomain 2 is related to the PML region previously presented. The subdomain Ω_1 is characterized by its density ρ_1, Young's modulus E_1, Poisson's coefficient ν_1, $\underline{b}_1$ the body force, $\underline{u}_1^D$ the Dirichlet prescribed displacement on Γ_1^D and $\underline{g}_1^N$ the traction force at the Neumann condition on Γ_1^N. The subdomain Ω_2 is characterized by its density ρ_2, Young's modulus E_2, Poisson's coefficient ν_2, $\underline{b}_2$ the body force, $\underline{u}_2^D$ the Dirichlet prescribed displacement on Γ_2^D, $\underline{g}_2^N$ the traction force at the Neumann condition on Γ_2^N.

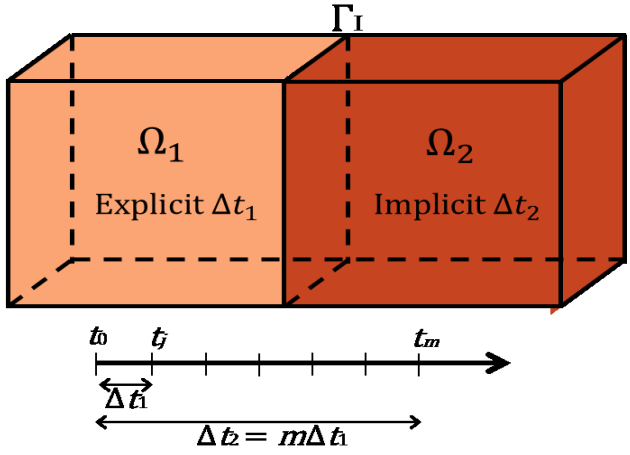

Figure 4-2 Domain Ω divided into two subdomains Ω_1 (Explicit) and Ω_2 (Implicit).

As already done in previous chapters for Rayleigh and Kosloff damping, we write writing the weak form of the coupled problem. Find the solution $\underline{u}_1(t) \in W_1$, $\underline{u}_2(t) \in W_2$ and $\underline{\lambda}(t) \in Q$, for which the following weak form is satisfied $\forall \underline{v}_1 \in W_1^*$, $\forall \underline{v}_2 \in W_2^*$ and $\forall \underline{\mu} \in Q$:

Cette thèse est accessible à l'adresse : http://theses.insa-lyon.fr/publication/2019LYSEI042/these.pdf
© [S. Li], [2019], INSA Lyon, tous droits réservés

$$\int_{\Omega_1} \rho_1 \underline{v}_1 \cdot \underline{\ddot{u}}_1 d\Omega + \int_{\Omega_1} \underline{\underline{\varepsilon}}(\underline{v}_1) : \underline{\underline{\sigma}}_1 d\Omega + \int_{\Omega_2} \rho f_M \underline{v}_2 \cdot \underline{\ddot{u}}_2 \mathrm{d}\Omega + \int_{\Omega_2} \rho f_C \underline{v}_2 \cdot \underline{\dot{u}}_2 \mathrm{d}\Omega + \int_{\Omega_2} \rho f_K \underline{v}_2 \cdot \underline{u}_2 \mathrm{d}\Omega$$
$$+ \int_{\Omega_2} \rho f_H \underline{v}_2 \cdot \underline{U}_2 \mathrm{d}\Omega + \int_{\Omega_2} \underline{\underline{\tilde{\varepsilon}}}^{ee} : \underline{\underline{\sigma}} \mathrm{d}\Omega + \int_{\Omega_2} \underline{\underline{\tilde{\varepsilon}}}^{ep} : \underline{\underline{\Sigma}} \mathrm{d}\Omega + \int_{\Omega_2} \underline{\underline{\tilde{\varepsilon}}}^{pp} : \underline{\underline{\tilde{\Sigma}}} \mathrm{d}\Omega$$
$$+ \int_{\Gamma_I} \underline{v}_1 \cdot \underline{\lambda} d\Gamma + \int_{\Gamma_I} \underline{v}_2 \cdot \underline{\lambda} d\Gamma + \int_{\Gamma_I} \underline{\mu} \cdot (\underline{\dot{u}}_1 - \underline{\dot{u}}_2) d\Gamma$$
$$= \int_{\Omega_1} \underline{v}_1 \cdot \underline{b}_1 d\Omega + \int_{\Gamma_1^N} \underline{v}_1 \cdot \underline{g}_1^N d\Gamma + \int_{\Gamma_2^N} \underline{v}_2 \cdot (\underline{\underline{\sigma}} \tilde{F}^{ee} + \underline{\underline{\Sigma}} \tilde{F}^{ep} + \underline{\underline{\tilde{\Sigma}}} \tilde{F}^{pp}) n \mathrm{d}\Gamma \quad (4.52)$$

Then, we follow the classical lines of the finite element discretization. At the interface between the subdomains, the continuity of velocities is imposed by the following condition:

$$\mathbf{L_1 \dot{U}_1 + L_2 \dot{U}_2} = 0 \quad (4.53)$$

where $\mathbf{L_1}$ and $\mathbf{L_2}$ are the constraint matrices of boolean type in the case of matching meshes at the interface Γ_I. They operate on nodal vectors associated with the two subdomains Ω_1 and Ω_2; they pick out the degrees of freedom belonging to the interface Γ in order to ensure the kinematic continuity at the interface. $\mathbf{L_1}$ can be viewed as a restricted operator, from the subdomain Ω_1 to the interface Γ_I, whereas the transpose operator $\mathbf{L_1^T}$ is a prolonged operator from the interface Γ_I to the subdomain Ω_1. In the case of non-matching meshes, mortar approach has to be applied, leading to non-boolean constraint matrices $\mathbf{L_1}$ and $\mathbf{L_2}$. (Zuchowski *et al.*, 2018). The interface terms in the weak form in Eq. (4.52), involving the Lagrange multiplier field, can be expressed as:

$$\begin{cases} \int_{\Gamma_I} \underline{v}_1 \cdot \underline{\lambda} d\Gamma = \mathbf{V_1^T L_1^T \boldsymbol{\lambda}} \\ \int_{\Gamma_I} \underline{v}_2 \cdot \underline{\lambda} d\Gamma = \mathbf{V_2^T L_2^T \boldsymbol{\lambda}} \end{cases} \quad (4.54)$$

From the weak form of the global problem in Eq. (4.52), the semi-discrete equations in space can be derived, corresponding to the two equations of motion related to the two subdomains, completed with a kinematic condition. In the following, the hybrid integration of this set of equations will be carried out in order to propose a hybrid asynchronous PML. For the time discretization, the GC method proposed by Gravouil and Combescure is employed. Adopting the continuity of velocities at the interface, it was demonstrated that the coupling GC method is stable

Cette thèse est accessible à l'adresse : http://theses.insa-lyon.fr/publication/2019LYSEI042/these.pdf
© [S. Li], [2019], INSA Lyon, tous droits réservés

for any time integrators (implicit and explicit) belonging to the Newmark family (Newmark, 1959) with their own time step depending on subdomains. Different time integrators with their own time step can be adopted depending on the considered subdomain, making the proposed framework very useful to couple complex PML formulations while conserving classical finite element formulations and time integrators in other subdomains.

Here, the subdomain Ω_1 is integrated independently in time with a second-order accurate Newmark explicit time integration scheme, whereas the subdomain Ω_2 is handled by an extended third-order accurate Newmark implicit time integration scheme (Fathi *et al.*, 2015). As illustrated in Fig.1-4, an explicit time integrator with a fine time step Δt_1 imposed by the CFL condition is adopted for the subdomain Ω_1 and an implicit time integrator with a large time step Δt_2 is used for subdomain Ω_2, because implicit scheme is unconditionally stable, with $\Delta t_2 = m\Delta t_1$, m being the time step ratio between two subdomains. In this way, hybrid (different schemes) asynchronous (different time steps depending on subdomains) absorbing layers can be obtained. The equilibrium of subdomain 2 is prescribed at time t_m at the end of the large time step $\Delta t_2 = [t_0; t_m]$ while the equilibrium of subdomain 1 is prescribed at the end of every fine time step $\Delta t_1 = [t_{j-1}; t_j]$. The gluing of the velocity at the interface is written at the fine time scale.

Finally, the weak form given in Eq. (4.52) with the velocity continuity equation in Eq. (4.53) and the expression of the interface terms as a function of the Lagrange multipliers in Eq. (4.54), can be expressed in the following discrete form in space and time:

$$\mathbf{M_1}\ddot{\mathbf{U}}_\mathbf{1}^\mathbf{j} + \mathbf{K_1}\mathbf{U}_\mathbf{1}^\mathbf{j} = \mathbf{F}_\mathbf{1}^{\mathbf{ext,j}} - \mathbf{L}_\mathbf{1}^\mathbf{T}\boldsymbol{\lambda}^\mathbf{j} \tag{4.55}$$

$$\mathbf{M_2}\ddot{\mathbf{U}}_\mathbf{2}^\mathbf{m} + \left(\mathbf{C_2} + \tilde{\mathbf{C}}_\mathbf{2}\right)\dot{\mathbf{U}}_\mathbf{2}^\mathbf{m} + \left(\mathbf{K_2} + \tilde{\mathbf{K}}_\mathbf{2}\right)\mathbf{U}_\mathbf{2}^\mathbf{m} + \bar{\mathbf{K}}_\mathbf{2}\bar{\mathbf{U}}_\mathbf{2}^\mathbf{m} + \mathbf{P_2}\left(\boldsymbol{\varepsilon}_\mathbf{0}, \mathbf{E_0}, \boldsymbol{\Sigma}_\mathbf{0}, \tilde{\boldsymbol{\Sigma}}_\mathbf{0}\right) = \mathbf{F}_\mathbf{2}^{\mathbf{ext,m}} - \mathbf{L}_\mathbf{2}^\mathbf{T}\hat{\boldsymbol{\lambda}}^\mathbf{m} \tag{4.56}$$

$$\mathbf{L_1}\dot{\mathbf{U}}_\mathbf{1}^\mathbf{j} + \mathbf{L_2}\dot{\mathbf{U}}_\mathbf{2}^\mathbf{j} = \mathbf{0} \tag{4.57}$$

The first equation is the discrete in space equation of motion of the subdomain Ω_1 written at the end of the fine time step $\Delta t_1 = [t_{j-1}; t_j]$, whereas the second equation is the discrete equation of motion of the subdomain Ω_2, corresponding to the PML medium, written at the end of the large time step $\Delta t_2 = [t_0; t_m]$. The third equation is the discrete in space velocity continuity at the interface. Subdomain Ω_1 is integrated in time with a Newmark explicit scheme ($\beta_1 = 0$ and $\gamma_1 =$

Cette thèse est accessible à l'adresse : http://theses.insa-lyon.fr/publication/2019LYSEI042/these.pdf
© [S. Li], [2019], INSA Lyon, tous droits réservés

$1/2$), with a lumped mass matrix M_1. We define $\mathbf{U_1^{j-1,p}}$ as the predictor displacement and $\dot{\mathbf{U}}_\mathbf{1}^{\mathbf{j-1,p}}$ as the predictor acceleration, classically introduced in approximate Newmark formula:

$$\mathbf{U_1^{j-1,p}} = \mathbf{U_1^{j-1}} + \Delta t \dot{\mathbf{U}}_\mathbf{1}^{\mathbf{j-1}} + \left(\frac{1}{2} - \beta_1\right)\Delta t^2 \ddot{\mathbf{U}}_\mathbf{1}^{\mathbf{j-1}} \tag{4.58}$$

$$\dot{\mathbf{U}}_\mathbf{1}^{\mathbf{j-1,p}} = \dot{\mathbf{U}}_\mathbf{1}^{\mathbf{j-1}} + \Delta t(1-\gamma_1)\ddot{\mathbf{U}}_\mathbf{1}^{\mathbf{j-1}} \tag{4.59}$$

The classical approximate Newmark formulas in terms of the displacements and velocities at the end of this time step t_j are expressed in acceleration format as below:

$$\mathbf{U_1^j} = \mathbf{U_1^{j-1,p}} + \beta_1 \Delta t^2 \ddot{\mathbf{U}}_\mathbf{1}^{\mathbf{j}} \tag{4.60}$$

$$\dot{\mathbf{U}}_\mathbf{1}^{\mathbf{j}} = \dot{\mathbf{U}}_\mathbf{1}^{\mathbf{j-1,p}} + \gamma_1 \Delta t \ddot{\mathbf{U}}_\mathbf{1}^{\mathbf{j}} \tag{4.61}$$

Concerning the subdomain Ω_2, we use an implicit third-order extended Newmark scheme, as proposed by Fathi *et al.* (2015). For the implicit third-order extended Newmark scheme, β_2 and γ_2 are usual Newmark parameters related to the classical constant average acceleration scheme, equal to $1/4$ and $1/2$, respectively. α_2 is an additional parameter required for the third-order extended Newmark scheme, equal to $1/12$. Velocities, displacements and time-integrals of displacement are expressed as a function of predictors as follows:

$$\bar{\mathbf{U}}_\mathbf{2}^{\mathbf{m}} = \bar{\mathbf{U}}_\mathbf{2}^{\mathbf{0,p}} + \alpha_2 \Delta t^3 \ddot{\mathbf{U}}_\mathbf{2}^{\mathbf{m}} \tag{4.62}$$

$$\mathbf{U_2^m} = \mathbf{U_2^{0,p}} + \beta_2 \Delta t^2 \ddot{\mathbf{U}}_\mathbf{2}^{\mathbf{m}} \tag{4.63}$$

$$\dot{\mathbf{U}}_\mathbf{2}^{\mathbf{m}} = \dot{\mathbf{U}}_\mathbf{2}^{\mathbf{0,p}} + \gamma_2 \Delta t \ddot{\mathbf{U}}_\mathbf{2}^{\mathbf{m}} \tag{4.64}$$

with predictors $\dot{\mathbf{U}}_\mathbf{2}^{\mathbf{0,p}}$, $\bar{\mathbf{U}}_\mathbf{2}^{\mathbf{0,p}}$, $\bar{\mathbf{U}}_\mathbf{2}^{\mathbf{0,p}}$ defined by:

$$\bar{\mathbf{U}}_\mathbf{2}^{\mathbf{0,p}} = \bar{\mathbf{U}}_\mathbf{2}^{\mathbf{0}} + \Delta t \mathbf{U_2^0} + \frac{\Delta t^2}{2}\dot{\mathbf{U}}_\mathbf{2}^{\mathbf{0}} + \left(\frac{1}{6} - \alpha_2\right)\Delta t^3 \ddot{\mathbf{U}}_\mathbf{2}^{\mathbf{0}} \tag{4.65}$$

$$\mathbf{U_2^{0,p}} = \mathbf{U_2^0} + \Delta t \dot{\mathbf{U}}_\mathbf{2}^{\mathbf{0}} + \left(\frac{1}{2} - \beta_2\right)\Delta t^2 \ddot{\mathbf{U}}_\mathbf{2}^{\mathbf{0}} \tag{4.66}$$

$$\dot{\mathbf{U}}_\mathbf{2}^{\mathbf{0,p}} = \dot{\mathbf{U}}_\mathbf{2}^{\mathbf{0}} + (1-\gamma_2)\Delta t \ddot{\mathbf{U}}_\mathbf{2}^{\mathbf{0}} \tag{4.67}$$

Cette thèse est accessible à l'adresse : http://theses.insa-lyon.fr/publication/2019LYSEI042/these.pdf
© [S. Li], [2019], INSA Lyon, tous droits réservés

By introducing the above approximate Newmark formulas into Eqs. (4.55-4.56), it leads to the equations of motion whose unknowns to be solved are the acceleration, written as:

$$\begin{cases} \mathbf{M_1}\ddot{\mathbf{U}}_1^{\mathbf{j}} = \mathbf{F}_1^{\mathbf{ext,j}} - \mathbf{K_1}\mathbf{U}_1^{\mathbf{j-1,p}} - \mathbf{L}_1^{\mathbf{T}}\boldsymbol{\lambda}^{\mathbf{j}} \\ \widetilde{\mathbf{M}_2}\ddot{\mathbf{U}}_2^{\mathbf{m}} = -\mathbf{P_2}\left(\boldsymbol{\varepsilon_0}, \mathbf{E_0}, \boldsymbol{\Sigma_0}, \widetilde{\boldsymbol{\Sigma}}_{\mathbf{0}}\right) - \left(\mathbf{C_2} + \tilde{\mathbf{C}}_2\right)\dot{\mathbf{U}}_2^{\mathbf{0,p}} - \left(\mathbf{K_2} + \widetilde{\mathbf{K}}_2\right)\mathbf{U}_2^{\mathbf{0,p}} - \overline{\mathbf{K}}_2\overline{\mathbf{U}}_2^{\mathbf{0,p}} - \mathbf{L}_2^{\mathbf{T}}\boldsymbol{\lambda}^{\mathbf{m}} \\ \mathbf{L_1}\dot{\mathbf{U}}_1^{\mathbf{j}} + \mathbf{L_2}\dot{\mathbf{U}}_2^{\mathbf{j}} = \mathbf{0} \end{cases} \quad (4.68)$$

where effective stiffness matrices $\widetilde{M}_2$ in the PML subdomain is defined by:

$$\widetilde{\mathbf{M}}_{\mathbf{2}} = \mathbf{M_2} + \gamma_2 \Delta t\left(\mathbf{C_2} + \tilde{\mathbf{C}}_2\right) + \beta_2 \Delta t^2\left(\mathbf{K_2} + \widetilde{\mathbf{K}}_2\right) + \alpha_2 \Delta t^3 \overline{\mathbf{K}}_2 \quad (4.69)$$

Then, the kinematic quantities are divided into two parts: the free and the linked quantities. The free quantities are calculated by taking into account the internal and external forces, without considering the interface forces, whereas the linked quantities are obtained from the interface loads given by the Lagrange multiplier vector $\boldsymbol{\lambda}$. As a result, the equation of motion of the PML subdomain is split into two equations:

$$\widetilde{\mathbf{M}_2}\ddot{\mathbf{U}}_2^{\mathbf{free,m}} = -\mathbf{P_2}\left(\boldsymbol{\varepsilon_0}, \mathbf{E_0}, \boldsymbol{\Sigma_0}, \widetilde{\boldsymbol{\Sigma}}_{\mathbf{0}}\right) - \left(\mathbf{C_2} + \tilde{\mathbf{C}}_2\right)\dot{\mathbf{U}}_2^{\mathbf{0,p}} - \left(\mathbf{K_2} + \widetilde{\mathbf{K}}_2\right)\mathbf{U}_2^{\mathbf{0,p}} - \overline{\mathbf{K}}_2\overline{\mathbf{U}}_2^{\mathbf{0,p}} \quad (4.70)$$

$$\widetilde{\mathbf{M}_2}\ddot{\mathbf{U}}_2^{\mathbf{link,m}} = -\mathbf{L}_2^{\mathbf{T}}\boldsymbol{\lambda}^{\mathbf{m}} \quad (4.71)$$

The complete accelerations are obtained by summing the two parts as:

$$\ddot{\mathbf{U}}_2^{\mathbf{m}} = \ddot{\mathbf{U}}_2^{\mathbf{free,m}} + \ddot{\mathbf{U}}_2^{\mathbf{link,m}} \quad (4.72)$$

The same procedure is applied to the subdomain Ω_1 at each time t_j. Furthermore, the kinematic quantities of the subdomain Ω_2 at t_j are interpolated between the free quantities at the beginning and at the end of the large time step. Then, by decomposing the velocities into free and linked velocities, we can write the velocity continuity at the interface as:

$$\mathbf{L_1}\dot{\mathbf{U}}_1^{\mathbf{link,j}} + \mathbf{L_2}\dot{\mathbf{U}}_2^{\mathbf{link,j}} = -\mathbf{L_1}\dot{\mathbf{U}}_1^{\mathbf{free,j}} - \mathbf{L_2}\dot{\mathbf{U}}_2^{\mathbf{free,j}} \quad (4.73)$$

Following the lines of the coupling GC method, it can be shown that the above velocity continuity leads to reduced-size interface problem whose unknowns are the Lagrange multipliers:

$$\mathbf{H}\boldsymbol{\lambda}^{\mathbf{j}} = \mathbf{b}^{\mathbf{j}} \quad (4.74)$$

with the interface operator and the right-hand side member vector defined by:

Cette thèse est accessible à l'adresse : http://theses.insa-lyon.fr/publication/2019LYSEI042/these.pdf
© [S. Li], [2019], INSA Lyon, tous droits réservés

$$\begin{cases} \mathbf{H} = \gamma_1 \Delta t_1 \mathbf{L_1} \widetilde{\mathbf{M}}_\mathbf{1}^{-\mathbf{1}} \mathbf{L}_\mathbf{1}^{\mathbf{T}} + \gamma_2 \Delta t_2 \mathbf{L_2} \widetilde{\mathbf{M}}_\mathbf{2}^{-\mathbf{1}} \mathbf{L}_\mathbf{2}^{\mathbf{T}} \\ \mathbf{b^j} = \mathbf{L_1} \dot{\mathbf{U}}_\mathbf{1}^{\mathbf{free,j}} + \mathbf{L_2} \dot{\mathbf{U}}_\mathbf{2}^{\mathbf{free,j}} \end{cases} \tag{4.75}$$

Finally, once derived the Lagrange multiplier vector, the quantities related to the interface forces in the first equation of the set of equations (4.68) can be computed and the fine time step $\Delta t_1 = [t_{j-1}; t_j]$ is completed by summing these linked quantities to the free quantities previously obtained. Same procedure is applied for every fine time steps Δt_1, by looping over the large time step $\Delta t_2 = [t_0; t_m]$. The last Lagrange multiplier $\boldsymbol{\lambda^m}$ over the large time step allows to complete the large time step and we can then proceed to the next large time step Δt_2. The algorithm for multi-subdomain coupling has been summarized in Fig. 4-3.

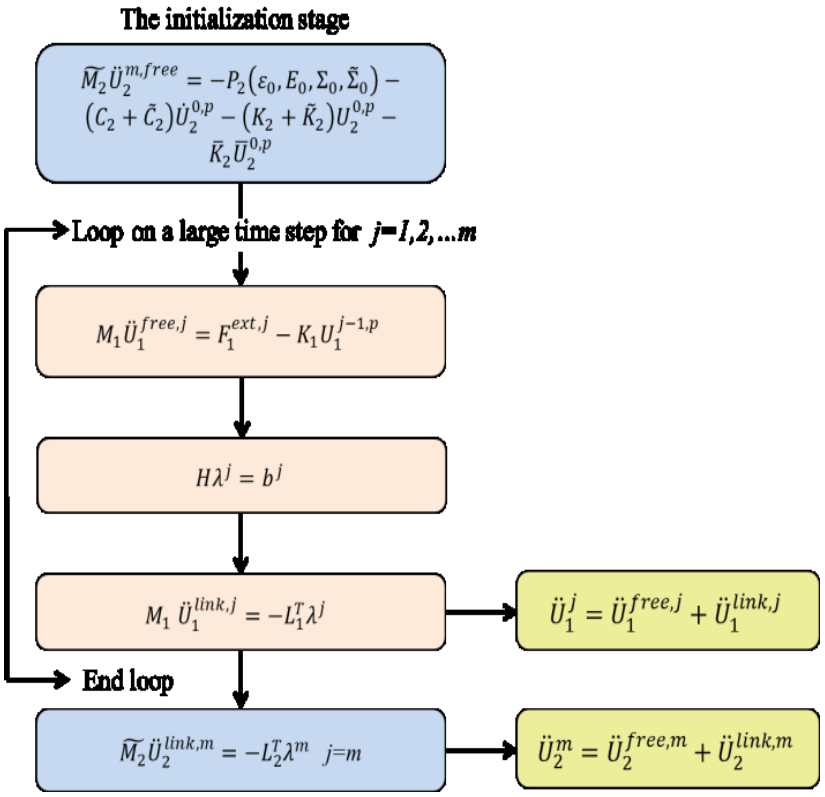

Figure 4-3 The algorithm for multi-subdomain coupling in the initialization stage and over a large time step

Cette thèse est accessible à l'adresse : http://theses.insa-lyon.fr/publication/2019LYSEI042/these.pdf
© [S. Li], [2019], INSA Lyon, tous droits réservés

4.4 Numerical examples

4.4.1 Numerical test of a semi-infinite 3D elastic bar

Numerical models of a semi-infinite elastic bar subjected to horizontal displacement at the free end are established as shown in Figure 4-4. Thus, it simulates the propagation of P waves from a non-dissipative elastic medium to a PML medium. The soil subdomain is assumed to be linear elastic with the following material characteristics: ρ_1=1700 kg/m3, E_1=10 MPa and ν_1= 0.24. The velocity of P-waves C_p is 83m/s. The same material characteristics are applied in the PML subdomain.

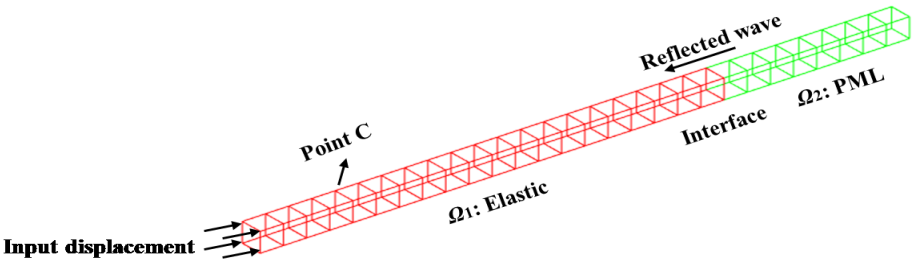

Figure 4-4 Numerical model of a semi-infinite elastic 3D bar subjected to horizontal displacement

To investigate the influence of γ_0 on the accuracy, the model is composed of a soil subdomain of 300m and a PML subdomain with $R_{attenuation}$ equal to 0.01, n equal to 2. Different lengths from 10m to 300m are investigated, leading to different β_0, on the basis of the general design formulae given in Eq. (4.24). The observation point C is located at 20m from the left end of the model. The simulation is conducted by using a homogeneous time step in both subdomains and will be compared to the reference results using extended mesh.

In order to distinguish the difference between the PML results and reference results, the error in the PML solution is computed with respect to the reference results from the extended mesh as:

$$\text{error}(\%) = \frac{\max_n \left| u_p(t_n) - u_{ref}(t_n) \right|}{\max_n \left| u_{ref}(t_n) \right|} \tag{4.76}$$

Cette thèse est accessible à l'adresse : http://theses.insa-lyon.fr/publication/2019LYSEI042/these.pdf
© [S. Li], [2019], INSA Lyon, tous droits réservés

where u_{ref} and u_p are the displacements of the extended mesh model and the PML model. In fact, one part of the error comes from the reflections at the interface between the soil and the PML subdomain because of the spatial discretization, the other part comes from the end of the PML model, depending on $R_{attenution}$. Therefore, the error in the PML solution is the maximal reflection between the two parts with respect to the amplitude of the incident wave, which can be called maximal numerical reflection coefficient.

Non-harmonic waves are investigated by considering a Ricker incident wave defined by the chosen values: t_p=3s, t_s=3s and A =1. Thus, the finite element size of the 8-node hexahedral elements in the longitudinal direction composing the mesh displayed in Figure 4-4, has to be designed to accurately reproduce the propagation of the input Ricker wave. The minimal period for the Ricker input can be assessed by the relationship: $T_{min} = 2.5\ t_p$. To reach a sufficient accuracy, the FE size for linear finite elements, should respect the following relationship: $L_{EF} < \frac{\lambda_{min}}{20}$, with the minimal wavelength equal to $c_P\ T_{min}$.

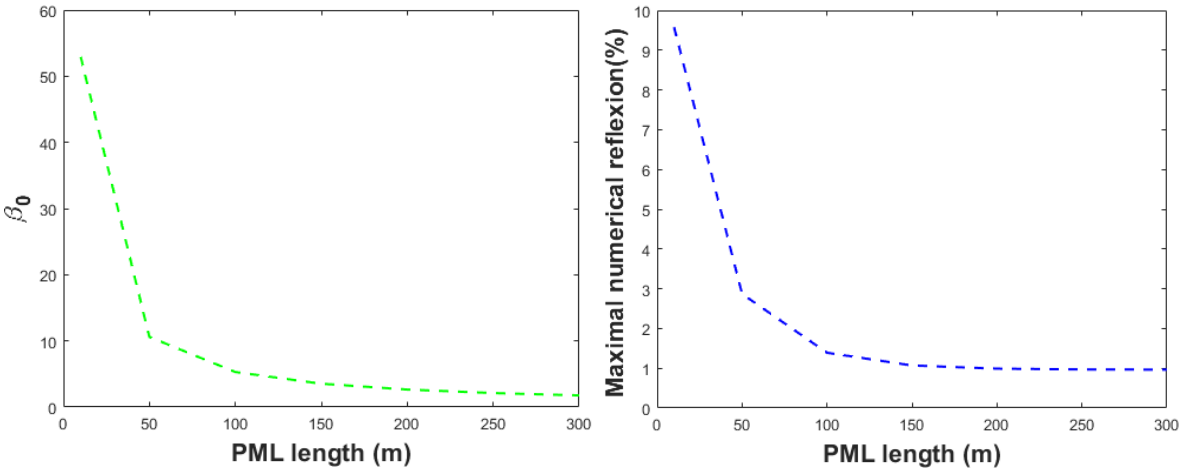

Figure 4-5 β_0 and maximal numerical reflection as a function of PML length

On the left-hand side of Figure 4-5, the value of attenuation coefficient γ_0, given in the design equation of the PML in Eq. (4.24), is plotted as a function of the PML length, for $R_{attenuation}$ equal to 0.01 and n equal to 2. On the right-hand side of Figure 4-5, the maximum numerical reflection is plotted as a function of the PML length as well. It is obvious that the longer the PML subdomain is, the smaller the necessary β_0 is. It is also clearly highlighted that, with a larger length, maximal numerical reflection coefficient decreases and better accuracy can be achieved. It is

Cette thèse est accessible à l'adresse : http://theses.insa-lyon.fr/publication/2019LYSEI042/these.pdf
© [S. Li], [2019], INSA Lyon, tous droits réservés

because that the larger the length is, the more elements there are in the PML region and the smaller discretization error becomes, so that less spurious reflections will be produced at the interface between the soil and the PML subdomain.

The time history of wave propagation at the observation point C with PML length equal to 200m is shown in Figure 4-6. The first reflection from the interface is 0.99%, and the second refection from the end of PML subdomain defined by the $R_{attenution}$ equal to 0.01, is 0.78%. In short, the principle for the design of PML subdomain is to control the reflections from the interface and the end of the model. The reflections from the end can be easily controlled by $R_{attenution}$. In terms of the reflections at the interface, appropriate length should be applied to obtain satisfactory results.

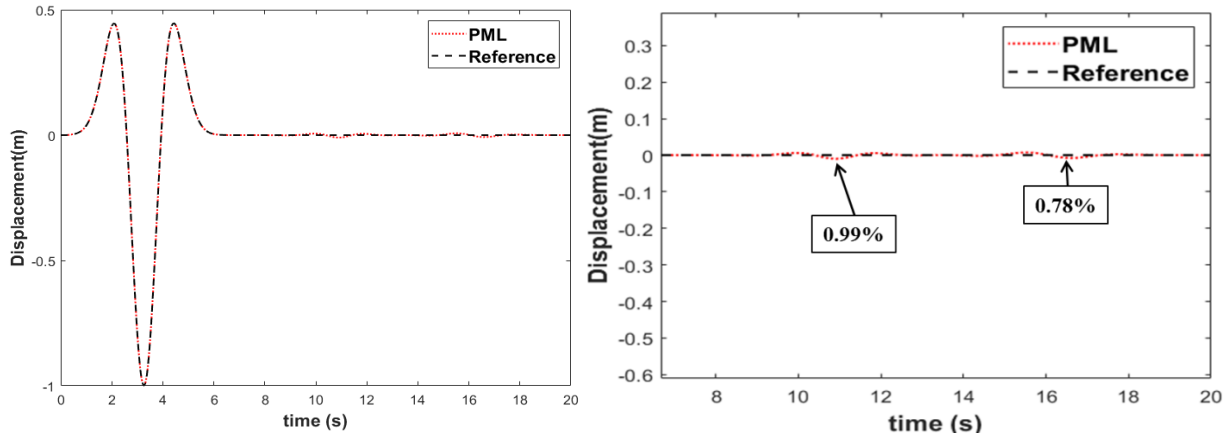

Figure 4-6 The time history of wave propagation at the observation point C with PML length equal to 200m

4.4.2 3D Lamb's test

In order to evaluate the effectiveness of hybrid asynchronous PML, 3D Lamb's test has been simulated. In Lamb's test, the concentrated load applied to the surface of an infinite half-space medium generates three types of waves propagating through the soil, involving P, S waves and Rayleigh waves. Consequently, Lamb's test can be considered as a good test for assessing the performance of PML. Non-harmonic waves are investigated by considering a Ricker incident waves as used in section 4.4.1 with the chosen parameters t_p=3s, t_s=3s and A =2MN.

Cette thèse est accessible à l'adresse : http://theses.insa-lyon.fr/publication/2019LYSEI042/these.pdf
© [S. Li], [2019], INSA Lyon, tous droits réservés

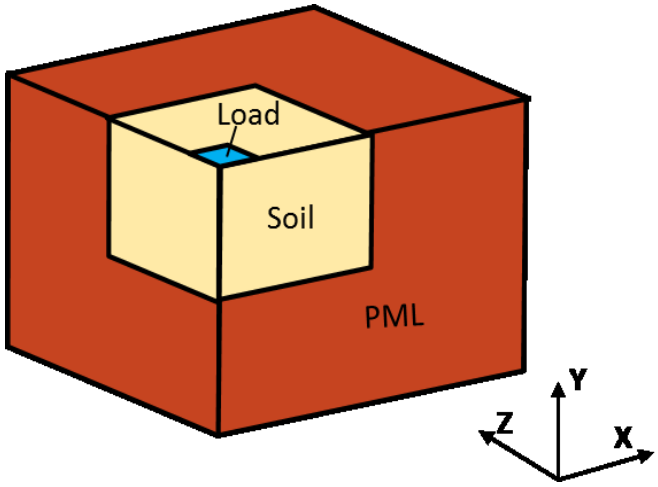

Figure 4-7 3D Lamb's test modeled using PML: quarter model of a PML-truncated semi-infinite homogeneous media subjected to a concentrated force

As illustrated in Figure 4-7, the numerical model is a quarter model of a PML-truncated semi-infinite homogeneous media subjected to a concentered force. It is composed of a bounded soil (subdomain 1) with a size of 50m and PML (subdomain 2) with the thickness of 50m. The same material characteristics are adopted as in the previous numerical model of the semi-infinite elastic bar. The size of eight-node hexahedral element of 5m x 5m x 5m has been taken into account so as to control the inherent wave dispersion. The reference results are computed from an extended mesh. The PML design employed the following parameters: $R_{attenution}$ equal to 0.01, n equal to 2. A recording point is located on the surface of the subdomain soil at 20m from each symmetric side.

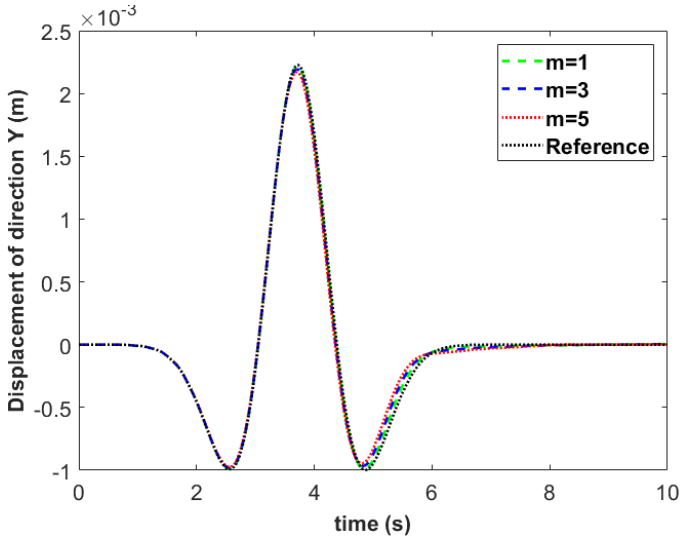

Cette thèse est accessible à l'adresse : http://theses.insa-lyon.fr/publication/2019LYSEI042/these.pdf
© [S. Li], [2019], INSA Lyon, tous droits réservés

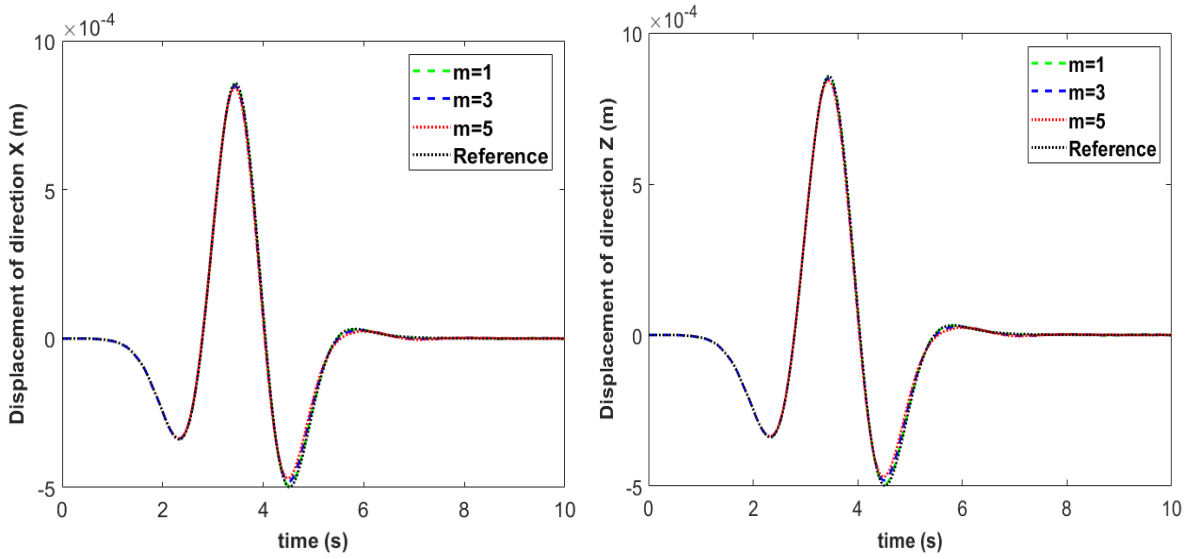

Figure 4-8 Displacements recorded at the observation point using different time step ratios

In the case of a homogeneous time step, the time step satisfying the CFL condition imposed by the mechanical properties in the soil subdomain and the finite element size, is applied in both subdomains, that is m=1, and $\Delta t_1 = \Delta t_2 = 0.025$s. We can observe that the displacements obtained by the PML agree with the reference results: the reflected spurious wave is 1.15% in X and Z directions, 2.82% in Y direction, as shown in Table 4-1. In this numerical example, the bounded soil subdomain and PML is limited to a size of 50m, corresponding only to 1/5 of the P wavelength. With larger model, better accuracy can be achieved. Using the GC method, classical second-order Newmark explicit time integration scheme is conserved in soil subdomain without introducing complex-coordinate-stretched equations in interior domain. Moreover, thanks to the versatility and the stability of the HATI, it is possible to use a larger time step in the PML domain, as done in the following.

In the case of heterogeneous time steps, the subdomain soil is integrated with a fine time step $\Delta t_1 = 0.025$s, whereas the PML subdomain is dealt with a large time step $\Delta t_2 = m\Delta t_1$ in order to reduce the computation time. The time histories of displacements in the three directions at the observation point with different time step ratios m ($\Delta t_2 = m\Delta t_1$) equal to 1, 3 and 5, are shown in Figure 4-8. The errors in comparison to the reference results are given in Table 4-1. It can be noted that the different curves are quite close and reflections increase as the time step ratio increases. In X and Z direction, in comparison to the reference results, the amplitude of the spurious wave varies

Cette thèse est accessible à l'adresse : http://theses.insa-lyon.fr/publication/2019LYSEI042/these.pdf
© [S. Li], [2019], INSA Lyon, tous droits réservés

from 1.15% to 5.31% with respect to the amplitude of the incident wave. In Y direction, the maximal reflection increases from 2.82% to 7.70%. The observed decrease of accuracy as the time step ratio increases can be explained by the following points. First, it is thought that the loose of accuracy can mainly be explained by the additional first-order accurate assumptions assumed in Eqs. (4.43-4.44), in order to perform the time integration of the complex strain-deformation relation in Eq. (4.30). With a bigger time step, more numerical errors will be introduced due to the approximation. Fathi *et al.* (2015) employed a mixed formulation, expressed in terms of kinematic and stress quantities, avoiding the use of the first order approximations previously pointed out. It leads to a significant gain in terms of accuracy in comparison to displacement-based formulation. The price to pay for this improved accuracy is the increasing size of the systems to be solved as well as a greater complexity for the implementation in time-domain elastodynamic codes. Secondly, the GC coupling algorithm is known to be dissipative as soon as heterogeneous time steps are used between the subdomains, generating spurious waves at the interface. It has been demonstrated that for GC method, when adopting the same time step, the second order of accuracy is achieved and it leads to the first order of accuracy when adopting different time steps due to a slight spurious dissipation at the interface (Combescure *et al*., 2002; Gravouil *et al*., 2001).

Table 4-1 Displacement errors using different time step ratios

	Displacement X	Displacement Y	Displacement Z
m=1	1.15%	2.82%	1.15%
m=3	3.18%	5.24%	3.18%
m=5	5.31%	7.70%	5.31%

Cette thèse est accessible à l'adresse : http://theses.insa-lyon.fr/publication/2019LYSEI042/these.pdf
© [S. Li], [2019], INSA Lyon, tous droits réservés

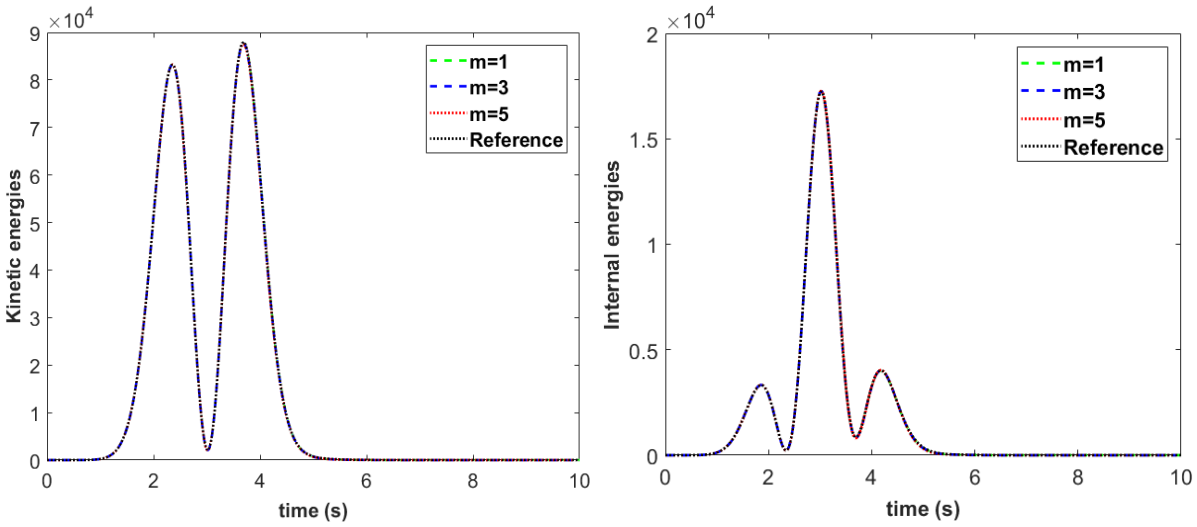

Figure 4-9 Time histories of kinetic and internal energies computed using different time step ratios

Table 4-2 Energy errors using different time step ratios

	Kinetic energy	Internal energy
m=1	0.343%	0.126%
m=3	0.554%	0.213%
m=5	0.772%	0.300%

The kinetic and internal energies of the soil subdomain are computed for different time step ratios m as shown in Fig.4-9. The errors in comparison to the reference results are computed using Eq. (4.76) and shown in Table.4-2. It can be observed that the errors are small for different time step ratios and the errors increase with time step ratios. The CPU times for time-stepping using different time step ratios m are resumed in Table.4-3 in a normalized form divided by CPU time of the homogeneous time step case. It shows that, with the time step ratio increasing, the CPU times decrease significantly, highlighting the interest of the hybrid asynchronous time integration. It implies that using explicit/implicit co-computation, not only classical Newmark explicit time integration scheme can be conserved in soil subdomain without introducing complex-coordinate-stretched equations, but also large time steps can be adopted in the PML subdomain in order to reduce the computation time.

Cette thèse est accessible à l'adresse : http://theses.insa-lyon.fr/publication/2019LYSEI042/these.pdf
© [S. Li], [2019], INSA Lyon, tous droits réservés

Table 4-3 Normalized CPU Time for different time step ratios

	m=1	m=3	m=5
Normalized CPU time	1	0.334	0.189

4.4.3 3D rigid foundation on a layered heterogeneous elastic half-space

The classical soil-structure interaction problem of a rigid foundation on a heterogeneous half-space is considered, as displayed in Figure 4-10. The load is defined by a Ricker wave with the same parameters as in Lamb's test. Three different subdomains are considered: the soil medium (subdomain 1), the PML medium (subdomain 2), and rigid foundation (subdomain 3). The soil subdomain is assumed to be linear elastic and composed of two layers. The thickness of each layer is 25m with a surface 50m x 50m. A recording point is located on the surface of the subdomain soil at 20m from each symmetric side in order to assess the efficiency of the PML layers to model an infinite heterogeneous half-space medium. The common material parameters of soil layers are ρ_1=1700kg/m^3, ν_1= 0.24. The second layer is characterized by Young's modulus which is two times bigger than the first one (10MPa). Similarly, in order to match the soil subdomain, the interface between the layers has to be taken into account in the PML subdomain around the soil with the thickness of 50m in three directions, leading to two PMLs with the same material properties as the two soil layers. The PML is designed by the following parameters: $R_{attenution}$ equal to 0.01, n equal to 2.

Cette thèse est accessible à l'adresse : http://theses.insa-lyon.fr/publication/2019LYSEI042/these.pdf
© [S. Li], [2019], INSA Lyon, tous droits réservés

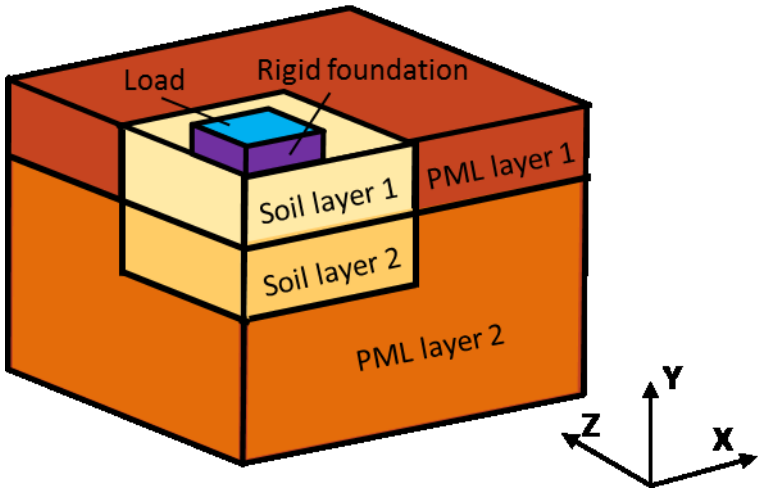

Figure 4-10 Rigid foundation on a layered soil: quarter model of a PML-truncated semi-infinite heterogeneous media subjected to a uniform force

The rigid foundation on the soil is characterized by a thickness of 5m, a surface of 10m x 10m, ρ_3=1700kg/m^3, ν_3= 0.24 and E_3=1000MPa which is 100 times bigger than Young's modulus in soil subdomain. Consequently, the time step satisfying the CFL condition imposed by the mechanical properties of the rigid foundation is 0.0025s which is 10 times smaller than the time step required in soil subdomain. If the same explicit time integration scheme is adopted for the soil subdomain as well as for the rigid foundation subdomain, the time step in soil subdomain will be reduced and lead to additional computational time. As a result, it is of great interest to couple soil subdomain and the rigid foundation by coupling algorithm and adopt implicit time integration scheme for the rigid foundation subdomain. Finally, by using the subdomain coupling strategy, three different subdomains are coupled within the multi time step explicit/implicit co-simulation. The soil medium is integrated with a time step Δt_1, whereas the rigid foundation is integrated using classical second-order Newmark implicit scheme and the PML is integrated using extended third-order Newmark implicit scheme, with a time step $\Delta t_3=\Delta t_2 = m\Delta t_1$, m denoting the time step ratio.

Cette thèse est accessible à l'adresse : http://theses.insa-lyon.fr/publication/2019LYSEI042/these.pdf
© [S. Li], [2019], INSA Lyon, tous droits réservés

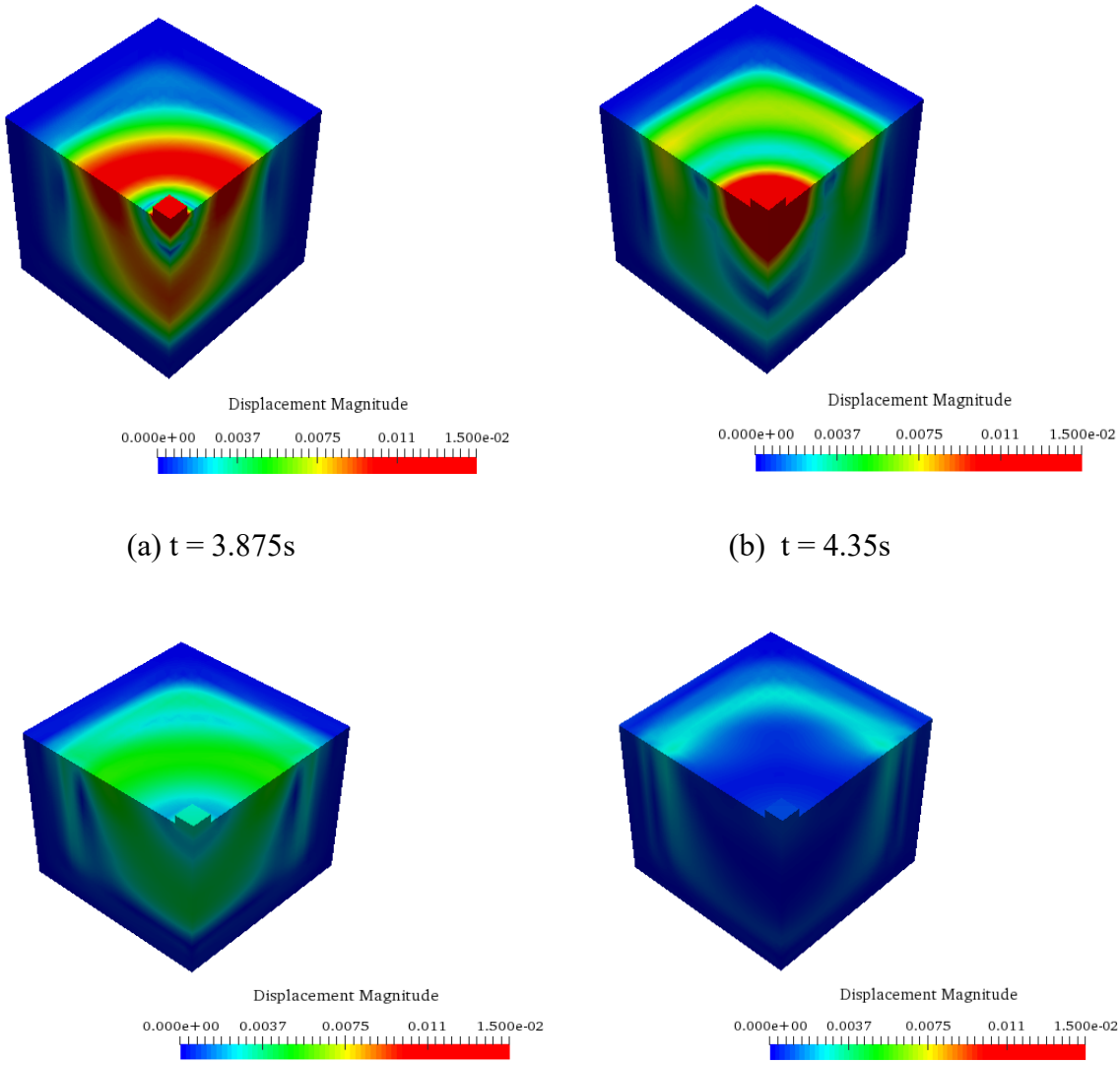

(a) t = 3.875s (b) t = 4.35s

(c) t = 5.05s (d) t = 5.9s

Figure 4-11 Snapshots of displacement magnitude at different times

First, we consider the case with the time step ratio m = 1, Δt_1=0.025s satisfying the CFL condition imposed by the mechanical properties of the soil subdomain, the displacements recorded at point C are compared with the reference results obtained with an extended mesh. Here, the coupling is only between different time integrators because the same time step size is adopted in all the subdomains. From Figure 4-12 and Table 4-4, it can be seen that good agreement is achieved in comparison to the reference results. The reflected spurious wave is 1.11% in X and Z directions, 2.97% in Y direction. The snapshots of displacement magnitude at different times are displayed in

Cette thèse est accessible à l'adresse : http://theses.insa-lyon.fr/publication/2019LYSEI042/these.pdf
© [S. Li], [2019], INSA Lyon, tous droits réservés

Figure 4-11. The first snapshot at time 3.875s shows the propagation of the maximal peak of Ricker incident waves. The second snapshot at time 4.35s shows that the maximal peak of the Ricker incident waves begins to be absorbed in the PML region, followed by an additional smaller peak produced in the soil subdomain. The third snapshot at time 5.05s shows that the maximal peak has been absorbed by PML and smaller peak begins to be absorbed. The last snapshot at 5.9s demonstrates that the absorption of waves in the PML region is almost completed. No obvious reflections can be observed at the PML interface or from the boundaries, indicating very satisfactory performance of the PML.

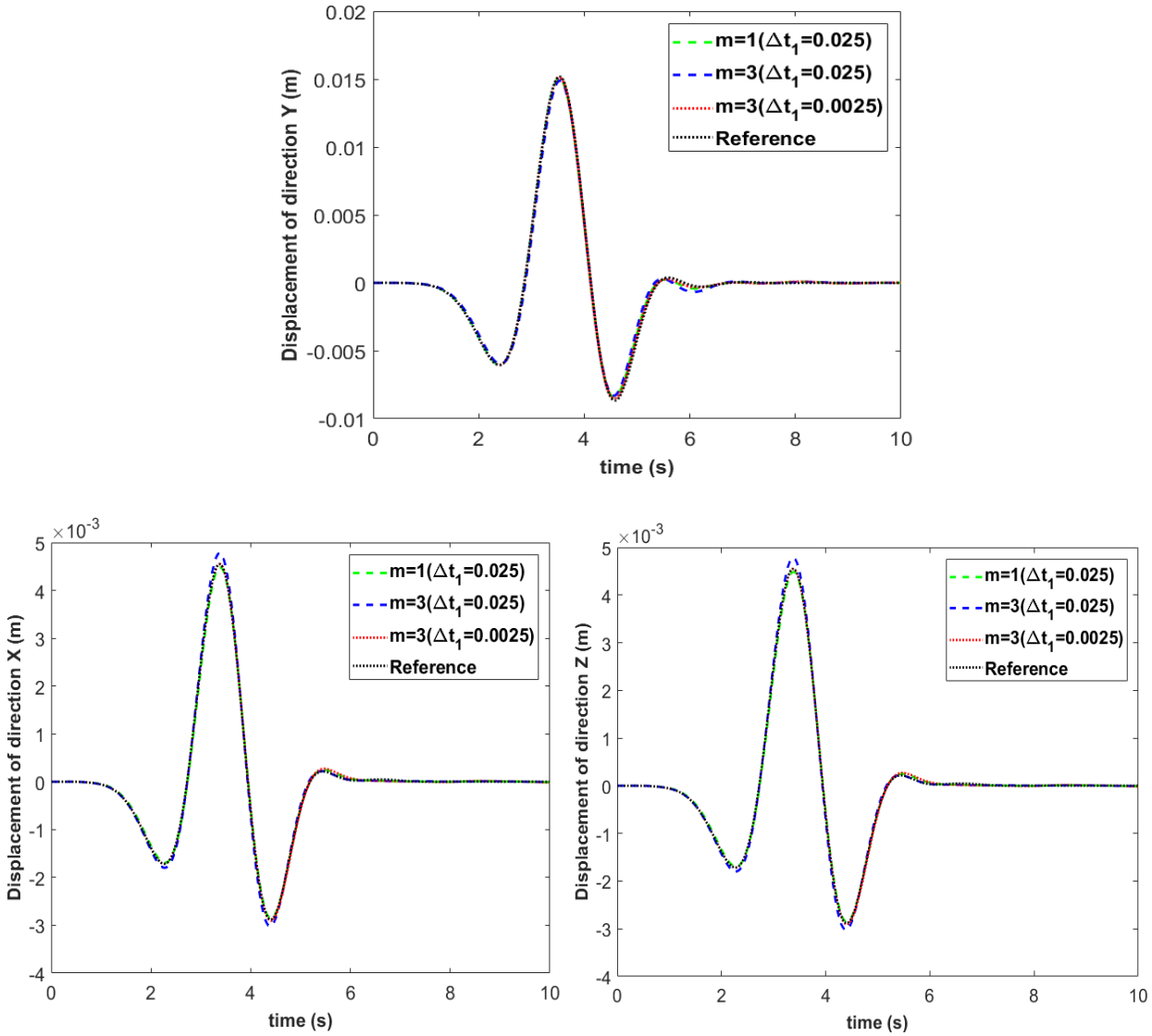

Figure 4-12 Displacements recorded at the observation point using different time step ratios and time steps

Cette thèse est accessible à l'adresse : http://theses.insa-lyon.fr/publication/2019LYSEI042/these.pdf
© [S. Li], [2019], INSA Lyon, tous droits réservés

Table 4-4 Displacement errors using different time step ratios and time steps

	Displacement X	Displacement Y	Displacement Z
m=1, Δt_1=0.025	1.11%	2.97%	1.11%
m=3, Δt_1=0.025	6.55%	5.26%	6.55%
m=3, Δt_1=0.0025	1.51%	1.87%	1.51%

In the case of heterogeneous time steps, two examples are considered. The first one is carried out by using a time ratio m=3 and time step Δt_1 =0.025s. As shown in Table 4-4, the accuracy decreases with increasing time step ratio, similar to Lamb's test. The other computation is with a finer time step size Δt_1 =0.0025s and time ratio m=3. In other words, the time step Δt_1 is taken as the CFL critical time step in the rigid foundation, corresponding to the time step of a full explicit computation. As shown in Figures 4-12, the PML results have good agreement with respect to the reference results, achieving an error of 1.51% in direction X and Z, 1.87% in direction Y. In comparison to the first case with the time step size Δt_1 =0.025s and the same time ratio m=3, it demonstrates that PML accuracy mainly depends on the size of the time step and not on the time step ratio, as previously discussed. In short, the size of time step has an important influence on the accuracy of PML. The smaller is the time step in the PML, the better is the accuracy.

Table 4-5 Normalized CPU Time for different time step ratios and time steps

	m=1, Δt_1=0.025	m=3, Δt_1=0.025	m=3, Δt_1=0.0025
Normalized CPU time	1	0.287	3.53

In terms of computation times normalized by CPU time of the case with the time step size Δt_1 =0.025s and the time ratio m=1, given in Table.4-5, an important reduction in computation time can be obtained by using the time step size Δt_1 =0.025s and the time ratio m=3. With a finer time step size Δt_1 =0.0025s corresponding to the time step of a full explicit computation, more time steps should be calculated in the numerical simulation, resulting in a longer computation time.

Cette thèse est accessible à l'adresse : http://theses.insa-lyon.fr/publication/2019LYSEI042/these.pdf
© [S. Li], [2019], INSA Lyon, tous droits réservés

4.5 Conclusion

A novel 3D PML, suitable for finite element implementation, has been proposed in this chapter for transient elastodynamics. The displacement-based PML making use of the unsplit formulation for calculating the internal force in PML domain is integrated into the Heterogeneous (different time integrators) Asynchronous (different time steps) Time Integrator framework. First, by studying the strong form of wave propagation in PML media, its design equation is derived as well as non-reflecting characteristics between the interior domain and PML domain. Then, the weak formulation leading to a novel efficient method for calculating the internal force in PML domain is developed and has been coupled with interior domain using the dual Schur approach, in order to avoid the introduction of complex-coordinate-stretched equations in interior domain and enable the appropriate time integration scheme in the PML with its own time step to be chosen, independently of the choice of the time scheme in the domain of interest.

Examples of three-dimensional semi-infinite bar, Lamb's test, and classical soil–structure interaction problem with PML-truncated semi-infinite heterogeneous media are implemented to illustrate the efficiency of the hybrid formulation in terms of accuracy and CPU time. The proposed 3D Hybrid Asynchronous PML turns out to be efficient in terms of accuracy and CPU time thanks to the versatility of the employed HATI framework.

Cette thèse est accessible à l'adresse : http://theses.insa-lyon.fr/publication/2019LYSEI042/these.pdf
© [S. Li], [2019], INSA Lyon, tous droits réservés

Cette thèse est accessible à l'adresse : http://theses.insa-lyon.fr/publication/2019LYSEI042/these.pdf
© [S. Li], [2019], INSA Lyon, tous droits réservés

Chapter 5

Three-dimensional explicit asynchronous Perfectly Matched Layer for wave propagation and wave barriers

In this chapter, we focus on explicit time integration with Central Difference (CD) method, in order to reduce the computation time in three-dimensional PML. For comparison purposes, by taking advantage of the versatility of the HATI framework, ALID based on Rayleigh and Kosloff damping are also considered. In numerical application, a first simple 3D Lamb's problem, including only one hexahedral element in the thickness, is investigated; results obtained from PML are compared with results obtained from Rayleigh and Kosloff ALID, demonstrating the superiority of the PML in terms of accuracy and computation time. A 3D Lamb's test with same dimensions in the two horizontal directions is then simulated with the proposed PML as well as a more complex case, including two plates lied on the ground, the first one corresponding to the excited plate at a frequency 30 Hz and the second one corresponding to the Horizontal Wave Barrier (HWB). Influence of the design parameters, such as the length, width and depth of the HWB, is assessed in terms of reduction of ground displacement.

The main part of this chapter is planned to be submitted to Computers and Geotechnics.

Cette thèse est accessible à l'adresse : http://theses.insa-lyon.fr/publication/2019LYSEI042/these.pdf
© [S. Li], [2019], INSA Lyon, tous droits réservés

5.1 Introduction

Three-dimensional complex wave propagation problems are considered in this chapter, such as the mitigation of ground surface vibration through Horizontal Wave Barrier (HWB), set up close to an excited plate, representing, for instance, the slab track excited by the tramway wheels (Grau and Laulagnet, 2015). For this purpose, a full explicit three-dimensional PML with a novel efficient method for calculating the internal force is developed using the HATI framework, enabling us to adopt the Central Difference (CD) method with a fine time step in the PML. Meanwhile, the classical finite element formulation is kept in the interior domain, without complex-valued stretched coordinates, and Newmark explicit scheme is adopted with a time step satisfying the CFL condition. Using the proposed HATI framework, other absorbing layers, more convenient to be implemented in FE software, are also investigated and compared with PML: Absorbing Layers with Increasing Damping (ALID) using viscous Rayleigh damping and ALID with Kosloff damping, detailed in Chapters 2 and 3. In the case of Rayleigh damping, it was widely known that introducing Rayleigh damping reduces the critical time step (Belytschko *et al*., 2000). As a consequence, fine time steps can be employed in the ALID based on Rayleigh damping thanks to the proposed HATI framework, while the interior domain is integrated with a time step satisfying the CFL condition, not affected by the introduction of Rayleigh damping. Moreover, in the cases of PML and Kosloff ALID, the critical time step in explicit dynamics is unchanged but employing fine time steps can improve the accuracy of the absorbing layers.

5.2 Space and time discretization for explicit asynchronous PML

Here, the coupling between two explicit time integrators is considered, with two different time scales, the large time step $\Delta t_1 = [t_0; t_m]$ for the interior domain and the fine time step $\Delta t_2 = [t_{j-1}; t_j]$ for the absorbing layers. This choice is imposed by the fact that we want to keep explicit time integrators in both subdomains for the calculation efficiency in three-dimensional complex modelling and the use of different damping formulations in the absorbing layers. For instance, it is well known that the introduction of Rayleigh damping matrix reduces the critical time step size of the Central Difference scheme (Belytschko *et al*., 2000). Secondly, it was shown in Brun *et al.*

Cette thèse est accessible à l'adresse : http://theses.insa-lyon.fr/publication/2019LYSEI042/these.pdf
© [S. Li], [2019], INSA Lyon, tous droits réservés

(2016) and Li *et al*. (2019) that PML accuracy of Basu's formulation is very sensitive to the time step size, advocating for a fine time step in the PML.

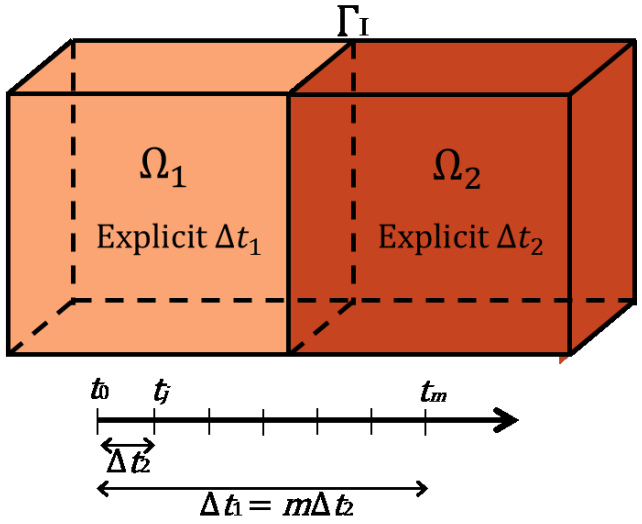

Figure 5-1 Domain Ω divided into two subdomains Ω_1 (interior domain) and Ω_2 (PML region)

From the weak form in Eq. (4.52), we write the equation of motion related to the interior subdomain Ω_1, at the time t_m, that is the end of the large time step $\Delta t_1 = [t_0; t_m]$:

$$\mathbf{M_1}\ddot{\mathbf{U}}_\mathbf{1}^\mathbf{m} + \mathbf{K_1}\mathbf{U}_\mathbf{1}^\mathbf{m} = \mathbf{F}_\mathbf{1}^{\mathbf{ext,m}} - \mathbf{L}_\mathbf{1}^\mathbf{T}\boldsymbol{\lambda}^\mathbf{m} \tag{5.1}$$

Concerning the PML subdomain, we write the equation of motion at the time t_j , at the end of the fine time step $\Delta t_2 = [t_{j-1}; t_j]$:

$$\mathbf{M_2}\ddot{\mathbf{U}}_\mathbf{2}^\mathbf{j} + \left(\mathbf{C_2} + \tilde{\mathbf{C}}_\mathbf{2}\right)\dot{\mathbf{U}}_\mathbf{2}^{\mathbf{j-1/2}} + \left(\mathbf{K_2} + \tilde{\mathbf{K}}_\mathbf{2}\right)\mathbf{U}_\mathbf{2}^\mathbf{j} + \bar{\mathbf{K}}_\mathbf{2}\bar{\mathbf{U}}_\mathbf{2}^\mathbf{j} + \mathbf{P_2}\left(\boldsymbol{\varepsilon}_\mathbf{j-1}, \mathbf{E_{j-1}}, \boldsymbol{\Sigma}_\mathbf{j-1}, \tilde{\boldsymbol{\Sigma}}_\mathbf{j-1}\right) = \mathbf{F}_\mathbf{2}^{\mathbf{ext,j}} - \mathbf{L}_\mathbf{2}^\mathbf{T}\hat{\boldsymbol{\lambda}}^\mathbf{j} \tag{5.2}$$

where the inertial system matrices $\mathbf{M_2}$, $\mathbf{C_2}$, $\mathbf{K_2}$ and $\bar{\mathbf{K}}_\mathbf{2}$are assembled from their respective element-level matrices. The derivation and expression of all previous PML matrices and the internal force are detailed in Chapter 4.The element-level matrices are obtained by adopting a quadrature formula in every hexahedral element. In Eq. (5.2), the other PML matrices $\tilde{\mathbf{C}}_\mathbf{2}$ and $\tilde{\mathbf{K}}_\mathbf{2}$ come from the space and time discretization of the internal force corresponding to the terms $\int_{\Omega_2} \underline{\underline{\tilde{\varepsilon}}}^{ee} : \underline{\underline{\sigma}} \mathrm{d}\Omega +$

Cette thèse est accessible à l'adresse : http://theses.insa-lyon.fr/publication/2019LYSEI042/these.pdf
© [S. Li], [2019], INSA Lyon, tous droits réservés

$\int_{\Omega_2} \underline{\underline{\tilde{\varepsilon}^{ep}}} : \underline{\underline{\Sigma}} \mathrm{d}\Omega + \int_{\Omega_2} \underline{\underline{\tilde{\varepsilon}^{pp}}} : \underline{\underline{\tilde{\Sigma}}} \mathrm{d}\Omega$ in the weak form in Eq. (4.52). Indeed, the internal force can be decomposed in two parts: the first part is related to the previous PML matrices $\mathbf{\tilde{C}^e}$ and $\mathbf{\widetilde{K}^e}$, operating on velocities and displacements and the second part, $\mathbf{P_2}\left(\boldsymbol{\varepsilon_{j-1}}, \mathbf{E_{j-1}}, \boldsymbol{\Sigma_{j-1}}, \boldsymbol{\widetilde{\Sigma}_{j-1}}\right)$. The equations of motion in Eq. (5.1) and Eq. (5.2) are complemented with the velocity continuity condition written at the fine time scale:

$$\mathbf{L_1 \dot{U}_1^j + L_2 \dot{U}_2^j = 0} \tag{5.3}$$

Subdomain Ω_1 is integrated in time with a Newmark explicit scheme ($\beta_1 = 0$ and $\gamma_1 = 1/2$), with a lumped mass matrix M_1. We define $\mathbf{U_1^{0,p}}$ as the predictor displacement and $\mathbf{\dot{U}_1^{0,p}}$ as the predictor acceleration, classically introduced in approximate Newmark formulas:

$$\mathbf{U_1^{0,p}} = \mathbf{U_1^0} + \Delta t \mathbf{\dot{U}_1^0} + \left(\frac{1}{2} - \beta_1\right) \Delta t^2 \mathbf{\ddot{U}_1^0} \tag{5.4}$$

$$\mathbf{\dot{U}_1^{0,p}} = \mathbf{\dot{U}_1^0} + \frac{1}{2} \Delta t (1 - \gamma_1) \mathbf{\ddot{U}_1^0} \tag{5.5}$$

The classical approximate Newmark formulas in terms of the displacements and velocities at the end of this time step t_j are expressed in acceleration format as below:

$$\mathbf{U_1^m} = \mathbf{U_1^{0,p}} + \beta_1 \Delta t^2 \mathbf{\ddot{U}_1^m} \tag{5.6}$$

$$\mathbf{\dot{U}_1^m} = \mathbf{\dot{U}_1^{0,p}} + \gamma_1 \Delta t \mathbf{\ddot{U}_1^m} \tag{5.7}$$

In Newmark explicit computation, the final displacement $\mathbf{U_1^m}$ is known at the beginning of the time step because $\beta_1 = 0$. The final acceleration vector $\mathbf{\ddot{U}_1^m}$ has to be computed in order to update the final velocity vector $\mathbf{\dot{U}_1^m}$. Concerning the subdomain Ω_2, we use a central difference scheme with the terms related to velocities written at the mid step $\left(\mathbf{C_2} + \tilde{\mathbf{C}}_2\right)\mathbf{\dot{U}_2^{j-1/2}}$, in order to avoid system solving and keeping a diagonal mass matrix. The explicit approximate update formulas of the central difference explicit scheme for subdomain Ω_2 are expressed as:

$$\mathbf{\dot{U}_2^{j-1/2}} = \mathbf{\dot{U}_2^{j-3/2}} + \Delta \mathrm{t}\, \mathbf{\ddot{U}_2^{j-1}} \tag{5.8}$$

$$\mathbf{U_2^j} = \mathbf{U_2^{j-1}} + \Delta \mathrm{t}\, \mathbf{\dot{U}_2^{j-1/2}} \tag{5.9}$$

Cette thèse est accessible à l'adresse : http://theses.insa-lyon.fr/publication/2019LYSEI042/these.pdf
© [S. Li], [2019], INSA Lyon, tous droits réservés

$$\bar{\mathbf{U}}_2^{\mathbf{j}} = \bar{\mathbf{U}}_2^{\mathbf{j-1}} + \Delta t \mathbf{U}_2^{\mathbf{j}} \tag{5.10}$$

All the above quantities are known at the beginning of the time step, at the time t_{j-1}. It remains to compute the acceleration $\ddot{\mathbf{U}}_2^{\mathbf{j}}$ at the end of the time step, the following mid step velocity being computed by: $\dot{\mathbf{U}}_2^{\mathbf{j+1/2}} = \dot{\mathbf{U}}_2^{\mathbf{j-1/2}} + \Delta t\, \ddot{\mathbf{U}}_2^{\mathbf{j}}$. Finally, by introducing the above approximate formulas for time integration into Eqs. (5.1) and (5.2), it leads to the set of equations of motion, complemented with the velocity continuity relationship, whose unknowns to be solved are the acceleration, written as:

$$\begin{cases} \mathbf{M_1}\ddot{\mathbf{U}}_1^{\mathbf{m}} = \mathbf{F}_1^{\mathbf{ext,m}} - \mathbf{K_1}\mathbf{U}_1^{\mathbf{0,p}} - \mathbf{L}_1^{\mathbf{T}}\boldsymbol{\lambda}^{\mathbf{m}} \\ \mathbf{M_2}\ddot{\mathbf{U}}_2^{\mathbf{j}} = -\mathbf{P_2}\left(\boldsymbol{\varepsilon}_{\mathbf{j-1}}, \mathbf{E}_{\mathbf{j-1}}, \boldsymbol{\Sigma}_{\mathbf{j-1}}, \widetilde{\boldsymbol{\Sigma}}_{\mathbf{j-1}}\right) - \left(\mathbf{C_2} + \tilde{\mathbf{C}}_2\right)\dot{\mathbf{U}}_2^{\mathbf{j-\frac{1}{2}}} - \left(\mathbf{K_2} + \widetilde{\mathbf{K}}_2\right)\mathbf{U}_2^{\mathbf{j}} - \bar{\mathbf{K}}_2\bar{\mathbf{U}}_2^{\mathbf{j}} - \mathbf{L}_2^{\mathbf{T}}\boldsymbol{\lambda}^{\mathbf{j}} \\ \mathbf{L_1}\dot{\mathbf{U}}_1^{\mathbf{j}} + \mathbf{L_2}\dot{\mathbf{U}}_2^{\mathbf{j}} = \mathbf{0} \end{cases} \tag{5.11}$$

It can be remarked that the effective stiffness matrix in PML subdomain only corresponds to the mass matrix. As classically done for the explicit interior subdomain Ω_1, we also assume a lumped mass matrix in the PML subdomain Ω_2. It enables us to carry out a complete explicit computation in the PML region leading to important gain in terms of computation time in comparison to an implicit solving in the PML region, although large time steps larger than the CFL condition can be adopted in the case of an implicit time integration. This reduction of computation time is particularly suitable for 3D problems. It will be shown in numerical applications that the CFL condition related to the interior subdomain is also valid for the PML region without stability problems. In Eq. (5.11), it is important to note that the velocity continuity is prescribed at the end of the fine time step, whereas the velocity is computed at the mid step in the PML subdomain. As a consequence, the final velocity in the velocity continuity equation is calculated as:

$$\dot{\mathbf{U}}_2^{\mathbf{j}} = \dot{\mathbf{U}}_2^{\mathbf{j-1/2}} + \frac{1}{2}\Delta t\, \ddot{\mathbf{U}}_2^{\mathbf{j}} \tag{5.12}$$

To solve the set of coupled equations in Eq. (5.11), we first determine the Lagrange multipliers ensuring the velocity continuity at the interface and second, we solve the accelerations in both subdomains. Following the lines of the coupling GC method, the kinematic quantities are divided into two parts: the free and the linked quantities. The free quantities are calculated by taking into account the internal and external forces, without considering the interface forces, whereas the

Cette thèse est accessible à l'adresse : http://theses.insa-lyon.fr/publication/2019LYSEI042/these.pdf
© [S. Li], [2019], INSA Lyon, tous droits réservés

linked quantities are obtained from the interface loads given by the Lagrange multiplier vector $\boldsymbol{\lambda}$. It can be demonstrated that the kinematic continuity condition can be expressed as a reduced-size interface problem as follows:

$$\mathbf{H}\boldsymbol{\lambda}^{\mathbf{j}} = \mathbf{b}^{\mathbf{j}} \tag{5.13}$$

with the interface operator and the right-hand side member vector defined by:

$$\begin{cases} \mathbf{H} = \frac{1}{2}\Delta t_1 \mathbf{L_1}\mathbf{M_1}^{-1}\mathbf{L_1^T} + \frac{1}{2}\Delta t_2 \mathbf{L_2}\mathbf{M_2}^{-1}\mathbf{L_2^T} \\ \mathbf{b}^{\mathbf{j}} = \mathbf{L_1}\dot{\mathbf{U}}_{\mathbf{1}}^{\mathbf{free,j}} + \mathbf{L_2}\dot{\mathbf{U}}_{\mathbf{2}}^{\mathbf{free,j}} \end{cases} \tag{5.14}$$

Finally, once derived the Lagrange multiplier vector $\boldsymbol{\lambda}^{\mathbf{j}}$, the quantities related to the interface forces in the second equation of the set of equations (5.11) can be computed and the fine time step $\Delta t_2 = [t_{j-1}; t_j]$ is completed by summing these linked quantities to the free quantities previously obtained. Same procedure is applied for every fine time steps Δt_2, by looping over the large time step $\Delta t_1 = [t_0; t_m]$. The last Lagrange multiplier $\boldsymbol{\lambda}^{\boldsymbol{m}}$ over the large time step allows to complete the large time step and we can then proceed to the next large time step Δt_1.

5.3 Absorbing Layers with Increasing Damping using Rayleigh and Kosloff damping

In the finite element setting, it can be much more convenient to employ different damping formulations from the PML. For instance, Rayleigh damping is classically available in FE code. In Chapter 3, Kosloff damping was investigated and turned out to be suitable for modelling unbounded domains, due to its frequency independent feature. Here, the explicit PML discussed previously will be compared to the cases of Absorbing Layers with Increasing Damping (ALID) using Rayleigh and Kosloff damping.

As done in section 2.7, in the case of Rayleigh damping, the coupling problem, discretized in space and time, can be written as:

Cette thèse est accessible à l'adresse : http://theses.insa-lyon.fr/publication/2019LYSEI042/these.pdf
© [S. Li], [2019], INSA Lyon, tous droits réservés

$$\begin{cases} \mathbf{M_1}\ddot{\mathbf{U}}_1^{\mathbf{m}} = \mathbf{F}_1^{\mathbf{ext,m}} - \mathbf{K_1}\mathbf{U}_1^{\mathbf{0,p}} - \mathbf{L}_1^{\mathbf{T}}\boldsymbol{\lambda}^{\mathbf{j}} \\ \mathbf{M_2}\ddot{\mathbf{U}}_2^{\mathbf{j}} = -\mathbf{C}_{\mathbf{2,Rayleigh}}\dot{\mathbf{U}}_2^{\mathbf{j-1/2}} - \mathbf{K_2}\mathbf{U}_2^{\mathbf{j}} - \mathbf{L}_2^{\mathbf{T}}\boldsymbol{\lambda}^{\mathbf{j}} \\ \mathbf{L_1}\dot{\mathbf{U}}_1^{\mathbf{j}} + \mathbf{L_2}\dot{\mathbf{U}}_2^{\mathbf{j}} = \mathbf{0} \end{cases} \tag{5.15}$$

where the Rayleigh matrix is linearly dependent on the mass matrix and the stiffness matrix, as:

$$\mathbf{C}_{\mathbf{2,Rayleigh}} = \alpha_M \mathbf{M_2} + \alpha_K \mathbf{K_2} \tag{5.16}$$

In the case of Kosloff damping, the governing discrete coupling problem is given by:

$$\begin{cases} \mathbf{M_1}\ddot{\mathbf{U}}_1^{\mathbf{m}} = \mathbf{F}_1^{\mathbf{ext,m}} - \mathbf{K_1}\mathbf{U}_1^{\mathbf{0,p}} - \mathbf{L}_1^{\mathbf{T}}\boldsymbol{\lambda}^{\mathbf{j}} \\ \mathbf{M_2}\ddot{\mathbf{U}}_2^{\mathbf{j}} = -\mathbf{C}_{\mathbf{2,Kosloff}}\dot{\mathbf{U}}_2^{\mathbf{j-1/2}} - \widetilde{\mathbf{K}}_{\mathbf{2,Kosloff}}\mathbf{U}_2^{\mathbf{j}} - \mathbf{K_2}\mathbf{U}_2^{\mathbf{j}} - \mathbf{L}_2^{\mathbf{T}}\boldsymbol{\lambda}^{\mathbf{j}} \\ \mathbf{L_1}\dot{\mathbf{U}}_1^{\mathbf{j}} + \mathbf{L_2}\dot{\mathbf{U}}_2^{\mathbf{j}} = \mathbf{0} \end{cases} \tag{5.17}$$

where the Kosloff matrices are defined by:

$$\mathbf{C}_{\mathbf{2,Kosloff}} = \sum 2 \int_\Omega \rho\gamma \quad [\mathbf{N}]^{\mathbf{T}}[\mathbf{N}] d\Omega \tag{5.18}$$

$$\widetilde{\mathbf{K}}_{\mathbf{2,Kosloff}} = \sum \int_\Omega \rho\gamma^2 [\mathbf{N}]^{\mathbf{T}}[\mathbf{N}] d\Omega. \tag{5.19}$$

5.4 Design of the PML and of the ALID using Rayleigh and Kosloff damping

The general formula to design PML has been proposed in section 4.1. After choosing the $R_{attenuation}$, the total thickness L and the power n of the damping function, β_0 can be obtained:

$$\beta_0 = \frac{(n+1)}{2L} \times v_\rho \times \ln(\frac{1}{R_{attenuation}}) \tag{5.20}$$

When $R_{attenution}$ is equal to 1%, it means that the incident wave is attenuated by 99% theoretically before the space and time discretization.

Cette thèse est accessible à l'adresse : http://theses.insa-lyon.fr/publication/2019LYSEI042/these.pdf
© [S. Li], [2019], INSA Lyon, tous droits réservés

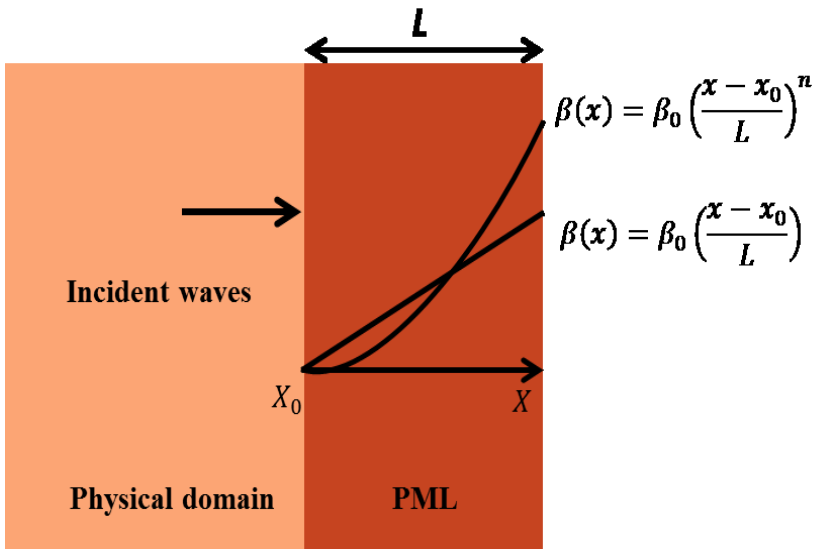

Figure 5-2 Evolution of the damping functions in PML subdomain

Concerning Kosloff damping, it was shown in section 3.2 that the scalar-valued γ parameter in Eqs. (5.18) and (5.19) can be defined in the same manner as the damping function f^p in Fig.5.2, that is: $\gamma(x) = \gamma_0 \left(\frac{x-x_0}{L}\right)^n$. It leads to the same design relationship given by:

$$\gamma_0 = \frac{(n+1)}{2L} \times v_\rho \times \ln\left(\frac{1}{R_{attenution}}\right) \tag{5.21}$$

It is important to remind that the capability of the ALID with Kosloff damping to damp out incident wave is independent of frequency and very similar to the PML. All waves with different frequencies can be attenuated in the same way. Nonetheless, at the interface, the behavior is different in the two cases. Indeed, it is well known that no reflection occurs at the PML interface for all the frequencies. This is not the case for Kosloff damping. Even though the optimal conditions are applied to minimize the spurious reflections at the interface, Kosloff ALID is not reflectionless for all the frequencies, as shown in Chapter 3. The parameters of each layer, indexed by (i) varying from 1 to N, which satisfies the optimal conditions at each interface, are given by:

Cette thèse est accessible à l'adresse : http://theses.insa-lyon.fr/publication/2019LYSEI042/these.pdf
© [S. Li], [2019], INSA Lyon, tous droits réservés

$$\begin{cases} E_2^{(i+1)} = \dfrac{1+(\dfrac{\gamma_i}{\omega_0})^2}{1+(\dfrac{\gamma_{i+1}}{\omega_0})^2} E_2^{(i)} \\ E_2^{(i)} = \dfrac{1}{1+(\dfrac{\gamma_i}{\omega_0})^2} E_1 \\ \nu_2^{(i)} = \nu_1 \\ \rho_2^{(i)} = \rho_1 \\ \gamma_i = \ \gamma_0 \left(\dfrac{x}{L}\right)^n \end{cases} \tag{5.22}$$

Finally, concerning Rayleigh damping, the same polynomial profile for the damping ratio can be considered, that is $\xi(x) = \xi_0 \left(\frac{x-x_0}{L}\right)^{\mathrm{n}}$. For a design angular frequency ω_0 , the design relationship for the ALID based on Rayleigh damping is given by:

$$\xi_0 = \frac{(\mathrm{n}+1)}{2L\omega_0} \times v_\rho \times \ln(\frac{1}{R_{attenution}}) \tag{5.23}$$

Here, it can be observed that the design of the Rayleigh ALID introduces a design angular frequency ω_0. In fact, the absorbing ability of Rayleigh damping is dependent of frequency, which is different from PML and Kosloff damping, as discussed in section 3.2. At the interface, optimal conditions should be applied, as in the case of Kosloff damping:

$$\begin{cases} E_2^{(i+1)} = \dfrac{1+\xi_i^2}{1+\xi_{i+1}^2} E_2^{(i)} \\ E_2^{(1)} = \dfrac{1}{1+\xi_1^2} E_1 \\ \nu_2^{(i)} = \nu_1 \\ \rho_2^{(i)} = \rho_1 \\ \xi_i = \ \xi_0 \left(\dfrac{x}{L}\right)^n \end{cases} \tag{5.24}$$

Cette thèse est accessible à l'adresse : http://theses.insa-lyon.fr/publication/2019LYSEI042/these.pdf
© [S. Li], [2019], INSA Lyon, tous droits réservés

5.5 Numerical examples

5.5.1 Pseudo-3D Lamb's test for PML and ALID comparisons

In order to evaluate the effectiveness of three-dimensional PML, 3D Lamb's test is carried out. Non-harmonic waves are investigated by considering a Ricker incident wave, defined by: the fundamental period t_p, the time shift t_s and the amplitude A. The chosen values are: t_p=3s, t_s=3s and A =1MN.

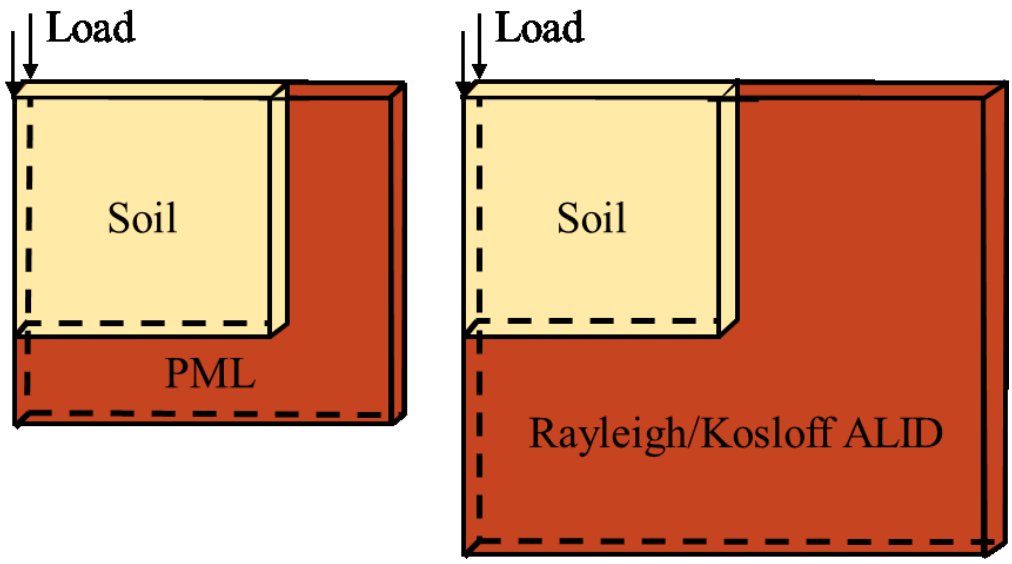

Figure 5-3 3D Lamb's test using PML and Rayleigh/Kosloff ALID

The example of 3D Lamb's test is simulated with only one 3D element in the thickness direction as shown in Fig.5-3. This simple 3D mesh is considered in this first numerical application so as to reduce the computation time in comparison to a full 3D case and to easily compare the performance of the different approaches, the PML, ALID with Rayleigh damping and ALID with Kosloff damping. The Ricker load is applied vertically at the top left edge of the 3D mesh. One observation point is located on the soil surface, at 20m from the applied load. The soil is assumed to be linear elastic with the dimension 250m x 250m x 5m. All hexahedral finite elements are of dimension 5m x 5m x 5m. The material characteristics for the interior subdomain Ω_1 and the PML subdomain Ω_2 are: ρ_1=1700kg/m^3, E_1=10MPa and ν_1= 0.24 for the density, Young's modulus and Poisson's ratio, respectively. The P-wave, S-wave and Rayleigh wave velocities are: V_P =83.27m/s, V_S=48.7m/s,

Cette thèse est accessible à l'adresse : http://theses.insa-lyon.fr/publication/2019LYSEI042/these.pdf
© [S. Li], [2019], INSA Lyon, tous droits réservés

V_R=44.73m/s. The minimal period for the Ricker input can be assessed by the relationship: $T_{min} = 2.5\ t_p$. To reach a sufficient accuracy, the FE size for linear finite elements, should respect the following relationship: $L_{EF} < \frac{\lambda_{min}}{20}$, with the minimal wavelength λ_{min} equal to $c_P\ T_{min}$. The length L of the PML is taken as equal to 50m, corresponding to 10 finite elements in the length. The other parameters for the PML design, given in Eq. (5.20), are the power of polynomial function representing the damping function of the PML and the target attenuation coefficient, given by: $n = 2$ and $R_{attenution} = 0.01$. The subdomain soil is integrated in time by the Newmark explicit scheme without damping and with the time step Δt_1=0.025s, imposed by the CFL condition, whereas the PML is integrated by the Central Difference scheme, with damping terms written at the mid step, with the same time step $\Delta t_1 = \Delta t_2$.

The efficiency and accuracy of Rayleigh and Kosloff ALID in modeling three-dimensional unbounded domain are compared with the PML. The ALID is established with a length of 250m, in order to reduce the reflection at the interface between the interior subdomain and the absorbing subdomain. As shown in Fig.3-3 and Fig.3-4, Rayleigh and Kosloff ALID are not reflectionless for all the frequencies. Larger length is mandatory to reduce the damping ratio, based on the design formulas in Eqs. (5.21) and (5.23). The number of elements in the length of the ALID is thus five times bigger than the one of the PML, in order to reach a sufficient good accuracy. From this point of view, it is clear that PML is much more efficient than Rayleigh and Kosloff ALID.

The multi-time step capability of the proposed approach is employed in the case of the Rayleigh damping, because the stability of the Central Difference scheme with the viscous damping terms is altered by the introduction of Rayleigh damping, leading to the reduction of the critical time step size. As a consequence, it is particularly convenient to adopt an explicit multi-time step strategy in order to satisfy the reduced CFL condition in the Rayleigh ALID while keeping the unchanged CFL condition in the interior subdomain. Here, we adopt a fine time step given by: $\Delta t_1 = 10\Delta t_2$=0.025s. For Kosloff ALID, the introduction of Kosloff damping does not alter the critical time step, leading to same time step in the Kosloff ALID as in the interior subdomain $\Delta t_1 = \Delta t_2$.

In order to assess the accuracy of the PML and ALID methods, the error with respect to the reference results obtained from an extended mesh, free of spurious reflected waves coming from the truncated mesh, is computed as:

Cette thèse est accessible à l'adresse : http://theses.insa-lyon.fr/publication/2019LYSEI042/these.pdf
© [S. Li], [2019], INSA Lyon, tous droits réservés

$$\text{error}(\%) = \frac{\max_n \left| u_p(t_n) - u_{ref}(t_n) \right|}{\max_n \left| u_{ref}(t_n) \right|} \tag{5.25}$$

where u_{ref} and u_p are the displacements of the extended mesh model and the PML model. The above error allows to quantify the spurious reflections.

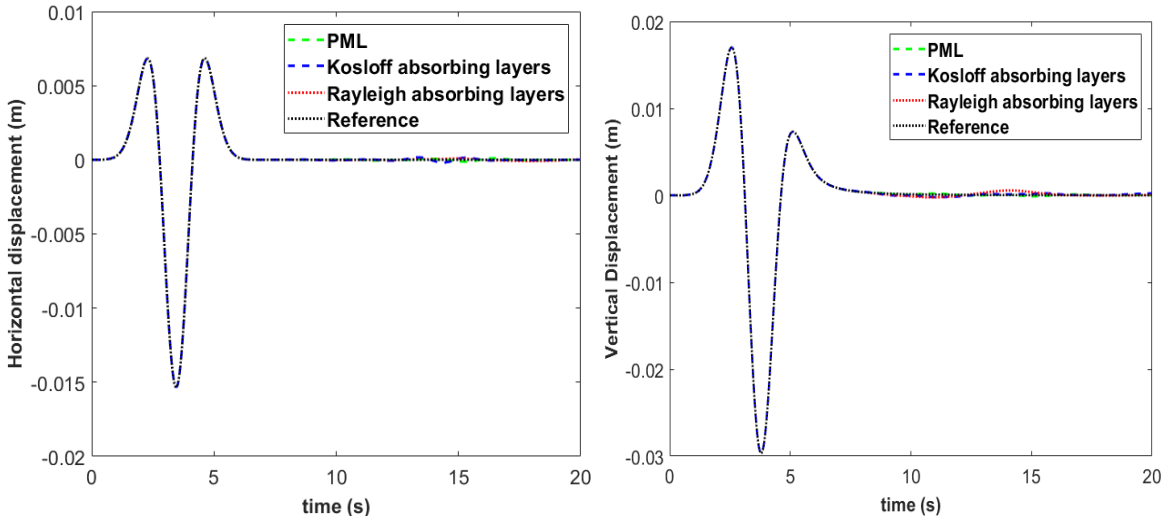

Figure 5-4 Vertical and horizontal displacements at the observation point using different absorbing layers (PML length equal to 50m , Rayleigh and Kosloff ALID length equal to 250m)

In Fig.5-4, three absorbing layers are compared in terms of horizontal displacement and vertical displacement. It can be observed that all the displacements obtained by the three kinds of absorbing layers agree very well with the reference results. Nonetheless, as shown in Table 1, PML is the most accurate one, with both vertical and horizontal reflections under 1%. The CPU times are resumed in Table 5-1 in a normalized form divided by the CPU time of Rayleigh absorbing layer, corresponding to the less efficient method. Indeed, Rayleigh ALID costs higher computation time than Kosloff ALID, because the time steps in the absorbing region are reduced due to the introduction of the Rayleigh matrix in Central Difference method. The computation time of PML is about 4 times less than the Rayleigh and Kosloff ALID, mainly due to its reduced length of 50m in comparison to 250m. In more complex three-dimensional numerical simulations, this advantage is significantly important.

Cette thèse est accessible à l'adresse : http://theses.insa-lyon.fr/publication/2019LYSEI042/these.pdf
© [S. Li], [2019], INSA Lyon, tous droits réservés

Table 5-1 Displacement errors using different absorbing layers

	Vertical displacement	Horizontal displacement
PML ($\Delta t_1 = \Delta t_2$)	0.46%	0.82%
Rayleigh-ALID ($\Delta t_1 = 10\Delta t_2$)	1.80%	0.58%
Kosloff-ALID ($\Delta t_1 = \Delta t_2$)	1.26%	0.98%

Table 5-2 Normalized CPU Time using different absorbing layers

	Rayleigh-ALID	Kosloff-ALID	PML
Normalized CPU time	1	0.76	0.26

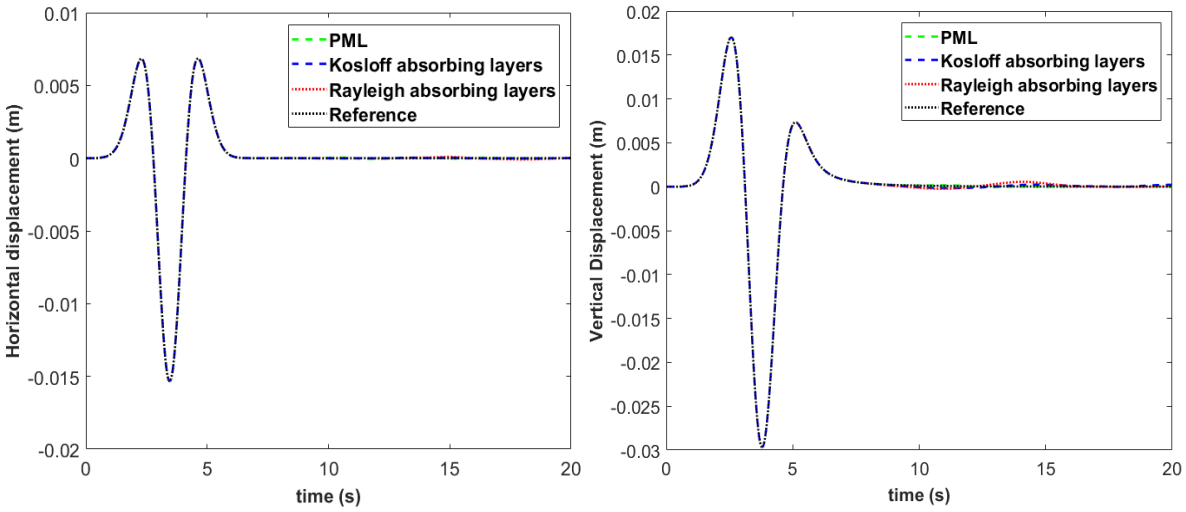

Figure 5-5 Vertical and horizontal displacements at the observation point using different absorbing layers ($\Delta t_1 = 10\ \Delta t_2$, PML length equal to 50m, Rayleigh and Kosloff ALID length equal to 250m)

It is also interesting to decrease the time step in the PML and in the Kosloff ALID ($\Delta t_1 = 10\ \Delta t_2$), so as to improve the accuracy of the absorbing layers. The time histories of the horizontal displacement and vertical displacement at the interest point are shown in Fig.6, using $\Delta t_1 = 10\ \Delta t_2$ in three absorbing layers. It is obvious, as observed in Table 5-3, that a better accuracy is achieved at the expense of the computation time as given in Table 5-4. Using a fine time step, the PML takes

Cette thèse est accessible à l'adresse : http://theses.insa-lyon.fr/publication/2019LYSEI042/these.pdf
© [S. Li], [2019], INSA Lyon, tous droits réservés

longer time than Rayleigh and Kosloff ALID, because the computation time related to one FE, integrated over one time step in the PML, is bigger than the one in Rayleigh and Kosloff ALID.

Table 5-3 Displacement errors using different absorbing layers ($\Delta t_1=10\Delta t_2$)

	Vertical displacement	Horizontal displacement
PML ($\Delta t_1= 10\Delta t_2$)	0.29%	0.32%
Rayleigh-ALID ($\Delta t_1= 10\Delta t_2$)	1.80%	0.58%
Kosloff-ALID ($\Delta t_1= 10\Delta t_2$)	0.82%	0.21%

Table 5-4 Normalized CPU Time for different absorbing layers ($\Delta t_1=10\Delta t_2$)

	Rayleigh-ALID	Kosloff-ALID	PML
Normalized CPU time	1	0.84	1.59

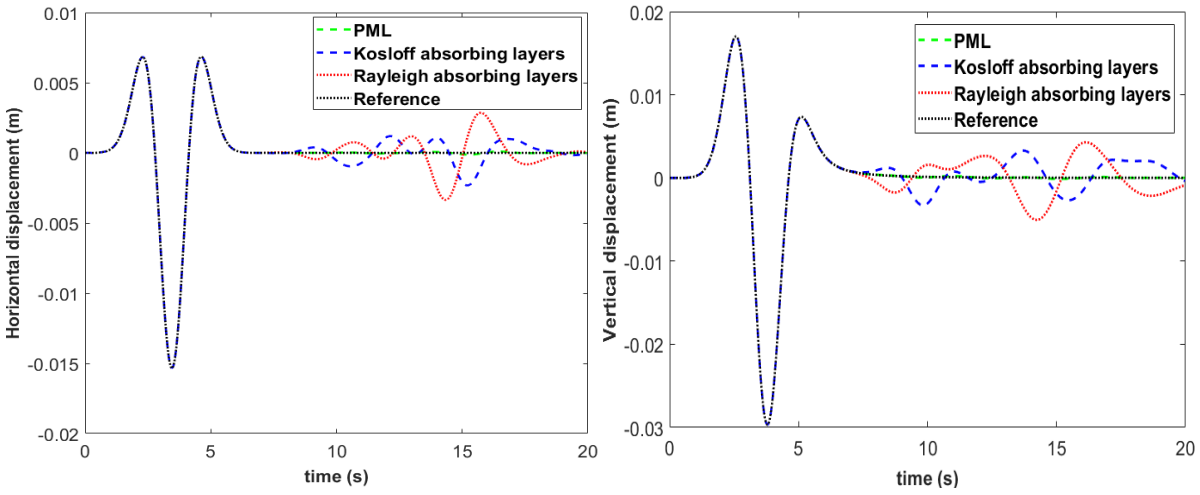

Figure 5-6 Vertical and horizontal displacements at the observation point using different absorbing layers (the length of three absorbing layers equal to 50m)

Cette thèse est accessible à l'adresse : http://theses.insa-lyon.fr/publication/2019LYSEI042/these.pdf
© [S. Li], [2019], INSA Lyon, tous droits réservés

Owing to the frequency-independence of the damping in the PML and its reflectionless feature at the interface, the PML achieves the best accuracy and computation efficiency when adopting the same time step as the interior domain, confirming that it is the most efficient method to model unbounded domain in three-dimensional simulation among the three investigated absorbing layers. Finally, to further illustrate the advantage of the reflectionless feature of the PML at the interface, Rayleigh and Kosloff absorbing layers are established with a length of 50m, that is the same as PML (10 elements in the length). In Fig.5-6, it can be seen that significant reflections are produced at the interface between the soil subdomain and the Rayleigh and Kosloff ALID. Although optimal conditions at the interface were employed to reduce the reflection at the interface for Rayleigh and Kosloff ALID, the size of the ALID still needs to be defined longer than PML, because they are not reflectionless for all the frequencies.

Table 5-5 Pros and cons of the three absorbing layers based on Rayleigh, Kosloff damping and PML

	Rayleigh	**Kosloff**	**PML**
Absorbing ability	Frequency - dependent	Frequency-independent	Frequency-independent
Behavior at the interface	Optimal conditions	Optimal conditions	Reflectionless
Time step in explicit scheme	Reduced	No influence	No influence
Difficulty in implementation	Easy	Easy	Difficult
Size of the absorbing region	Large	Large	Small
Computation time	Long	Long	Short

Table 5-5 summarizes the different characteristics of the tree absorbing layers. Even though PML is more complex to be implemented, the size of the absorbing region and the calculation time of three-dimensional needed for PML is much less than Rayleigh and Kosloff absorbing layers, because of the reflectionless characteristic at the interface and the same attenuation for all

Cette thèse est accessible à l'adresse : http://theses.insa-lyon.fr/publication/2019LYSEI042/these.pdf
© [S. Li], [2019], INSA Lyon, tous droits réservés

frequencies. Taking into account both accuracy and computation efficiency, PML turns out to be the most efficient method to model unbounded domain in three-dimensional simulation among the three investigated absorbing layers. As a consequence, for the following application focused on wave barrier, only PML strategy with a time step ratio m equal to 1, is considered.

5.5.2 Lamb's test with explicit 3D PML

In order to further evaluate the effectiveness of the proposed PML, more realistic Lamb's test has been simulated with same dimensions in the two horizontal directions as done in section 4.4.2 and displayed in Fig.4-7. The numerical model is a quarter model of a PML-truncated semi-infinite homogeneous media subjected to a concentered force. It is composed of a bounded soil (subdomain 1) with a size of 100m and PML (subdomain 2) with the thickness of 50m. Same material characteristics as before are adopted. Non-harmonic waves are investigated by considering a Ricker incident waves with the chosen parameters t_p=3s, t_s=3s and A =2MN. The PML design employed the previous parameters: n equal to 2 and $R_{attenution}$ equal to 0.01. A recording point is located on the surface of the subdomain soil at 20m from each symmetric side. The subdomain soil is integrated in time by Newmark explicit scheme with the time step (Δt_1=0.025s), and the PML is integrated by the Central Difference scheme with the same time step $\Delta t_2=\Delta t_1$, imposed by the condition CFL.

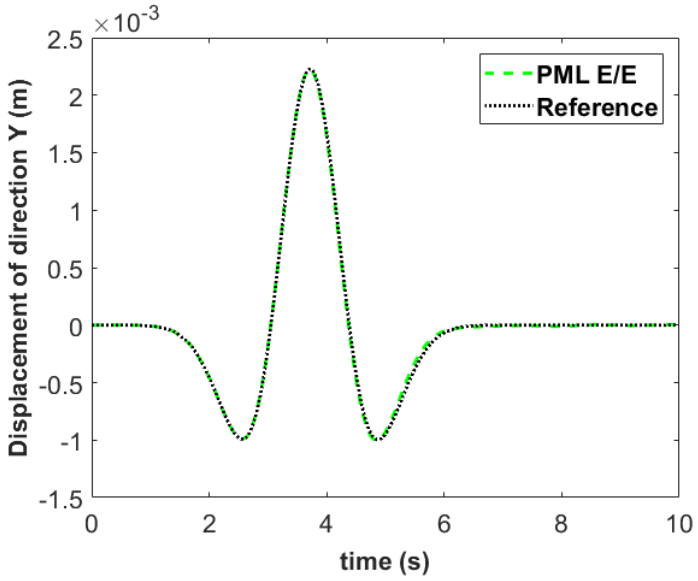

Cette thèse est accessible à l'adresse : http://theses.insa-lyon.fr/publication/2019LYSEI042/these.pdf
© [S. Li], [2019], INSA Lyon, tous droits réservés

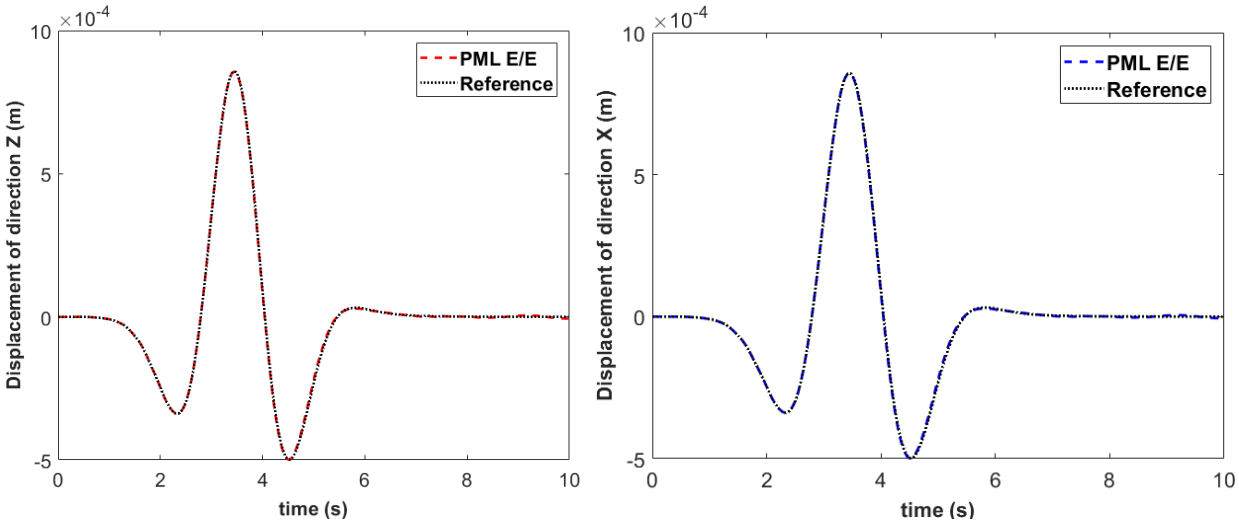

Figure 5-7 Displacements recorded at the observation point using explicit 3D PML (soil length equal to 50m)

We can observe that the displacements obtained agree very well with the reference results: the reflected spurious wave is 1.32% in X and Z directions, 2.64% in Y direction, as shown in Table 5-7. The reflections are at the same level as the most precise case using co-simulation explicit/implicit (m=1) in section 4.4.2. In terms of the computation time, in comparison with co-simulation explicit/implicit (m=5), the computation time for co-simulation explicit/explicit is even quicker, thanks to the diagonalization of the effective stiffness matrix of PML subdomain.

Table 5-6 Normalized CPU Time for different co-simulation strategies (PML)

	E/I (m=5)	E/E
Normalized CPU time	1	0.6868

Table 5-7 Displacement errors in different directions using explicit/explicit co-simulation (PML)

	Displacement X	Displacement Y	Displacement Z
PML	1..32%	2.64%	1.32%

Cette thèse est accessible à l'adresse : http://theses.insa-lyon.fr/publication/2019LYSEI042/these.pdf
© [S. Li], [2019], INSA Lyon, tous droits réservés

Secondly, the numerical model of Lamb's test is established with a bounded soil (subdomain 1) with a size of 100m, twice larger than the size in the first example, and the PML (subdomain 2) with the same thickness of 50m. The same material characteristics are adopted as in the previous numerical model. In this case, we can observe that the displacements are in very good agreement with respect to the reference result as shown in Fig.5-8. The reflected spurious wave is 0.68% in X and Z directions, 1.24% in Y direction, as shown in Table 5-8. We can see that the results have been improved, in comparison to the first example with a smaller soil bounded domain. It means that not only the length of the PML affects the accuracy as shown in section 4.4.1, but also the size of the soil subdomain has an influence on the accuracy of the PML. In fact, when the bounded soil subdomain is larger, there will be more elements at the interface of the soil subdomain and the PML and spurious reflections at the interface introduced by the spatial discretization will decrease.

Thanks to explicit-explicit co-simulation, in the framework of HATI, the interior domain is handled by the classical finite element formulation and Newmark explicit time integrator, instead of introducing complex-coordinate-stretched equations, whereas the PML subdomain is handled by the Central Difference scheme, in order to make use of the diagonal lumped mass matrix of the subdomain Ω_2. Taking into account its advantages in accuracy and CPU time, the proposed three-dimensional explicit PML is efficient for complex three-dimensional wave propagation simulation. In next section, it will be applied in the study of the screening effect provided by an horizontal wave barrier in mitigating ground surface vibration generated by an excited plate.

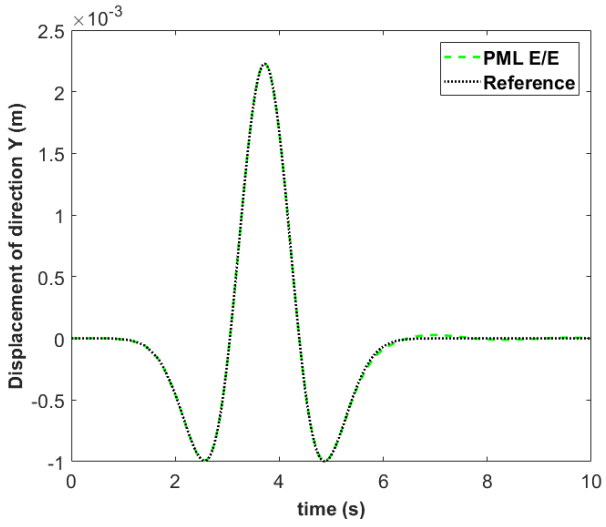

Cette thèse est accessible à l'adresse : http://theses.insa-lyon.fr/publication/2019LYSEI042/these.pdf
© [S. Li], [2019], INSA Lyon, tous droits réservés

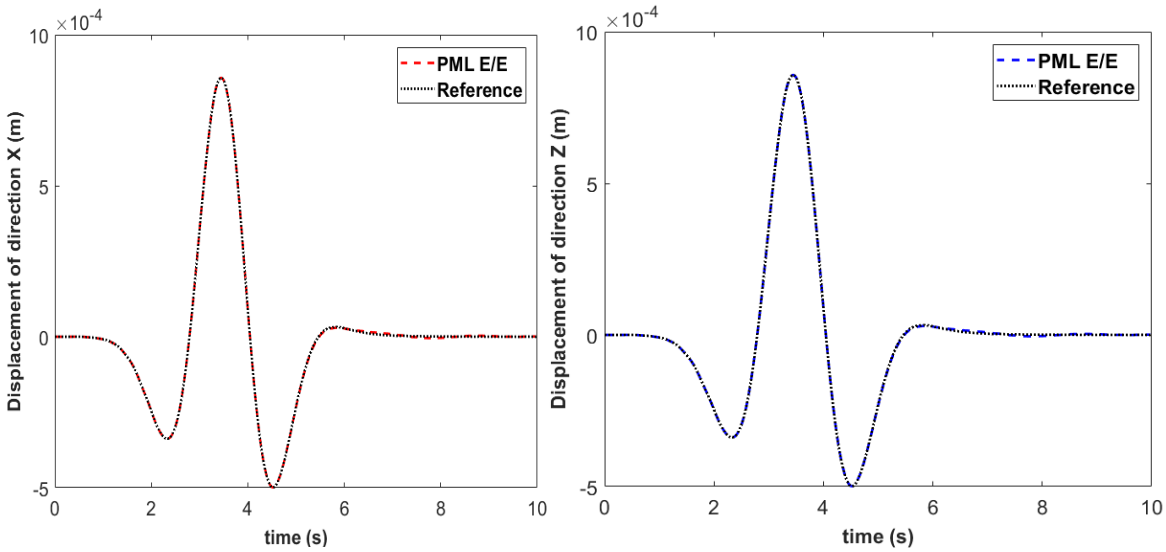

Figure 5-8 Displacements recorded at the observation point using explicit 3D PML (soil length equal 100m)

Table 5-8 PML displacement errors in different directions with larger soil subdomain

	Displacement X	Displacement Y	Displacement Z
PML	0.68%	1.24%	0.68%

5.5.3 Horizontal Wave Barrier efficiency with explicit 3D PML

Due to the increasing vibrations caused by human activities, the performance of wave barriers for reducing the distress to adjacent structures and annoyance to people, have been studied for more than 30 years. To further demonstrate the efficiency of the proposed approach for modeling unbounded domains, a three-dimensional application is carried out concerning an Horizontal Wave Barrier (HWB), in the context of vibration isolation against the ground surface wave propagation produced by trains and tramways. In this case, the major part of the vibration energy is transferred by Rayleigh waves which may cause strong ground motions on nearby structures (Al-Hussaini and Ahmad, 1991; Beskos *et al*., 1986).

Cette thèse est accessible à l'adresse : http://theses.insa-lyon.fr/publication/2019LYSEI042/these.pdf
© [S. Li], [2019], INSA Lyon, tous droits réservés

As illustrated in Figure 5-9, the numerical model is composed of the bounded soil, the PML, the rigid foundation and the horizontal wave barrier. The bounded soil (40m x 8m x 8m) is assumed to be linear elastic with the following material characteristics: ρ_1=1200kg/m^3, E_1=187.5MPa and ν_1 = 0.25. In the soil, the P-wave, S-wave and Rayleigh-wave velocities are: V_P =433m/s, V_S=250m/s, V_R=230m/s. The PML region is established with the thickness of 4m in the three directions around the bounded soil, following the parameters: n equal to 2 and $R_{attenution}$ equal to 0.01. The rigid foundation on the soil is characterized by a thickness of 0.5m, a surface of 2m x 2m, ρ_3=1200kg/m3, ν_3= 0.25 and E_3=100E_1, that is 100 times bigger than Young's modulus in soil subdomain. The dynamic periodic load, imposed on every node of the rigid foundation surface in the numerical model, is defined by: $P = P_0\sin(\omega_0 t)$, ω_0 =2πf_0, P_0 =500kN, f_0 =30Hz. The wavelength for P-wave, S-wave and Rayleigh-wave are 14.43m, 8.33m, 7.67m, respectively.

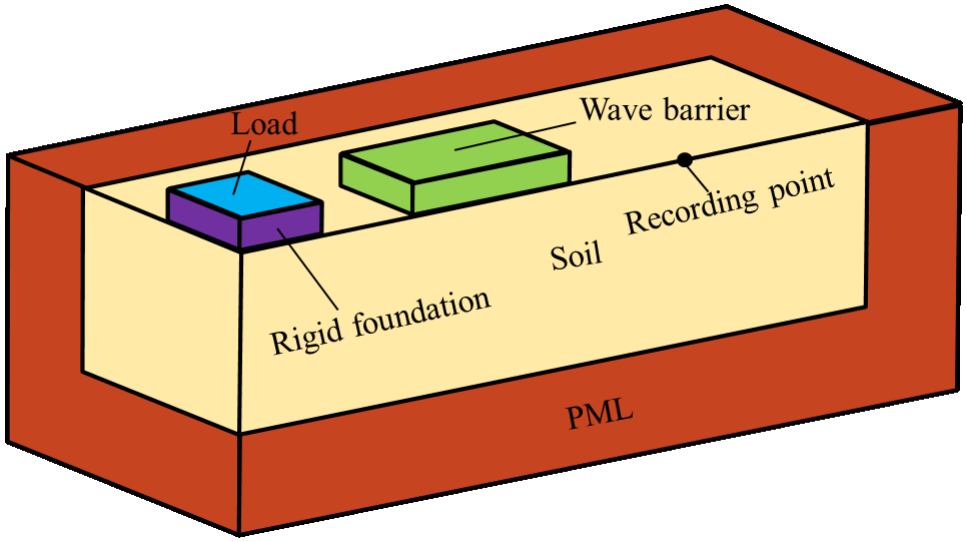

Figure 5-9 Configuration of the numerical model of three-dimensional wave barrier problem

For the horizontal wave barrier, D represents the depth of the barrier, W is the width of the barrier, L is the length of the barrier. The horizontal wave barrier is installed behind the rigid foundation with the distance equal to 2m. The distance from the rigid foundation to the point of interest is 30m. The material parameters of the HWB is the same as the rigid foundation. The isolation effect of the installation of the HWB can be assessed by the parameter A_r (amplitude reduction ratio), which provides a quantitative evaluation of the screening effect of the barrier. Its expression is given by: $A_r = A_b/A_s$, where A_b is the displacement amplitude with the barrier and

Cette thèse est accessible à l'adresse : http://theses.insa-lyon.fr/publication/2019LYSEI042/these.pdf
© [S. Li], [2019], INSA Lyon, tous droits réservés

A_s the displacement amplitude without the barrier. For example, A_r = 0.8 means that 20% reduction of the vibration has been reached due to the installation of the barrier. The screening effect of HWB is studied by considering various geometric parameters, such as the length L, the width W and the depth of the barrier D. In the following, the screening effect of the horizontal wave barrier with various geometric parameters in Table.5-9 will be studied with PML absorbing region around the bounded soil by using co-simulation strategy.

Table 5-9 Different geometric parameters of horizontal wave barriers

(m) / i	L	W	D	(m) / i	L	W	D
1	2	2	0.5	13	10	4	0.5
2	4	2	0.5	14	12	4	0.5
3	6	2	0.5	15	14	4	0.5
4	8	2	0.5	16	16	4	0.5
5	10	2	0.5	17	2	2	1.0
6	12	2	0.5	18	4	2	1.0
7	14	2	0.5	19	6	2	1.0
8	16	2	0.5	20	8	2	1.0
9	2	4	0.5	21	10	2	1.0
10	4	4	0.5	22	12	2	1.0
11	6	4	0.5	23	14	2	1.0
12	8	4	0.5	24	16	2	1.0

Because of the different material characteristics of the coupled problem, the co-simulation strategy will be applied to satisfy the requirement of each part so as to achieve the best computation efficiency. The numerical model is divided into four subdomains: the bounded soil subdomain, the PML subdomain, the rigid foundation subdomain and the HWB subdomain. The explicit scheme is used to simulate the wave propagation in the soil and PML subdomains as explained previously. Here, Young's modulus of the rigid foundation and the horizontal wave barrier is 100

Cette thèse est accessible à l'adresse : http://theses.insa-lyon.fr/publication/2019LYSEI042/these.pdf
© [S. Li], [2019], INSA Lyon, tous droits réservés

times bigger than the one in soil subdomain. Consequently, the time step satisfying the CFL condition imposed by the mechanical properties of the rigid foundation should be 10 times smaller than the time step required in soil subdomain. As a result, it has been chosen to treat the rigid foundation and HWB subdomains with an unconditionally stable implicit Newmark time integration scheme (Constant Average Acceleration scheme.

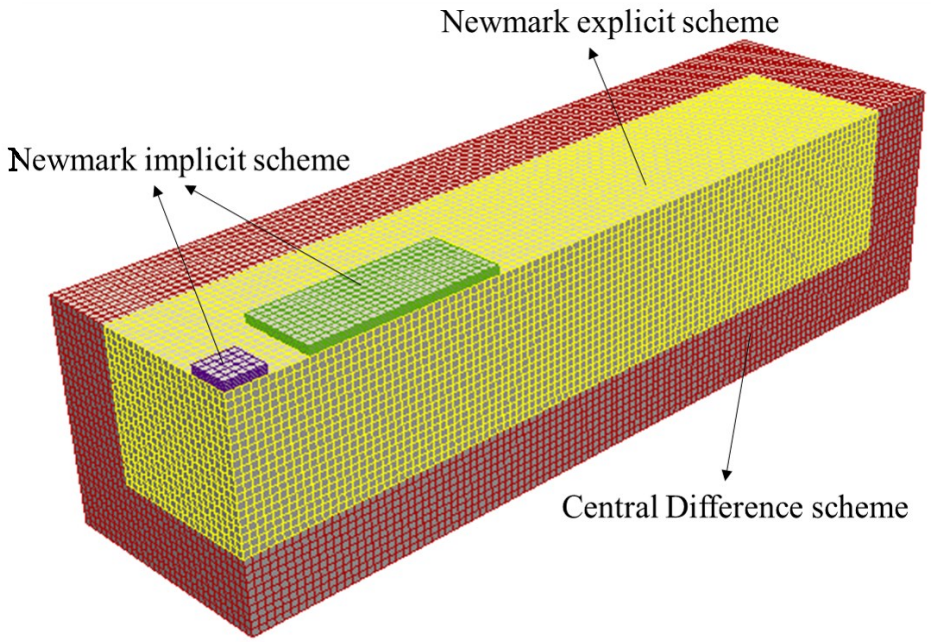

Figure 5-10 Different time integrations scheme for different subdomains

The four subdomains are coupled by GC coupling algorithm to execute explicit/implicit co-simulation. Fig.5-10 shows the discretization of the numerical model. Taking advantage of the partition strategy, the three-dimensional horizontal wave barrier problem is divided into four partitions integrated in time with their own time integrator in the most efficient way: soil subdomain (Newmark explicit scheme), barrier subdomain (Newmark implicit scheme), rigid foundation domain (Newmark implicit scheme), and PML (Central Difference scheme). In order to achieve a good accuracy in predicting the propagating waves into the soil, the finite element size is kept as 0.4m x 0.4m x 0.4m for the soil and PML subdomains, 0.4m x 0.4m x 0.1m for the horizontal wave barrier and soil foundation subdomains.

Cette thèse est accessible à l'adresse : http://theses.insa-lyon.fr/publication/2019LYSEI042/these.pdf
© [S. Li], [2019], INSA Lyon, tous droits réservés

The snapshots of displacement magnitude at different times for the wave propagation simulation are displayed in Fig.13-15, in the case of HWB with the dimension 0.5m x 4m x 10m. It is observed that the installation of the horizontal wave barrier reduces efficiently the wave intensity. No obvious reflection can be observed at the interface between the soil subdomain and the PML or from the end of the PML, indicating very satisfactory performance of the PML.

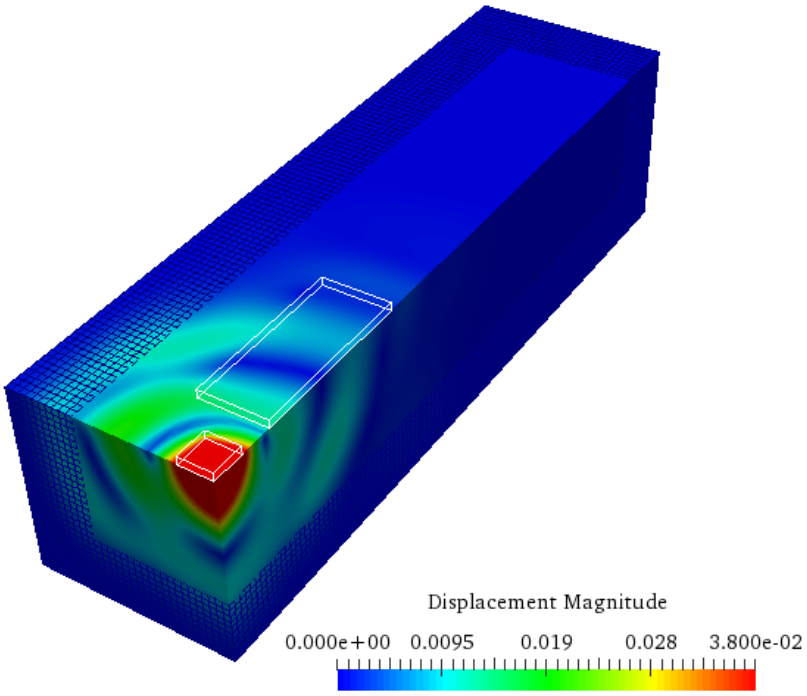

Figure 5-11 Snapshots of displacement magnitude at 0.05s

Cette thèse est accessible à l'adresse : http://theses.insa-lyon.fr/publication/2019LYSEI042/these.pdf
© [S. Li], [2019], INSA Lyon, tous droits réservés

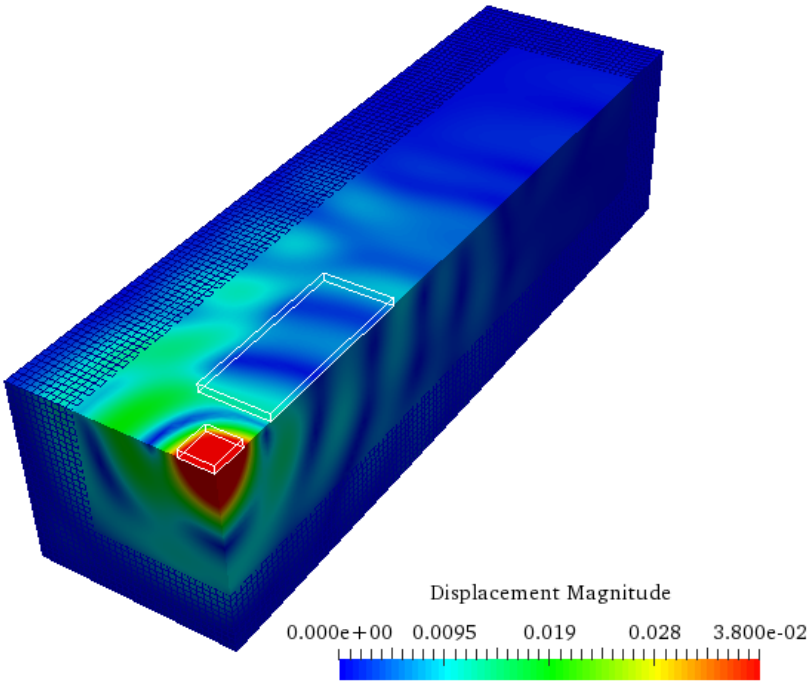

Figure 5-12 Snapshots of displacement magnitude at 0.1s

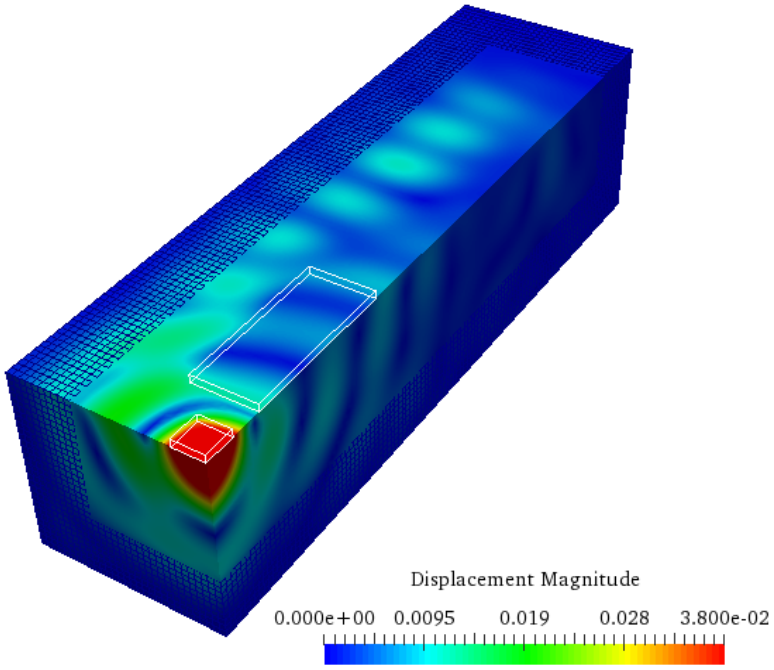

Figure 5-13 Snapshots of displacement magnitude at 0.15s

Cette thèse est accessible à l'adresse : http://theses.insa-lyon.fr/publication/2019LYSEI042/these.pdf
© [S. Li], [2019], INSA Lyon, tous droits réservés

Fig.5-14 displays the time histories of displacement at the observation point with different lengths L, compared to the results obtained without barrier. No obvious spurious waves are observed, highlighting the accuracy of the proposed three-dimensional PML. A length L of the HWB equal to 4m is insufficient to provide a significant screening effect, whereas 10m and 16m provide significant reductions in displacement. In terms of the influence of the wave barrier width, which cannot be studied in a simple 2D simulation, we can observe in Fig.5-15 that with the same length and depth, the wave barriers with the width equal to 4m can reduce the wave amplitude more efficiently than the wave barriers with the width equal to 2m. It shows that it is necessary to carry out three-dimensional simulations to thoroughly investigate the isolation effect of wave barrier in realistic situations. In the end, the influence of the wave barrier depth on the isolation effectiveness is also studied. Fig.5-16 shows the time histories of displacement at the observation point with two different depths, compared to the results obtained without barrier. With a length equal to 10m, the HWB is able to provide a significant effect with a depth equal to 0.5m. The depth parameter seems less sensitive than the length and width of the HWB.

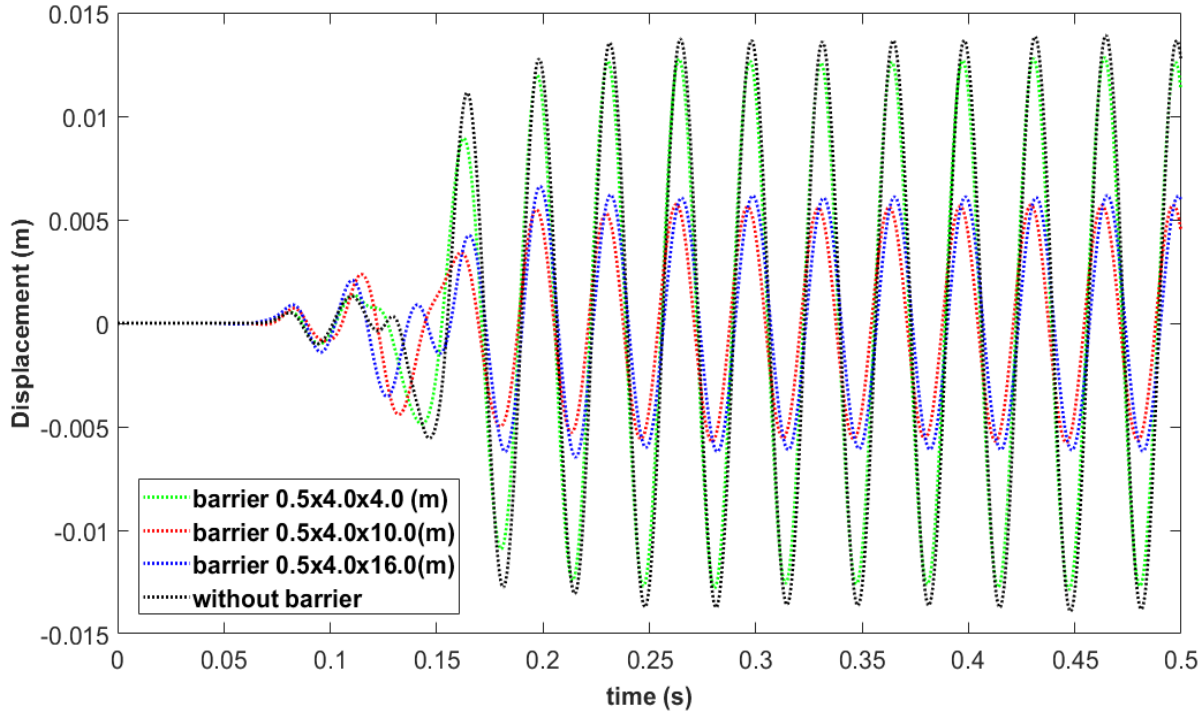

Figure 5-14 Time histories of displacement at the observation point in case of wave barriers with different lengths, compared to the results obtained without barrier.

Cette thèse est accessible à l'adresse : http://theses.insa-lyon.fr/publication/2019LYSEI042/these.pdf
© [S. Li], [2019], INSA Lyon, tous droits réservés

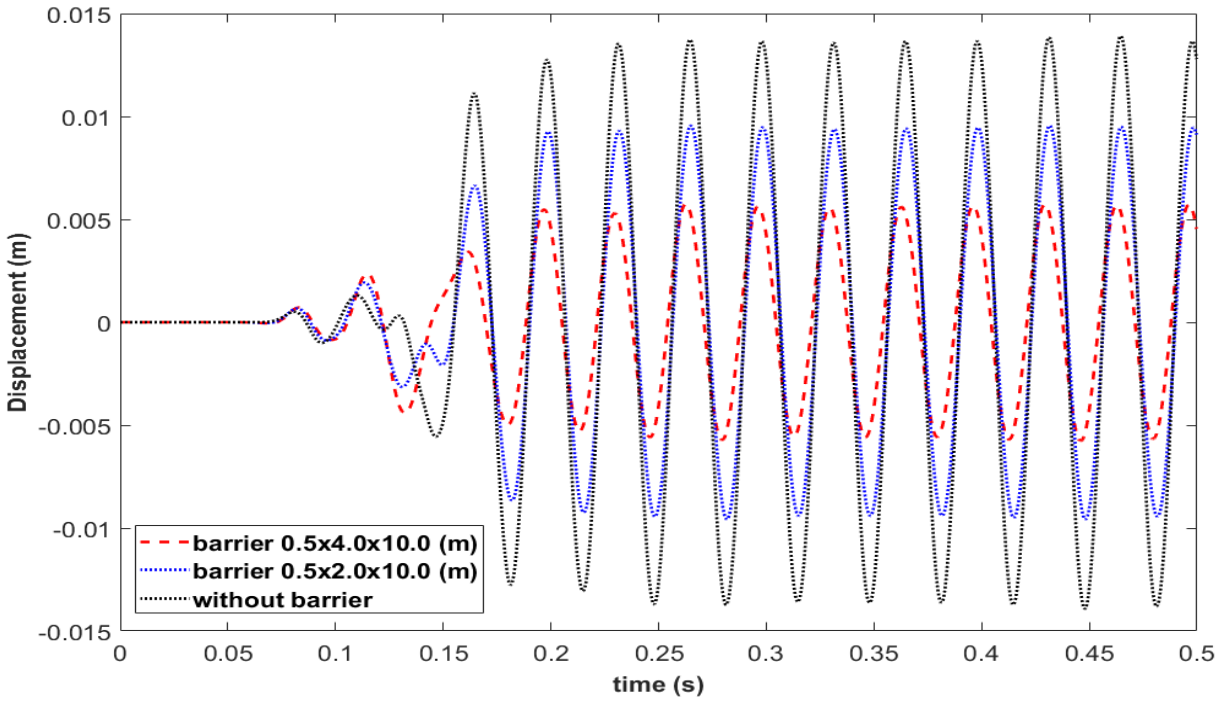

Figure 5-15 Time histories of displacement at the observation point in case of wave barriers with different widths, compared to the results obtained without barrier

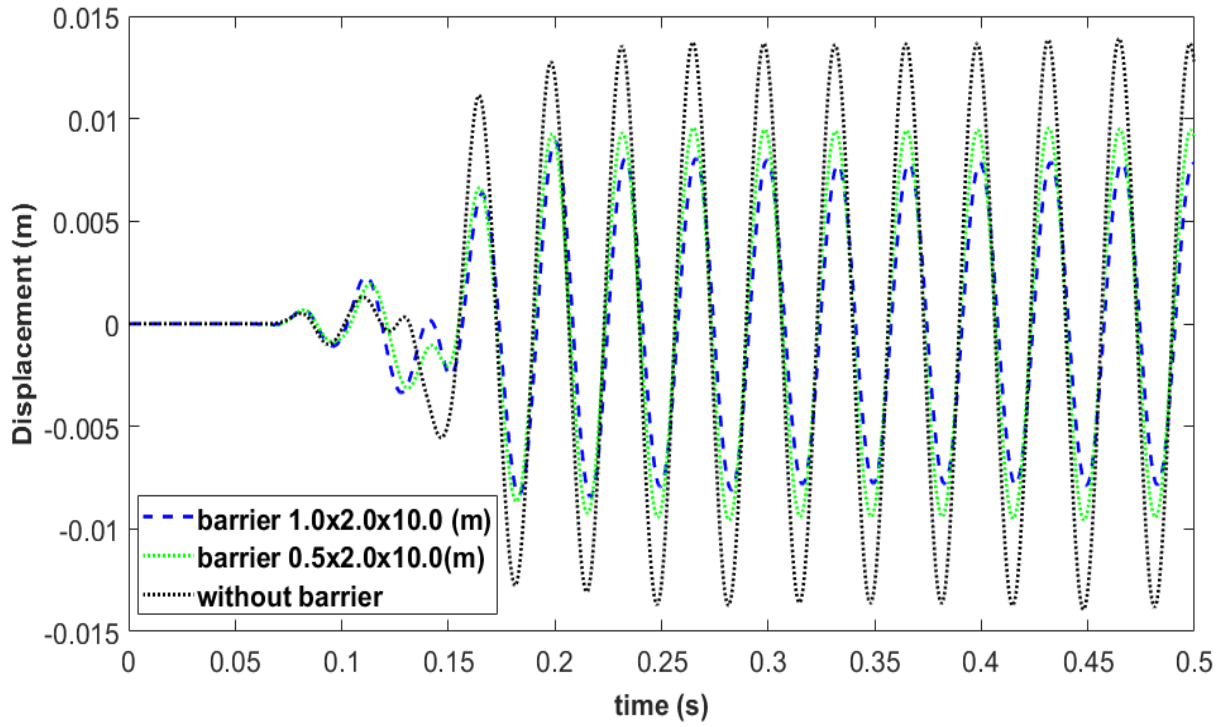

Figure 5-16 Time histories of displacement at the observation point in case of wave barriers with different depths, compared to the results obtained without barrier.

Cette thèse est accessible à l'adresse : http://theses.insa-lyon.fr/publication/2019LYSEI042/these.pdf
© [S. Li], [2019], INSA Lyon, tous droits réservés

Finally, the screening effect of the horizontal wave barrier is investigated with various geometric parameters by plotting, in Fig.5-17, the reduction ratio of the vertical displacement versus the length of the HWB. It can be seen that for the amplitude reduction ratio A_r decreases with the length L increasing. For a length L equal to about 8m, the reduction is optimal. Increasing the length L after this point does not seem to provide further reduction. In addition, it can be remarked that the width of the HWB plays also an important role, contrarily to the depth of the HWB which does not provide significant reduction when the depth is increased from 0.5m et 1m. It has to be reminded that the Rayleigh wave length is equal to 7.67 m which corresponds approximately to the optimal length observed. As remarked in the literature (Grau and Laulagnet, 2015), it is well known that the length of HWB should be chosen a little longer than the Rayleigh wavelength to obtain a good isolation effectiveness.

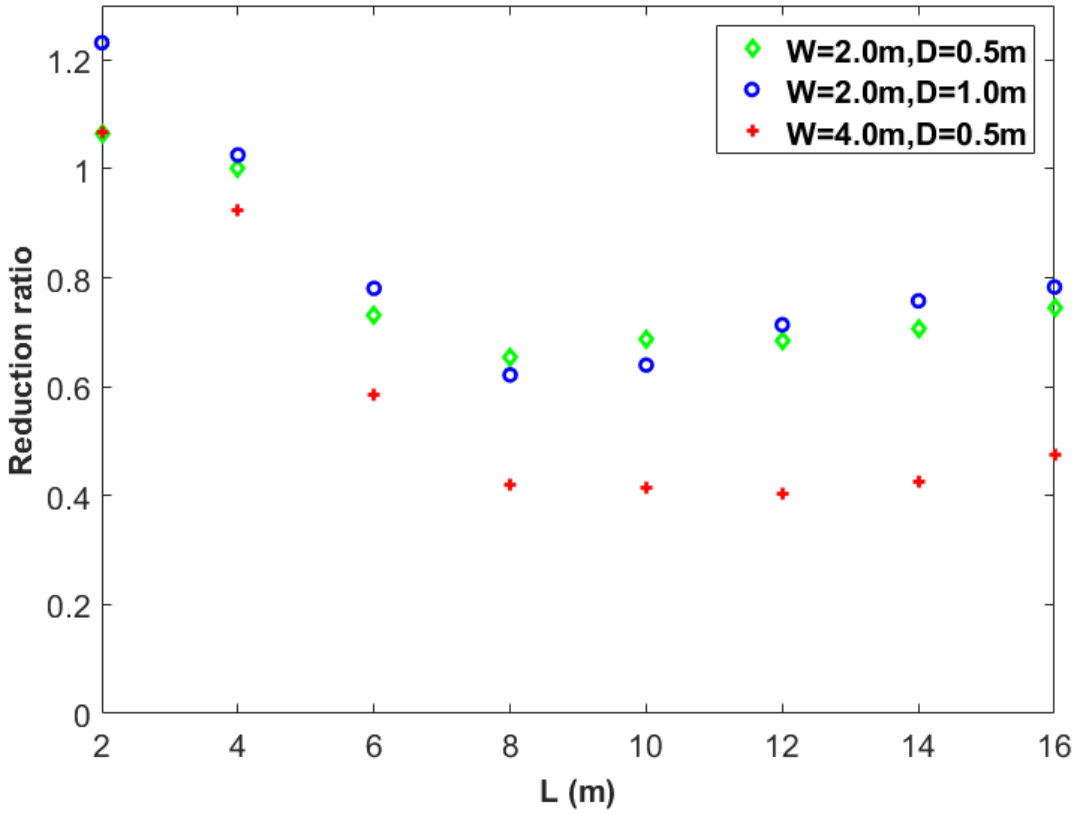

Figure 5-17 Reduction ratios of the horizontal wave barrier with various geometric parameters

Cette thèse est accessible à l'adresse : http://theses.insa-lyon.fr/publication/2019LYSEI042/these.pdf
© [S. Li], [2019], INSA Lyon, tous droits réservés

5.6 Conclusion

This chapter presents an explicit asynchronous three-dimensional PML for modeling unbounded domains through a standard displacement-based finite element method, using a novel efficient method for calculating the internal force. The coupled problem, including the interior subdomain and the PML, is implemented in the framework of Heterogeneous Asynchronous Time Integrator (HATI), enabling the interior domain to be handled by the classical finite element formulation without complex-valued stretched coordinates, whereas the PML is dealt with an explicit Central Difference scheme, with fine time steps, independently from the time stepping procedure adopted in the interior subdomain. Simple 3D Lamb's tests are considered by using different kinds of absorbing layers: the proposed PML and Absorbing Layers with Increasing Damping based on Rayleigh and Kosloff damping formulations. The superiority of the PML in terms of accuracy and computation time is highlighted. Finally, realistic 3D applications are investigated, such as Lamb's test and study of the screening effect provided by an horizontal wave barrier in mitigating ground surface vibration generated by an excited plate.

Cette thèse est accessible à l'adresse : http://theses.insa-lyon.fr/publication/2019LYSEI042/these.pdf
© [S. Li], [2019], INSA Lyon, tous droits réservés

Conclusion and perspectives

The thesis aims to propose novel designs and formulations of different methods for modeling 2D and 3D infinite media in wave propagation simulation. Three absorbing layers (Rayleigh Absorbing Layer, Kosloff Absorbing Layer, and Perfectly Matched Layer) are developed and implemented by the finite element method. Taking into account the different characteristics of each subdomain in the numerical model of wave propagation problem, the hybrid asynchronous formulations using the dual Schur approach, are developed to enable the appropriate time integration scheme and independent time step in each subdomain, in the framework of Heterogeneous (different time integration schemes) Asynchronous (different time steps depending on subdomains) Time Integration (HATI).

- Firstly, a simple and accurate Absorbing Layers with Increasing Damping (ALID) based on Rayleigh damping is presented. Thanks to the availability of the viscous Rayleigh damping matrix in commercial FE codes, it can be easily set up for damping out the incident waves at the boundary of a Finite Element mesh. In order to not reduce the critical time step in the domain of interest handled with an explicit time integration by the introduction of Rayleigh damping, Hybrid (different time integrators) Asynchronous (different time steps) Absorbing Layers using Increasing Damping (HA-ALID), is proposed, allowing for coupling different finite element codes with different time integrators and time-scales depending on the partitions of the domain. Very satisfactory results have been achieved in Lamb's test and a wave barrier problem, using Abaqus co-simulation and self-developed FEM codes.
- Secondly, the capabilities of the Kosloff damping formulation are investigated to set up efficient HA-Kosloff ALID and compared with Rayleigh formulation. The design of Kosloff absorbing layer is proposed by studying analytically the strong form of elastic wave propagation in Kosloff medium. The absorbing ability independent of frequency is derived in the form of a logarithmic decrement, as well as optimal conditions to reduce the spurious

Cette thèse est accessible à l'adresse : http://theses.insa-lyon.fr/publication/2019LYSEI042/these.pdf
© [S. Li], [2019], INSA Lyon, tous droits réservés

waves reflected at the interface between physical domain and Kosloff absorbing layer domain. The weak formulation of the coupled problem, involving the interior and Kosloff absorbing layer, is given according to a dual coupling approach with the introduction of Lagrange multipliers, which enables integrate different subdomains in time with different time integrators associated with their own time step, belonging to more general HATI methods. Kosloff formulation turns out to have a very simple finite element expression which corresponds to two new matrices, similar to the mass matrix, operating on velocities and displacements in semi-discrete equation of motion. Numerical tests are carried out to illustrate the efficiency of HA-Kosloff ALID in terms of accuracy and CPU time, and the advantages of the Kosloff damping have been highlighted in comparison to Rayleigh damping and PML.

- Thirdly, a novel three-dimensional PML, suitable for finite element implementation, has been proposed for transient elastodynamics. The displacement-based PML making use of the unsplit formulation and efficient method for calculating the internal force in PML domain is integrated into the Hybrid (different time integrators) Asynchronous (different time steps) Time Integrator framework. The frequency-independent absorbing ability and reflectionless characteristic at the interface between the non-dissipative interior domain and the PML are proved by the analytical method, on the basis of the wave propagation strong form in PML media. The weak formulation has been coupled with interior domain using the dual Schur approach proposed by Gravouil and Combescure, enabling the appropriate time integration scheme in the PML with its own time step to be chosen, whereas the interior domain is handled by the classical finite element formulation and explicit second-order accurate time integrator with a time step satisfying the CFL condition, instead of introducing complex-coordinate-stretched equations. Examples of three-dimensional semi-infinite bar, Lamb's test, and one classical soil–structure interaction problem with PML-truncated semi-infinite heterogeneous media are implemented to illustrate the efficiency of the hybrid asynchronous formulation, complemented by the comparison to HA-Rayleigh ALID and HA-Kosloff ALID. It turns out that the PML is the most efficient method for modelling three-dimensional unbounded domains in terms of accuracy and CPU time.
- Finally, in order to further demonstrate the efficiency of the hybrid approach for modeling unbounded domains, a three-dimensional application is considered for the numerical study

Cette thèse est accessible à l'adresse : http://theses.insa-lyon.fr/publication/2019LYSEI042/these.pdf
© [S. Li], [2019], INSA Lyon, tous droits réservés

of the Horizontal Wave Barrier (HWB), in the context of vibration isolation against the ground surface wave propagation produced by trains and tramways. Taking advantage of the partition strategy, the four subdomains, that is to say the two concrete plates, the soil interior domain and the PML, are coupled by GC coupling algorithm and integrated in time with their own time integration in the most efficient way. In this complex SSI situation, involving a large number of degrees of freedom, PML is integrated using a Central Difference scheme in order to reduce the computation time, as well as the interior soil domain, whereas the stiffer plates, on the soil ground, are handled with an implicit time integrator. Compared to the results obtained without barrier, it turns out that explicit-implicit co-simulation can well simulate the isolation effect of the horizontal wave barrier.

In the last years, the Spectral Element Method (SEM) is becoming more and more popular for wave propagation problems. So it will be meaningful to implement the explicit version of HA PML using spectral elements in order to be available for very large-scale wave propagation simulations. In addition, the coupling between SEM and FEM will be useful for soil-structure integration problems.

The numerical simulations in the thesis, are always carried out in the context of matching meshes. In the case of non-matching meshes, mortar approach has to be applied to treat the interface problem. It will be interesting to investigate the efficiency of the proposed hybrid approach for modeling unbounded domains in the context of non-matching meshes.

The wave propagation problems studied here is elastic. The further work will take into consideration non-linear mechanical behaviors and uncertain mechanical parameters of the soil, in order to further investigate the efficiency of the proposed hybrid approaches for modeling realistic complex soil structure interaction situations.

Cette thèse est accessible à l'adresse : http://theses.insa-lyon.fr/publication/2019LYSEI042/these.pdf
© [S. Li], [2019], INSA Lyon, tous droits réservés

Cette thèse est accessible à l'adresse : http://theses.insa-lyon.fr/publication/2019LYSEI042/these.pdf
© [S. Li], [2019], INSA Lyon, tous droits réservés

Appendix A

In the following, we summarize the matrices expressed as a function of scaling and attenuation functions f^e and f^p related to the PML.

$$\underline{\underline{F}}^e = \begin{bmatrix} 1+f_1^e(x_1) & 0 & 0 \\ 0 & 1+f_2^e(x_2) & 0 \\ 0 & 0 & 1+f_3^e(x_3) \end{bmatrix} \quad \underline{\underline{F}}^p = \begin{bmatrix} f_1^p(x_1) & 0 & 0 \\ 0 & f_2^p(x_2) & 0 \\ 0 & 0 & f_3^p(x_3) \end{bmatrix}$$

$$\underline{\underline{\tilde{F}}}^{ee} = \begin{bmatrix} f_{23}^{ee} & 0 & 0 \\ 0 & f_{13}^{ee} & 0 \\ 0 & 0 & f_{12}^{ee} \end{bmatrix} \quad \underline{\underline{\tilde{F}}}^{ep} = \begin{bmatrix} f_{23}^{ep} & 0 & 0 \\ 0 & f_{13}^{ep} & 0 \\ 0 & 0 & f_{12}^{ep} \end{bmatrix} \quad \underline{\underline{\tilde{F}}}^{pp} = \begin{bmatrix} f_{23}^{pp} & 0 & 0 \\ 0 & f_{13}^{pp} & 0 \\ 0 & 0 & f_{12}^{pp} \end{bmatrix} \qquad (A.1)$$

with

$$\begin{cases} f_{ij}^{ee} = [1+f_i^e(x_i)]\left[1+f_j^e\left(x_j\right)\right] \\ f_{ij}^{ep} = [1+f_i^e(x_i)]f_j^p\left(x_j\right) + \left[1+f_j^e\left(x_j\right)\right]f_i^p(x_i) \\ f_{ij}^{pp} = f_i^p(x_i)f_j^p\left(x_j\right) \end{cases} \qquad (A.2)$$

The scalar values involved in the right member of the equation of motion (28) are given below:

$$\begin{cases} f_M = [1+f_1^e(x_1)][1+f_2^e(x_2)][1+f_3^e(x_3)] \\ f_C = [1+f_1^e(x_1)][1+f_2^e(x_2)]f_3^p(x_3) + [1+f_1^e(x_1)][1+f_3^e(x_3)]f_2^p(x_2) \\ \qquad +[1+f_2^e(x_2)][1+f_3^e(x_3)]f_1^p(x_1) \\ f_K = f_1^p(x_1)f_2^p(x_2)[1+f_3^e(x_3)] + f_2^p(x_2)f_3^p(x_3)[1+f_1^e(x_1)] \\ \qquad +f_1^p(x_1)f_3^p(x_3)[1+f_2^e(x_2)] \\ f_H = f_1^p(x_1)f_2^p(x_2)f_3^p(x_3) \end{cases} \qquad (A.3)$$

Then, we introduce the element-wise finite element discretization for the weak form of the internal force terms in Eq. (4.42). The matrices containing shape function derivatives of 8-node hexahedral element combined with the previous scaling and attenuation functions are expressed as below:

Cette thèse est accessible à l'adresse : http://theses.insa-lyon.fr/publication/2019LYSEI042/these.pdf
© [S. Li], [2019], INSA Lyon, tous droits réservés

$$\widetilde{\mathbf{B}}_{\mathbf{I}}^{\mathbf{ee}} = \begin{bmatrix} \widetilde{N}_{I1}^{ee} & 0 & 0 \\ 0 & \widetilde{N}_{I2}^{ee} & 0 \\ 0 & 0 & \widetilde{N}_{I3}^{ee} \\ \widetilde{N}_{I2}^{ee} & \widetilde{N}_{I1}^{ee} & 0 \\ \widetilde{N}_{I3}^{ee} & 0 & \widetilde{N}_{I1}^{ee} \\ 0 & \widetilde{N}_{I3}^{ee} & \widetilde{N}_{I2}^{ee} \end{bmatrix} \tag{A.4}$$

$$\widetilde{\mathbf{B}}^{\mathbf{ee}} = [\widetilde{\mathbf{B}}_{\mathbf{1}}^{\mathbf{ee}} \quad \widetilde{\mathbf{B}}_{\mathbf{2}}^{\mathbf{ee}} \quad \cdots \quad \widetilde{\mathbf{B}}_{\mathbf{8}}^{\mathbf{ee}}] \tag{A.5}$$

The components of the above derivatives matrix are given for an index $i = 1,2,3$, without the summation convention:

$$\widetilde{N}_{Ii}^{ee} = \tilde{F}_{ii}^{ee} N_{I,i}, \qquad \widetilde{N}_{Ii}^{ep} = \tilde{F}_{ii}^{ep} N_{I,i}, \qquad \widetilde{N}_{Ii}^{pp} = \tilde{F}_{ii}^{pp} N_{I,i} \tag{A.6}$$

$\widetilde{\mathbf{B}}^{\mathbf{ep}}$ and $\widetilde{\mathbf{B}}^{\mathbf{pp}}$ are defined similarly, by replacing $\widetilde{N}_{Ii}^{ee}$ with $\widetilde{N}_{Ii}^{ep}$ and $\widetilde{N}_{Ii}^{pp}$, respectively.

The Voigt notation is adopted for the stress and strain tensors, giving the following vectors:

$$\hat{\boldsymbol{\sigma}} = \begin{Bmatrix} \sigma_{11} \\ \sigma_{22} \\ \sigma_{33} \\ \sigma_{12} \\ \sigma_{13} \\ \sigma_{23} \end{Bmatrix} \qquad \hat{\boldsymbol{\varepsilon}} = \begin{Bmatrix} \varepsilon_{11} \\ \varepsilon_{22} \\ \varepsilon_{33} \\ 2\varepsilon_{12} \\ 2\varepsilon_{13} \\ 2\varepsilon_{23} \end{Bmatrix} \tag{A.7}$$

with the constitutive relationship for an isotropic elastic medium:

$$\hat{\boldsymbol{\sigma}} = \mathbf{D}\, \hat{\boldsymbol{\varepsilon}} \tag{A.8}$$

$\mathbf{D}$ is the material constitutive matrix expressed as:

$$\mathbf{D} = \begin{bmatrix} k + 4\mu/3 & k - 2\mu/3 & k - 2\mu/3 \\ k - 2\mu/3 & k + 4\mu/3 & k - 2\mu/3 \\ k - 2\mu/3 & k - 2\mu/3 & k + 4\mu/3 \\ \mu & 0 & 0 \\ 0 & \mu & 0 \\ 0 & 0 & \mu \end{bmatrix} \tag{A.9}$$

Further, additional matrices have to be defined for the strain-deformation relationship given in Eq. (45). We express the $\hat{\mathbf{F}}^{\boldsymbol{\varepsilon}}$ and $\mathbf{B}^{\boldsymbol{\varepsilon}}$ matrices depending on shape function derivatives as well as scaling and attenuation functions:

Cette thèse est accessible à l'adresse : http://theses.insa-lyon.fr/publication/2019LYSEI042/these.pdf
© [S. Li], [2019], INSA Lyon, tous droits réservés

$$\widehat{\boldsymbol{F}}^{\boldsymbol{\varepsilon}} = \begin{bmatrix} (F_{11}^{\varepsilon})^2 & 0 & 0 & 0 & 0 & 0 \\ 0 & (F_{22}^{\varepsilon})^2 & 0 & 0 & 0 & 0 \\ 0 & 0 & (F_{33}^{\varepsilon})^2 & 0 & 0 & 0 \\ 0 & 0 & 0 & F_{11}^{\varepsilon}F_{22}^{\varepsilon} & 0 & 0 \\ 0 & 0 & 0 & 0 & F_{11}^{\varepsilon}F_{33}^{\varepsilon} & 0 \\ 0 & 0 & 0 & 0 & 0 & F_{22}^{\varepsilon}F_{33}^{\varepsilon} \end{bmatrix} \tag{A.10}$$

$$\boldsymbol{B}^{\boldsymbol{\varepsilon}} = \begin{bmatrix} F_{11}^{\varepsilon}N_{I1}^{l} & 0 & 0 \\ 0 & F_{22}^{\varepsilon}N_{I2}^{l} & 0 \\ 0 & 0 & F_{33}^{\varepsilon}N_{I3}^{l} \\ F_{11}^{\varepsilon}N_{I2}^{l} & F_{22}^{\varepsilon}N_{I1}^{l} & 0 \\ F_{22}^{\varepsilon}N_{I3}^{l} & 0 & F_{33}^{\varepsilon}N_{I1}^{l} \\ 0 & F_{22}^{\varepsilon}N_{I3}^{l} & F_{33}^{\varepsilon}N_{I2}^{l} \end{bmatrix} \tag{A.11}$$

with the matrices:

$$\underline{\underline{F}}^{l} = \left[\underline{\underline{F}}^{p} + \frac{\underline{\underline{F}}^{e}}{\Delta t}\right]^{-1} \quad \underline{\underline{F}}^{\epsilon} = \underline{\underline{F}}^{e}\underline{\underline{F}}^{l} \tag{A.12}$$

And the component in $\boldsymbol{B}^{\boldsymbol{\varepsilon}}$ matrix given by: $N_{Ii}^{l} = F_{ii}^{l}N_{I,i}$, for $i = 1,2,3$. Finally, $\widehat{\boldsymbol{F}}^{\boldsymbol{\varepsilon Q}}$ and $\boldsymbol{B}^{\boldsymbol{Q}}$ are defined similarly, by replacing $\underline{\underline{F}}^{\epsilon}$ with $\underline{\underline{F}}^{Q}$, defined by $\underline{\underline{F}}^{Q} = \underline{\underline{F}}^{p}\underline{\underline{F}}^{l}$.

Cette thèse est accessible à l'adresse : http://theses.insa-lyon.fr/publication/2019LYSEI042/these.pdf
© [S. Li], [2019], INSA Lyon, tous droits réservés

Cette thèse est accessible à l'adresse : http://theses.insa-lyon.fr/publication/2019LYSEI042/these.pdf
© [S. Li], [2019], INSA Lyon, tous droits réservés

References

ABAQUS (2013). Abaqus Analysis User's Guide.

Al-Hussaini TM and Ahmad S (1991). Simplified design for vibration screening by open and in-filled trenches. Journal of Geotechnical and Geoenvironmental Engineering, ASCE, 17(1), 67–88.

Basu U and Chopra A (2003). Perfectly matched layers for time-harmonic elastodynamics of unbounded domains: theory and finite-element implementation. Computer Methods in Applied Mechanics and Engineering, 192, 1337-1375.

Basu U and Chopra A (2004). Perfectly matched layers for transient elastodynamics of unbounded domains. International Journal for Numerical Methods in Engineering, 59, 1039–1074.

Basu U (2009). Explicit finite element perfectly matched layer for transient three-dimensional elastic waves. International journal for numerical methods in engineering, 77,151–176.

Basu U and Chopra A (2010). Perfectly matched layers for transient elastodynamics of unbounded domains. International Journal for Numerical Methods in Engineering, 59, 1039–1074.

Belytschko T, Yen HJ and Mullen R (1979). Mixed methods for time integration, Computer Methods in Applied Mechanics and Engineering, 17-18, 259–275.

Belytschko T and Lu YY (1992). Stability analysis of elemental explicit–implicit partitions by Fourier methods, Computer Methods in Applied Mechanics and Engineering, 95 (1), 87–96.

Belytschko T and Lu YY (1993). Explicit multi-time step integration for first and second order finite element semidiscretizations. Computer Methods in Applied Mechanics and Engineering, 108, 353–383.

Belytschko T, Liu W and Moran B (2000). Nonlinear finite elements for continua and structures. Wiley, New York.

Cette thèse est accessible à l'adresse : http://theses.insa-lyon.fr/publication/2019LYSEI042/these.pdf
© [S. Li], [2019], INSA Lyon, tous droits réservés

Bérenger JP (1994). A perfectly matched layer for the absorption of electromagnetic waves. Journal of Computational Physics, 114, 185-200.

Beskos DE, Dasgupta B and Vardoulakis IG (1986). Vibration isolation using open or filled trenches, Computational Mechanics, 1, 43-63.

Brun M, Batti A, Limam A and Combescure A (2012). Implicit/explicit multi-time step co-computations for predicting reinforced concrete structure response under earthquake loading. Soil Dynamics and Earthquake Engineering, 33, 19–37.

Brun M, Batti A, Limam A and Gravouil A (2012). Explicit/implicit multi-time step co-computations for blast analyses on a reinforced concrete frame structure. Finite Elements in Analysis and Design, 52, 41–59.

Brun M, Batti A, Combescure A and Gravouil A (2014). External coupling software based on macro-and micro-time scales for explicit/implicit multi-time-step co-computations in structural dynamics. Finite Elements in Analysis and Design, 86, 101–119.

Brun M, Gravouil A, Combescure A and Limam A (2015). Two FETI-based heterogeneous time step coupling methods for Newmark and α-schemes derived from the energy method. Computer Methods in Applied Mechanics and Engineering, 283, 130–176.

Brun M, Zafati E, Djeran-Maigre I and Prunier F (2016). Hybrid asynchronous perfectly matched layer for seismic wave propagation in unbounded domains. Finite Elements in Analysis and Design, 122, 1–15.

Brun M, Zafati E, Li S and Djeran-Maigre I. (2017) Coupling implicit multi-time step Perfectly Matched Layers with FE explicit codes for seismic wave propagation in 2D unbounded domains. VII International Conference on Coupled Problems in Science and Engineering, Rhodes, Greece.

Carcione JM and Kosloff D (2013). Representation of matched-layer kernels with viscoelastic mechanical models. International Journal of Numerical Analysis and Modeling, 10, 221–232.

Çelebi E, Fırat S, Beyhan G, Çankaya İ, Vural İ and Kırtel O (2009). Field experiments on wave propagation and vibration isolation by using wave barriers. Soil Dynamics and Earthquake Engineering, 29, 824–833.

Cette thèse est accessible à l'adresse : http://theses.insa-lyon.fr/publication/2019LYSEI042/these.pdf
© [S. Li], [2019], INSA Lyon, tous droits réservés

Chew WC and Weedon WH (1994). A 3D perfectly matched medium from modified Maxwell's equations with stretched coordinates. Microwave and Optical Technology Letters, 7, 599–604.

Chew WC and Liu QH (1996). Perfectly matched layers for elastodynamics: a new absorbing boundary condition. Journal of Computational Acoustics, 4, 341–359.

Collino F and Tsogka C (2001). Application of the perfectly matched absorbing layer model to the linear elastodynamic problem in anisotropic heterogeneous media. Geophysics, 66 (1), 294–307.

Combescure A and Gravouil A (2002). A numerical scheme to couple subdomains with different time-steps for predominantly linear transient analysis, Computer Methods in Applied Mechanics and Engineering, 191, 1129–1157.

Courant R, Friedrichs K and Lewy H (1928). On the Partial Difference Equations of Mathematical Physics. Mathematische Annalen, 100, 32-74.

Daniel WJT (1998). A study of the stability of subcycling algorithms in structural dynamics, Computer Methods in Applied Mechanics and Engineering, 156, 1–13.

Demailly JP (2006). Analyse numérique et équations différentielles, EDP Sciences.

DIANA (2016). DIANA User's Manual, Version10.1, DIANA FEA BV.

Farhat C and Roux FX (1991). A method of finite element tearing and interconnecting and its parallel solution algorithm. International Journal for Numerical Methods in Engineering, 32, 1205–1227.

Farhat C, Crivelli L, and Roux FX (1994). Transient FETI methodology for large-scale parallel implicit computations in structural mechanics. International Journal for Numerical Methods in Engineering, 37, 1945–1975.

Fathi A, Poursartip B and Kallivokas LF (2015). Time-domain hybrid formulations for wave simulations in three-dimensional PML-truncated heterogeneous media. International Journal for Numerical Methods in Engineering, 101, 165–198.

Fekak FE, Brun M, Gravouil A and Depale B (2017). A new heterogeneous asynchronous explicit–implicit time integrator for non smooth dynamics. Computational Mechanics, 60, 1-21.

Cette thèse est accessible à l'adresse : http://theses.insa-lyon.fr/publication/2019LYSEI042/these.pdf
© [S. Li], [2019], INSA Lyon, tous droits réservés

Flanagan DP and Belytschko T (1981). A uniform strain hexahedron and quadrilateral with orthogonal hourglass control. International Journal for Numerical Methods in Engineering, 17, 679–706.

Gravouil A and Combescure A (2001). A multi-time-step explicit–implicit method for non-linear structural dynamics, International Journal for Numerical Methods in Engineering, 50, 199–225.

Gravouil A, Combescure A and Brun M (2015). Heterogeneous asynchronous time integrators for computational structural dynamics. International Journal for Numerical Methods in Engineering, 102, 202–232.

Grau L and Laulagnet B (2015). Effect of horizontal wave barriers on ground vibration propagation, The Journal of the Acoustical Society of America,138(3): 1334-45.

Harari I and Albocher U (2006). Studies of FE/PML for exterior problems of time-harmonic elastic waves. Computer Methods in Applied Mechanics and Engineering,195, 3854-3879.

Heirbrant K (2006). Identification du bruit sismique ambiant sur le réseau de Parkfield en Californie. Université Joseph Fourier, France.

Hilber H, Hughes T and Taylor R (1977). Improved numerical dissipation for time integration algorithms in structural dynamics, Earthquake Engineering and Structural Dynamics; 5: 283–292.

Hughes TJR and Liu WK (1978). Implicit–explicit finite elements in transient analysis: implementation and numerical examples, Journal of Applied Mechanics, 45, 375–378.

Hughes TJR (1987). The Finite Element Method: Linear static and dynamic finite element analysis. Prentice-Hall, Englewood Cliffs, NJ.

Irons BM (1966). Engineering applications of numerical integration in stiffness method. AIAA Journal, 4(11), 2035-2037.

Israeli M and Orszag SA (1981). Approximation of radiation boundary conditions. Journal of Computational Physics; 41:115–135.

Klisinski M and Mostrom A (1998). On stability of multitime step integration procedures. Journal of engineering Mechanics, 124 (7), 783–793.

Cette thèse est accessible à l'adresse : http://theses.insa-lyon.fr/publication/2019LYSEI042/these.pdf
© [S. Li], [2019], INSA Lyon, tous droits réservés

Kosloff D and Kosloff R (1986). Absorbing boundaries for wave propagation problems. Journal of Computational Physics, 63, 363-376.

Kucukcoban S and Kallivokas LF (2011). Mixed perfectly-matched-layers for direct transient analysis in 2d elastic heterogeneous media. Computer Methods in Applied Mechanics and Engineering, 200, 57-76.

Kucukcoban S and Kallivokas LF (2013). A symmetric hybrid formulation for transient wave simulations in PML-truncated heterogeneous media. Wave Motion, 50, 57–79.

Lamb H (1903). Proceedings of the 38th Royal Society of London, 72, 128–130.

Li S, Brun M, Djeran-Maigre I and Kuznetsov S (2018). Explicit/implicit multi-time step co-simulation in unbounded medium with Rayleigh damping and application for wave barrier. European Journal of Environmental and Civil Engineering.

Li S, Brun M, Djeran-Maigre I and Kuznetsov S (2019). Hybrid asynchronous absorbing layers based on Kosloff damping for seismic wave propagation in unbounded domains. Computers and Geotechnics, 109, 69-81.

Li S, Brun M, Djeran-Maigre I and Kuznetsov S (2017). Modélisation des barrières d'ondes sismiques en milieu semi-infini à l'aide de co-simulation explicite/implicite, multi-pas de temps. Colloque International France – Colombie, Lyon, France.

Li S, Brun M, Djeran-Maigre I and Kuznetsov S (2018). Numerical modelling of wave barrier in 2D unbounded medium using Explicit/Implicit multi-time step co-simulation. IOP Conference Series: Materials Science and Engineering Safety in Construction.

Li S, Brun M, Djeran-Maigre I and Kuznetsov S (2018). Hybrid asynchronous absorbing layers for seismic wave propagation in 2D unbounded domains. International Congress 16ECEE, Thessaloniki, Greece, 2018

LS-DYNA (2019). LS-DYNA Keyword User's Manual. Livermore Software Technology Corporation.

Mase GT and Mase GE (1999). Continuum mechanics for engineers, CRC Press.

Cette thèse est accessible à l'adresse : http://theses.insa-lyon.fr/publication/2019LYSEI042/these.pdf
© [S. Li], [2019], INSA Lyon, tous droits réservés

Matzen R (2011). An efficient finite element time-domain formulation for the elastic second-order wave equation: A non split complex frequency shifted convolutional pml. International Journal for Numerical Methods in Engineering, 88, 951-973.

Milsom J. Field Geophysics (2003). The geological field guide series, John Wiley and Sons, Ltd.

Newmark NM (1959). A method of computation for structural dynamics. Journal of the Engineering Mechanics Division (ASCE), 85, 67-94.

Nunez-Ramirez J, Marongiu JC and Brun M (2017). A partitioned approach for the coupling of SPH and FE methods for transient nonlinear FSI problems with incompatible time-steps. International Journal for Numerical Methods in Engineering, 109, 1391-1417.

Rajagopal P, Drozdz M, Skelton EA, Lowe MJS and Craster RV (2012). On the use of the absorbing layers to simulate the propagation of elastic waves in unbounded isotropic media using commercially available finite element packages. NDT and E International, 5, 30-40.

Schiavia A and Rossib L (2015). Vibration perception in buildings: a survey from the historical origins to the present day. Energy Procedia, 78, 2-7.

Semblat JF (1999). Validation des calculs de propagation d'ondes: approches par éléments finis et éléments de frontière. European Journal of Environmental and Civil Engineering, 3, 7-8.

Semblat JF and Pecker A (2009). Waves and vibrations in soils: Earthquakes, Traffic, Shocks, Construction works, IUSS Press.

Semblat JF, Lenti L and Gandomzadeh A (2011). A simple multi-directional absorbing layer method to simulate elastic wave propagation in unbounded domains. International Journal for Numerical Methods in Engineering, 85, 1543-1563.

Smith IM, Griffiths DV and Margetts L (2014). Programming the Finite Element Method, Fifth Edition, John Wiley and Sons, Ltd.

Viora P (2017). Phénomènes géologiques liés au fonctionnement de la Terre.

Wang T and Tang X (2003). Finite-difference modeling of elastic wave propagation: a nonsplitting perfectly matched approach. Geophysics, 68, 1749-1755.

Cette thèse est accessible à l'adresse : http://theses.insa-lyon.fr/publication/2019LYSEI042/these.pdf
© [S. Li], [2019], INSA Lyon, tous droits réservés

Zafati E, Brun M, Djeran-Maigre I and Prunier F (2014). Multi-directional and multi-time step absorbing layer for unbounded domain. Comptes Rendus Mécanique, 342, 539-557.

Zafati E, Brun M, Djeran-Maigre I and Prunier F (2015). Design of an efficient multi-directional explicit/implicit Rayleigh absorbing layer for seismic wave propagation in unbounded domain using a strong form formulation. International Journal for Numerical Methods in Engineering, 106, 83-112.

Zienkiewicz OC, Taylor RL and Zhu JZ (2005). The Finite Element Method, 5th edition. McGraw-Hill, London.

Zuchowski L, Brun M and De Martin F (2018). Co-simulation coupling spectral/finite elements for 3D soil/structure interaction problems. Comptes Rendus Mécanique, 346, 408-422.

Cette thèse est accessible à l'adresse : http://theses.insa-lyon.fr/publication/2019LYSEI042/these.pdf
© [S. Li], [2019], INSA Lyon, tous droits réservés

Cette thèse est accessible à l'adresse : http://theses.insa-lyon.fr/publication/2019LYSEI042/these.pdf
© [S. Li], [2019], INSA Lyon, tous droits réservés

FOLIO ADMINISTRATIF

THESE DE L'UNIVERSITE DE LYON OPEREE AU SEIN DE L'INSA LYON

NOM : LI DATE de SOUTENANCE : 08/07/2019
(avec précision du nom de jeune fille, le cas échéant)

Prénoms : SIJIA

TITRE : Couches absorbantes pour la propagation d'ondes dans les sols non bornés à l'aide de la décomposition en sous-domaines et l'intégration temporelle hybride asynchrone

NATURE : Doctorat Numéro d'ordre : 2019LYSEI042

Ecole doctorale : MEGA

Spécialité :Mécanique – Génie Mécanique – Génie Civil

RESUME :

Le travail de thèse a pour objet de proposer de nouvelles formulations de couches absorbantes artificielles aux frontières des maillages éléments finis pour la simulation numérique de la propagation d'ondes dans des milieux infinis 2D et 3D, afin de traiter des problèmes complexes d'interaction sol-structure en dynamique transitoire.

Trois couches absorbantes sont développées : les couches absorbantes basées sur les amortissements de Rayleigh ou de Kosloff et les PML (Perfectly Matched Layers). En étudiant analytiquement la forme forte de la propagation des ondes dans chaque milieu, il est montré que les amortissements de Kosloff et ceux provenant de PML sont indépendants de la fréquence, ce qui n'est pas le cas de l'amortissement de Rayleigh. Le problème de propagation des ondes à l'interface entre un milieu élastique non dissipatif et un milieu dissipatif est aussi étudié, afin de dégager des conditions optimales permettant de calibrer les caractéristiques mécaniques des couches absorbantes.

La discrétisation spatiale des couches absorbantes est conduite à l'aide de la méthode des éléments finis, tandis que la discrétisation temporelle s'appuie sur le cadre performant et flexible des méthodes dites HATI (Heterogeneous Asynchronous Time Integrator), permettant de sélectionner, selon les caractéristiques des sous-domaines du problème et les phénomènes physiques qui s'y déroulent, les schémas d'intégration temporelle et les pas de temps les mieux adaptés.

L'efficacité des trois couches absorbantes hybrides asynchrones pour la modélisation de domaines non bornés a été illustrée dans diverses applications numériques, 2D et 3D, telles que le test de Lamb dans des milieux hétérogènes stratifiés ou des problèmes d'interaction sol-structure comportant des barrières d'ondes. Finalement, des versions implicite ou explicite de PML asynchrone sont mises en place et testées pour des problèmes avec un nombre important de degrés de liberté. Elles s'avèrent être plus précises et performantes que les couches absorbantes basées sur des amortissements de Rayleigh et Kosloff.

MOTS-CLÉS : Couches absorbantes de Rayleigh ; Couches absorbantes de Kosloff ; Couches parfaitement adaptées (PML) ; Propagation d'ondes ; Milieux infinis ; Couplage sous-domaines ; Intégration Temporelle Hybride Asynchrone (HATI) ; Analyse transitoire ; Barrière d'ondes

Laboratoire (s) de recherche : Laboratoire GEOMAS, INSA de Lyon

Directeurs de thèse: DJERAN-MAIGRE, Irini; BRUN, Michaël

Président de jury :

Composition du jury :

CHAILLAT, Stéphanie	Chargée de recherche (HDR) ENSTA ParisTech	Rapporteur
LENTI, Luca	Chargé de recherche (HDR) IFSTTAR	Rapporteur
SHAHROUR, Isam	Professeur Université de Lille	Examinateur
KUZNETSOV, Sergey	Professeur IPM Académie des sciences de Russie	Examinateur
DJERAN-MAIGRE, Irini	Professeur INSA Lyon	Directrice de thèse
BRUN, Michaël	Maître de Conférences (HDR) INSA Lyon	Directeur de thèse

Cette thèse est accessible à l'adresse : http://theses.insa-lyon.fr/publication/2019LYSEI042/these.pdf
© [S. Li], [2019], INSA Lyon, tous droits réservés